Medical Grade Bioabsorbable Composites for the 3D Printing of Multi-Material Orthopaedic Devices

by

Cillian Thompson

A dissertation submitted in partial fulfillment of the requirements for the degree of Doctor of Philosophy in

Material Science and Engineering

Universidad Carlos III de Madrid

Advisor(s):

Javier Llorca
Carlos Daniel González

Tutor:

Mónica Campos Gómez

December 2023

To my family,
Mam and Dad, my sisters Maria and Orlaith, and my granny, Maura.

Acknowledgements

Writing the acknowledgements for this thesis has been something that I have thought about for the last 4 years, using it as a motivation to keep me going when times were difficult and experiments were not working, but also when times were good. However, I never thought the day would actually arrive where I would be writing them, it always seemed so far away. This section of the thesis is dedicated to all the people that have helped me along the way, both professionally and personally, and for all the friendships made.

"One basic human need is to be appreciated. We all think wonderful things about people but rarely tell them. Praise becomes valuable only when you impart it." - Romans 12:6-8

First of all, I would like to thank my supervisors, Javier Llorca, and Carlos González. Without you both, I simply would not have succeeded in this PhD. You have been there for me and supported me in ways that not all supervisors would do. From the beginning when I was adjusting to life in Spain, to the more difficult times during COVID when it looked like experiments were a thing of the past, and in the last year when experiments appeared to never end, your constant support kept me focused and motivated. Your expertise in the area of material science and now with the added touch of biomedical material science has been nothing short of incredible; you have both always pushed me to think more critically, you always asked the difficult questions (which were definitely needed), and got me to repeat experiments to find the answers to the questions that remained. I will always feel grateful to you both for everything you have done for me in the last 4 years. I would also like to use these acknowledgements to pay my respects to Dr. Claudio Lopes, another great scientist that was sadly taken from the world too soon, may you rest in peace Claudio.

If there are special acknowledgements that need to be given, it is without a doubt to my family. My parents Enda and Síle, my sisters Maria and Orlaith, and my grandmother Maura. Although I would rarely find the words to say this to you in person, in writing it's a little bit easier. You have all shaped me into the man I am today, and that is something that I will forever be grateful for. From the weekly calls, keeping me informed on all of the local news and gossip over the last few years, to showing interest in my PhD as something that you only had the slightest idea about, you always made me feel that what I was doing was worthwhile. The love and support I have received from you not just throughout the PhD but throughout my life has always encouraged me and drove me on to better myself. It was you in the end that convinced me that moving to Spain to do a PhD would be worth it despite my difficulties in believing it at the time, and now to have reached this point, over 4 years later, I can safely say it is something I will never regret. I will

always feel indebted to you all and I will never be able to thank you enough for supporting me throughout this journey.

Within IMDEA there are so many people that have made an impact on my life, however, there are some which have made such a profound impact, they have to mentioned here. Carolina, I feel like we started the journey together and finished it together, you have always been a huge source of support to me, it is something I will always be grateful for. From meeting continuously to tell each other about our problems, to offering advice and support to each other, and to celebrating the good times too, most recently in Monção, it is an honour to call you a friend. To Keayvan 'the iranian massage specialist' Keramati, my brother, we grew closer and closer together after spending many late evenings in IMDEA working, and to have reached this level in our friendship is something I will always cherish, you're a gentle soul that was always there to listen and help me whenever I needed, from all the smoking breaks, to the football pitch and everything in-between you are a gentleman, and I thank you for that. I can only wish you the very best of luck in your future career especially now going to Tenerife. To Davide 'Villaverde Alto' Mocerino, the Napolitano that never ever ever talks about Napoli or how much better it is than everywhere else, although you don't like to show it you're really a big softie with a big heart. I appreciate all the help you have offered since your time here, and of course our big trip from last year will be something I will always remember and cherish (#nuggets). I think most of all I will miss getting to annoy you in the mornings with my positivity. To one of the true broders, Nacho R., you are without a doubt one of the biggest gentlemen I have come across, from the first day knowing you in IMDEA being shocked at the amount of Irish numbers you had in your phone, to my last day (and of course the present day), we have built a very strong relationship. From the countless nights out, to the more meaningful conversations and everything in between, thank you from the bottom of my heart. To my other true broder, Guille, I cannot put into words how happy I am to have shared my time at IMDEA with you, both professionally and personally. Whether it was nights out, hiking and having conversations about life, or showing you the Irish breakfast, for your constant support throughout the PhD and help with the bioexperiments and everthing else, thank you my man, it is an honour to have you as a friend.

To Lucía Echevarría Pastrana, the robots expert, although I only got to really know you in the last 6 or 7 months of the thesis, they were very important months for me and I am especially grateful that you were a part of them. For all of the laughs, the random distractions in the lab, the dinners whether at home or out, the walks, the conversations, the local gastronomía, the lifts to and from IMDEA, and the "what would you do if..." questions. For all the talks about which apartments you would buy, for making me speak Spanish (and helping me improve it 10-fold), for never freaking out when my tooth fell out, and for always convincing me to stay the extra 10 minutes at breakfast at UPM or at lunch (they were always worth it, even though I pretended they weren't). For all your support, advice, and every other impact you have made, thank you. You are a special person and a great scientist with a bright future ahead of you, whether it is in robots or not, or in Switzerland or not, and I'm very excited to see how far you go.

"Determination, with an optimistic attitude, is the key factor for success" - Dalai Lama

To the other people in the composite group and on the 0 floor. To my deskmate/adopted sister for the last 7 months of my PhD, Sofía. Your constant smiles and positivity in the mornings gave me energy and it is something I hope you never change, you always knew how to make the day better for everyone around you, so thank you. To my prodigy/adopted sister, Ángela, you are such a kind-hearted and funny person, always supportive (except when making fun of my spanish), I will miss all of our conversations about everything. Above all else from what I have seen you're a great scientist always asking the right questions, and I leave you to continue my work with full confidence in your capabilities. To María, a small girl with a huge heart, thank you for absolutely everything, one of my favourite times of the day would be seeing you approaching myself and Sofía to have our morning meeting, and again in the evening when it was just me left before you would leave, and we would talk about the most random things. Your constant attempts to scare me always worked, and I hope you continue to do the same with Ángela when the time comes. To Cristian, for always joining those morning meetings at our desks as well, for always smiling and being such a positive person, for all the conversations at lunch, I will really miss seeing you on a daily basis, thank you for everything. To Moises, the man who never eats, unless it's a going away party or from catering, never change, you were always asking interesting questions, so thank you. To Radouan, Jerry, and Lucia Doyle, although you all entered a month before I left you all integrated really well to the group full of smiles and I wish you all the best in your futures. To Venkatesh, for always sending me the best Dad jokes, for being a great man for a drink and always up for a chat, thank you.

A number of colleagues from the composites group have left IMDEA but made a profound impact on my time here and should be acknowledged, Andrea F, for taking me under her wing on my very first day in IMDEA and helping me to speak Spanish and feel integrated at a time when everything appeared very different to me. To Joaquín, the machine learning expert and the man I always said that when I understood him in Spanish I could call myself fluent, thank you, and to David A, for providing me with the very important python code for analysing DIC results. To Cristina Pascual-González, for all of your help at the beginning of my time in IMDEA, and for all of your work, which helped pave the way for my thesis, thank you. To Pilar Bardisa also, for all of your help with the mechanical degradation tests last year it was greatly appreciated, thank you.

To Richard, the man with the best mix of german/mexican efficiency I have ever seen. I will never be able to thank you enough for all the times you brought me home from work and the times you took me there too. You and your smart car 100% saved my PhD. From all the interesting conversations about our professional and personal lives, to trying to get the perfect run with green lights, to the 15 minute workouts, and all things rage cage, it was such a huge pleasure sharing those times with you. You are a person that is bound for success and it is an honour to call you a friend. I wish you nothing but the best in your future my man.

"True friendship multiplies the good in life and divides its evils. Strive to have friends, for life without friends is like life on a desert island... to find one real friend in a lifetime is good fortune; to keep him is a blessing." - Baltasar Gracián

To Delabat, one of the very few men to enjoy going out as much if not more, than me. I will miss telling you my monday morning stories. You always stood up for us PhD students and I

have no doubt you have a bright future ahead, thank you for everything. To Claudia, for being so supportive and kind, and for always making sure everything was going ok, I sincerely thank you for everything you did for me last year and wish you the absolute best in your future and of course now while you're in Germany, you deserve it. To Nacho E. (el guapetón), for always being there for me throughout the 4 years, for always supporting and being a positive presence, all the random hugs, and of course for all the rugby conversations, another holiday is due in Portugal. To Ángela C. and Andrea G. for always providing the positive vibes and the "vengaaa Cillian tu puedessss, animooooo" it might have seemed insignificant to you both but to me it helped a lot, so thank you. To Blanca and Carlota, for all the breakfast mornings, and for always being so supportive and always offering to help me whenever you saw me approaching the biolab depressed, because I had to repeat experiments for the n^{th} time. Your positivity is something that always motivated me and your help in the lab is something I will always be grateful for, thank you.

To Cyril (one of the very few frenchmen that everyone likes), for always being the most positive person in IMDEA on any given morning, always greeting me with a smile and a "Bonjouuurrr Cillian". For the weekend in your pueblo full of laughs, the BBQ, and of course the padel tournament. For all of the daps trying to get it perfect just to make the sound more crisp, you are a true gentleman Cyril and I will miss you dearly.

To Alessandro de Nardi, for always being supportive, always providing the most interesting conversation topics, especially concerning salads, and for your random video calls man I really appreciate you and wish you nothing but the best for your future, wherever it may be! To Rafa, for being the one man I have full confidence would have a good chance in the animal fighting scenarios that we create, for always knowing how to break an awkward silence with a "pues se ha quedado una buena tarde", and a master of accent imitations. Thank you for everything, I am proud to call you a brother. To Nabil (my Palestinian brother), for always providing the laughs at coffee and at lunch, for knowing more about Irish history than some Irish people I know, I am beyond grateful to have met you. To Isa, my car competition with Richard, but always happy to let me take the seat in the evenings, thank you for everything. To Elena (for asking that one time for my SEM session), and to Phuong and Ellie (the best breakfast companions), thank you all, it has been a pleasure knowing you over the last months/years.

To José Mancias, the man from outside Chicago, thank you for everything my man, for all the memories, whether it was during the big trip last year with our Italian comrade, the more meaningful conversations, the nights out, and everything in between. To Jorge V. (a.k.a. George Best) for all of your support in the form of Instagram reels you always helped take my mind off things, for all the nights out and everything else, thank you. To Paul Williams (my fellow guiri), the truest form of a man from Tenerife, it was a huge pleasure getting to know you my man, you were a great form of support for me over the last year, thank you for everything. To Marcos, el futbolista, for always being there supporting me after coming out of a meeting with a load of corrections to do, a real gentleman. To Saumya, I just want to thank you for being you, you always made me laugh with your impersonations of me, your questions about Spanish, and how much you believed my stories that weren't true, please never change. To Eugenia, one of my PhD partners, to finish at the same time as you has given me strength and motivation to keep going especially when I had lost that motivation which I will always be grateful for, thank you so much. To Yuyao,

the 3D printing genius, I wish you nothing but good fortune and luck for the future Yuyao it was a pleasure to have known you and worked with you. To Wahaaj, the expert on all things magnesium wires and PEO coatings. Similarly to Carolina we started the journey together and almost finished it at the same time, for your constant support over the last number of years it has also been a pleasure getting to know you, for sharing the memories together and a few wonderful meals, thank you! To Carmen, Oscar, Jesús, and the many others from the second floor that I regularly spoke to, thank you for everything!

To Jose Hobson, for always being a calming influence, encouraging me to speak Spanish, for all of your help with polymers and all the interesting conversations, and simply for being one of the truest forms of a gentleman, I thank you. To Alba (maquinaa), for all the memories, for the invitation to la granja, it has been such a pleasure getting to know you more over the last year, you are such a kind and gentle person and I wish you the absolute best for your future, both inside and outside science. Berti for "primero de todo como están los maquinas" and for your incredible rendition of salsa tequila corazón, I was mesmerised, thank you for everything my man. A thank you as well to Jorge for always rubbing la barriga telling me it will all be fine. To Lola (la futbolista), you are such a kind-hearted person, it has been a huge pleasure getting to know you both professionally, personally and on the football pitch, thank you! To Jimena, thank you from the bottom of my heart for all the help you have given me throughout my time here, for all of the GPC data and molecular weight tests, and for your expertise, I will always be grateful. I wish you the absolute best in your future career and wherever it may take you.

I also need to acknowledge Mónica Echeverry for all of her help and feedback with everything to do with the biological testing. For your help in designing and analysing the results of the bio-experiments and organising the necessary training needed for me, thank you for everything Mónica, I wish you the best for your future career. To Jose Sanchez (Pepe), for all of your help and support over the last year, your expertise in all things electrical and for our shared trip to Ireland, it has been a pleasure getting to know you Pepe, I wish you the best for the future. To Juan Pedro (Juan Pe), your expertise in the area of polymers has been an absolute blessing for me throughout this thesis. Your constant support and the time you dedicate to explaining things is something that I will always be grateful for, so thank you. To Damien Tourret and Adrián Boccardo, and the rest of the research group for all of your help developing and implementing the python script that changed the way the wire was 3D printed for the better, it was a huge help and I am so grateful for the work you both did so thank you!

Desde la 4ª planta tengo que agradecer toda la gente, pero especialmente a Mariana por toda su ayuda y apoyo desde que me mudé a España hasta mi último día. Fue un gran placer trabajar contigo participando en las charlas invitadas a IFEMA y todo lo demás. Espero que nos crucemos en el futuro. También quiero reconocer y agradecer a Ainhoa toda su ayuda con todos los documentos oficiales, contratos, y todo lo demás que necesité firmar a lo largo de los años.

A los técnicos. El trabajo que haceis es nada menos que mágico. Dr. Vanesa Martínez, José Luis Jiménez, Miguel de la Cruz, Amalia San Román, Mónica Sales, Dr. Manuel Avella, Dr. Javier García, y Jonathan Espinoza. Todos me habéis ayudado de una manera que nunca podré agradeceros lo suficiente. Un comentario especial para Vanesa y José Luis, por todo el trabajo que habéis hecho por mí, por toda la ayuda, toda la preparación de muestras para los ensayos

de tracción y los ensayos del push-out, para cada vez que tenia que repitir los experimentos, todos vuestros consejos y apoyo especialmente en el último año, y por supuesto por los constantes recordatorios de que debería haber estado escribiendo cada vez que me veíais en el laboratorio. Gracias del fondo de mi corazón.

Al personal de la limpieza, Cristina, Paco, Juanja y Gemma. Por recibirme siempre con una sonrisa, por todas las conversaciones, las risas y la positividad, muchas gracias.

To everyone else in IMDEA that I have crossed paths with, although you may not be listed here in the acknowledgements, I want you to know that each and every one of you made my life easier in IMDEA, you are all some of the friendliest people I have met in my life, and the atmosphere in IMDEA is something that should always be cherished. Thank you to you all!

To the BioImplant consortium and project, it was a huge honour to have worked with all of you over the years, the expertise made available to us was incredible. A special thanks to Ted Vaughan and Eva Barrett for their organisation of all the meetings, reports, and workshops. A special thanks also to James Wall, Jacqui O'Connor and Johannes Werner from 3D Technology Ltd., your expertise in the area of 3D printing were unmatched and Johannes, your work on the 3D printer made a huge difference in the research of this PhD, thank you all!

Now for outside of my family, and work; To all of my friends that I have made here in Madrid and to the Madrid Harps. Thank you all for always being able to take my mind off the PhD when I needed it and for also always showing interest in what I have been doing even when it wasn't always understood you have all provided such a welcoming and good community. You have all been asking me for months if I was finished with the PhD yet and here it is, finally done. To Matty, Paddy, KK, Aido, Brian, Seany, Pat, Benny and of course Pa, you have all kept me sane and provided the support that I 100% needed throughout the course of my PhD, I cannot thank ye all enough!

To the lads at home, you have all been a source of support for me over the last 4 years and have always encouraged me to go further in life, ye are all true bruds (insert ric flair). From the trips to Madrid to Tenerife we definitely took advantage of my time here. To Kealan, for all the phone calls listening to my problems, you were always there to offer advice and support and also to provide a much-needed laugh, I cannot thank you enough. To Conor for also always being one phone call away, for showing interest in my work, for offering advice, and for the constant reminder that biodegrable is actually spelt biodegradable. To Daire for always thinking of a new way for us to make money, for the trips, living the good life, and always encouraging me to do the same. To Richard, the endless messing around each other has always and will always be something to keep me grounded and sane, thank you brud. To Pete, the man who never stops travelling, always a pleasure having you visit Madrid, always great conversations and better nights out had with you. To Donnchadh, Eoghan, Ruairi, Steve, and Mark again boys, you have always shown interest in what I was doing and were always there to offer support, but more importantly go for a pint or a night out whenever I was home, and for that I thank you! To Rachel, who was there for me for a significant portion of my PhD, thank you for all of your support, for all of the interest you have shown and for always being there for me, it is greatly appreciated!

I also want to acknowledge Denis Sulta, a man who has provided me with the necessary listening entertainment that I have needed during this PhD to keep me from losing my mind entirely.

And finally, I want to thank you, the reader, for making it to the end of these long acknowledgements, as you can see a lot of people have helped make this PhD possible. In one way it has been a long journey, but in another way the time has also flown by. I hope that all the blood, sweat and tears in the form of passion and effort are reflected in the rest of this thesis.

This investigation was supported by the European Union's Horizon 2020 research and innovation program under the European Training Network BioImpant (Development of improved bioresorbable materials for orthopaedic and vascular implant applications), Marie Skłodowska-Curie grant agreement No 813869. Additional support from the Spanish Research Agency through the grant PID2021-124389OB-C21 is also gratefully acknowledged.

"Nothing in life is to be feared, it is only to be understood. Now is the time to understand more, so that we may fear less." - Marie Skłodowska-Curie

Published and submitted content

- Pascual-González, C., **Thompson, C.**, de la Vega, J., Biurrun Churruca, N., Fernández-Blázquez, J.P., Lizarralde, I., Herráez-Molinero, D., González, C. and LLorca, J., 2022. Processing and properties of PLA/Mg filaments for 3D printing of scaffolds for biomedical applications. Rapid Prototyping Journal, 28(5), pp.884-894. https://doi.org/10.1108/RPJ-06-2021-0152
  This study was wholly included in Chapter 3. The material from this source is not singled out with typographic means and references.

- Pascual-González, C., de la Vega, J., **Thompson, C.**, Fernandez-Blazquez, J.P., Herraez-Molinero, D., Biurrun, N., Lizarralde, I., Del Rio, J.S., Gonzalez, C. and LLorca, J., 2022. Processing and mechanical properties of novel biodegradable poly-lactic acid/Zn 3D printed scaffolds for application in tissue regeneration. Journal of the Mechanical Behavior of Biomedical Materials, 132, p.105290. https://doi.org/10.1016/j.jmbbm.2022.105290
  This study was wholly included in Chapter 3. The material from this source is not singled out with typographic means and references.

- **Thompson, C.**, Dominguez, G., Bardisa, P., Liu, Y., Fernandez-Blazquez, J.P., Sánchez del Rıo, Echeverry-Rendon, M., González, C., and Llorca, J., "Medical grade 3D printable bioabsorbable PLDL/Mg and PLDL/Zn composites for biomedical applications", Submitted for Publication, Journal of Biomedical Material Research, Aug. 2023.
  This study was wholly included in Chapter 4. The material from this source is not singled out with typographic means and references.

- **Thompson, C.**, González, C., and Llorca, J., "3D printing of continuous metal wire-reinforced polymer-matrix composites", Submitted for Publication, Additive Manufacturing, Oct. 2023.
  This study was wholly included in Chapter 5. The material from this source is not singled out with typographic means and references.

Articles to be submitted for publication

- **Thompson, C.**, González, C., and Llorca, J., "Additively Manufactured Continuous Wire-Reinforced PLDL/Mg Composites", Planned submission, Jan. 2024.
  This study was wholly included in Chapter 6. The material from this source is not singled out with typographic means and references.

Other research merits

This work has also been well-reviewed by experts at the following International Conferences:

Cillian Thompson, Cristina Pascual-González, Mónica Echeverry Rendón , Carlos González , Javier Llorca, Characterisation of additively manufactured bioabsorbable PLDL/Mg composites for orthopaedic applications, Bioengineering in Ireland Conference, Galway, Ireland 20-21 May 2022, (Oral Presentation) - 3rd Place Award for Best Presentation in the area of Biomaterials.

Cillian Thompson, Cristina Pascual-González, Mónica Echeverry Rendón , Carlos González , Javier Llorca, Additive manufacturing of bioabsorbable polymer/metal particle (Mg or Zn) composites for orthopaedic applications, European Solid Mechanics Conference (Ireland) 4-8 July 2022, (Oral Presentation)

Cillian Thompson, Carlos González , Javier Llorca, 3D Printing of Medical Grade Polymer Composites for Orthopaedic Applications, European Society of Biomaterials, Bordeaux, France 4-8 September 2022, (Poster Presentation)

The author of this thesis was also the recipient of the Directors Choice Award for his Three-Minute Thesis presentation in IMDEA Materials Institute in March 2022.

The author of this thesis was also a finalist in the Thesis Talk 2022 competition in UC3M in July 2022, for his presentation "Creating Bioabsorbable Materials to Repair Bones".

Furthermore, the author of this thesis also supervised a Bachelor's student as a co-tutor described in the following table:

Thesis Type	Dates	Student Name	Title
Bachelor's	Oct. 2022 - Jan. 2023	Pilar Bardisa	Development of medical grade bioabsorbable composite materials and determine the effect of in vitro degradation on the mechanical properties of the materials

Abstract

Biodegradable polymer composites fabricated by 3D printing may overcome many of the challenges associated with permanent non-degradable metals (Ti, stainless steel, Co-Cr) or with biodegradable polymers (PLA, PLGA, and PCL) and biodegradable metals (Mg, Zn, Fe) by achieving a final material with synergistic properties for orthopaedic implant applications.

This thesis deals with the development of a filament production process for combining biodegradable polymers and metals through a two-step extrusion process. PLA was combined with Mg or Zn particles and extruded into filaments with constant diameter and a homogeneous dispersion of particles, suitable for 3D printing. This strategy was then used to 3D print biocompatible composites comprised of medical grade PLDL with a 4% volume fraction of Mg or Zn metallic particles. The addition of Mg and Zn to the PLDL material was able to increase the degradation rate of PLDL, and reduce the acidity of the PBS environment at 37°C over a 1-year period. The addition of the particles slightly increased the stiffness, but reduced the strength of the PLDL due to the stress concentrations around the metallic particles. The composite materials exhibited excellent biocompatibility properties in terms of the material-cell interactions and cell proliferation. This study demonstrates that the addition of metallic particles to the polymer matrix can tailor the degradation properties but does not improve the mechanical properties.

To overcome this latter limitation, a customised FFF 3D printer was developed to incorporate continuous metallic wires into a polymer matrix. The 3D printer comprised of 4 individual print heads capable of printing with 4 different materials, one of which was a continuous metallic wire, while the others could print thermoplastic polymers/composites. Unidirectionally reinforced PLA/Al wire composites were manufactured with 15% and 25% volume fractions of Al wire. The composite reinforced with 25% volume fraction of Al wires showed a six-fold increase in elastic modulus while the strength improved by 63% with respect to the polymeric matrix. Furthermore, medical grade PLDL composite coupons unidirectionally reinforced with a 15% volume fraction of Mg wires were manufactured by 3D printing. Mg wires with and without a surface treatment by plasma electrolytic oxidation were used. The mechanical properties showed a three-fold increase in the elastic modulus and up to a 80% increase in tensile strength compared to the matrix in air and at ambient temperature. Excellent interface strength was observed in the composites containing the Mg wire modified by plasma electrolytic oxidation. The oxide layer on the Mg wires reduced the degradation rate of the Mg wires and suppressed pitting corrosion. The mechanical properties of the PLDL matrix in the composite decreased dramatically when tested in water at 37°C very likely because of the increased chain mobility induced by the disruption of the intermolecular interactions due to the synergistic contribution of water and temperature.

Finally, a multi-material composite material was fabricated using three print heads on the customised printer. The coupon consisted of various layers of PLA, PLA reinforced with Mg particles, and PLA reinforced with Mg wires. This proof-of-concept demonstrates the possibility to create 3D printed multilayer scaffolds in which the properties of each layer can be tailored to meet specific requirements in terms of mechanical properties, degradation rate, and cytocompatibility, opening the path to manufacturing 3D printed multimaterial biomedical devices.

"A mind stretched by a new experience can never go back to its old dimensions."

Ancient Proverb

Contents

List of Figures

List of Tables

Introduction

1

1.1 Bone

Bones serve multifaceted roles within the human body, encompassing critical functions that collectively contribute to the organism's overall health and functionality. Primarily, bones offer vital support by serving as the foundational framework that preserves the body's structural integrity and bears the substantial loads exerted by muscles and organs. Additionally, they act as a protective barrier, shielding crucial organs like the brain, heart, lungs, and spinal cord, thereby safeguarding these essential components from external harm. Moreover, bones play an indispensable role in facilitating movement, as they provide attachment sites for muscles via tendons. When muscles contract, they exert force on these attachments, resulting in coordinated bodily motion. Beyond structural and mechanical functions, bones house red bone marrow, which serves as a prolific site for hematopoiesis, the process of generating red blood cells, white blood cells, and platelets. Furthermore, bones serve as reservoirs for essential minerals, particularly calcium and phosphorus, which can be mobilised into the bloodstream as needed to support a diverse array of physiological functions. Lastly, bones actively contribute to metabolic regulation, modulating calcium levels in the bloodstream to maintain the delicate balance of calcium homeostasis, which is vital for numerous cellular processes and overall bodily health. Collectively, these roles underscore the profound significance of bones in sustaining human health and well-being. A breakdown of bone in terms of its composition, structure, mechanical properties, and fracture/healing mechanisms is provided to understand the scope and objectives of this thesis.

1.1.1 Bone composition

Bones are made up of a number of components such as minerals, organic matrix, and bone cells. Bone is comprised of the mineral phase, primarily made up of 60-70% of hydroxyapatite ($Ca_{10}(PO_4)6(OH)_2$), a type of calcium phosphate; 20-30% of organic matrix in the form of proteins (primarily collagen type I), and up to 10% of water. The actual proportions depend on the bone type and region [1, 2, 3]. The mineral phase is responsible for the stiffness of the tissue [4, 5], and it is arranged in the form of plate- or rod-like nano-crystals [6, 7, 8, 9]. Collagen type I represents the major structural component of bone and provides the strength and toughness [1, 6, 7]. It is made by the agglomeration of collagen fibrils that are constituted by triple helical arrangement of amino acid chains and serves as a framework for the nucleation of hydroxyapatite

mineral crystals to form the bone [2, 10]. Collagen is not only present in bones but also in tendons and ligaments [6].

A number of bone cells are found in the bone composition, which are responsible for bone homeostasis [11]. There are three cell types which are responsible for the modeling and remodeling of bone. (i) Osteoblasts, a bone forming cell, which convert into (ii) osteocytes when enriched in minerals and mature. They reside in the lamellae and sense when the bone is damaged (Figure 1.1). Finally, bone-destroying (iii) osteoclasts which cleave away at old bone cells to allow for new bone formation [7, 12, 13].

1.1.2 Bone types and structure

Bones can be classified into five types; long bones, short bones, flat bones, irregular bones and sesamoid bones [14]. From the viewpoint of the bone structure, there are two types of bone, namely cortical (compact) bone and trabecular bone, also referred to as cancellous or spongy bone [3, 7, 12, 13, 14].

Cortical bone is the dense, calcified bone that forms the outermost layer, a shell-like structure that surrounds the marrow cavity and comprises 80% of the skeleton [3, 14]. In terms of bone remodelling, cortical bone has a slow turnover rate, in the form of cleavage of old bone and deposition of new bone [3]. It is made up of concentric ring structures at a micro-level, called lamellae. Haversian canals are found within these lamellae and supply the bone with blood vessels and nerves [14] (Figure 1.1) [3, 12, 14].

Trabecular bone fills the interior of long bones, the metaphyseal region of long bones, and the epiphyseal ends of bones. It stands for 20% of skeletal mass, but accounts for 80% of the bone surface area due to its interconnected porous architecture (trabeculae) separated by marrow spaces [3, 14]. The bone marrow is found in the unoccupied cavities of the trabecular bone, and these cavities are lined with the endosteum at the interface between the marrow and the bone (Figure 1.1) [10]. It is less dense and has a much higher remodeling rate (26% volume per year) than cortical bone (3% volume per year), thereby demonstrating a major metabolic function. Trabecular bone contributes to mechanical support in bones such as the vertebrae and provides initial mineral supplies in states of acute deficiency [3, 14].

1.1.3 Mechanical properties of bone

The mechanical properties of bone depend on a number of factors such as anatomical location, structure, gender, age, and race [5, 15, 16]. In general, the mechanical properties encompass remarkable strength, stiffness, and hardness, rendering bones capable of withstanding compressive, tensile, and shear forces while safeguarding the body's structural integrity [17]. Cortical bone is known to be much stiffer and stronger than trabecular bone (Figure 1.2 (a)) and one study reported that trabecular bone contributed <10% to the tensile strength of the femoral neck [18]. The higher strength associated with cortical bone can be attributed to the lower turnover rate and therefore greater mineralisation compared to trabecular bone [19].

In relation to the affect of age and sex on the mechanical properties of bone, Mosekilde et al.[20] were able to show an age-related decrease in bone density within the vertebrae of up to 50%

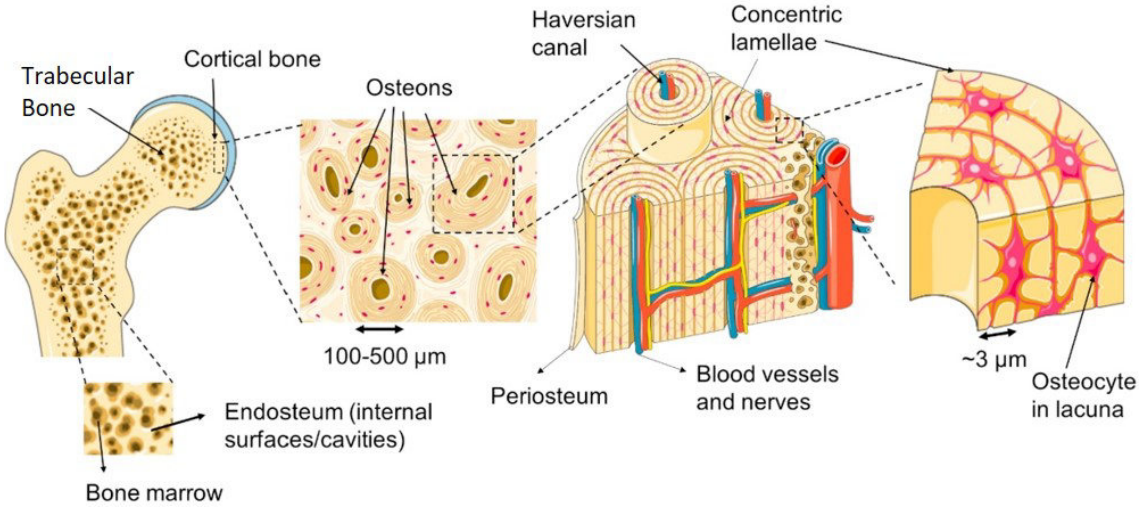

Figure 1.1: Macro-to-micro representation of the structure of bone from left to right. Cortical and trabecular bone form the internal macroscopic structure. Cortical bone is comprised of tightly packed osteons with a periosteum membrane. Haversian canals, which supply the bone with blood and nerve vessels, are surrounded by organised concentric lamellae structures. The osteocytes reside in very small spaces called lacuna between the lamellae [10].

from the age of 20 to 80. This reduction in density also led to a dramatic reduction in strength (Figure 1.2 (b)). Women undergo higher levels (up to 50%) of bone mass loss and strength over their lifespan in comparison to men. These loss in bone mass and strength are driven by a loss of mechanosensitivity correlated with a loss of oestrogen, especially in the postmenopause stage, leading to osteoporosis [21].

At a microscopic level, the mechanical properties of bone depend on the density, mineralisation, osteon orientation, and the composition of the bone with respect to the ratio of collagen to hydroxyapatite. Bones are anisotropic materials and their mechanical properties depend on the loading direction: they are stronger in the longitudinal direction compared to the transverse direction, as shown in Figure 1.2 (c) [6, 20, 22].

The elastic modulus for human cortical bone in the femur is reported as 17 $\pm$ 3 GPa, while the tensile strength is the 160$\pm$12 MPa [23]. However, different experimental reports have shown a large variability (elastic modulus of cortical bone as high as 27 GPa and as low as 10 GPa were measured [24]). In general, cortical bone is stiffer and stronger than trabecular bone but more brittle, and fails at approximately 3% tensile strain, while trabecular bone can reach 25% strain. The elastic modulus of trabecular bone is around 8 GPa for the human vertebra and up to 12 GPa in the femoral neck according to nanoindentation tests in the wet condition of the bone (fresh) [16, 19]. It should be noted that nanoindentation tends to overestimate the elastic modulus. The tensile strength of trabecular bone is in the range from 2 MPa in the vertebrae up to 7 MPa in the femoral bone, while other reports indicate values of up to 50 MPa [19, 24].

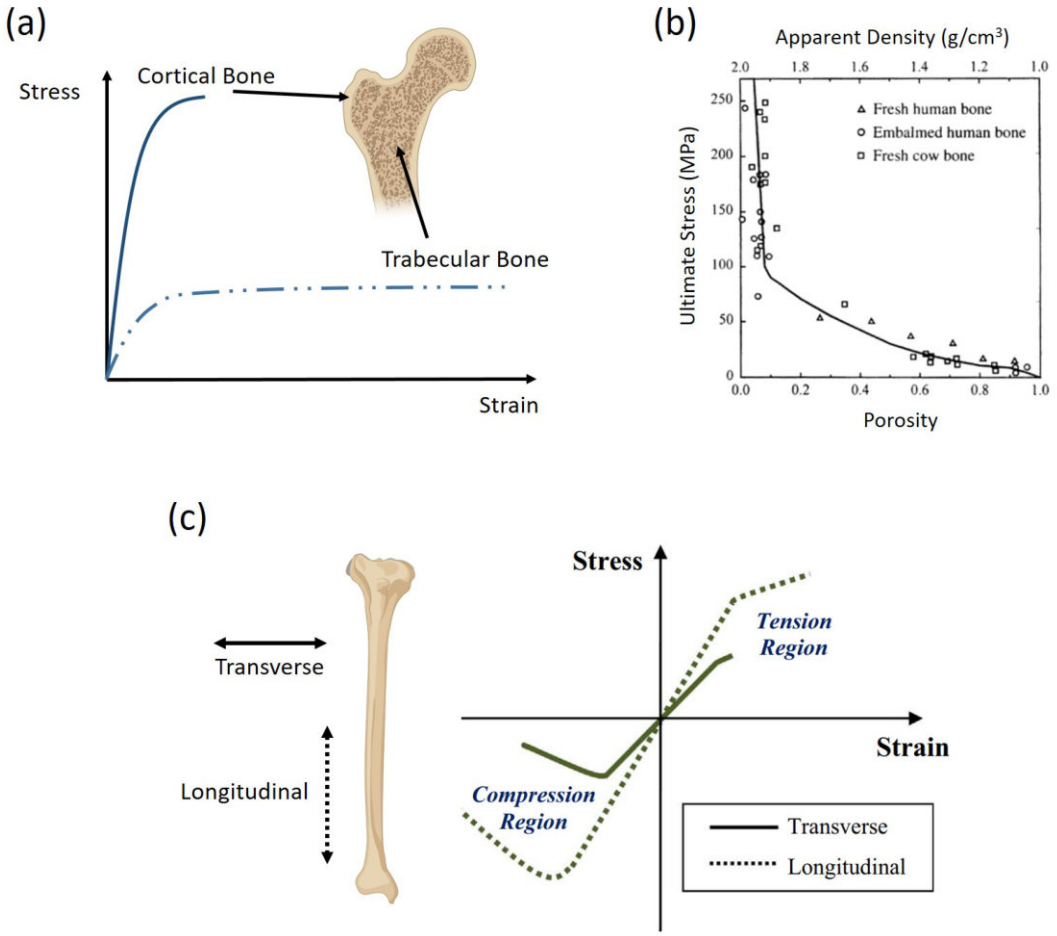

Figure 1.2: (a) Typical tensile stress-strain curves of cortical and trabecular bone. (b) Effect of porosity on the tensile strength of different types of bone [6]. (c) Stress-strain curves ob bone in both tension and compression in the longitudinal and transversal directions [22].

1.1.4 Bone fractures and healing process

Bone fractures were often life-threatening injuries until the beginning of the 20th century. There was a high prevalence of amputations carried out and, even in the event of a fracture healing, the incidence of deformity and loss of function was high [25]. More than 28 million orthopaedic surgeries were carried out annually according to a 2019 report, and this number expected to increase because of the aging of the population [26]. It has been shown that there is a significant correlation between the elderly age of the population and the number of orthopaedic injuries such as fractures. More recently the Centre for Disease Control and Prevention in the U.S. indicated that approximately half of the patients that suffered orthopaedic fractures were over the age of 65. It is also estimated that the elderly population of the world will increase by 2 billion in 2050 hence the market for orthopaedics is expected to grow accordingly [25].

There are two main mechanisms of bone fracture. The first one is driven by accidental loads that lead to mechanical stresses higher than the bone strength resulting in a traumatic fracture

[27]. The second mechanism is creep or fatigue which can result in what are referred to as stress fractures. Stress fractures are caused when the bone is subjected to constant and/or cyclic loads for long periods of time which cause microdamage in the form of microcracks. If the accumulation of microdamage is faster than the rate at which the bone can heal through remodelling, it results in a macrocrack or fracture.

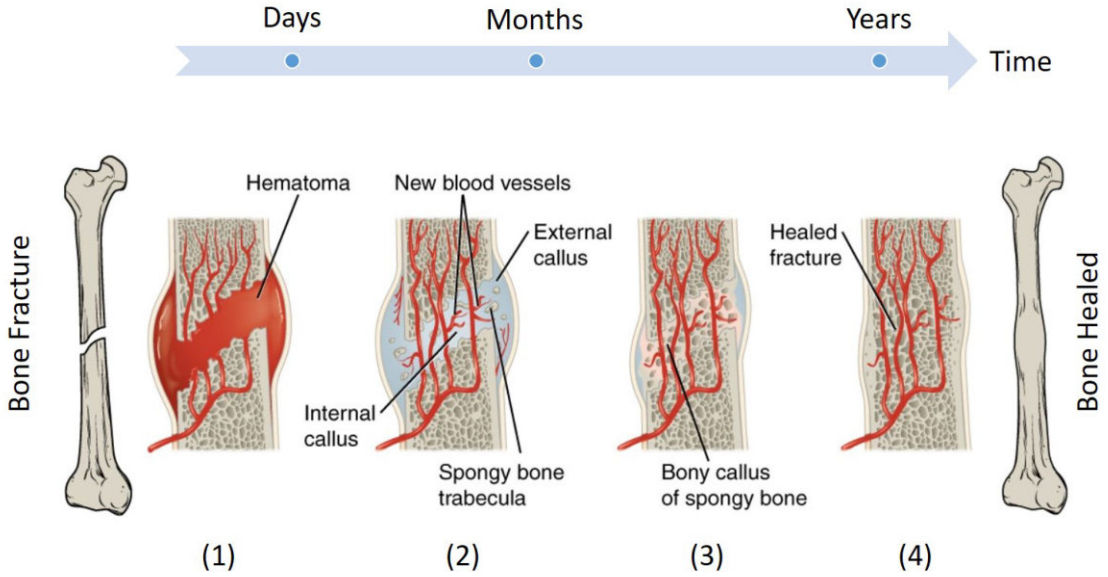

Figure 1.3: Schematic diagram of the bone healing process after fracture. The corresponding bone healing timelines are also indicated [28]. The bone healing phases are numbered from 1 to 4.

Stress fractures are termed highly stable compressed fractures that heal by direct remodelling across the fracture line with minimal callus formation. They are common injuries in athletes, affecting children, adolescents, and adults at all levels of training [29]. In general, fractures heal through a combination of intramembranous and endochondral ossification. Intramembranous ossification occurs internally to the periosteum through the formation of a hard callus, while endochondral bone formation starts external to the periosteum, adjacent to the fracture site, in the regions with lower mechanical stability. The repair process consists of four phases that overlap (Figure 1.3) [30]: (1) there is an immediate inflammatory response after the fracture, which leads to the recruitment of mesenchymal stem cells (MSCs) which differentiate (2) into chondrocytes and osteoblasts capable of creating cartilage and bone, respectively [29]. (3) Once the cartilage matrix is produced, it transitions from mineralised cartilage to bone and this primary bone formation is followed by remodelling. During this phase, the original bony callus is reshaped through resorption, followed by secondary bone formation (4), which is composed of continuous remodelling coupled with osteoblast activity and the establishment of the bone marrow. This sequence of events aims to reestablish the functional load-bearing anatomical structure [30, 31]. It is also worth noting the timeline for this sequence of events. The inflammatory response is immediate and lasts up to 7 days, the formation of the haematoma, the differentiation into cartilage and subsequent bone (phases 2 and 3), can take from 3-6 months, while the final phase of remodelling is in the order of magnitude of years [32].

1.1.5 Orthopaedic fixation devices

There are a number of clinical indications for the use of orthopaedic fixation devices: fractures (small/long bone, open or closed, transverse or longitudinal), soft tissue fixations (cruciate/medial ligament repairs, rotator cuff repairs, meniscal repairs, biceps and shoulder repairs), osteotomies (surgical removal of part of the bone to correct an abnormality caused by variable growth of paired bones, limb length discrepancies, torsional deformities), and arthrodesis (fusion of bone forming joints in the ankle, wrist, and spine) [33, 34, 35]. The goal of fixation devices is to treat and stabilise the fracture with techniques that result in complete healing and recovery of the bone(s) with little to no morbidity after surgery.

Open Reduction Internal Fixation (ORIF) surgeries are carried out when the simple cast/splint method (closed reduction) will not work, or the critical defect size has been reached ($\approx$ 2 cm), hence further intervention is required. ORIF surgeries use a series/combination of plates, screws, or rods/wires to induce fracture healing in bones (Figure 1.4(a)). The primary function of the devices is to stabilise fractured bone fragments by immobilisation, or torn soft tissue by holding replaced soft tissue over the bone to allow for fast healing. Bone screws are the most commonly used orthopaedic fixation device [25, 33].

External fixation devices are used to hold individual bone fragments in place using wires or pins attached to an external frame. They are used in patients that are suffering from multiple injuries which require rapid application and in patients which experience severe soft-tissue injury or contamination associated with the fracture. Therefore, surgical trauma is minimised, while also providing the surgeon with control over the flexibility of the fixation [25, 36]. External fixators are made of pins or wires that are placed percutaneously in the bone above and below the fracture site and are connected via clamps to external fixation rods [36] (Figure 1.4(b)).

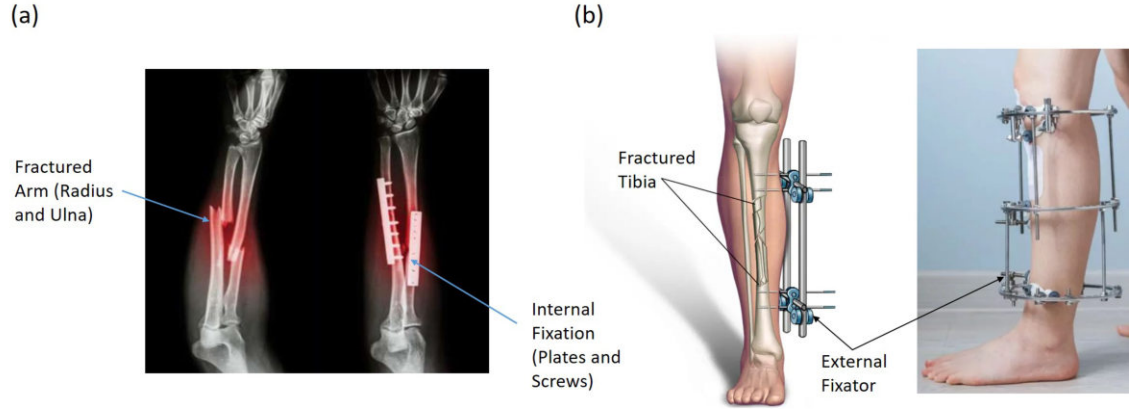

Figure 1.4: (a) Example of a fractured arm where both the radius and ulna have fractured. Plates and screws internal fixation devices were delivered to stabilise and treat the fracture. (b) External fixation devices in the case of complex tibial fracture or extensive soft tissue damage [37, 38].

The current materials most commonly used in internal fixation devices are metals, either Ti, stainless steel, or Co-Cr alloys, and several commercially available devices can be seen in Figure 1.5. These materials are very strong and durable but there are a number of problems associated with their use, namely stress shielding, toxic/carcinogenic corrosion products, and the need for a

second surgery to remove the device after it has served its purpose. For instance, in Germany in 2010, there were 180,000 surgeries to remove the fixation devices used to heal the bone, either due to complications or due to the device reaching the end of its life [39]. Implant removal is subject to the risks associated with any surgery such as infection, in addition to injury to soft tissues and the risk of re-fracturing the bone on removal. Morbidity from the second surgery, time, and financial costs also add to the disadvantages of a second surgery to remove the implant [25, 40]. Fixed metallic implants removal is one of the most common elective orthopaedic surgeries in industrial countries and accounts for approximately 5% of all orthopaedic surgeries. Additionally, the cost of these surgeries is estimated to be €1.6 Bn annually [41]. Therefore, these problems led to the exploration of biodegradable materials for these devices.

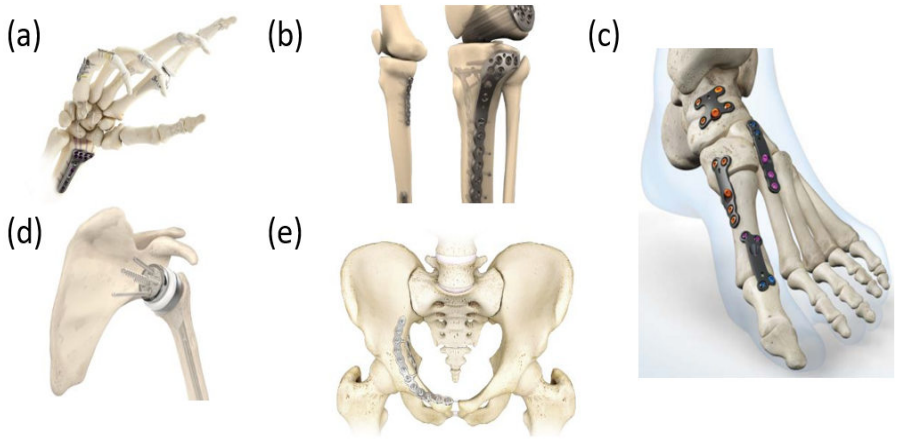

Figure 1.5: Internal fixation devices (plates and screws) offered by Stryker. (a) Hand and wrist. (b) Tibia and femur. (c) Foot and ankle. (d) Shoulder, elbow and humeral. (e) Pelvis and hip (Images obtained from Stryker website)

1.2 Biodegradable Materials for Orthopaedic Applications

In orthopaedic fixation, non-degradable materials like metals (stainless steel, titanium, cobalt-chromium alloys), ceramics, polymers, and composites are common. Metals, although popular in biomedical applications, have drawbacks like potential release of toxic ions and mismatched elastic moduli, causing stress shielding. Ceramics offer biocompatibility and strength, but they are brittle and amenable of catastrophic failures. Polymers are biocompatible, customisable, and easy to work with but have limited mechanical properties, particularly for orthopaedic applications. Composites may provide balanced properties, but manufacturing of biomedical implants and scaffolds in more challenging [40, 42, 43, 44, 45, 46] and, in addition, the composition and microstructure has to be tailored to meet the mechanical requirements and to avoid any unfavourable response from the host tissue [46].

It is more desirable that orthopaedic fixation implants used to repair serious bone fractures (such as screws, plates, and bone scaffolds) are made up of materials that degrade over time while allowing the bone to heal, especially considering that hard tissue repair takes approximately 12 weeks [47]. The use of biodegradable materials will eliminate the need for a second surgery to remove temporary

implants after the bone has healed, thereby reducing patient financial costs in addition to patient morbidity [47, 48]. However, biodegradable materials possess additional criteria that must be met as outlined by Nair et al. [49]; The degradation time should be parallel to the regeneration time of the tissue (see Figure 1.6), and the degradation products should be nontoxic and have the ability to be metabolised and excreted from the body. The concept of employing biodegradable materials for temporary applications, where they fulfil their intended function and are subsequently naturally degraded, metabolised, and excreted from the body, is indeed a promising one. This approach has significant potential, particularly in the context of paediatric fractures, where permanent metal implants could potentially inhibit bone growth [40, 47, 49, 50, 51, 52].

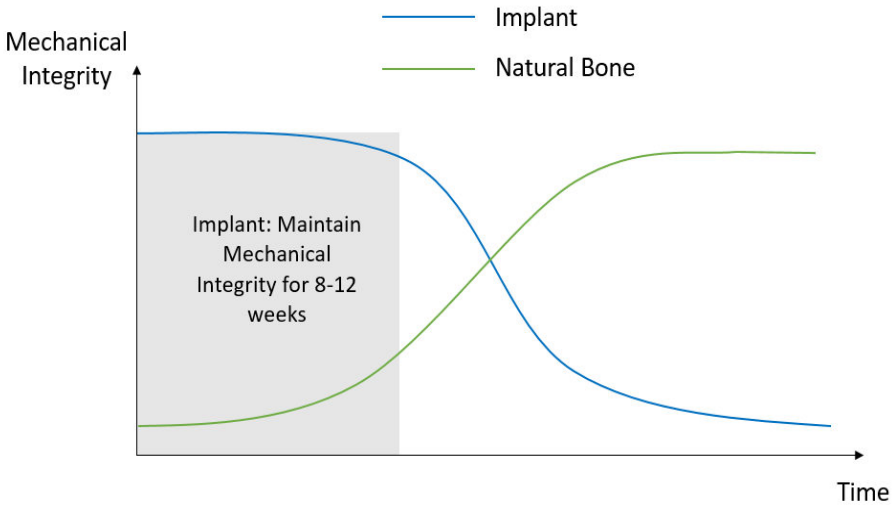

Figure 1.6: Requirements for a bioabsorbable medical devices in terms of its mechanical integrity over time for orthopaedic applications.

It is very common to use terms such as ”biodegradable”, ”bioabsorbable”, and ”bioresorbable” interchangeably but they should be defined to avoid confusion. Biodegradable refers to the gradual breakdown of materials, either by biological processes in the body or by corrosion in the case of biodegradable metals, with no remaining implant residues. Bioabsorbable describes the material's ability to degrade in the body and then be metabolised or assimilated by cells or tissues in the body. Bioresorbable refers to a material or device that is completely eliminated or bioassimilated through natural pathways. It effectively means that the implant material, and the degradation of the by-products takes place with no residual side effects [53, 54, 55]. In summary, all bioabsorbable and bioresorbable materials are biodegradable, but not all biodegradable materials are bioabsorbable or bioresorbable.

1.2.1 Biodegradable polymers

In recent years, there has been a growing demand for biodegradable polymers in medical applications, including temporary prostheses, implants, tissue scaffolds, and drug-eluting devices. These polymers fall into two main categories: natural and synthetic. Natural polymers, such as collagen, fibrin, and elastin, originate from living organisms, whereas synthetic polymers, such as polyesters

(polylactide, polyglycolide), polycaprolactone, and polyanhydrides, are man-made. Synthetic polymers are generally bioinert, do not cause adverse reactions in biological tissue, and offer more consistent properties and batch-to-batch similarity compared with natural polymers. They also allow for adjustable strength and degradation rates through the synthesis process. Polyglycolic Acid (PGA) was among the earliest synthetic biodegradable polymers used for biodegradable sutures in the late 1960s. However, PGA was found to degrade too quickly for orthopaedic applications, resulting in acid accumulation near the implant and leading to local inflammation [49, 56, 57].

The degradation of biodegradable polymers falls into two primary modes based on the type of polymer: hydrophilic or hydrophobic. Hydrophilic polymers are permeable to water, whereas hydrophobic polymers are impermeable. Degradation within these categories can be classed as bulk erosion (involving inhomogeneous cleavage of ester bonds) or surface erosion (gradual and uniform breakdown from the outer surface) for hydrophilic and hydrophobic polymers, respectively (see Figure 1.7) [58, 59].

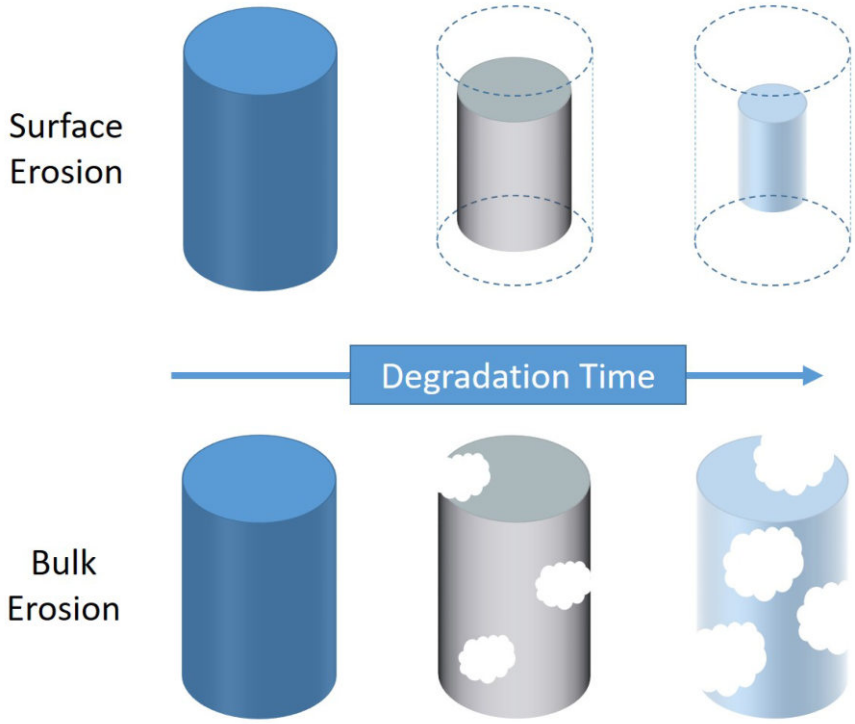

Figure 1.7: Schematic of degradation of polymers by surface erosion (hydrophobic polymers) and bulk erosion (hydrophilic polymers).

Polyesters

Poly(α-esters) are very popular for biodegradable orthopaedic devices, such as screws and plates, and are primarily used in orthopaedic maxillofacial surgeries [60]. PLA, PGA, and their co-polymer Polylactic-co-glycolic acid (PLGA) are aliphatic polyesters, which are hydrolytically degradable. The synthesis of these polymers is achieved through ring opening polymerisation, a chemical reaction that involves the polymerisation of cyclic glycolide or lactide diester, and catalysts such as

antimony, zinc, or lead [49, 51, 52, 56]. This process is depicted in Figure 1.8.

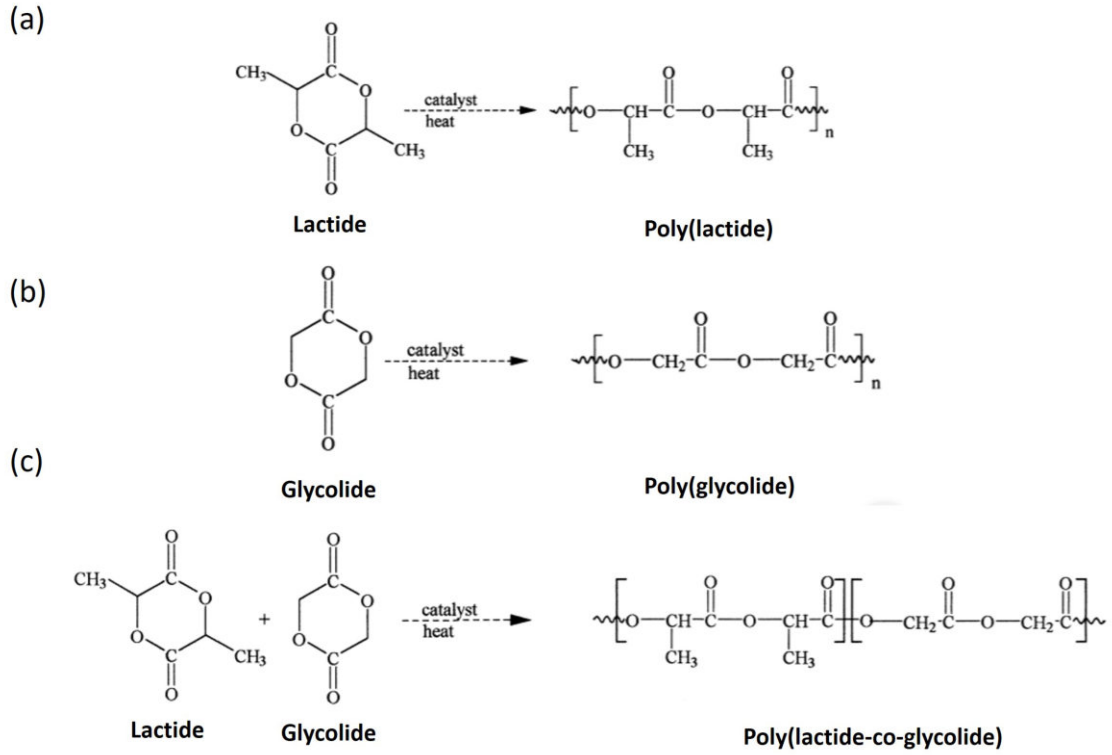

Figure 1.8: Chemical synthesis of polyesters (a) PLA, (b) PGA and (c) PLGA. The diagram shows the monomers followed by the process involving a catalyst and heat in order to turn them into polymers.

PLA is an aliphatic polyester that occurs naturally in various sources like wheat, rice bran, potato starch, and corn [51]. It finds extensive use in biomedical applications due to its exceptional biocompatibility, biodegradability, and renewability [51]. Upon exposure to biological media or water, PLA initiates a rapid degradation process through the hydrolysis of its ester backbone. This degradation is frequently heterogeneous and can result in bulk erosion [49]. The hydrolysis of PLA leads to the production of lactic acid, oligomers, and other water-soluble products, which are subsequently broken down into water and CO_2 (Figure 1.9) [51].

The mechanical properties and degradation rate of PLA and other polymers are influenced by several factors such as molecular weight, crystallinity, hydrophilicity or hydrophobicity, polydispersity, chemical stability, additives, implant geometry, implant condition, and processing route [51]. Generally, PLA experiences mass loss after approximately 2 years in physiological environments, though this can vary depending on factors such as the chirality. PLA can exist in two forms, L-lactide and D-lactide, representing variations in the chiral molecule or optical isomer [49, 56]. L-lactide is the naturally occurring isomer, while DL-lactide is a synthetic blend of D-lactide and L-lactide. The semi-crystalline L-lactide homopolymer (PLLA) is a common form of PLA that presents relatively high mechanical properties and long degradation time. Poly(LD-lactide) (PLDL) also features a semicrystalline structure, the extent of which depends on the L-isomer to

D-isomer ratio. This polymer demonstrates slightly lower mechanical properties and faster degradation rate in comparison with PLLA [61]. Notably, the mechanical properties and degradation time correlate with the L-isomer ratio, with higher ratios resulting in increased mechanical properties and longer degradation times. Poly(DL-lactide) (PDLLA) is an amorphous polymer with a random distribution of both isomeric forms of lactic acid that hinders crystallization. PDLLA is associated with lower mechanical properties, higher elongation, and rapid degradation, making it advantageous for drug delivery applications. The degradation time associated with PLLA is much slower than that of PDLLA, and it has been reported that PLLA can take more than 2 years *in vivo* to completely absorb [56, 61].

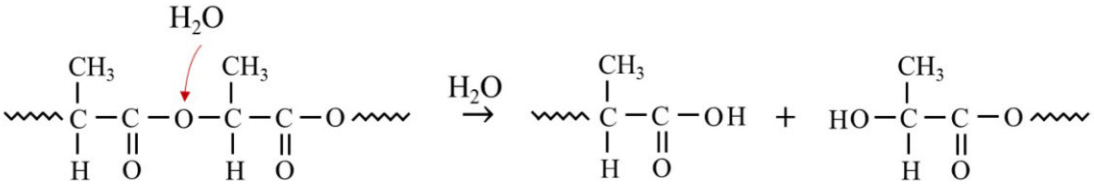

Figure 1.9: Schematic degradation of PLA in contact with water through the breaking of ester bonds.

PGA is a highly crystalline polymer (45-55%), resulting in high tensile strength and low solubility in organic solvents. Despite its low solubility, PGA has been shaped into various forms and structures through extrusion, injection moulding, solvent casting, and particle leaching [49, 62]. Extensive research has been conducted on PGA over the years, revealing its excellent mechanical properties for particular applications. In particular, PGA has been explored for bone fixation devices due to its initial high mechanical properties *in vivo* [49]. Regarding degradation, PGA undergoes a very similar process to PLA, characterised by bulk erosion. PGA is known to lose its strength in 1-2 months and its mass in 12 months [49]. Polyglycolides in the body break down into glycine, which can be excreted in the urine or converted into carbon dioxide and water through the citric acid cycle. The advantages associated with PGA are also linked to its disadvantages. PGA degrades rapidly, which has been associated with unwanted inflammatory responses due to an influx of acid by-products from its degradation [49, 56].

The copolymer of PLA and PGA is referred to as Poly(lactic-co-glycolic) acid (PLGA). Extensive research efforts have been dedicated to Poly(lactic-co-glycolic acid) (PLGA) over the years. The specific ratio of PLA to PGA can be customised to achieve particular material properties and degradation rates. In practice, a higher proportion of PLA is often incorporated to enhance degradation rate.

Polycaprolactone

Polycaprolactone (PCL) is a semicrystalline polyester synthesised by ring opening polymerisation of a monomeric unit 'ϵ-caprolactone'. PCL is easily processable because it can be dissolved in a large number of organic solvents, has a relatively low melting temperature (55-60°C) and a glass transition temperature of -60°C [49]. PCL undergoes hydrolytic degradation similar to PLA, PGA, and PLGA. However, the degradation in physiological fluids is rather slow (2-3 years). The long

degradation time and high permeability initially led researchers to investigate PCL for long-term drug delivery applications such as the contraceptive device Capronor®, which has been developed for long-term release of the drug Levonorgestrel [49]. PCL has low strength but the elongation to fracture is extremely high (up to 700%) [62].

Biodegradable polymer devices for orthopaedic applications

There are a number of companies which have started to offer orthopaedic fixation devices made up of bioabsorbable materials. These devices are intended for paediatric or adult patients in non-load bearing tissues mainly for craniomaxillofacial applications. DePuy Synthes use PLGA (85:15) in their entire Rapidsorb® line and are confident that their products are fully resorbed in 12 months (Johnson and Johnson medical devices).

In recent years, caution has been taken in the area of biodegradable devices since the urgent recall of the Abbott ABSORB® coronary stent in 2017 due to significant adverse reactions such as myocardial infarction [69]. This major event led to many questions being asked surrounding the efficacy and suitability of bioabsorbable devices. Lopez et al. [70] reported after a systematic and comprehensive review into the use of bioabsorbable plating systems in paediatric craniomaxillofacial surgeries, that these plates were relatively safe and presented low-risk to adverse events. A list of biodegradable polymer orthopaedic devices can be seen in Table 1.1.

Biodegradable polymers summary

The properties of the most common bioabsorbable polymers are depicted in Table 1.2. It is important to note that degradation time within this table indicates the time for complete mass loss and refers to the raw material before processing, which may affect the degradation times.

1.2.2 Biodegradable metals

Metals have always played and will continue to play a central role in biomedical engineering, particularly in cardiovascular and orthopaedic applications for tissue repair or replacement. Their excellent mechanical properties, including strength and fracture toughness, make metals highly suitable for load-bearing applications when compared to polymeric and ceramic materials [74].

Biodegradable metals are materials that gradually corrode in the body, leading to a suitable host response through released corrosion products and eventually complete dissolution, leaving no implant residues. These metals should made up of essential metallic elements that can be metabolised by the human body and exhibit appropriate degradation rates and modes [32].

The historical use of biodegradable metals dates back to around 200 AD when iron (Fe) was used clinically in a dental implant [75]. Other early applications included sutures, fracture fixation plates, and screws, although research on these applications has been limited. Mg, Zn and Fe are among the most widely used biodegradable metals, while Mn and Ca also investigated for orthopaedic use. These metals are essential nutrients for the body, but excessive amounts can have adverse health effects.

The enhanced strength of biodegradable metals makes them ideal for load-bearing medical applications, particularly since many medical devices experience complex loading modes. It should be noted that mechanical loading can accelerate the degradation rate of these materials Fluid shear

Table 1.1: Commercially available biodegradable orthopaedic devices.

Company	DePuy Synthes/Johnson and Johnson[63]	Zimmer/ Biomet [64, 65]	Stryker [66]	Bioretec [67]	Medical Magnesium [68]
Product Line	Rapidsorb®	LactoSorb®	Delta®	Activa™	mm.X®
Composition	85:15 (Poly-L-Lactide-co-glycolide) PLGA	82:18 Poly-L-lactic acid: Polyglycolic acid	85% Poly l-lactide, 10% polyglycolide, 5% poly d-lactide	PLGA 80L:20G and PLGA 85L:15G	Mg alloy (rare earths), and Mg-Ca-Zn alloy
Degradation and Strength Retention	85% strength in 8 weeks and fully resorbed in 12 months	70% strength in 8 weeks and fully resorbed in 12 months	78% strength in 8 weeks and 50% strength in 6 months. Fully resorbed in 8-13 months.	Almost 100% of its strength in 12 weeks, after 26 weeks the mechanical properties are about 10% and complete mass loss and resorption in 2 years	Data not available online
Application	Strictly non-load bearing Craniofacial surgeries only	Strictly non-load bearing craniofacial surgeries only	Strictly non-load Bearing craniofacial surgeries only	Upper and lower extremities. Foot and ankle, knee	Sports medicine, small bone fixation, athrodesis implants for hammer toe corrections
Products	Plate and screw system	Plate and screw system	Plate and screw system	Screws, nails, and pins for traumatology and interference screws for ACL repair	Interference screw, suture anchors, compression screw, arthrodesis implant, fracture foot surgery
Plate Profile (Thickness)	0.8 mm and 1.2 mm	1 mm and 1.4 mm	0.5 mm, 0.75 mm and 1 mm	N/A	N/A
Screw Profile (Diameter)	1.5 mm, 2 mm and 2.5 mm	1.5 mm and 2 mm, also 2.5/2.8 mm available	1.7 mm and 2.2 mm	2 mm, 2.7 mm, 3.5 mm and 4.5 mm	1.7, 2.1, 2.8, 3.5, 5-11 mm

Table 1.2: Mechanical properties and degradation time of bioabsorbable polymers.

Material	Elastic Modulus (GPa)	Strength (MPa)	Elongation (%)	Degradation (Complete)
Bone (Trabecular)	0.05-9	5-10	0.5-3	–
Bone (Cortical)	12-27	130-220	0.5-3	–
PLA [71]	3-6	40-65	1-5	>2 years
PGA [72]	5-7	60-80	15-20	2 months
PLGA [73]	2-4	55-80	3-10	3-18 months
PLLA [72]	3-4	45-70	5-10	>2 years
D,L(PLA) [61]	3-4	45-55	2-6	12-16 months
PCL [72]	0.4-0.6	10-35	300-700	>2 years
Polyanhydrides [49]	0.001-0.003	50-60	–	Months (Surface Erosion)

stress also affects the corrosion of biodegradable metals by influencing the deposition of corrosion products and locally generated ions [32, 76].

Magnesium and its alloys

Magnesium (Mg) is one potential candidate for biodegradable implants and has been used for both cardiovascular and orthopaedic applications. Several Mg-based devices have recently become commercial [40, 77, 78, 68, 79]. Mg ions are the 4th most abundant cation in the body, and are primarily stored in bone tissue. Thus, Mg can be completely resorbed in the body without any harmful effects. Mg is vital in metabolism processes, a co-factor in many enzymes, and a key component of ribosomes in translating genetic information encoded in mRNA to polypeptide structures [40]. Mg alloys have excellent biocompatibility and are capable of inducing the development of hard callous at bone fracture sites. In terms of mechanical properties, Mg has a density very similar to that of natural bone, and exhibits much higher stiffness and strength than any biodegradable polymer [40, 47]. In terms of the degradation, Mg and its alloys degrade rapidly in aqueous solutions to form hydrogen gas (see Equations 1.1-1.3).

$$Mg \rightarrow Mg^{2+} + 2e^{-} \qquad \text{(Anodic Reaction)} \tag{1.1}$$

$$2H_2O + 2e^{-} \rightarrow 2OH^{-} + H_2 \qquad \text{(Cathodic Reaction)} \tag{1.2}$$

$$Mg + 2H_2O \xrightarrow{yields} Mg^{2+} + 2OH^{-} + H_2 \tag{1.3}$$

The degradation of Mg differs between *in vitro* and *in vivo* environments. *In vitro* degradation is carried out in solutions like Phosphate Buffer Solution (PBS), Hanks Balanced Salts Solution (HBSS), Simulated Body Fluid (SBF), and biological media where water molecules interact with the Mg surface, forming a $Mg(OH)_2$ layer and releasing H_2 gas. The stability of the $Mg(OH)_2$ layer can be compromised by the presence of Cl^- ions, leading to the formation of soluble $MgCl_2$ and OH^- ions. The breakdown of the $Mg(OH)_2$ layer exposes the uncorroded Mg surface, and pitting corrosion continues with the formation and dissolution of $Mg(OH)_2$. Ca and P ions in the solution deposit within the corrosion layer, resulting in the formation of phosphates and carbonates

[80, 81]. A diagram describing the corrosion of Mg at the interface between biological media and the material can be seen in Figure 1.10.

Numerous publications delve into the mechanical properties, degradation behavior, characterisation, and biocompatibility of Mg and its alloys. Mg degradation leads to hydrogen release and tissue alkalisation, which can impede the healing response and potentially cause tissue necrosis. This issue has been effectively addressed through the use of a subcutaneous needle to remove the gas. The hydrogen evolution method is a more precise approach for quantifying Mg degradation, providing a direct correlation between gas evolution and corrosion [32, 82, 83, 84, 85, 86, 87, 88, 89].

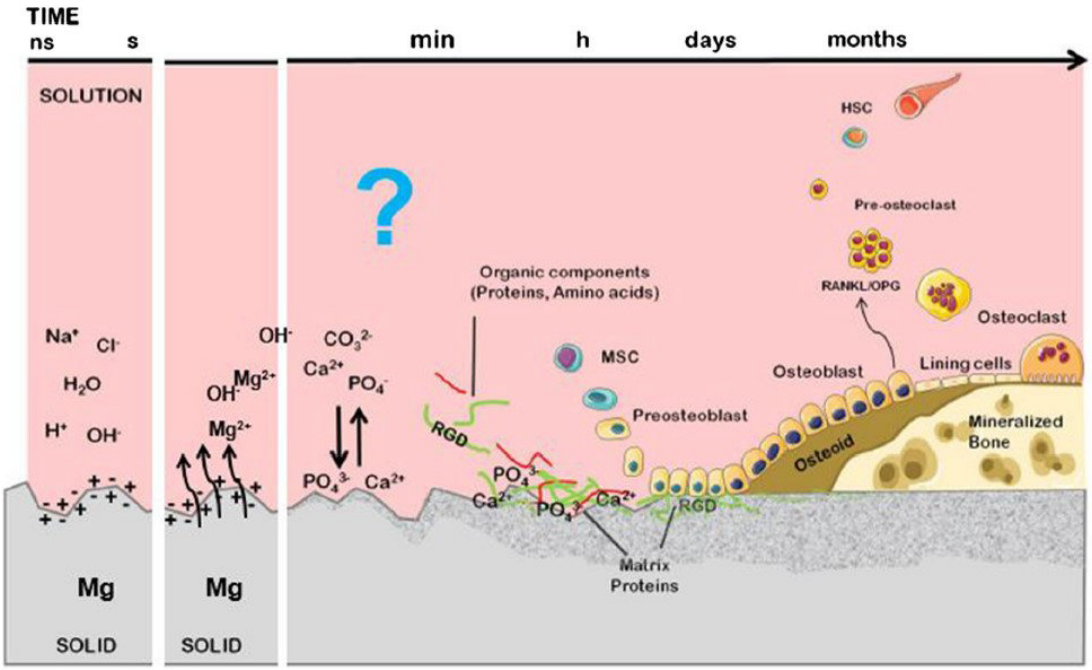

Figure 1.10: Schematic of the corrosion processes of Mg-based alloys in biological media/tissue [81].

Pure magnesium (Mg) exhibits suboptimal corrosion and mechanical properties, with a yield tensile strength ranging from 21 MPa for as-cast Mg to 115-140 MPa for as-rolled Mg [90]. Mg alloys have been developed to improve these properties, including Ca and Sr as alloying elements. While these additions improve creep resistance and strength, they also increase brittleness and corrosion rates. The optimal Ca content is around 0.6-1%, leading to enhanced compressive and bending strength. *In vitro* studies on Mg-Ca alloys show increased cell viability and bone growth in the *in vivo* animal models [91]. Binary Mg-Sr alloys also exhibit improved strength but reduced ductility, with corrosion resistance decreasing as Sr content increases. However, a Mg-2% Sr alloy displayed the highest ultimate tensile strength and slower degradation. To maintain good mechanical and degradation properties, Sr content should remain below 3% [92]. Mg-Zn alloys exhibit increased strength and elongation up to 4% Zn content, beyond which properties decline. Mg-1% Zn has the lowest degradation rate among several magnesium alloys [32].Mg-Zr alloys, typically combined with Zn and rare earth elements (Y) enhance the mechanical properties. Additionally, magnesium-

aluminium (Mg-Al) alloys enhance strength and elongation up to 6% Al content, with higher percentages decreasing strength. Al also improves corrosion resistance by forming an Al_2O3 film on the alloy's surface. However, the neurotoxicity associated with Al products in the body limits the use of Mg-Al alloys in humans [93].

Mg-Y alloys aim to improve high-temperature strength and creep resistance. Y has high solubility in Mg and WE43, an Mg-Y-Nd alloy, offers excellent mechanical properties and cytocompatibility [40, 85, 80, 86].

Zn and its alloys

Zn is also a trace element found in the body and therefore in appropriate amounts it is non-toxic and biocompatible. Zn plays a vital role in the human body, serving as an essential element required for various physiological functions. It acts as a co-factor for six classes of enzymes, participates in nucleic acid metabolism, gene expression, wound healing, protein regulation, and signal transduction [32, 94]. Despite its biological advantages as a biomaterial, the mechanical properties of pure Zn are very low for orthopaedic applications [95].

The corrosion rate of Zn is in between that of relatively fast-corroding Mg and very slow-corroding Fe, and does not generate any hydrogen gas upon degradation, unlike Mg. Zn degrades via an oxygen reduction reaction [73], and therefore has a major advantage over Mg because gas pockets are not formed around the implant [96, 95]. The corrosion of Zn in an aqueous environment such as that of PBS with a neutral pH is based on the reactions given by equations 1.4 - 1.7. These equations show the formation of $Zn(OH)_2$ and ZnO but no gas is released during the process.

$$2Zn \rightarrow 2Zn^{2+} + 4e^- \qquad \text{(Anodic Reaction)} \tag{1.4}$$

$$O_2 + 2H_2O + 4e^- \rightarrow 4OH^- \qquad \text{(Cathodic Reaction)} \tag{1.5}$$

$$2Zn^{2+} + 4OH^- \rightarrow 2Zn(OH)_2 \qquad (Zn(OH)_2 \text{ Formation}) \tag{1.6}$$

$$Zn(OH)_2 \rightarrow ZnO + H_2O \qquad \text{(ZnO Formation)} \tag{1.7}$$

Alloying with Mg, Sr, Ca, and Cu has been extensively use to address the challenges associated with the low mechanical properties of Zn [95, 94]. To date, Mg appears to be the most efficient element to improve the mechanical properties for biomedical applications [95]. Binary Zn-Mg alloys with 1 wt. % of Mg led to excellent improvements in strength and and elongation [97]. The strength of pure Zn ($\approx$ 30 MPa) was increased $\approx$ 110 MPa with the addition of 1 wt. % Mg. Moreover, the corrosion rates of Zn and Zn-Mg were relatively close ($\approx$ 0.018-0.145 mm/yr) and much lower than that of Mg-based alloys [97].

Summary of biodegradable metals

Biodegradable metals offer significant advantages in terms of mechanical properties but are limited by their degradation rates. Mg alloys degrade too quickly, Fe-based alloys degrade too slowly, and Zn alloys fall in between. Balancing mechanical properties and degradation time is crucial for biomedical applications, particularly in orthopaedics, where the implant's elastic modulus should match that of natural bone, maintain mechanical strength for 3 months and be able to be assimilated by the body in less than 2 years.

Mg-based alloys are the most commonly used biodegradable metals for bone applications due to their high strength. Zn-based alloys are also under investigation for orthopaedic use, with ongoing research to establish conclusive results. A list of biodegradable metals and their respective properties can be seen in Table 1.3.

Biodegradable metals can be used in additive manufacturing, including selective laser melting (SLM) and selective laser sintering (SLS), allowing for the creation of detailed scaffolds. Combinations of biodegradable metals with polymers are also explored, especially in fused filament fabrication (FFF). However, there is limited research on these composites.

Table 1.3: Summary of various biodegradable metals.

Material	**Elastic Modulus (GPa)**	**Strength (MPa)**	**Elongation (%)**	**Degradation (Complete)**
Bone (Trabecular)	0.05-9	5-10	0.5-3	–
Bone (Cortical)	12-27	130-220	0.5-3	–
Mg Alloys [40]	≈40	65-100	<37	Weeks-Months
AZ91 [98, 99]	30-40	288-305	15	1.23 mm/year
WE43 [100, 101, 84]	41-44	183-260	2-10	3-6 months
Mg-Ca [102, 103]	46-58	170-274	10	1.5 mm/year
Zn-1Mg [95, 94]	38-45	170-190	1.5-12	0.07-0.2 mm/year
Iron-Alloys [71]	150-210	300-1550	0.5-45	0.001-0.1 mm/year

1.2.3 Bioresorbable bioceramics

Bioresorbable bioceramics primarily consist of calcium phosphates which have been reported in medical applications such as orthopaedics, maxillofacial repair, and dental implants as early as the 1970s [104, 105].

Calcium Phosphates

Synthetic calcium phosphates have been used in dentistry and orthopaedics since the 1970s and 1980s, respectively. The most commonly used calcium phosphates are Hydroxyapatite (HA) and β-TriCalcium Phosphate (β-TCP). HA has the chemical formula $Ca_{10}(PO_4)_6(OH)_2$ with a Ca to P ratio of 1.67. It is similar to the mineralised phase of natural bone, making it highly biocompatible and osteoconductive. HA is stable in body fluids and in dry or moist air up to 1200°C, and is bioactive due to its resorbable behaviour. It can be produced via a high-temperature reaction, wet methods, or solid-state reactions.

β-TCP is represented by the chemical formula $Ca_3(PO_4)_2$ and the Ca/P ratio is 1.5. It is highly soluble in body fluids and turns into α-TCP at approximately 1200°C. HA and β-TCP are often combined to achieve optimal resorbability. HA and β-TCP are commonly used due to their excellent osteoconduction and integration with host tissue. HA has been used for coatings in dental and orthopaedic implants, but its use is relatively limited due to its low solubility rate. In addition, the mechanical properties that are much higher than that of natural bone. HA has been combined with Mn and Zn to increase the resorption rate. HA has an elastic modulus in the range

of 70-110 GPa and a compressive strength of approximately 600 MPa, whereas β-TCP generally has a lower compressive strength than HA, and degrades much quicker than HA *in vivo*.

1.2.4 Composites

Composite materials can be defined as materials that consist of two or more different components that are able to act synergistically to give properties superior to those provided by either component alone [106]. Examples of composite materials with various reinforcement types are shown in Figure 1.11. Within this chapter, composites will be defined as any reinforcement material dispersed through a continuous phase (matrix).

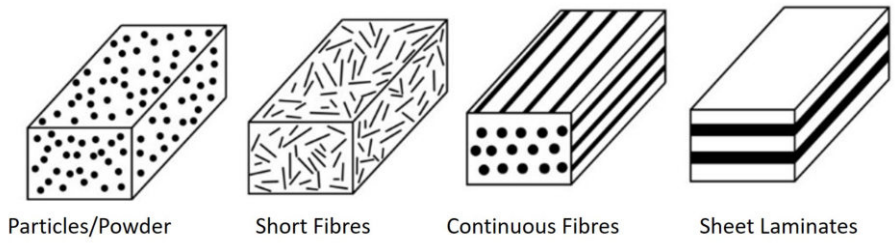

Figure 1.11: Schematic diagram of the various composite reinforcement types that can be created [107].

Biodegradable Composites

Biodegradable materials, such as those discussed in the biodegradable polymers and biodegradable metals sections above, have gained popularity in orthopaedic fixation devices and temporary applications, such as cardiovascular stents. Resorbable bone plates and screws are particularly valuable as they allow for a gradual increase in stress on healing bones, reducing issues such as stress shielding and osteopenia (loss of bone mass and density). Their appeal lies in their ability to eliminate the need for a second surgery, thereby saving time, money, and significantly reducing patient morbidity [40, 47].

There are instances in orthopaedic fixation where the use of a standalone biodegradable polymer or metal may be limiting due to mechanical properties or the degradation rate. For instance, biodegradable polymers, such as PLLA, PGA, and PLGA, have been approved for clinical use in humans [108] but they release acids during degradation, potentially causing inflammation in the surrounding tissues and compromising mechanical integrity. In contrast, biodegradable metals release alkaline by-products upon degradation, and their combination with polymers could result in the release of relatively neutral by-products. The combination of PLLA and PLGA with Mg have found that the pH remains relatively neutral during degradation when these materials are used together [83, 109, 110, 111]. This combination of polymers and metals could address their individual disadvantages, significantly improving the mechanical properties of polymers while slowing the rapid degradation associated with metals such as Mg (Figure 1.12) [40, 47, 49, 106, 109]. In fact, bone itself is a natural composite material comprising collagen fibres with dispersed hydroxyapatite. A well-tailored polymer matrix composite can mimic bone properties, making it a suitable

replacement or healing material. However, considerations such as biocompatibility, practicality, and cost are also vital in material development [108].

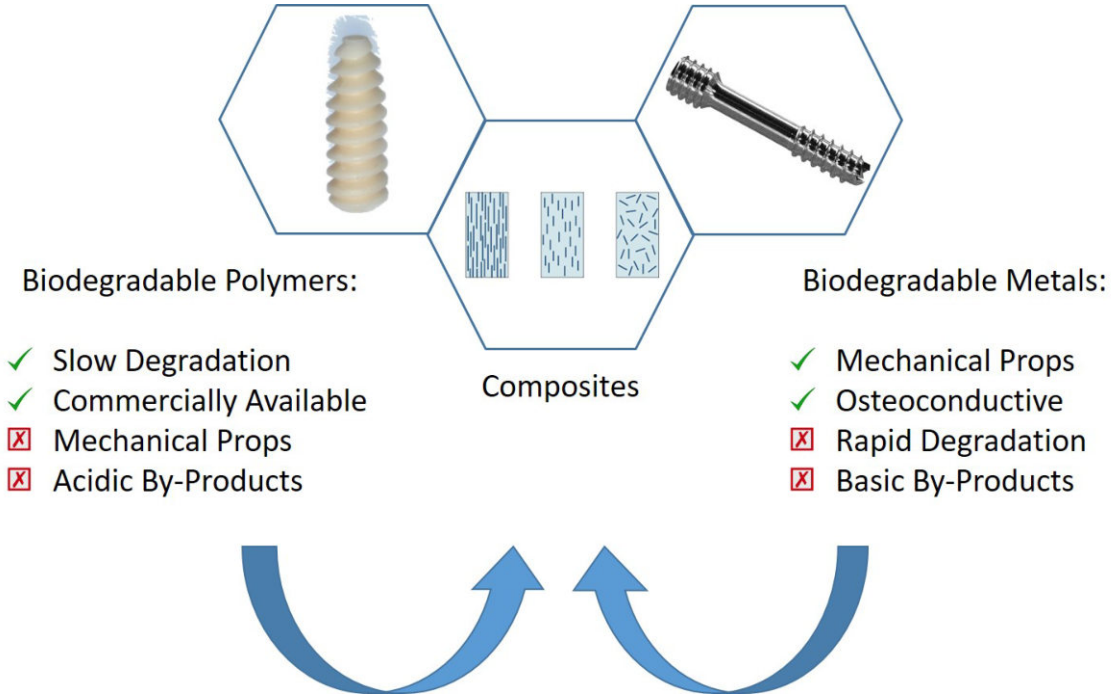

Figure 1.12: Synergistic advantages of combining biodegradable polymers and metals to form a biodegradable composite.

Composites use two main types of reinforcement: fibres (continuous or short) and particles. Continuous fibre reinforcement typically leads to the greatest improvement in mechanical properties, followed by short fibres and particle reinforcement, respectively [112, 113].

It is important to be aware of the current biodegradable composite devices that are on the market. Ossio has received approval from the Federal Drug Administration in the USA for a new bioabsorbable composite screw which uses a novel fibre technology. The screw apparently takes 18-24 months for complete resorption, and their primary area of focus is foot and ankle surgeries to eliminate the need for a second surgery. Interference screws, and suture anchors used in Anterior Cruciate Ligament (ACL) repair and reconstruction appear to be the most common application for biodegradable composites. The current biodegradable composite devices on the market can be found in Table 1.4. It is important to note that the degradation time is not available for some devices.

Research into biodegradable composites continues to seek the ideal material for various biomedical applications, each with its specific requirements. Initial research has explored self-neutralizing PLGA/Mg composites for orthopaedics. Xu et al. [110] combined PLGA with both pure Mg and an Mg-Zn alloy in powder form using the solvent-casting method, creating square and rectangular samples for mechanical and degradation testing. The results demonstrated a significant increase in tensile modulus and strength in the samples containing Mg. In vitro experiments indicated enhanced biocompatibility, with increased ALP expression and cellular mineralisation in MC3T3

Table 1.4: Biodegradable devices from composite materials currently on the market

Company name	Biocomposites® (Stryker) [114]	Teknimed [115]	BIOMET (Zimmer) [116]	Ossio [117]
Product line	Biosteon®	EUROSCREW®	ComposiTCP™	Ossiofibre™
Composition	Hydroxyapatite in PLLA matrix	70% PLA and 30% β-TCP	70% PLDLA and 30% β-TCP or 40% PLDLA and 60% β-TCP	50% Mg, Ca, Silica fibres and 50% Poly (L-Lactide-co-DL-lactide) matrix
Degradation and strength retention	Not Available	Mechanically stable for 6 months, resorbed in 2 years	Not Available	77.8% strength in 2 weeks, 62% strength in 6 months, fully resorbed in 1 year
Application	Interference screws for ACL/PCL reconstruction	Interference screws for ACL/PCL reconstruction	Interference screws for ACL/PCL reconstruction	Foot and ankle surgeries possible. Hammertoe fixation surgeries
Products available	Screws only	Screws only	Screws only	Screws only
Screw sizes available	7-11 mm	7-11 mm	6 mm	2.5 mm, 2.9 mm, and 3.2 mm

pre-osteoblast cells. The 5 wt.% Mg composite exhibited nearly neutral pH degradation profile and a 35-40% increase in the elastic modulus, showing its potential for biomedical applications.

Another study by Wu et al. [83] investigated AZ31 Mg alloy short fibres ($\approx 2.5 \pm 0.5$ mm) embedded in a PLGA matrix through compression moulding. They found that a higher weight percentage of AZ31 fibres led to increased tensile strength, elongation, and increased pH levels, making the environment more alkaline. However, the environment reached a neutral pH with the right fibre content. Additionally, the fibres promoted adhesion and proliferation of MC3T3 cells.

Brown et al. [111] developed a porous Mg/PLGA composite scaffold to enhance bone regeneration following tooth extraction. They used the solvent-casting method to fabricate the scaffolds, incorporating high-purity Mg particles with diameters less < 300 μm. Their research revealed that the higher Mg content in PLGA resulted in a higher compressive strength and a higher compressive modulus. Over a 10-week degradation period, extracts from degrading Mg/PLGA scaffolds increased bone marrow stromal cell proliferation *in vitro*. Furthermore, a canine model study demonstrated that Mg/PLGA scaffolds were safer and more effective in preserving bone height compared to empty controls.

Although several biodegradable polymers such as PLLA and PGA are available, PLGA is often preferred due to its customisable properties. However, it is worth noting that the effects of

processing on the materials can reduce both mechanical properties and degradation times further due to breaking of the chains with every processing step where the polymer reaches its melting point [52].

A valuable study by Ali et al. [86] evaluated PLA-based composites reinforced with Mg wires in terms of their mechanical, degradation, and cytocompatibility properties. The surface of the WE43 wires was modified by plasma electrolytic oxidation to increase the interface strength between the wires and the PLA from 11 MPa to 27 MPa. The surface modification also greatly reduced the corrosion of the Mg wires, exhibiting only a 3% mass loss after 180 days compared to the bare Mg wires. In terms of cytocompatibility, the cells tended to migrate away from the surface of the Mg wires toward the PLA. The findings of this study have offered valuable insights into the creation of wire-reinforced composites for biomedical applications. However, the possibility of 3D printing the wires themselves could introduce an additional level of flexibility to the manufacturing process, enabling a higher degree of customisation.

Ma et al. [111] investigated the antibacterial and cytocompatibility in vitro of PLGA/Mg scaffolds. Although they mentioned using a low temperature rapid prototyping technique, specific manufacturing details were not provided. Their findings indicated that scaffolds with 20 wt.% Mg exhibited higher antibacterial activity than those with 10 wt.% Mg content. However, higher Mg content also led to decreased cell attachment and proliferation compared to scaffolds with lower Mg content, presenting interesting results considering that increased Mg content typically correlates with higher osteogenesis rates in other studies.

3D Printing of Composites

The most prevalent processing methods for composite manufacturing typically involve techniques such as compression moulding, resin transfer moulding, and solvent casting. However, these conventional manufacturing methods, while widely used, have certain limitations. They often lack the capacity for intricate and personalised part production [118].

These limitations may be overcome through the use of 3D printing or fused filament fabrication (FFF). The FFF process entails the use of a continuous fused filament composed of a thermoplastic polymer [119]. This filament is fed through a tube into the hot end of the 3D printer's nozzle, where it is heated into a semi-liquid state. The semi-liquid polymer is then extruded through the nozzle onto a heated bed for adhesion, and a 3D object is fabricated layer by layer,. This process leverages the thermoplastic property of the polymers, which allows them to be fused in filament form before printing, transitioning to a semi-liquid state, and then cooling to form a solid 3D object (Figure 1.13) [119].

Standard filament diameters in commercial printers are 1.75 mm and 2.85 mm (e.g., Prusa, Makerbot, Ultimaker, Stratasys). The FFF process offers several advantages, including the ability to produce geometrically complex parts at a low cost and high speed, with minimal process complexity. However, there are also disadvantages associated with FFF, such as relatively poor mechanical properties, a layered appearance, surface roughness, and limitations in terms of compatible materials [119]. The mechanical properties of the printed parts depend on various parameters, including material, layer thickness, orientation, printing temperature, and bed temperature. It has been observed that inter-layer distortion is a primary factor contributing to the lack of mechanical

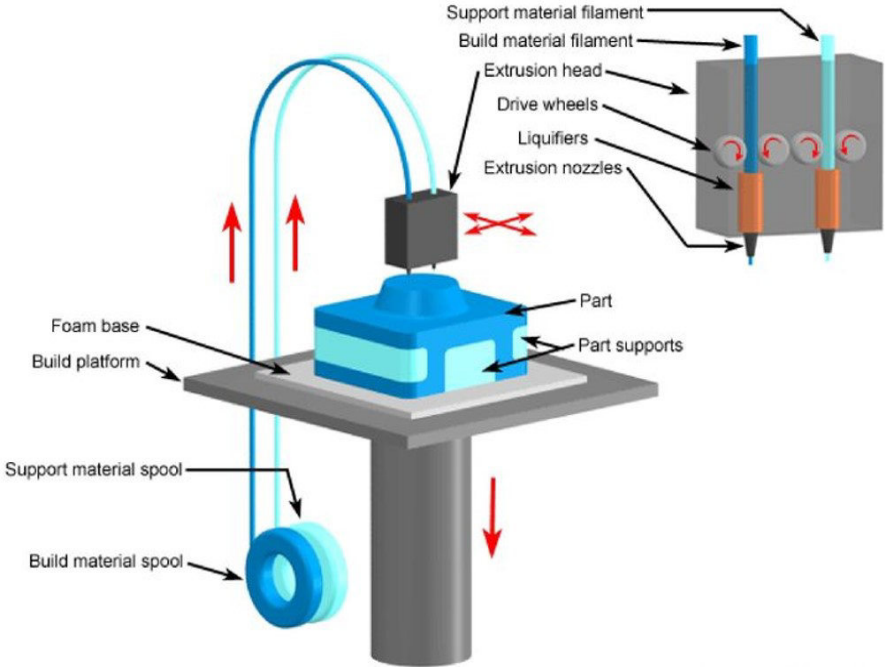

Figure 1.13: Schematic diagram of the 3D printing process known as FFF [120].

properties in FFF-printed objects [121, 122]. However, one of the major causes of the limited mechanical properties is the material selection. Most commercially available filaments comprising of polymers whose strength is not suitable for functional part use, especially in the realm of orthopaedic applications that require any form of load-bearing capacity.

Recent developments in FFF have led to the production of continuous fiber-reinforced composite parts, such as Carbon Fiber (CF)-reinforced Nylon, which has successfully addressed some of the mechanical property limitations and it has been commercialised by companies like Markforged. However, these materials are not biodegradable nor biocompatible. Additionally, achieving strong bonding between the polymer matrix and fiber material can still be challenging. Moreover, the selection of suitable fiber materials for reinforcement remains limited, although ongoing research aims to expand these options to enable diverse applications in various industries [119, 123, 124, 125, 126].

Currently, the most popular materials used in FFF are synthetic polymers, including PLA and Acrylonitrile Butadiene Styrene (ABS) [127]. Particle, short fibre, and continuous fibre reinforcements are used to enhance the mechanical properties [128]. Despite the availability of commercial printers capable of producing continuous fibre-reinforced polymers, ongoing research has primarily focused on short fibre and particle reinforcements because commercially available continuous fibre reinforced printers are not able to produce medical grade parts/materials [128]. FFF has played a pivotal role in the study of various composites. For example, the addition of vapor-grown carbon

fibres (VGCFs) to an ABS matrix via FFF led to a significant increase in tensile strength and modulus of approximately 40% and 60%, respectively albeit with a decrease in strain to failure [129]. In another study, the addition of 5% and 7.5% carbon fibre content in an ABS matrix through FFF substantially improved the elastic modulus and tensile strength [130]. Additionally, Tian et al. [131] demonstrated the feasibility of 3D printing continuous fibre-reinforced polymer composites with FFF, achieving a modulus of 30 GPa and a flexural strength of 335 MPa with 27 wt% carbon fibre.

Other studies have aimed to enhance the mechanical properties of bone scaffolds by incorporating ceramic particles into polymeric matrices through FFF. For instance, β-TCP particles were added to PCL scaffolds to improve their strength, resulting in a 107% increase in compressive modulus with 20 wt. % β-TCP content [132]. Senatov et al. [133] dispersed HA particles throughout a PLA matrix, leading to increased compressive strength and crack resistance during cyclic loading. These scaffolds had 30% of porosity with pore sizes of 700 μm but were capable of withstanding cyclic loads of 21 MPa for an extended period.

A notable breakthrough was achieved by Antoniac et al. [134], who successfully employed the FFF technique to 3D print interference screws designed for ACLs. In this innovative approach, Mg powder was incorporated into a PLA matrix. Vitamin E was added to improve the interface between the Mg particles and the polymer matrix. The mechanical properties and degradation rate were not measured but it is worth noting that achieving a homogeneous dispersion of the particles throughout the polymer matrix remained a challenge in this work [134].

Additionally, Ibrahim et al. [123] conducted a study capable of 3D printing unidirectional composites with a continuous Ni-Cu wire embedded in a polymer matrix. They modified a commercial 3D printer's print head to incorporate a metal wire into a molten polymer matrix (Figure 1.14). As the polymer's viscosity increased, it would pull the wire out of the needle and through the nozzle of the print head. While this study provided valuable insights into 3D printing methods, a major limitation was the inability to cut the metallic wire after depositing each layer, severely limiting the wire volume content (just 0.7 vol.%) in addition to the printer's potential to fabricate more complex shapes.

Hamidi et al. [135] used a different strategy to incorporate Cu wires (127 μm in diameter) or stainless steel wires (178 μm in diameter) into a 0.8 mm diameter nozzle to print coupons for tensile tests with the wires orientated parallel to the loading direction. Nevertheless, the wire volume fraction only reached 1.5 % vol. and there was no significant increase in mechanical properties because the porosity of the printed samples was around 20%. Finally, Kim et al. [136] were able to develop a process for embedding Cu wires into a 3D printed part after FFF. However, this investigation focused on the design of the tool to embed the wires and no information was provided about the final composite and its mechanical properties.

In conclusion, the realm of 3D printing composite materials is highly intriguing, although it does come with certain limitations using current technologies. A summary of the current findings in literature with respect to composites that are relevant to this thesis in terms of their materials, processing methods, and mechanical properties can be seen in Table 1.5. Particle-reinforced composites in 3D printing have shown improvements in mechanical properties, though not to a sig-

Table 1.5: Literature review of relevant composite materials, their manufacturing processes and their effect on mechanical properties of the matrix material.

Ref	Reinforcement Material	Matrix Material	Manufacturing Type	Mechanical Properties
[110]	5 wt.% Mg and Mg-Zn powder	PLGA	Solvent Casting	35-40% increase in modulus
[83]	AZ31 Mg alloy short fibres	PLGA	Compression Moulding	150% increase in tensile strength
[111]	Pure Mg powder (<300μm) 25-100 wt.%	PLGA	Solvent Casting	Up to 300% increase in compressive modulus
[86]	WE43 wires 20% vol. with and without surface modification	PLDL	Compression Moulding	250% increase in shear strength
[129]	VGCFs	ABS	FFF	40% and 60% increase in tensile strength and elastic modulus, respectively
[130]	5 and 7.5 wt.% CFs	ABS	FFF	Up to 31% increase in elastic modulus
[131]	27 wt.% CF	PLA	FFF	1000% increase in tensile strength and modulus
[132]	20 wt.% % β-TCP powder	PCL	FFF	107% increase in compressive modulus
[133]	15 wt.% HA powder	PLGA	FFF	50% increase in compressive strength and modulus
[134]	4 wt.% Mg powder (100 μm)	PLA	FFF	No testing
[123]	0.7% vol. of Cu and Ni-Cr with 75 μm diameter	PLA	FFF customised print head	Up to 12% and 38% increase in strength and modulus, respectively
[135]	1.5 % vol. Cu or Stainless steel wires	PLA	FFF	20% and 40% increase in tensile strength for Cu and Stainless steel composites, respectively

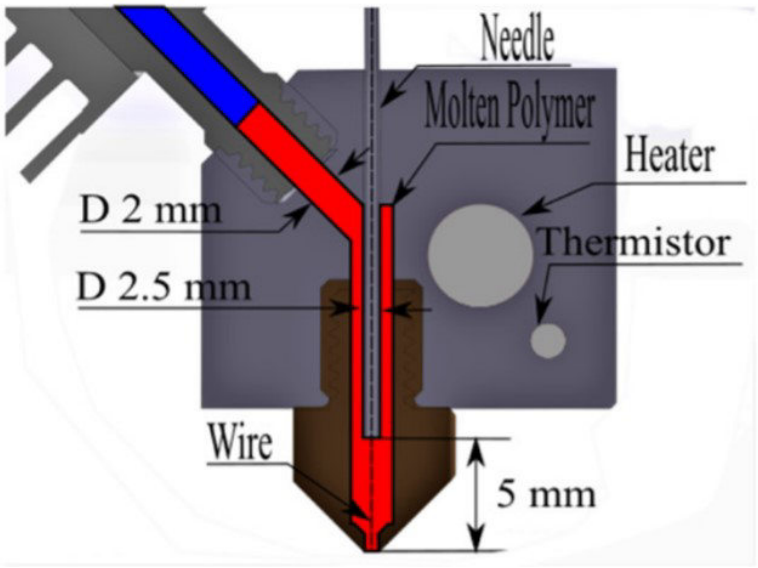

Figure 1.14: Schematic diagram of the modified print head for manufacturing continuous wire reinforced composites by FFF [123].

nificant extent. However, these particles have been instrumental in tailoring degradation rates and enhancing cytocompatibility. Thus, the potential of these parts as functional components is still limited. Therefore, the prospect of producing continuous wire-reinforced composites with enhanced mechanical properties is attractive, as it could provide FFF-produced parts with the mechanical strength required for functional use, rather than being restricted to prototyping purposes.

1.3 Objectives

In cases of paediatric care where a child or young person has experienced a bone fracture larger than the critical size defect (≈2 cm), further intervention in the form of internal bone fixation is required. Currently, the standard of care for this internal fixation involves the use of permanent metallic plates, screws, nails, or rods made from Ti, stainless steel or Co-Cr alloy. However, they must be removed after approximately 6 months to 1 year to prevent interference with ongoing bone growth, which could potentially result in asymmetrical features.

Bioresorbable materials are gaining popularity in orthopaedics as they can serve a temporary function and then gradually integrate into the bone before being naturally assimilated by the body. One of the primary advantages of these materials is the avoidance of a second surgery, which is especially critical in paediatric cases where additional surgeries are often needed.

Personalised medicine is also becoming a standard of care, particularly in cases involving complex injuries that require careful planning and customised treatment options. In this context, 3D printing offers significant advantages. Unlike subtractive manufacturing processes, such as machining, additive manufacturing can create complex, net-shaped parts with relatively high resolution. When combined with patient computer tomography scans, it allows for the creation of personalised models and devices. Limitations of parts produced through FFF are typically related to techno-

logical constraints and the selection of available commercial materials, and therefore mechanical properties. However, the development of new material combinations and customised FFF printing systems can expand the material portfolio and address many of the disadvantages currently associated with FFF.

Globally, more than 28 million orthopaedic surgeries are performed each year, with a steady increase expected in the future. The market for orthopaedic devices is currently valued at approximately €37 billion and is projected to reach €43 billion by 2030. Among the various segments within the orthopaedic devices market, trauma fixation devices are anticipated to experience the highest compound annual growth rate of 7%, with their market value expected to increase from €7 billion to €15 billion by 2030. The primary indications for fracture fixation devices are traffic accidents and sports injuries. Furthermore, the market for 3D printed medical devices is on the rise, with an estimated growth of €3.1 billion to €11.6 billion by 2028, reflecting a remarkable growth of over 30%. This presents significant opportunities for entering the 3D printed medical devices market [137, 138, 139].

Biodegradable polymers like PLA, PLLA, PLGA, and PGA have long been used in the biomedical industry. However, they have limitations, such as their mechanical properties and the release of acidic by-products during degradation. On the positive side, these materials offer the advantage of being able to tailor their degradation times. Biodegradable metals, on the other hand, exhibit excellent strength relative to their polymeric counterparts and have a stiffness of the same order of magnitude as natural bone. However, they often degrade relatively quickly compared to polymers and produce alkaline by-products upon degradation. The development of a composite material that combines these two material categories can yield significant benefits, such as enhancing the mechanical properties of polymers, extending the degradation times of metals, and neutralising the by-products generated during degradation.

The primary aim of this thesis is to produce a new generation of composite materials with the required mechanical properties, tailorable degradation times, and excellent biocompatibility for use in orthopaedic applications. These materials are also required to be suitable for 3D printing and be adaptable to customised 3D printing systems. The hypothesis is that powder reinforcement will be able to change the degradation behaviour of the polymers, and will provide some degree of change in mechanical properties however it will be minimal. A continuous wire reinforcement will be capable of substantially improving the mechanical properties and also providing a degree of tailorability regarding the degradation behaviour.

Therefore, the individual objectives of this thesis with respect to the primary aim can be summarised by the following:

1. Develop a process for producing particle reinforced composite materials for fused filament fabrication, compatible with commercial 3D printers.

2. Characterise 3D printed particle reinforced materials containing Mg or Zn particles in terms of their mechanical, degradation, and cytocompatibility properties.

3. Develop a process for producing filaments with a continuous wire reinforcement suitable for 3D printing.

4. Develop a 3D printer that is capable of producing both continuous wire-reinforced, and particle-reinforced composite parts.

5. Characterise the continuous wire reinforced parts in terms of their mechanical, microstructural, and degradation properties.

1.4 Outline of Thesis

This doctoral thesis is organised into various chapters. **Chapter 2** deals with the experimental techniques and processes developed in order to manufacture the composite materials in addition to the various characterisation methods used to understand the behaviour of the materials. **Chapter 3** is dedicated to the early work involved in producing and characterising 3D printed particle reinforced composites of PLA/Mg, PLA/Zn filaments in terms of their microstructural and physicochemical behaviour in addition to some 3D printing and mechanical testing of scaffolds. **Chapter 4** focuses on the 3D printing of medical grade PLDL/Mg, and PLDL/Zn materials using the methods developed in Chapter 3, and then characterising the materials in terms of their mechanical, degradation, and biocompatibility properties. **Chapter 5** gives an overview of the design of a customised 3D printer and the processes involved in creating continuous Al wire reinforced composites, followed by a full mechanical and microstructural characterisation of the materials. **Chapter 6** provides an extensive characterisation of medical grade Mg wire-reinforced composites produced by 3D printing. The composite materials were analysed in terms of their mechanical, degradation, and microstructural properties. Finally, **Chapter 7** presents the conclusions and future work regarding this thesis.

Experimental Techniques

2

2.1 Filament manufacturing

As discussed in Chapter 1, FFF uses a thermoplastic fused filament to fabricate 3D printed parts. However, a limited number of filaments of different materials are available, and thus customised filaments are necessary for creating parts with tailorable properties. In particular, composite filaments made up of thermoplastic polymers reinforced with metallic powders for FFF have to be manufactured following a double extrusion process (Figure 2.1).

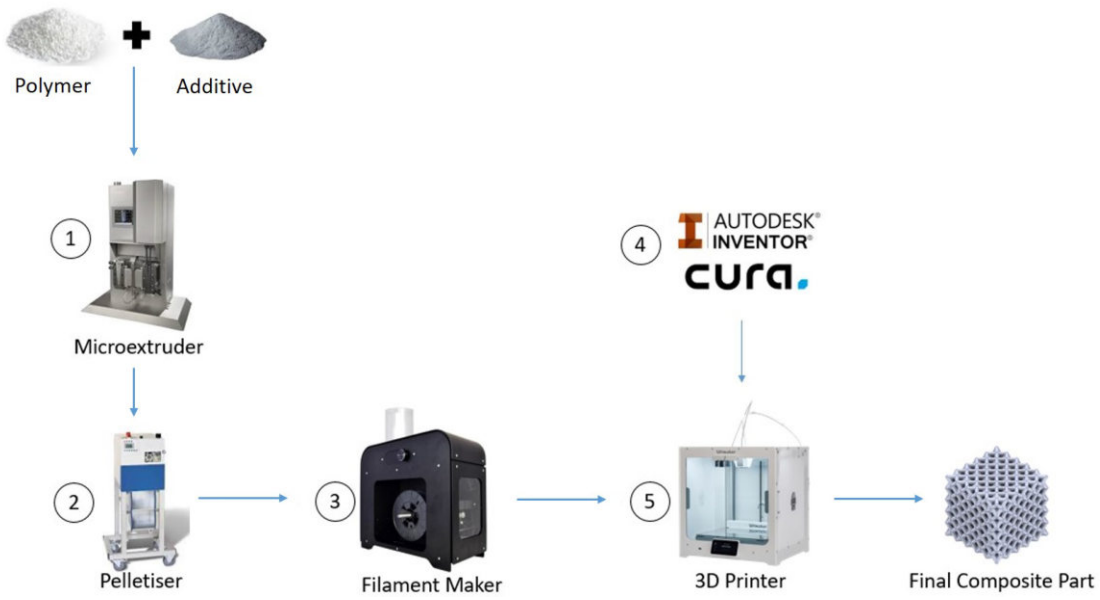

Figure 2.1: Roadmap for the fabrication of 3D printed components from polymer/metal composites. (1) Microextrusion of the polymer and metallic powder to create an inhomogeneous filament. (2) Pelletising the inhomogeneous filament. (3) Second extrusion in a precision filament maker desktop extruder. (4) Design of the component geometry. (5) 3D printing of the composite part.

To this end, polymer and metallic powders are mixed manually in the appropriate proportions to achieve the desired volume fraction. The thermoplastic polymer has to be dried in an oven for a specified period of time prior to mixing to eliminate the water absorbed due to their hygro-

scopic nature. The mixed powders were extruded in an MC 15 microcompounder (Xplore, Sittard, The Netherlands) with two conical mixing screws to obtain a filament. The residence time was approximately 2-3 minutes for all material combinations used in this thesis, while the extrusion temperature depended on the composition.

The filaments obtained from extrusion in the microcompounder were not suitable for FFF because they did not have a constant diameter and were not fully dense. They were pelletised (Brabender GmbH, Duisburg, Germany) and new filaments were extruded in a precision extruder (3devo B.V., Utrecht, The Netherlands). This precision extruder has 1 screw and 4 heaters placed along the screw to modify the extrusion temperature along the screw. Once the material exits the nozzle, a laser/pulley system measures the diameter every second and adjusts the speed at which the filament is drawn out to achieve the desired diameter (Figure 2.2). The average screw speed was 5 revolutions per minute (RPM) and the temperatures along the screw varied with the composition of the material. Fully dense filaments with a constant diameter and a homogeneous distribution of the metallic particles were obtained through this second extrusion and were suitable for FFF.

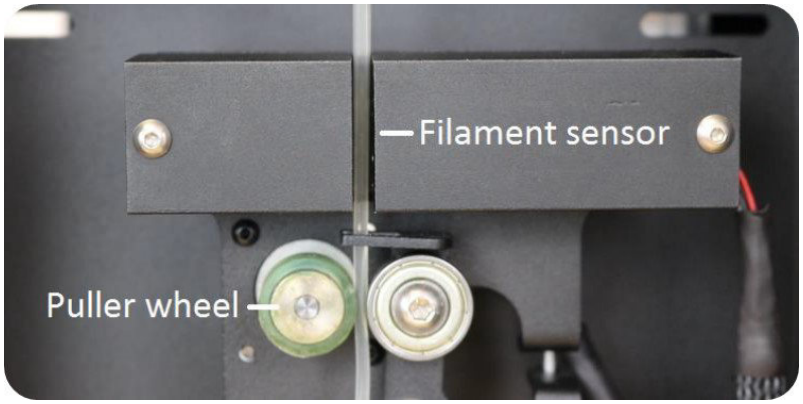

Figure 2.2: Laser-pulley system part of the 3devo, vital in achieving and maintaining the desired diameter of the filament.

2.2 Mechanical characterisation

2.2.1 Tensile tests

Tensile tests were performed following the recommendations of the ISO 527-A standard [140]. The mechanical properties of the materials in tension were measured in an Instron 5966 mechanical testing machine. The applied load was measured with a suitable load cell (from 500N to 10kN) depending on maximum applied load. The tests were carried out under displacement control and the approximate strain rate also depended on the materials and environment. A schematic of the experimental setup can be seen in Figure 2.3 (a).

The dogbone specimens were designed and manufactured by FFF according to ISO 527-A in the case of particle-reinforced materials. Coupons with dimensions 120 x 10 x 2.1 mm^3 were designed and fabricated using 3D printing in the case of unidirectional continuous wire-reinforced materials.

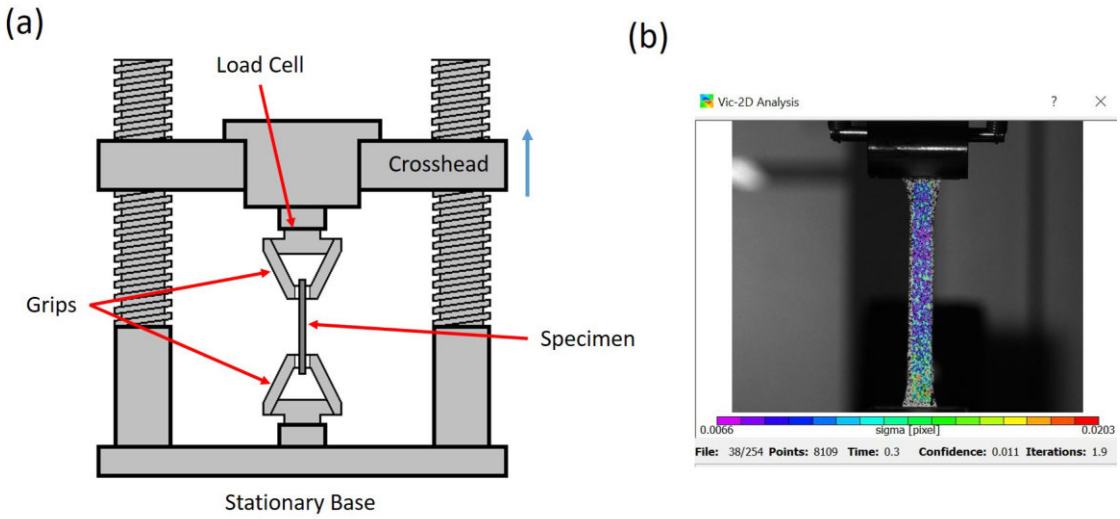

Figure 2.3: (a) Schematic diagram of the tensile test machine during a test [141]. (b) Determination of the strain at the gauge section of a dogbone specimen by digital image correlation software (DIC).

The strain in the central gauge section of the samples was measured by means of digital image correlation during the tensile tests. To this end, the gauge section was painted in white and then sputtered by black paint to create a random pattern of black dots on the surface. The position of the black dots on the surface was recorded every 0.3-0.7 s, depending on the material, with a high resolution camera and the displacement of each point during deformation was correlated through the Vic 2D-2009 DIC software (Correlated Solutions Inc., SC, USA) (Figure 2.3 (b)). The strain field in the gauge length was extracted from the displacement field on the surface and this information was used to plot the stress-strain curves during the tensile test.

In addition to the standard tensile tests in air at room temperature, tensile tests were also carried out in samples immersed in water at 37°C to assess the behavior of the materials in physiological conditions. The experimental setup to carry out the immersion tensile tests is depicted in Figure 2.4. The dimensions of the samples for the immersion tests were the same as those used for the tests in air.

2.2.2 Compression tests

The mechanical properties of the scaffolds in compression were measured using an Instron 3384 mechanical testing machine on cubic scaffolds of 20 x 20 x 20 mm^3 manufactured by FFF. The scaffolds were placed between two compression plates and a controlled displacement rate at crosshead speed of 0.5mm/min was applied (Figure 2.5). Teflon paste was inserted between the scaffold and the compression plates to minimise friction. The applied load was measured with a load cell, while the reduction in length was determined by means of a linear variable differential transducer (LVDT) in contact with the compression plates.

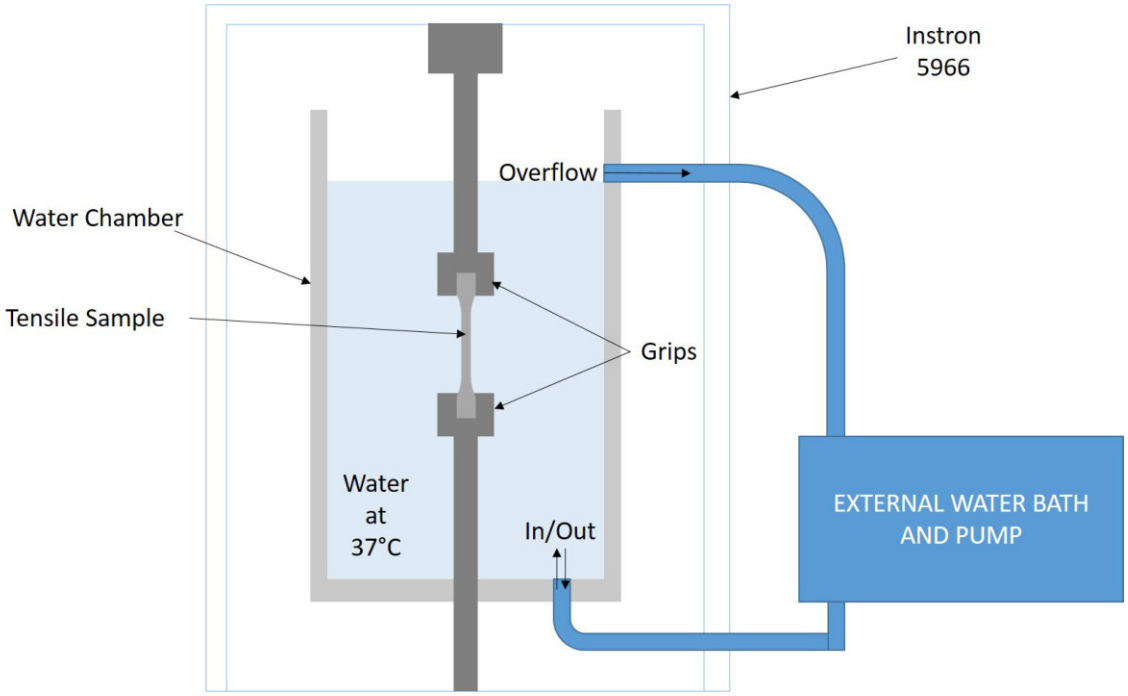

Figure 2.4: Schematic of the experimental set-up for the tensile tests in water at 37°C An external water bath and a pump controlled the temperature and the filling/draining of the water chamber.

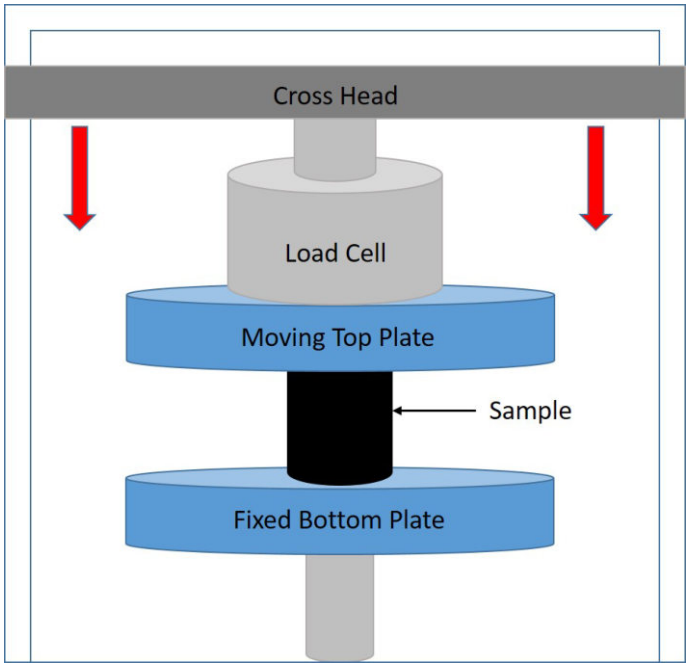

Figure 2.5: Schematic diagram of the uniaxial compression tests.

2.2.3 Wire push-out tests

Wire push-out tests were carried out to evaluate the interfacial shear strength between the wires deposited during 3D printing and the polymeric matrix, following the strategies developed in previous investigations [86, 142, 143].

To this end, samples of 10 x 10 x 2.1 mm^3 were cut from the wire-reinforced coupons perpendicular to the wires using a high precision punch and subsequently embedded in an epoxy resin (SpeciFix resin system, Struers, Denmark). The samples were then ground using a manual grinding machine (Vector-Metaserv 250, Buehler, IL, USA) with SiC paper ranging from P320 to P2500 up to a thickness of 0.6 ± 0.03 mm, because the thickness of the sample should be approximately twice the diameter of the wires [85, 144].

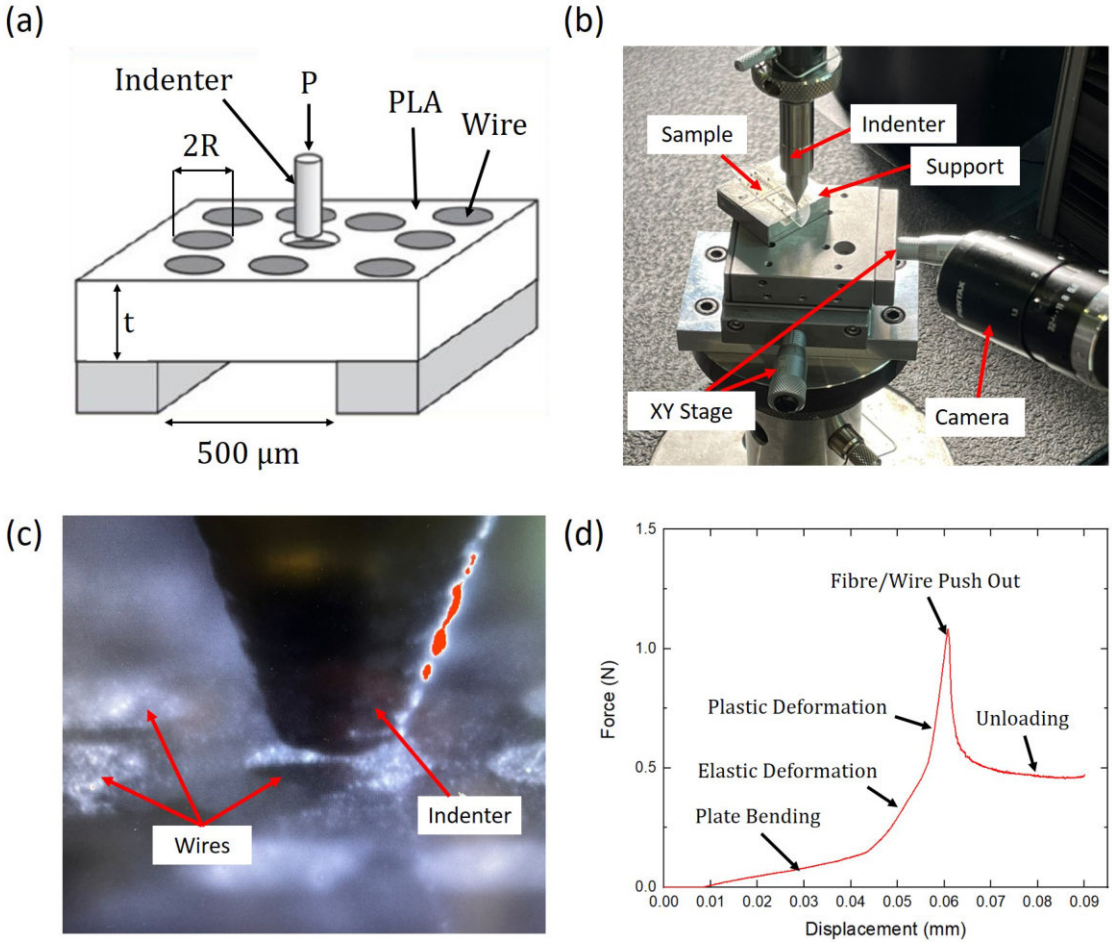

Figure 2.6: (a) Schematic diagram of the wire push-out experimental set up. The sample should have a thickness t, twice the diameter of the wire, and a force P is applied perpendicular to the wire until a push-out is achieved. (b) Experimental setup (c) Close-up image of the indenter being positioned above a wire prior to push-out. (d) Typical force *vs.* displacement curve from a fibre push out experiment with indications of the various stages of the test.

The thin slices of the composite were mounted on a stainless steel support with a groove of 500 μm in width to perform the wire push-out test (Figure 2.6 (a)). The wire to be tested was

positioned manually at the center of groove with the help of an optical microscope and the slice was fixed with tape. The support was attached to a stage capable of moving in X and Y directions to position the indenter punch over the desired wire. An indenter with a flat stainless steel tip of ≈ 250 μm diameter was mounted on an Instron 5966 mechanical test machine with a 100 N load cell. The compressive load was applied on the wire under displacement control at 20 μm/min until the wires were pushed-out from the matrix, which was indicated by a significant drop in load (Figure 2.6 (b)).

2.3 Thermal properties

2.3.1 Differential Scanning Calorimetry

Differential Scanning Calorimetry (DSC) was carried out in a Q200 Differential Scanning Calorimeter from TA Instruments. A sample of 5-10 mg is placed inside a small sample holder, also referred to as an Al pan and an empty reference pan is also used as a control. The sample is heated and cooled at a controlled rate while the changes in heat flow with temperature are recorded. They provide information about the thermal properties of the material such as the glass transition temperature (T_g), melting temperature (T_m), and crystallisation temperature (T_c) (Figure 2.7).

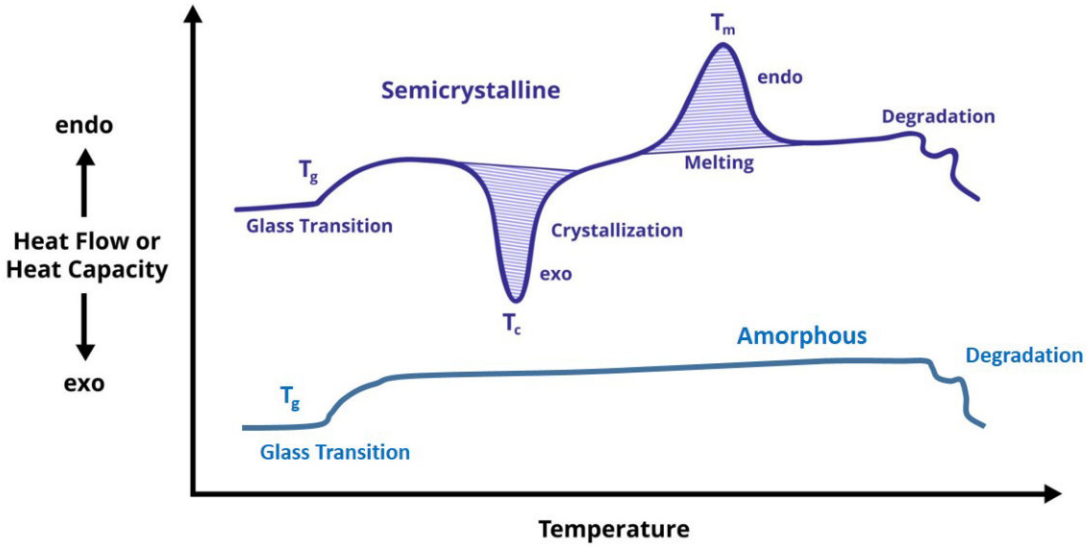

Figure 2.7: Typical DSC curves for both semicrystalline and amorphous materials [145].

2.3.2 Thermogravimetric Analysis

Thermogravimetric analysis (TGA) was carried out in Q50 Thermogravimetric Analyser (TA Instruments, DE, USA). During the test, a small amount of material (5-10 mg) is placed inside a crucible and heated at a constant rate while the weight of the sample is being continuously measured. With increasing temperature the polymeric material undergoes various thermal degradation processes such as evaporation, oxidation, and pyrolysis, which cause a variation in mass (Figure

2.8). TGA provides information about the thermal stability which is important to determine the processing window of polymeric materials.

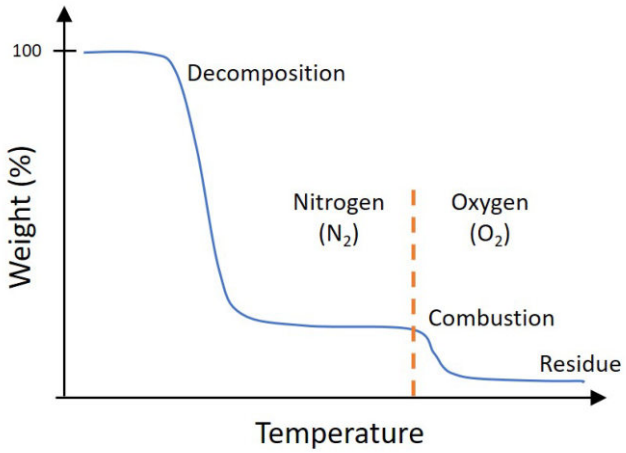

Figure 2.8: Typical TGA curve for polymeric-based materials [146].

2.3.3 Melt-Flow Index

Melt Flow Index (MFI) is a measure of the ease of flow of a molten polymer-based material. Essentially, it measures the flow rate of a polymer when melted, through a standard orifice or nozzle under set conditions of temperature and pressure. It is widely used to characterise the viscosity and processing parameters of polymer-based materials [147]. The MFI of polymers and polymer composites was measured in a KINSGEO MFI tester. To this end, between 2 and 10 grams of polymeric material is placed in a heated column, where it is melted and subsequently extruded through an orifice due to pressure exerted by a load of 2.6 kg to the molten polymer (Figure 2.9). The extrusion rate is measured, and the MFI value is calculated based on the mass of the plastic that has been extruded in a certain period of time and the MFI is expressed in units of grams per 10 minutes (g/10min). The MFI is an indicator of the melt flow rate and hence viscosity of the material, and it allows for the prediction of processing conditions. It provides valuable information in terms of rheological properties and determines if additives may be needed to aid in the processing of certain polymeric materials [147, 148, 149].

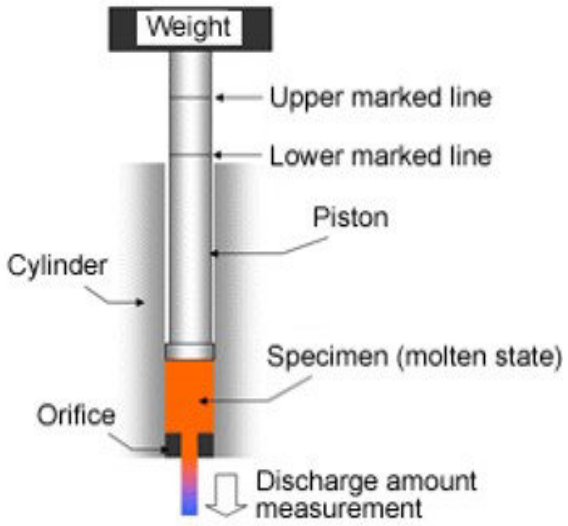

Figure 2.9: Schematic cross-section diagram of a typical MFI test [150].

2.4 Degradation tests

Degradation tests were carried out to assess the evolution of the properties of the biodegradable materials with immersion time in physiological environments. All degradation tests were conducted following the guidelines specified in ISO 13781 standard [151]. The degradation tests were performed by immersion at 37°C in Gibco Dulbecco's Phosphate Buffer Saline (PBS) from Merck Millipore Life Technologies Europe B.V., Bleiswijk (Product Number: 524650). The PBS solution had a composition of 140 mM NaCl, 10 mM phosphate buffer, and 3 mM KCl per litre.

The temperature of the PBS was controlled in a thermostatic water bath. Samples were periodically extracted in triplicate and the pH of the PBS was measured using a pH metre (Sension + PH3, Hach, Ames, Iowa, United States). Subsequently, the 'wet' mass was measured in an ES125SM balance (Precisa Gravimetrics, Dietikon, Switzerland) after drying the samples with tissue paper.

The production of hydrogen gas is an indicator of the corrosion of Mg. Thus, hydrogen gas was measured during immersion in PBS of both Mg powder-reinforced and continuous wire-reinforced composites using the experimental setup depicted in Figure 2.10. The samples were suspended using paper clips in a beaker filled with PBS to avoid inhomogeneous degradation in the contact points with the beaker. An inverted funnel was placed on top of the samples and a burette on top of the funnel. This set-up was sealed with paraffin wax (Parafilm M, Amcor, Switzerland) to minimise leakages. The burette was filled with a known volume of PBS and the displacement of the liquid due to the release of hydrogen was recorded on a daily basis.

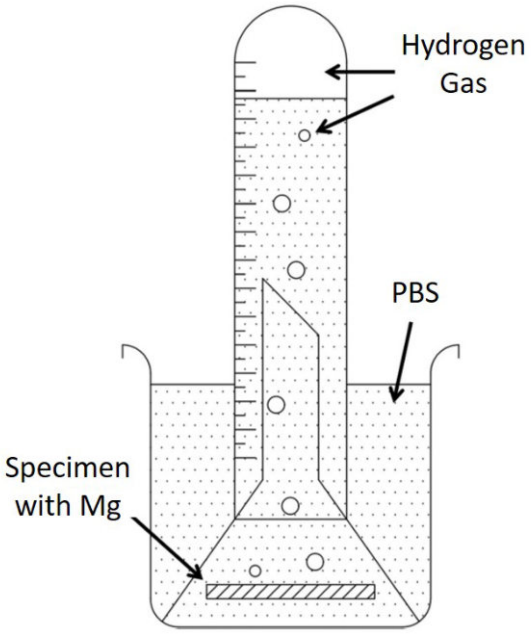

Figure 2.10: Schematic diagram of the experimental setup used to quantify the volume of hydrogen gas released by composites containing Mg [89, 152].

2.5 Molecular weight distribution

Gel Permeation Chromatography (GPC) was used to determine the molecular weight and the molecular weight distribution of the polymers using a Waters 2414 Refractive Index Indicator. The polymer is dissolved in a solvent and injected into the GPC column which is filled with porous polystyrene-based beads with a defined pore size distribution. As the solution moves through the column, larger molecules are excluded from the pores and elute first, while the smaller molecules that penetrate the pores elute later [153]. The molecular weight distribution is given by the elution volume or retention time of the sample, which is compared with a calibration curve obtained from a similar polymer of known molecular weight.

2.6 Microstructural characterisation

2.6.1 Scanning Electron Microscopy

In the case of samples where the cross section was desired to be analysed, the samples were embedded in an epoxy resin (SpeciFix resin system, Struers, Denmark) and polished before observation in the scanning electron microscope (SEM). Once polished, they were washed with water and ethanol before being dried and then sputtered with Au using a Quorum Q150T ES gold sputtering machine (Quorum Technologies Ltd., East Sussex, England) to improve conductivity and reduce the charging effects of the samples in the SEM. [154]. In the case of fractography studies, the fracture surfaces were cleaned using pressurised air and then sputtered with gold before being placed in the SEM.

SEM imaging was performed using both an Apreo-FIB 2S LoVac (Thermo Scientific, Waltham, MA, USA) and a Helios Nanolab 600i (FEI, Hillsboro, Oregon, USA) SEM. The accelerating voltage rarely exceeded 5kV, and the beam current was generally maintained between 50 pA and 0.8 nA. The exact parameters for the SEM images will be mentioned throughout the thesis. ETD was the primary detector used the analysis of the samples.

2.6.2 Energy-Dispersive X-ray Spectroscopy

Energy-Dispersive X-ray Spectroscopy (EDS) (Oxford Instruments, United Kingdom) was used within the SEM to analyse the elemental composition of the samples, especially during degradation studies to assess the degradation of the Mg and Zn particles and of the Mg wires. Elemental maps of the area of interest were taken and the predefined elements were always a selection of the following elements: carbon, oxygen, magnesium, zinc, phosphorous, and calcium. The accelerating voltage from the EDS was the same as the SEM, and the only reason that the 5kV would be increased was to obtain a better signal in the elemental analysis.

2.6.3 X-ray computed microtomography

Finally, X-ray computed microtomography (X-μCT) was used to determine the dispersion of reinforcement materials throughout the bulk of the matrix material and also to measure the porosity within the filaments and the samples manufactured by FFF. The tomography of the various samples throughout this thesis was carried out using a Phoenix Nanotom (Waygate Technologies, Huerth, Germany) using a W target, with a Cu filter and 0-mode nanofocus. Depending on the material being imaged, the voltage of the X-ray tube varied between 50 and 120 kV, the current varied between 80 and 300 μA, and the voxel size varied between 2 and 5.4 μm. The exact parameters used for each material will be specified throughout the thesis.

2.7 Biological tests

The cytocompatibility of the materials was assessed by means of indirect and direct tests, which were carried out following the guidelines of the ISO standard 10993 part 5 and part 12 [155, 156].

2.7.1 Indirect tests

Material extracts were obtained by immersing each individual sample in complete culture medium with an area/volume ratio of 3 cm^2 /ml. The samples were incubated under physiological conditions for 72 hours. Independently, cells are seeded for 24 hours. The culture medium was subsequently removed and replaced with diluted material extracts. Pure extracts should be evaluated followed by a 2-fold dilution of extracts (50%, 25%, 12.5%, 6.25% and 3.125%). Cells with their diluted medium extracts are then incubated for 24 hours. Next, 5 mg/ml of MTT (3-(4,5- dimethylthiazol-2-yl)-2,5-diphenyltetrazolium bromide) (Sigma-Aldrich, MO, USA) is diluted in PBS and added in each well. Cells along with the MTT assay are incubated at 37°C in the dark which react together to form formazan crystals. Dimethyl sulfoxide (DMSO) (Sigma-Aldrich, MO, USA) is subsequently added to dilute the formazan crystals. Finally, the absorbance is read on a spectrophotometer (BioTek EL800, Agilent, CA, USA) with a wavelength of 570 nm. Mitochondrial activity is calculated by

normalisation with respect to control wells, in which cells were seeded in the complete medium without extracts. Each experiment should be repeated three times, and the experimental procedure is depicted in Figure 2.11.

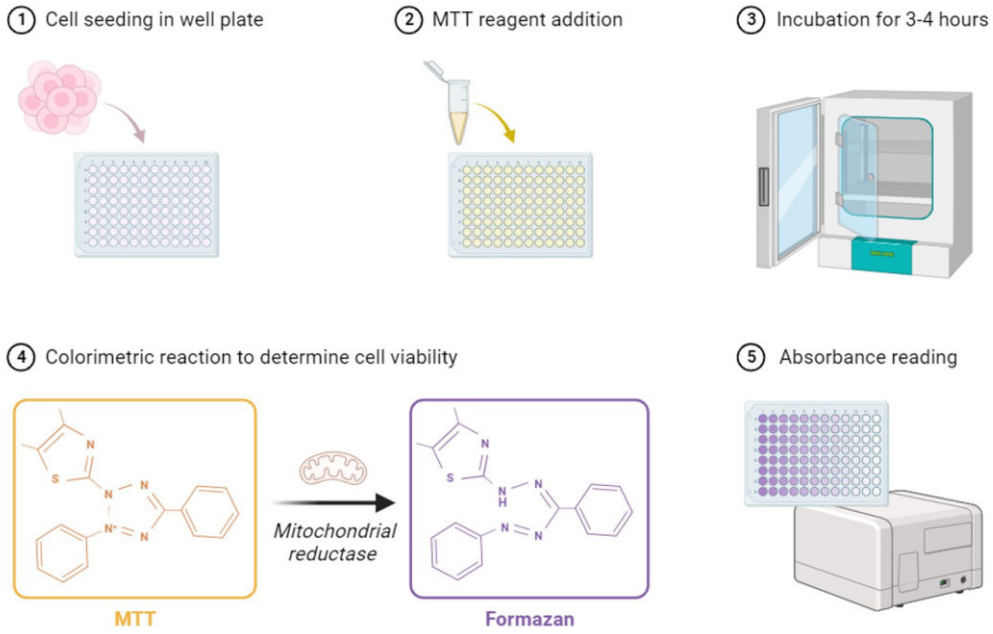

Figure 2.11: Indirect tests procedure [157].

2.7.2 Direct tests

Material-Cell Interaction

Material-cell interaction is studied by immunofluorescence staining of dapi-phalloidin to observe the morphology of cells under confocal microscopy, and by scanning electron microcopy to analyse the interaction between cells and materials. For both experiments, cells are seeded directly on top of samples at a specified concentration and incubated under physiological conditions. A set of samples is generally cultured for 1 hour to evaluate the early attachment of cells to the surface, while another set of samples is cultured for 24 hours to assess late attachment, cell morphology, and monolayer formation. At the end of each incubation time, cells are fixed with paraformaldehyde (PFA)(Sigma-Aldrich, MO, USA).

For the immunofluorescence staining technique, cells are permeabilised with Triton X-100 (Sigma-Aldrich, MO, USA) for 15 min. Next, cells are washed with PBS and then exposed to Alexa Fluor 488 phalloidin (Thermo Fisher, MA, USA) and to DAPI (Sigma-Aldrich, MO, USA) with various concentrations which will be provided in later chapters. Cells are then incubated at room temperature for 1 hour. Subsequently, they are observed in the confocal microscope (Confocal Olympus Fluoview FV-3000, Olympus, Tokyo, Japan).

Another set of samples was used to study the cell-material interaction. They were dehydrated in ethanol at different concentrations. A second dehydration process was carried out using hexamethyldisiloxane (HMDS) (Thermo Scientific, MA, USA) diluted in ethanol with various concentra-

tions, which will also be provided later. These dehydration steps are carried out after fixing the cells with PFA. After the final dilution, samples are left to dry at room temperature overnight. The cell-material interaction is subsequently observed in a scanning electron microscope (Apreo 2S LoVac, Thermo Scientific, MA, USA). The summary of the experimental procedure is depicted in Figure 2.12.

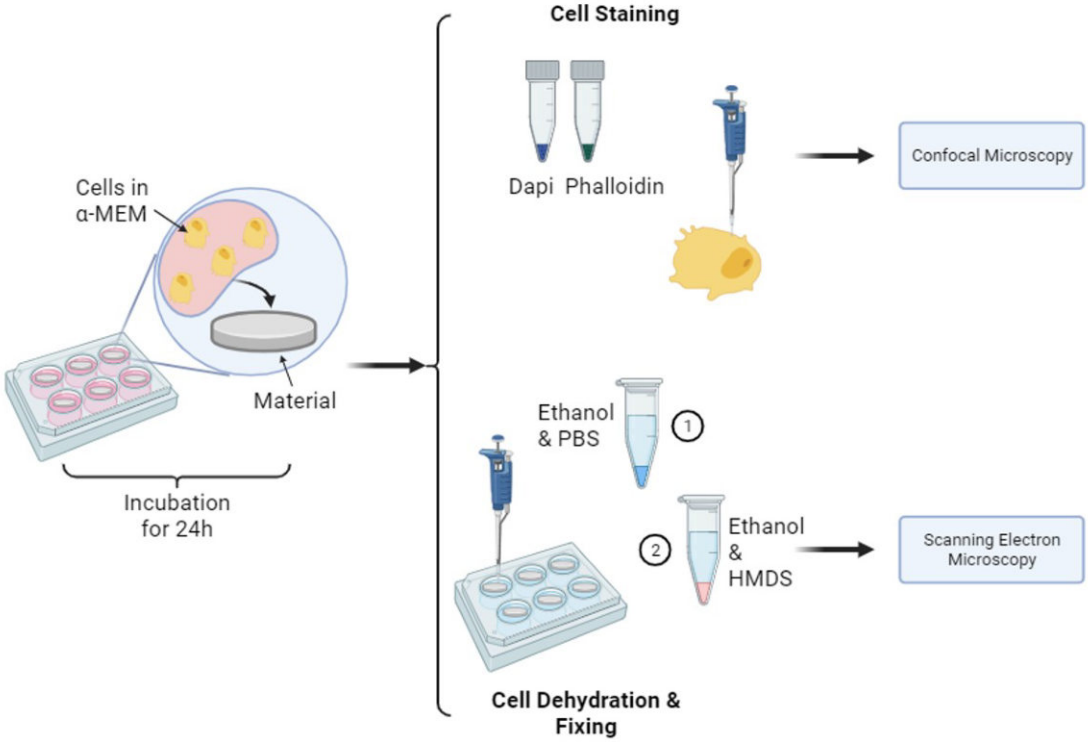

Figure 2.12: Direct tests procedure to study the cell-material interaction [157].

Live/Dead Assay

For live/dead assays, samples are placed in a well plate and cleaned with ethanol, followed by washing with PBS. Subsequently, cells are seeded on top of the samples with a concentration of cells depending on the standard, and immersed in complete culture medium before being placed in an incubator under physiological conditions. The medium should be changed every 2 days to allow the cells to continue to grow. The live/dead solution for the assay is prepared by diluting ethidium homodimer-1 (635 nm), and calcein AM (515 nm) in PBS, followed by thorough mixing. The exact concentrations will be provided later in the thesis. The live/dead solution is then added to the cells, ensuring that they are covered by the solution. The plate should be covered in order to protect the solution from light and incubated under physiological conditions. The live/dead solution is then removed in darkness, and the samples are washed with PBS. The sample should be left in PBS and immediately viewed under confocal microscopy. The experimental procedure is very similar to the cell staining technique indicated in Figure 2.12, with the only differences being the staining used and the number of days the samples are incubated.

Processing of PLA/Mg and PLA/Zn filaments for 3D Printing

3

3.1 Motivation

PLA is a widely used thermoplastic polymer for 3D printing through fused filament fabrication (FFF) [158]. This technique enables the production of patient-specific implants and scaffolds from medical images in orthopaedics and traumatology [159]. PLA filaments reinforced with metallic particles for 3D printing are usually created by extrusion of PLA/Mg pellets obtained by conventional extrusion [134] or through colloidal routes [160, 161]. However, these filaments are not suitable for 3D printing due to the inhomogeneous distribution of metallic particles, porosity, and variations in filament diameter [162]. It is also important to control the rheological properties of the filaments to ensure that they are within the appropriate range for 3D printing at a given temperature [163] because MgO catalyses the thermal degradation of PLA at high temperature, reducing the molecular weight, viscosity and mechanical properties of PLA/Mg composites [164, 165, 166, 167]. An alternative to Mg is Zn, which is an essential element for the body and has anti-inflammatory and anti-proliferative properties [168, 169, 170, 171, 172]. However, the development of PLA/Zn filaments for FFF has not been reported in the literature.

Thus, the first objective of this thesis was to develop a suitable strategy to manufacture PLA/Mg and PLA/Zn filaments with constant diameter, no porosity, homogeneous particle distribution, and controlled viscosity. Furthermore, the influence of Mg and Zn particles on the depolymerisation of PLA during filament fabrication was examined. Finally, porous PLA/Mg and PLA/Zn scaffolds were manufactured by FFF and their microstructure and mechanical properties were analysed. These results demonstrate the feasibility of fabricating PLA/Mg and PLA/Zn composite scaffolds for regenerative tissue engineering.

3.2 Materials

Ingeo Biopolymer 2003D from NatureWorks (NatureWorks BV, Netherlands) was selected as the PLA polymer matrix because it was used previously for 3D printing using the FFF technique [160, 173, 174, 175]. Furthermore, low molecular weight polyethylene glycol (PEG) (MW = 1000 g/mol) was selected as a plasticiser as it is one of the most common and effective agents [176].

The spherical particles of the WE43 Mg alloy were supplied by Meotec GmbH with a nominal composition of 1.4 - 4.2% Y, 2.5 - 3.5 % Nd, <1% (Al, Fe, Cu, Ni, Mn, Zn, Zr) and balance Mg (in wt%). They were manufactured for selective laser melting applications and the powder particle distribution was D_{10} = 29.1 μm, D_{50} = 45.8 μm and D_{90} = 64.4 μm [177]. The particles were covered with a thin passivation layer of Y_2O_3 which also limited the flammability of the powder during handling. Alloys with similar composition have been successfully applied in orthopaedic applications [178] and are well established as biodegradable and biocompatible alloys [179]. Spherical particles of Zn-1 wt.% Mg (Zn-1Mg) alloy were also produced by gas atomisation and provided by Meotec GmbH (Aachen, Germany). The nominal particle diameter distribution was 20<D<63 μm. In the case of Zn-1Mg particles, the size, morphology, and element distribution were examined by scanning electron microscopy (SEM) (Helios NanoLab 600i, FEI) using secondary electrons, and energy dispersive spectrometry (EDS) and the results are shown in Figure 3.1(a). They show a large content of small Zn particles (<5 μm).

The PLA/Mg filaments contained 1, 2, 3, 4, and 5 wt.% Mg and 5 wt.% of PEG was added in the filaments with 4 and 5 wt.% of Mg. 3.5, 7, 10.5, 14, and 17.5 wt.% of Zn were used in the case of PLA/Zn filaments. The difference in weight percentages between Mg and Zn is dictated by the differences in density and the mixtures were selected to obtain the same range of volume fractions in both materials. For instance, the volume fraction of 5 wt.% of Mg particles is the same as 17.5 wt.% of Zn-1Mg particles.

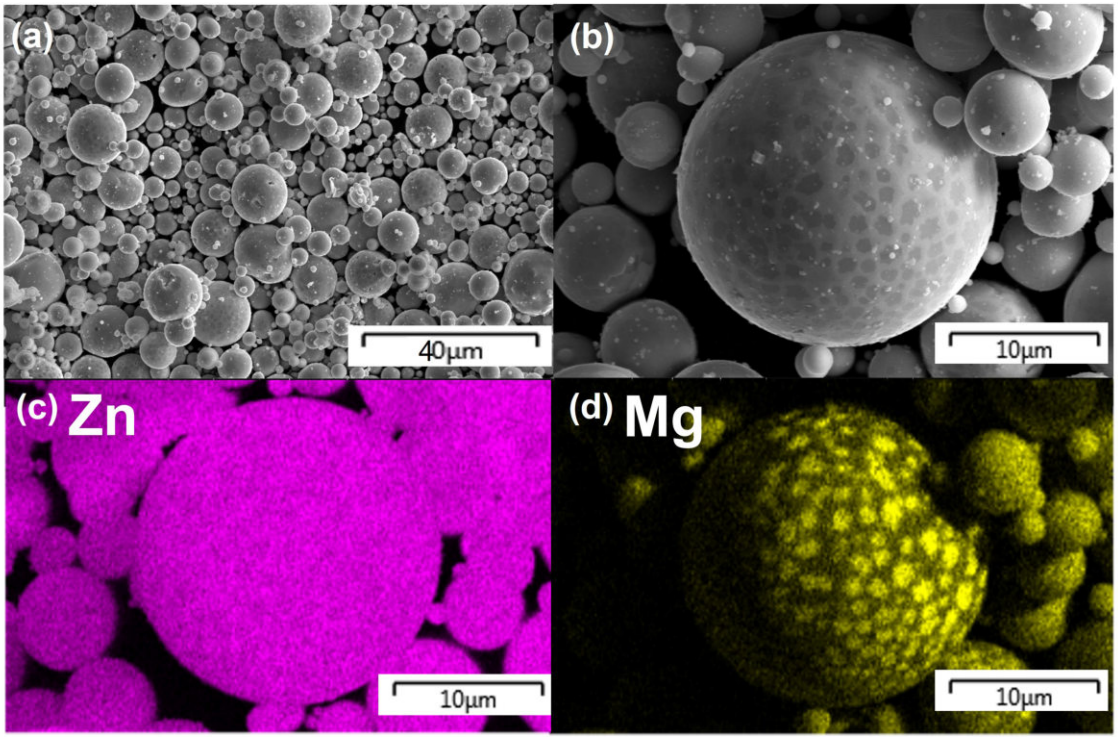

Figure 3.1: (a) and (b) Secondary electrons SEM images of the Zn-1Mg particles. (c) and (d) EDS analysis showing the distribution of Zn and Mg in the particles.

3.3 Methods

3.3.1 Filament production

A general explanation of the filament production process is given in Chapter 2 but the specific processing parameters will be detailed here. First, PLA pellets were dried in a conventional drying oven (Scientific Instrument Co. Ltd., Shanghai, China) at 60°C for 24 hours. Subsequently, they were manually mixed with Mg or Zn powders in the required weight proportions, and it was ensured that most of the metallic particles remained adhered to the pellet surface.

The mixture of PLA and Mg or Zn particles was extruded in a Xplore MC 15 Micro Compounder containing two conical mixing screws at 180°C with a residence time of $\sim$ 3 minutes and a screw rotating speed of 100 rpm. The extruded material went through an air-cooling channel attached to the extruder leading to a filament of $\approx$ 2.85 mm in diameter. It should be noted that the diameter of the filament could not be controlled in this step. The filaments were pelletised (Granulator, Brabender) and the corresponding feedstock of PLA/Mg or PLA/Zn pellets was introduced in the 3Devo Precision 450 filament maker. The temperature profiles for each combination of materials are shown in Tables 3.1 and 3.2. It is worth noting that the heaters are labelled counter-intuitively in the table from 4 to 1 instead of the expected 1 to 4. This is because of the manufacturer specifications on the 3devo as seen in Figure 3.2. The temperature profile increases initially along the barrel and then decreases to gradually melt the polymer before reaching the final heater nearest the nozzle with a lower temperature in order to increase the viscosity of the material before being further cooled by ambient temperature and spooled.

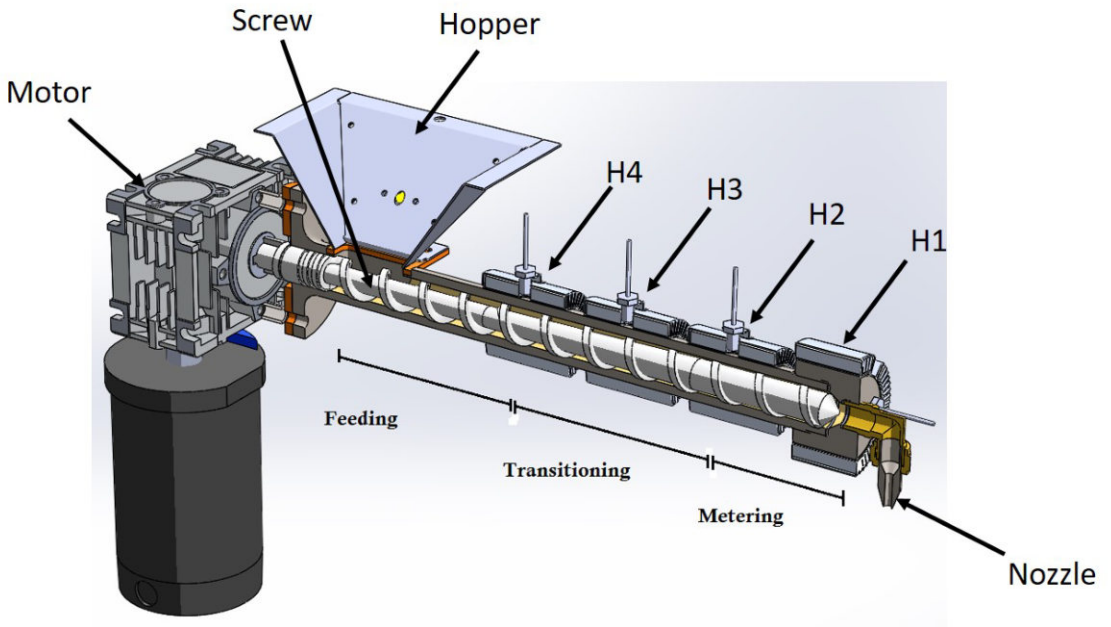

Figure 3.2: Schematic of the screw inside the barrel in the 3Devo Precision 450 filament maker. Heaters are shown in their relative positions labelled in HX format where H is heater and X corresponds to the relative number.

Table 3.1: Individual heater temperatures in the 3devo for PLA/Mg filaments.

Material	Heater 4 °C	Heater 3 °C	Heater 2 °C	Heater 1 °C
PLA	180	200	180	170
PLA/Mg (1%, 2%, 3%)	170	190	170	160
PLA/Mg (4%, 5%)	160	180	160	150
PLA/Mg (4%, 5%)/PEG (5%)	150	160	150	140

Table 3.2: Individual heater temperatures in the 3devo for PLA/Zn filaments.

Material	Heater 4 °C	Heater 3 °C	Heater 2 °C	Heater 1 °C
PLA and PLA/Zn (3.5%, 7%)	180	200	180	170
PLA/Zn (10.5%, 14%)	170	190	170	160
PLA/Zn (17.5%)	160	180	160	150

3.3.2 Filament characterisation

The physical and chemical properties of the filaments were characterized after standard extrusion (in the Xplore MC 15 Micro Compounder) and precision extrusion (in the 3Devo extruder). The Mg and Zn particle distribution in addition to the porosity were measured in filaments of 3 mm in length by means of X-ray computed micro-tomography (X-μCT) in a Phoenix Nanotom using a W target and 0-mode nanofocus. In the case of the PLA/Mg filaments, the voltage of the X-ray tube was set to 80 kV and the current was 150 μA and the voxel size in the tomograms was 2 μm, while a voltage of 50 KV with a current of 300 μA and a voxel size of 2 μm was used in the case of the PLA/Zn filaments.

The thermal characterisation of both composite filaments was performed by differential scanning calorimetry (DSC) (Q200, TA Instruments) up to 180°C with a heating/cooling rate of 10°C/min. The thermal degradation of the two materials up to 500°C in air was studied by thermogravimetric analysis (TGA) (Q50, TA Instruments) that provided the weight variation as a function of the temperature. The MW distribution of the different composites was measured by gel permeation chromatography (GPC), including a Waters 2424 refractive index detector with tetrahydrofuran as the mobile phase, and a series of narrow polystyrene standards employed to generate the calibration curve. 5 mg of the degraded sample was immersed in 5 ml of tetrahydrofuran under magnetic stirring for 24 hours. Prior to injection, all samples were filtered with 0.45 μm nylon discs to remove powder particles and prevent blocking the columns of the GPC analyser.

Melt flow index (MFI) tests of standard and precision extruded filaments were performed using an MFI tester (KJ-3092, Kinsgeo) with a load of 2,16 Kg for 10 minutes at 170°C and 190°C following ASTM standard D1238. The MFI is a common test performed to investigate the melt-

processability of polymers and to determine the optimum temperature for 3D printing. According to the literature, the MFI of the filament should be in the range of 10 g/10 min to 30 g/10 min to be successfully printed using the FFF technique [149, 180]. Finally, the mechanical properties of the filaments in tension were measured in an electro-mechanical mechanical testing machine (Instron 3384) under displacement control at displacement rate of 0.5 mm/min. The load was determined using a load cell and deformation with an extensometer of 12.5 mm gauge length attached to the filament.

3.3.3 Specimen fabrication and mechanical characterisation

An Ultimaker S5 (Ultimaker BV, The Netherlands) was used to print PLA/Mg and PLA/Zn specimens using precision extruded filaments, with a travel speed of 5 mm/s and a nozzle of 400 μm in diameter. The printing temperature for PLA was 210°C, while for PLA/Mg it was 190°C for wt.% 1, 2, 3, and 4, while the PLA/Mg/PEG composites with 4 and 5 wt.% Mg powder were printed at 170°C. In the case of the PLA/Zn filaments the printing temperature was 190°C for the PLA+3.5 wt.% Zn and 170°C for the composites with 7 and 10.5 wt.% of Zn powder. The bed temperature was maintained at 60°C when printing neat PLA and the PLA/Mg composites while for the Zn containing composites it was maintained at 70°C.

In the case of PLA/Mg, dogbone samples with a rectangular cross section of 5 x 2 mm^2, following ISO 527-1 type 1BA [181, 182, 183], were printed to measure the mechanical properties under tension. The specimens were printed with a raster angle of 0° (parallel to the loading direction) and a layer thickness of 0.1 mm with the aforementioned printing speed of 5 mm/s, leading to a print time of 3 hours instead of 30 minutes when subjected to a print speed of 70 mm/s as specified by the manufacturer. Tensile tests were carried out on an electromechanical testing machine (Instron 3384) and deformation was measured with an extensometer of 12.5 mm gauge length attached to the sample.

Porous scaffolds with a face-centred cubic (FCC) lattice were printed to carry out compression tests of PLA/Mg and PLA/Zn. The dimensions of the scaffolds were 20 x 20 x 20 mm^3 and made up of circular struts of 1.5 mm in diameter (Figure 3.3). The printing temperatures indicated above were used, but the printing speed was reduced to 5 mm/s. The standard 40 mm/s commonly used in commercial 3D printers, however, the quality of the printed parts was superior when the printing speed was reduced to 5 mm/s, however this slower speed increased the printing time from 3 hours to approximately 14 hours.

The microstructure of selected scaffolds was analyzed by means of X-μCT with the same voltage and current used in the case of the filaments. The sample and detector positioning were different, leading to a voxel size of 12 μm. Furthermore, the mechanical properties of the scaffolds in compression were measured using an Instron 3384 mechanical testing machine. The cubic scaffolds were compressed between two compression plates under displacement control at a cross head speed of 0.5 mm/min. Teflon paste was inserted between the scaffold and the compression plates to minimize friction. The applied load was measured with a load cell, while the reduction in length was determined by means of a linear variable differential transducer (LVDT) in contact with the compression plates.

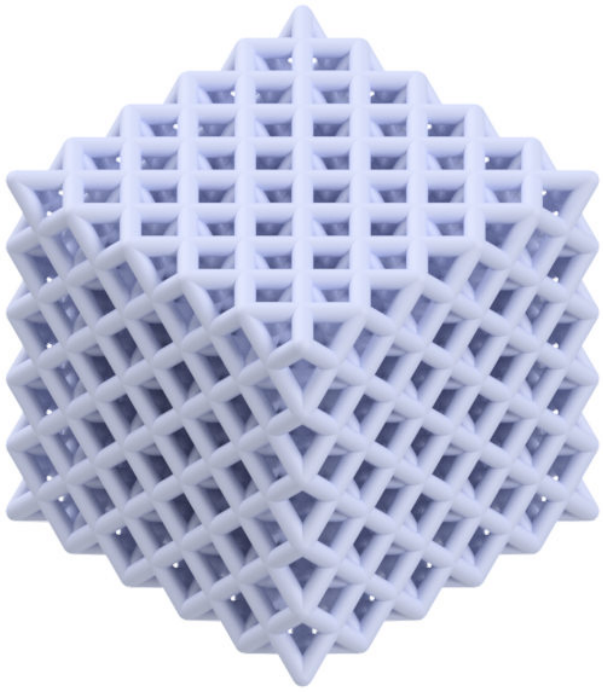

Figure 3.3: Model of the FCC scaffold.

3.4 Results and Discussion

3.4.1 Filament Characterisation

Representative sections of the PLA/Mg filament microstructure obtained by X-μCT are depicted in Figures 3.4 (a) and (b) for standard and precision extruded filaments, respectively. The black regions represent pores/voids, while the white dots are the spherical Mg particles. Spherical pores of 88 $\pm$ 19 μm in diameter were found in the filaments produced by standard extrusion regardless of the Mg content. The pore volume fraction was measured by segmentation of the tomograms in filaments of 3 mm in length and can be found in Table 3.3. Large pores were found in the filaments after standard extrusion, and, in addition, the filaments presented large variations in diameter and shape along their length. These features hinder their use during FFF, since the printing process is very sensitive to voids and variations in the filament diameter outside the tolerance.

On the contrary, precision extrusion led to filaments with 0 or negligible porosity (Figure 3.4 (b) and Table 3.3). Furthermore, the diameter of the filament was successfully controlled during precision extrusion (Figure 3.5), as shown by the measurements *in situ* of the diameter of the filament during extrusion of a PLA/5 wt.% Mg composite, which was the most difficult filament to produce. Oscillations were observed in the diameter between 2.92 mm and 2.76 mm, while the average diameter was 2.850 $\pm$ 0.004 mm. The fluctuations in diameter of 3 wt.% did not impede continuous printing by the FFF method. All of the PLA/Mg composite filaments manufactured by precision extrusion were within this tolerance in terms of diameter and could be successfully used to print scaffolds with complex geometries. Moreover, precision extrusion was a reproducible and robust process, demonstrating its potential for large scale production of composite filaments.

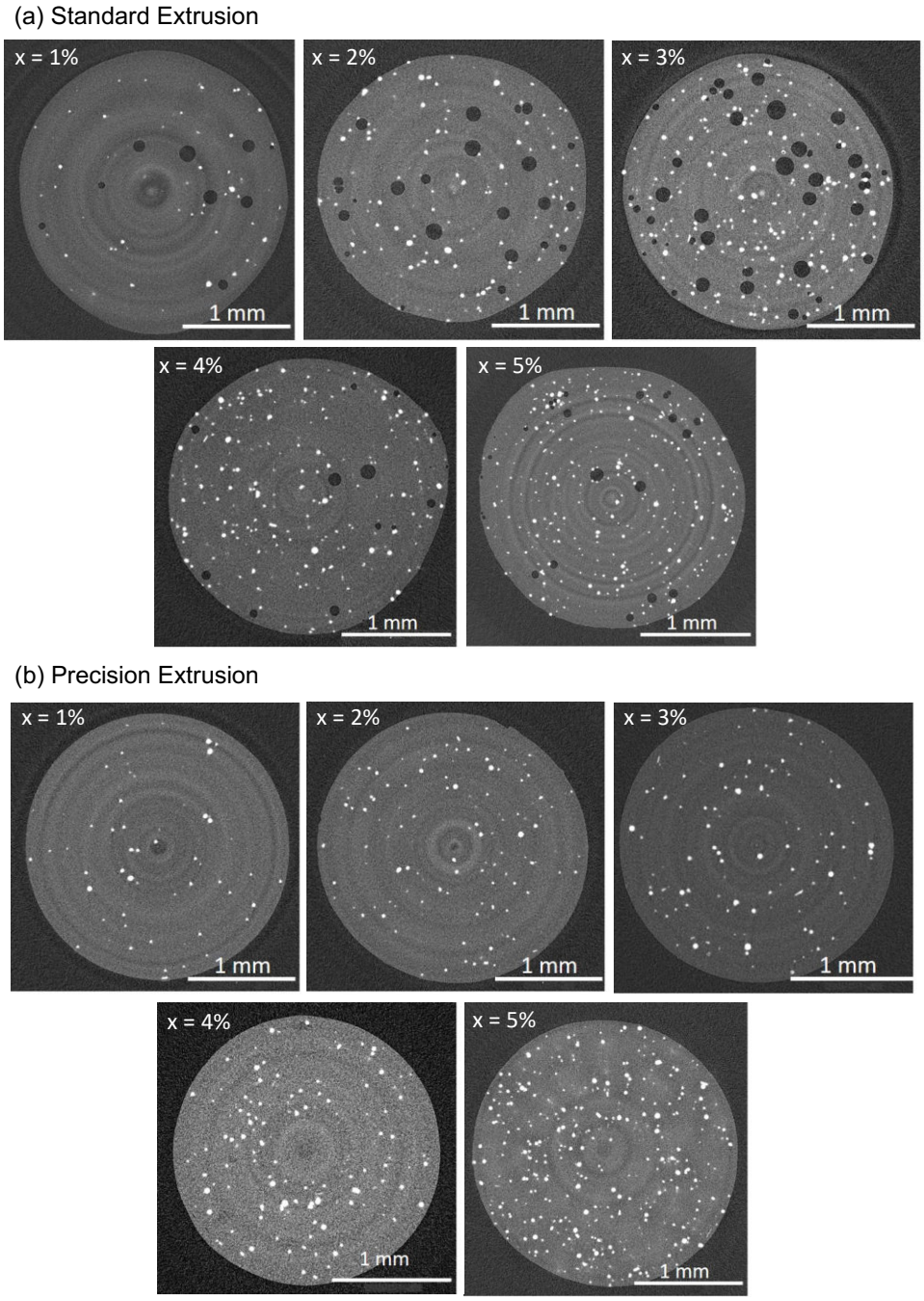

Figure 3.4: Representative cross sections obtained by X-μCT of PLA/Mg filaments after (a) standard extrusion and (b) precision extrusion. x stands for the weight fraction of Mg. Filament diameter was 2.85 mm in all cases.

The PLA/Zn filaments were also analysed by X-μCT and representative cross-sections are depicted in Figures 3.6 (a) and (b) for standard and precision extruded filaments, respectively. The black regions correspond to pores, while the white dots represent spherical Zn particles. In general, a homogeneous distribution of the Zn particles in the PLA matrix is obtained after standard or precision extrusion up to 14 wt.% of Zn. However, the concentration of the filler Zn particles

Table 3.3: Pore volume fraction (in %) in PLA/Mg filaments processed by standard and precision extrusion.

Mg content (wt. %)	Standard extrusion	Precision extrusion
1%	0.45	0
2%	2.72	0
3%	4.91	0
4%	0.61	0.03
5%	0.84	0

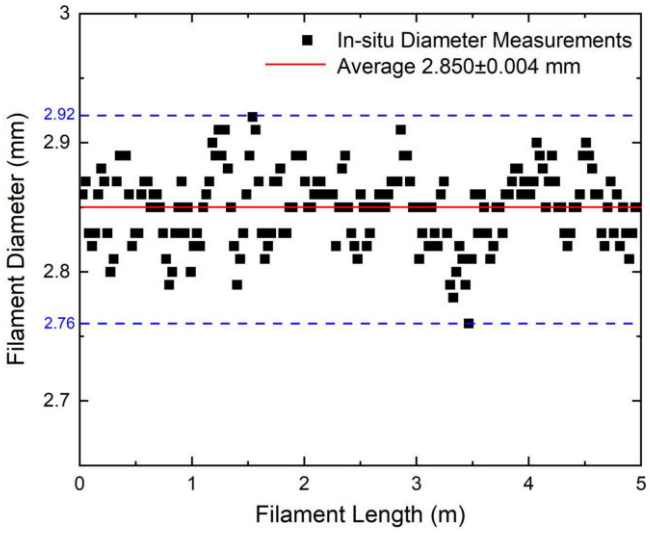

Figure 3.5: Oscillations of the filament diameter along the filament during precision extrusion of a PLA/5% Mg composite.

is higher near the center of the filament in the standard extruded filaments with 17.5 wt.% Zn. Filler migration towards the center of the filament during polymer extrusion has been previously reported [184, 185] and it is the result of the radial forces that develop on the filler particles during extrusion.

The tomograms of filaments of 3 mm in length were segmented to determine the pore volume fraction that can be found in Table 3.4. White regions stand for the Zn particle while black regions are pores. Standard extruded materials present non-constant diameter and irregular cross-section shape. The porosity was low except for the filaments with 17.5 wt.% Zn (Figure 3.6 (a)). Precision extruded filaments have constant diameter and circular shape and the porosity of the filaments is practically reduced to zero after precision extrusion when the Zn content is up to 10.5% (Figure 3.6 (b)). However, the porosity increases rapidly for 14 wt.% and 17.5 wt.% of Zn particles and large pores can be observed in the filament containing 17.5 wt.% Zn in Figure 2(b)).

The porosity of the PLA/Zn filaments is higher than that reported in PLA/Mg filaments processed by the same route and with equivalent volume fraction of metallic particles [180]. The

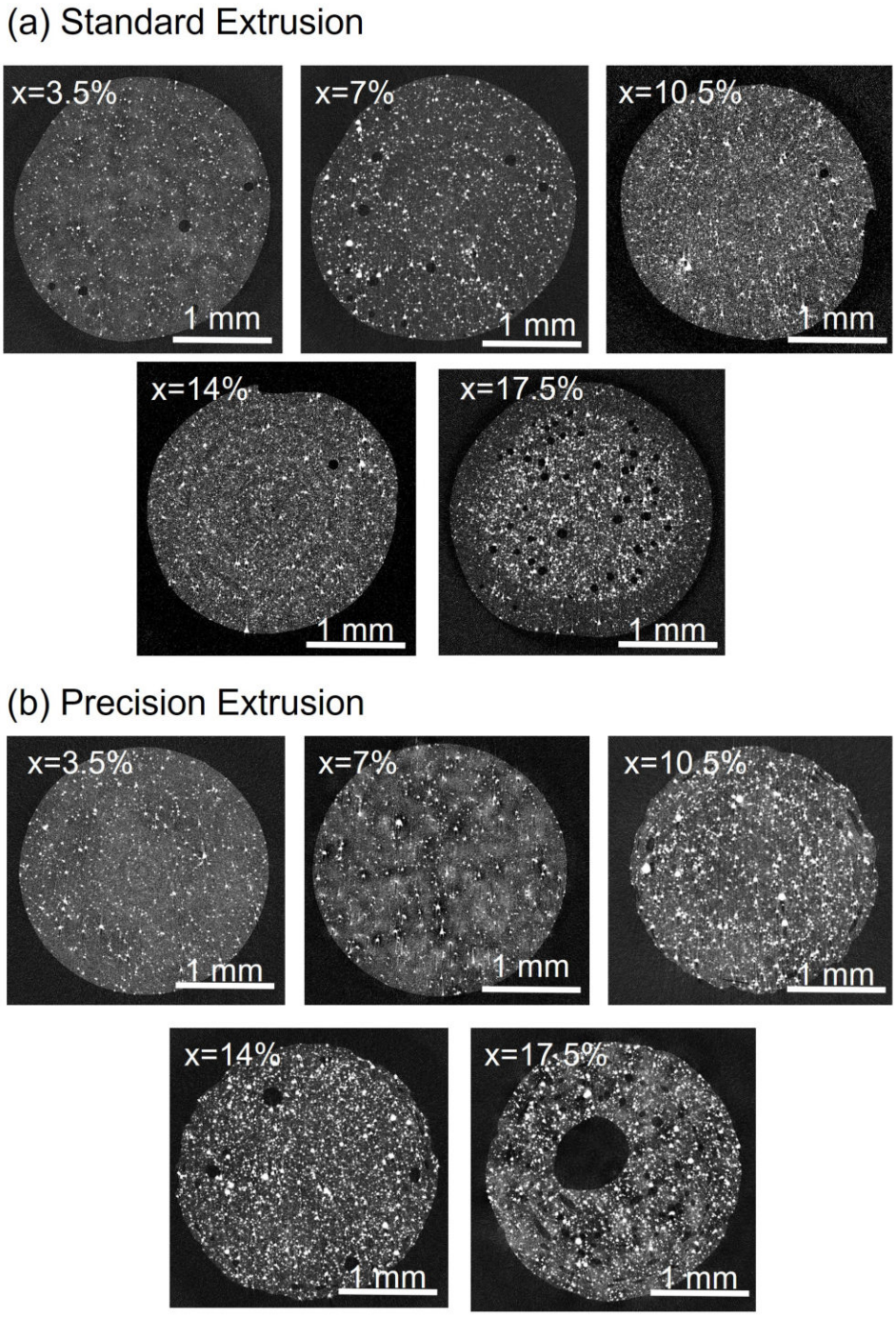

Figure 3.6: Representative cross sections obtained by X-μCT of PLA-x Zn (x in wt.%) filaments after (a) standard extrusion and (b) precision extrusion. x stands for the wt.% of Zn. The filament diameter was 2.85 mm in all cases. White regions stand for the Zn particle while black regions are pores.

higher porosity of the PLA/Zn filaments, especially the one with 17.5 wt.% Zn, may be attributed to the large content of small Zn particles (<5 μm), which increases the contact surface area between metal and polymer (See Figure 3.1). This phenomenon leads to higher porosity because of the gas

Table 3.4: Pore volume fraction (in %) in PLA/Zn filaments processed by standard and precision extrusion.

Zn content (wt. %)	Standard extrusion	Precision extrusion
3.5%	0.20	0
7%	0.80	0
10.5%	0.15	0.68
14%	0.16	2.23
17.5%	1.23	13.80

layers surrounding the particles [185] and the higher effective viscosity of suspension that results in higher gas volumes trapped in the melt, as well as improper filling of the gaps between adjacent particles [184]. Furthermore, the air trapped within the particle clusters and the limited metal flow within them can contribute to the formation of pores [184].

Overall, it should be noted that standard extrusion followed by precision extrusion is able to produce continuous, uniform and dense PLA/Zn filaments which are suitable for FFF. Furthermore, this process is reproducible, predictable and can be easily scaled up. The porosity in the filaments increased when the Zn content was around 14 wt.% and increased more rapidly for the precision extruded filament due to differences in the processing conditions.

3.4.2 Physicochemical properties of PLA/Mg and PLA/Zn filaments

Filament extrusion involves melting and shear, and these processes may modify the chemical structure and MW of the polymer. Thus, the physicochemical properties of the filaments after standard and precision extrusion were carefully analysed by DSC, TGA, and GPC to determine the impact of processing on the PLA properties.

PLA/Mg filaments

DSC curves of PLA/Mg composites for the first heating after standard and precision extrusion are plotted in Figures 3.7 (a) and 3.7 (b), respectively. The same curves for the PLA/4% Mg and PLA/5% Mg composites with 5% PEG after precision extrusion are plotted in Figure 3.7 (c). Three thermal transitions are observed in all samples, independently of the Mg concentration or the presence of PEG. The first transition with increasing temperature is an endothermic step associated with the glass transition of PLA (T_g). All of the PLA/Mg samples presented this transition at 58°C, even after the two extrusion processes. This fact indicates that Mg does not have a plasticiser effect and that PLA depolymerisation after extrusion was not large enough to increase the local chain mobility.

It should be noted that the T_g for pure PLA after standard extrusion is around 58-60°C and after precision extrusion is approximately 2°C higher. This small shift could be explained by the ageing of the PLA samples during storage. The sample densifies at room temperature after some time, decreasing the chain mobility and slightly increasing the T_g. On the other hand, the addition of low molecular weight PEG had a clear and expected plasticiser effect [186, 187] reducing the T_g

to $\sim$ 51°C (Figure 3.7 (c)). An exothermic process due to cold crystallisation (T_{cc}) appeared in all samples at higher temperature. The presence of Mg shifted the exothermic peak from 122°C in neat PLA to 116°C in PLA/5% Mg after standard extrusion, and a similar reduction has been reported in the literature [134].

This behaviour may be produced by two mechanisms, namely the nucleating effect of Mg particles and the higher polymer chain mobility due to the lower MW of PLA after depolymerisation during extrusion, as discussed below. T_{cc} further decreased to 111°C in PLA/5% Mg after precision extrusion and the differences after standard and precision extrusion can be explained by the higher reduction in MW due to PLA depolymerisation during precision extrusion, as well as by the increase in chain mobility due to the reduction of physical entanglements during the extrusion process. The increase in chain mobility is much more important in the presence of PEG plasticiser, leading to the lowest T_{cc} (Figure 3.7 (c)) [188].

Finally, PLA presented a melting peak (T_m) at 150°C, which remained constant for all the standard extruded composites and for the precision extruded composites up to 3 wt.% Mg. Nevertheless, the shape of the peak became broader with increasing Mg content and T_m decreased slightly in the precision extruded composites with 4 wt.% and 5 wt.% Mg, while a new endothermic peak appeared at higher temperature. This behavior can be explained by the relation between T_{cc} and T_m. Crystallisation at lower temperature produced less perfect crystals which melt at lower temperature, and that can recrystallise at slightly higher temperature. This melt-recrystallisation-melt process was more evident in the samples containing PEG, which presented the lowest T_{cc} and where both melting peaks were clearly observed (Figure 3.7 (c)).

The weight loss as a function of the temperature obtained from TGA is plotted in Figure 3.8 for the precision extruded composites with different weight fractions of Mg particles. All samples undergo one simple thermal decomposition step. Pure PLA degradation started at $\sim$ 300°C and reached the maximum weight loss at $\sim$ 371°C. The onset degradation temperature decreased as the Mg content increased. Thermal degradation started at $\sim$ 217°C and the maximum weight loss was reached at $\sim$ 298° C when the weight fraction of Mg was 5%. This trend has been previously reported for PLA/Mg composites because PLA is degraded by depolymerisation in the presence of Mg particles [167] and the reduction in MW may trigger degradation at lower temperatures [189]. It should be noted, however, that the onset degradation temperatures were always higher than the processing temperatures during extrusion and printing but the progressive reduction of the degradation temperature with higher Mg loads may become a problem to print filaments with higher Mg content [190].

The MW distributions (MWD) of PLA and PLA/Mg composites with 3, 4 and 5 wt.% of Mg obtained by GPC are plotted in Figures 3.9 (a) and (b) after standard and precision extrusion, respectively. Standard extrusion was carried out at 180°C and the MW distribution of extruded PLA was very similar to the one measured in the as-received PLA pellets (not shown in the figure), indicating that extrusion at this temperature did not reduce the MW. Moreover, the MW was independent of the Mg content in the PLA/Mg composites obtained by standard extrusion, except for the one with 5 wt.% Mg that showed a shift towards lower MWs. However, a large shift towards lower MWs was found in all the PLA/Mg composites after precision extrusion and the reduction was particularly important in the composite with 5 wt.% Mg. These results are

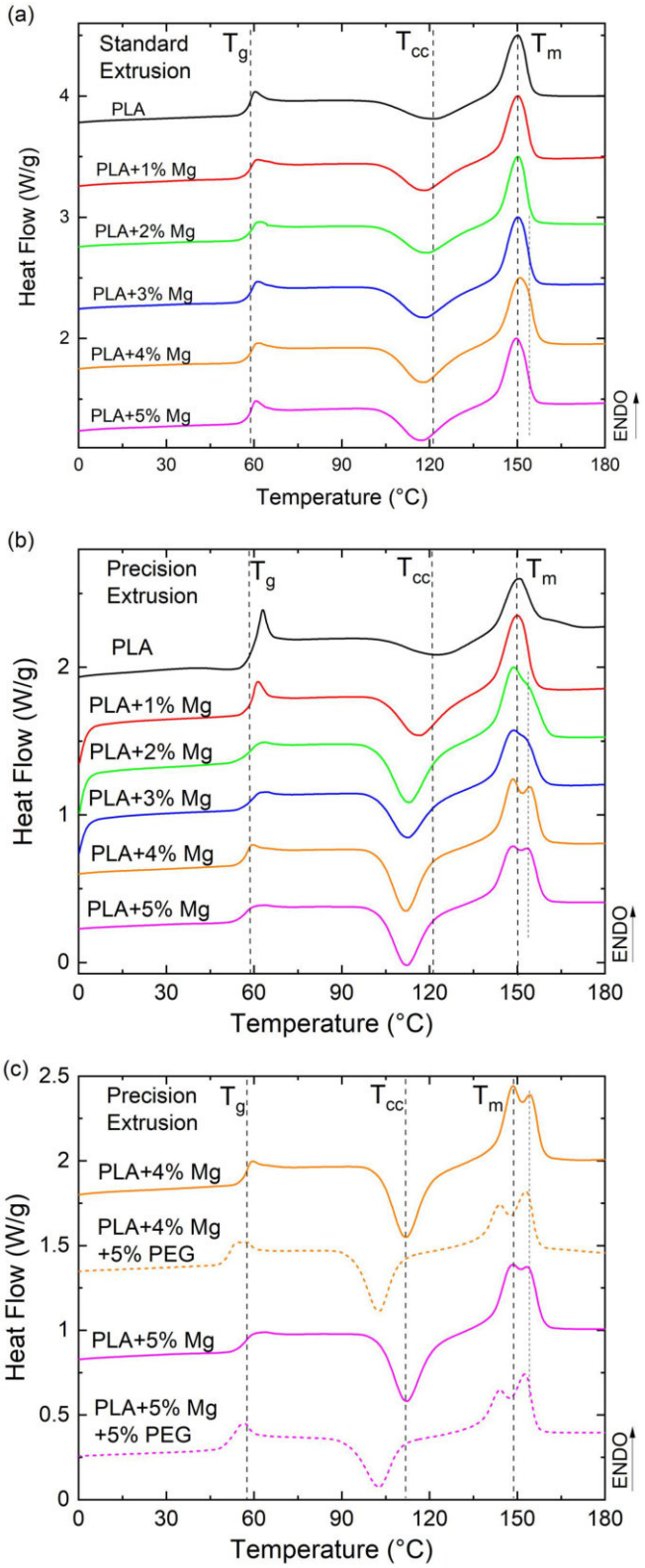

Figure 3.7: Heat flow curves of PLA/Mg filaments during DSC at a heating rate of 10°C/min. (a) After standard extrusion. (b) After precision extrusion. (c) Effect of PEG on the heat flow of PLA/Mg filaments. Glass transition temperature (T_g), cold crystallization temperature (T_{cc}), and melting point (T_m) are indicated with dashed lines.

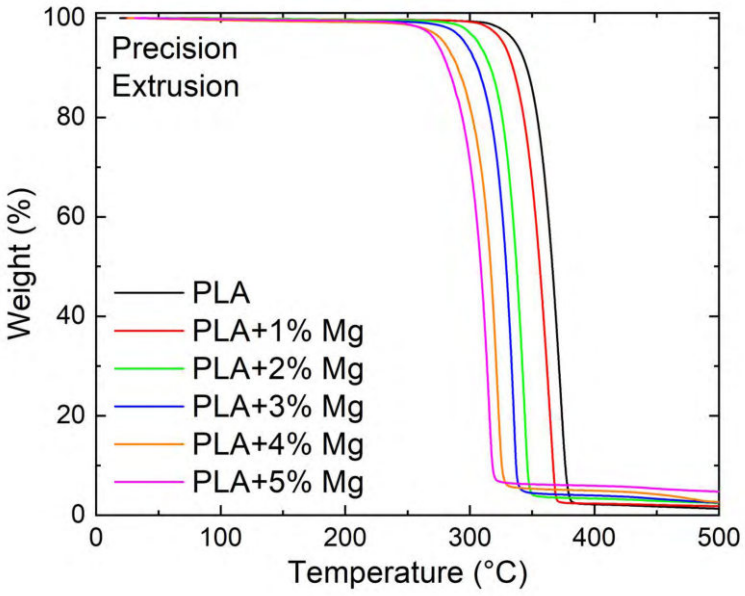

Figure 3.8: Weight loss as a function of temperature obtained from TGA for the precision extruded composite containing different weight fractions of Mg particles.

summarised in Figure 3.9 (d), where the number average MW, Mn, after standard and precision extrusion is plotted as a function of the Mg content.

They show that neat PLA degradation is limited during standard extrusion (maximum temperature 180°C, residence time 2-3 minutes) and more noticeable after precision extrusion (maximum temperature 200°C, residence time 10-12 minutes). The same trend was observed in the composites with Mg although the reduction in MW was much more important. The maximum temperatures during precision extrusion of PLA/Mg filaments were either 190°C or 180°C (Table 3.1), very similar to the maximum temperature during standard extrusion (180°C). However, the residence time during precision extrusion was much longer and the overall reduction in the MW was higher during precision extrusion due to the catalytic effect of the Mg particles on the PLA depolymerisation.

Large reductions in the MW of PLA lead to large decreases in viscosity and compromise the mechanical properties. Thus, 5 wt.% of PEG was added to the PLA/Mg mixture with 4% and 5% Mg to reduce the processing temperature during precision extrusion. In this case, the maximum temperature for precision extrusion was 160°C (Table 3.1) and, as result, the shift towards lower MW distributions was reduced in comparison with the composites extruded without PEG (Figure 3.9 (c)). The shoulder at low MW of filaments with PEG was attributed to the presence of low MW PEG. Overall, the TGA profile of PLA in the precision extruded filaments with PEG was similar to the degradation of the standard extruded filaments without PEG (Figure 3.9 (d)).

MFI tests were performed in the standard extruded and precision extruded filaments to assess their printability as well as to determine the optimum printing temperature. According to the literature, the MFI of the filament should be in the range of 10 g/10 min to 30 g/10 min to be successfully printed by the FFF technique [149]. The appropriate viscosity is necessary to ensure that the molten material flows easily through the nozzle but the viscosity has to be high enough to

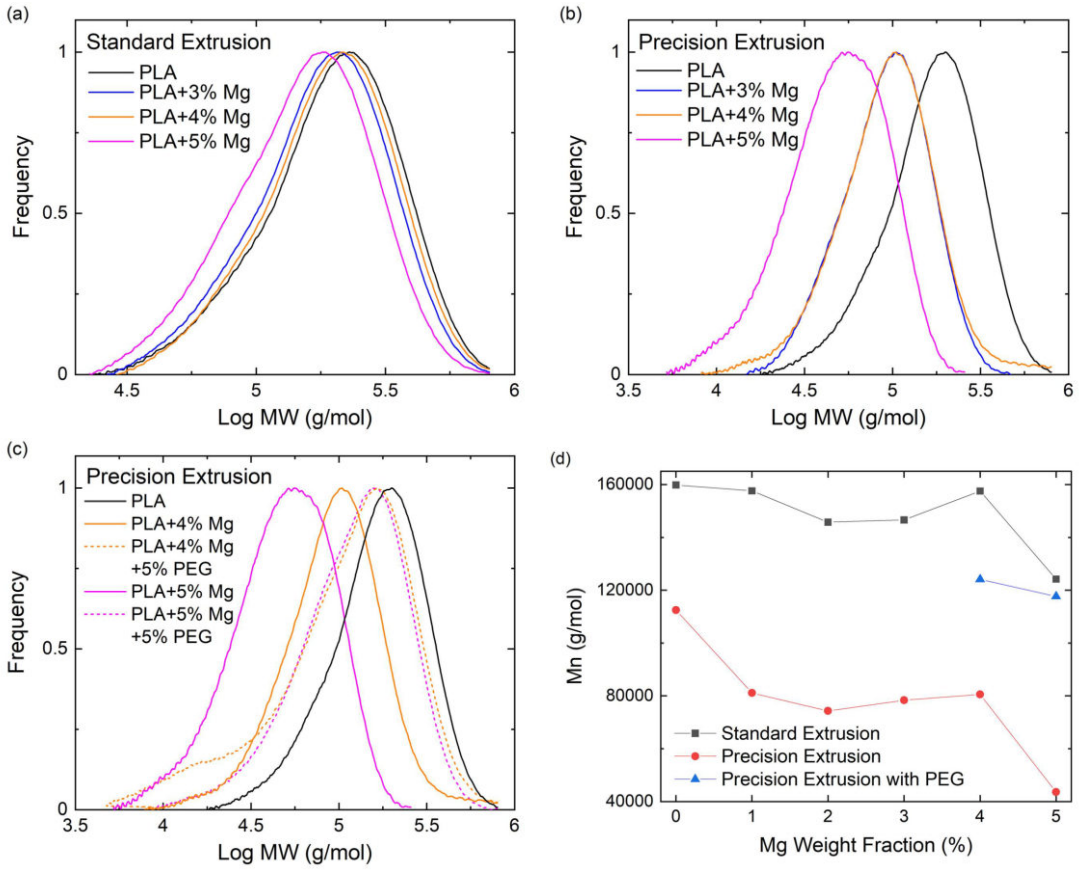

Figure 3.9: Molecular weight distributions of PLA/Mg composites. (a) After standard extrusion. (b) After precision extrusion. (c) Effect of PEG on the molecular weight distribution after precision extrusion. (d) Evolution of the average molecular weight with Mg content after standard and precision extrusion.

support the weight of the printed layers. The evolution of the MFI at 190°C with the Mg content for standard and precision extruded filaments is plotted in Figure 3.10 (a).

The MFI increased with the Mg content and the differences between both types of filaments were small when the Mg content was ≤ 2 wt.%. The MFI was close to the lower printability limit. However, large differences between both types of filaments were found for higher Mg contents. The MFI of standard extruded filaments increased with Mg content (except for the highest Mg loads of 5%) but it was always within the printability range. Nevertheless, the MFI of precision extruded filaments with 3% and 4% of Mg was very high and outside of the printability limit. The low viscosity of these filaments can be attributed to the reduction of the PLA MW during precision extrusion (Figure 3.9 (d)). Surprisingly, the MFI of the precision extruded filament with 5% Mg was lower than that of the filaments with 3% and 4% of Mg and this behaviour could be attributed to the increase in viscosity associated with the larger volume fraction of Mg particles in the molten polymer. Thus, filaments produced by standard extrusion exhibited an MFI within the printability range but they could not be used because of the porosity and inhomogeneities in the diameter. The viscosity of precision extruded filaments of pure PLA and of PLA with Mg content up to 3% was also within the printability range at 190°C and they were successfully used for 3D printing of

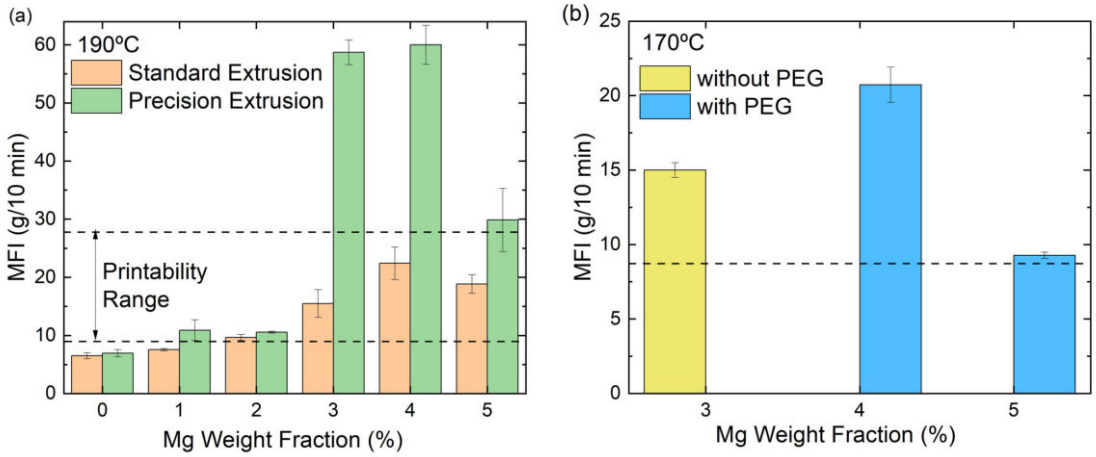

Figure 3.10: (a) MFI at 190°C of standard extruded and precision extruded PLA/Mg filaments as a function of the Mg content. (b) MFI at 170°C of precision extruded filaments of PLA/Mg and PLA/Mg/5%PEG as a function of the Mg content. The MFI range for printability is marked by the horizontal dashed lines.

scaffolds. However, 3D printing of PLA/3% Mg, PLA/4% Mg and PLA/5% Mg failed, even if the latter was within the printability range.

The MFI at 170°C of precision extruded PLA/3% Mg was within the printability range and could be printed at this temperature (Figure 3.10 (b)). Nevertheless, it was not possible to determine the MFI of precision extruded PLA/4% Mg at 170°C due to clogging in the nozzle. 3D printing of this material was possible, although it was complicated and required user intervention several times. To overcome these problems, precision extrusion of PLA/4% Mg/5% PEG filaments and PLA/5% Mg/5% PEG filaments were processed at the temperatures indicated in Table 3.1. The MFI at 170°C of the precision extruded filaments with PEG are shown in Figure 3.10 (b) and both were within the printability range. Moreover, they were successfully printed at this temperature.

PLA/Zn filaments

DSC curves during the first heating cycle of the PLA/Zn filaments after standard and precision extrusion are plotted in Figures 3.11 (a) and (b), respectively. All DSC curves exhibit a first peak corresponding to the glass transition (T_g), followed by an exothermic phase transition due to cold crystallisation (T_{cc}), and finally by an endothermic transition due to polymer melting (T_m). The glass transition of neat PLA occurs at approximately 58°C. The T_g of PLA/Zn composites after standard and precision extrusion remains unaffected regardless of the metal content (dashed line at the lowest temperatures in Figures 3.11 (a) and (b)), indicating that polymer chain mobility is not modified by the addition of Zn particles.

In contrast, the metal particles favour PLA crystallisation, which occurs at lower temperatures and with narrower exothermic peaks, evidencing the nucleating effect of Zn. PLA nucleation starts at $\sim$ 90°C and the cold crystallisation peak (T_{cc}) is reached at $\sim$ 122°C (dashed lines in Figures 3.11 (a) and (b)). T_{cc} decreases with increasing Zn content and reaches $\sim$ 114°C after standard extrusion and $\sim$ 110°C after precision extrusion in filaments with 17.5 wt.% Zn. The

difference in T_{cc} between standard and precision extrusion can be attributed to the reduction of MW and of physical entanglements in PLA due to shear stress during precision extrusion, since this second processing step was performed at higher temperatures and with longer residence times than standard extrusion. Cold crystallisation has also been reported to be facilitated by the addition of metal particles in PLA/Mg composites [134]. The melting peak (T_m) of PLA after standard and precision extrusion is found at 150°C (dashed lines in Figures 3.11 (a) and (b)). T_m of PLA/Zn composites after standard extrusion remains unaffected up to 14 wt.% of Zn, and a slight decrease (together with the emergence of a shoulder at higher temperature) is observed in PLA-17.5 wt.% Zn. T_m decreases slightly after precision extrusion due to the reduction in T_{cc} and new endothermic peaks appear at higher temperatures in PLA/Zn composites, which can be associated to melt/recrystallisation processes (marked by red short dashed lines on Figures 3.11 (a) and (b)). The split in the melting peak is more noticeable with increasing Zn content.

The weight loss as a function of temperature during TGA in air is plotted in Figure 3.12 for the PLA/Zn filaments subjected to standard and precision extrusion. PLA degradation begins at ∼300°C and ends at ∼390°C. PLA/Zn composites start to degrade at lower temperatures (220-240°C) and the end of the degradation also occurs at lower temperatures (275-310°C). Both temperatures decrease with increasing the Zn content but this effect is minor as compared with presence of relative small amounts of Zn particles. The residual mass increased upon Zn content, except for PLA/14 wt.% Zn, which was slightly higher than that of PLA/17.5 wt.% Zn. This difference may be attributed to differences in the actual Zn content due to the small size of the samples (between 10-15 mg).

The MWD of the PLA/Zn filaments after standard and precision extrusion were obtained from the GPC experiments and are plotted in Figures 3.13 (a) and (b), respectively. Data from the as-received PLA pellets are added in both figures. The presence of Zn particles led to an almost negligible reduction in the MW distribution of PLA after standard extrusion, which took place at 180°C with a residence time of 3 minutes. The reduction in MW was slightly more noticeable after precision extrusion, which was carried out at a maximum temperature 200°C with a residence time of 12 minutes. Thus, the presence of Zn particles induced some scission of the molecular chains during extrusion, which increases with the Zn content, as shown in the plot of the number average MW (Mn) of PLA/Zn filaments with Zn content in Figure 3.13 (c). This process was slightly accelerated during precision extrusion because of the higher temperature and residence time. These results are in contrast with those reported for PLA/Mg filaments processed using the same strategy and presented above (Figure 3.9 (d)). The average MW (Mn) of the PLA in PLA/5 wt.% Mg composites decreased more than 50% after precision extrusion at 190°C and the differences between PLA/Zn and PLA/Mg composites have to be attributed to the thermal degradation of the polymeric chains catalysed by the presence of the Mg particles.

The MFI of the PLA/Zn composites at 190°C after standard and precision extrusion is plotted in Figure 3.14 (a). These results are the average of five tests, and the error bars represent the standard deviation. The MFI of precision extruded filaments increased slightly with the incorporation of up to 7 wt.% of Zn and remained approximately constant (15 g/10 min) for larger Zn contents. These results are in agreement with the limited reduction in the average MW of PLA after standard extrusion, Figure 3.13 (c), which did not significantly influence the viscosity of the

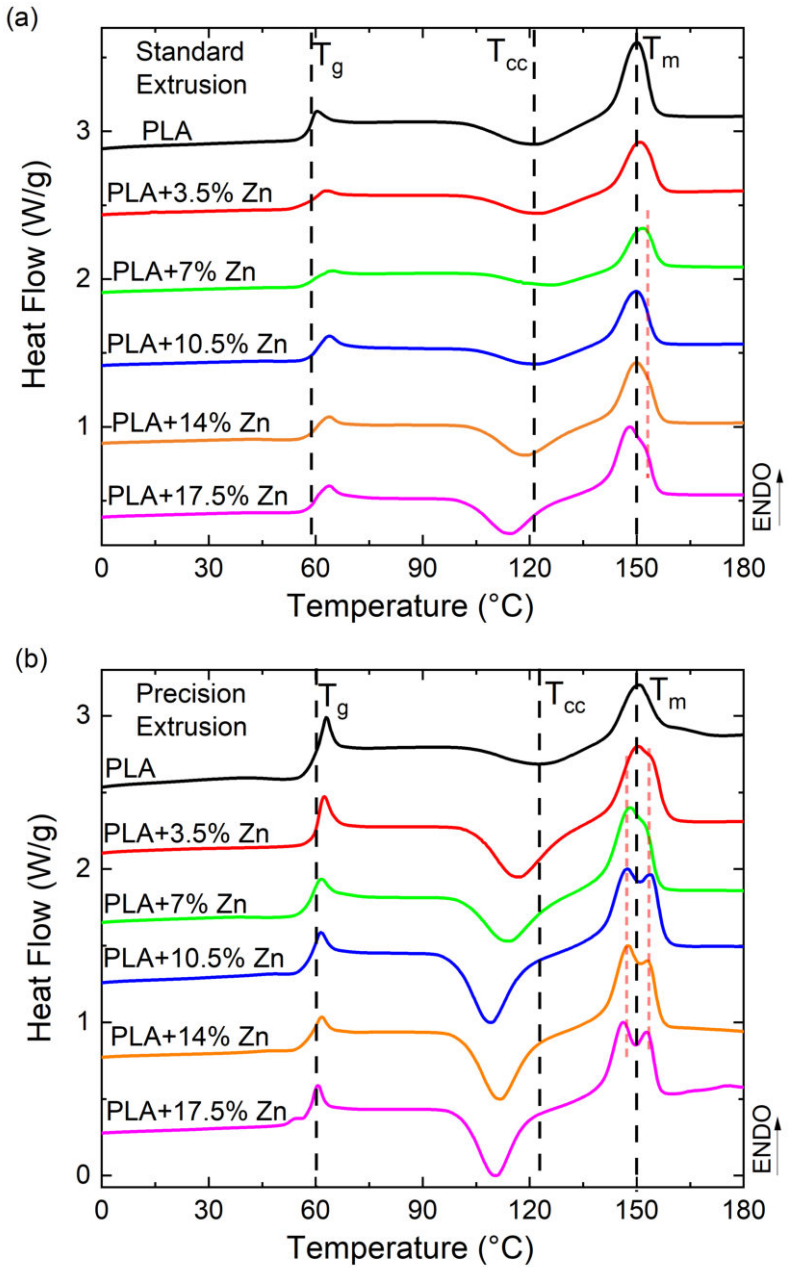

Figure 3.11: DSC curves during the heating cycle of PLA/Zn filaments at a scanning rate of 10°C/min. Glass transition (T_g), cold crystallization (T_{cc}) and melting temperature (T_m) of pure PLA are marked with black dashed lines for reference. New emerging peaks in the PLA/Zn composites are indicated with short red dashed lines.

composite. However, the MFI after precision extrusion increased rapidly with the Zn content due to the reduction of the average MW of PLA. As a result, composites with Zn content above 10.5 wt.% exceeded the printability range at 190°C and it was not possible to measure the MFI of the PLA/17.5 wt.% Zn composite because of its high fluidity. Thus, the MFI of the composites with more than 10 wt.% of Zn were determined at 170°C and the results are plotted in Figure 3.14 (b). They were within the printability range at this temperature.

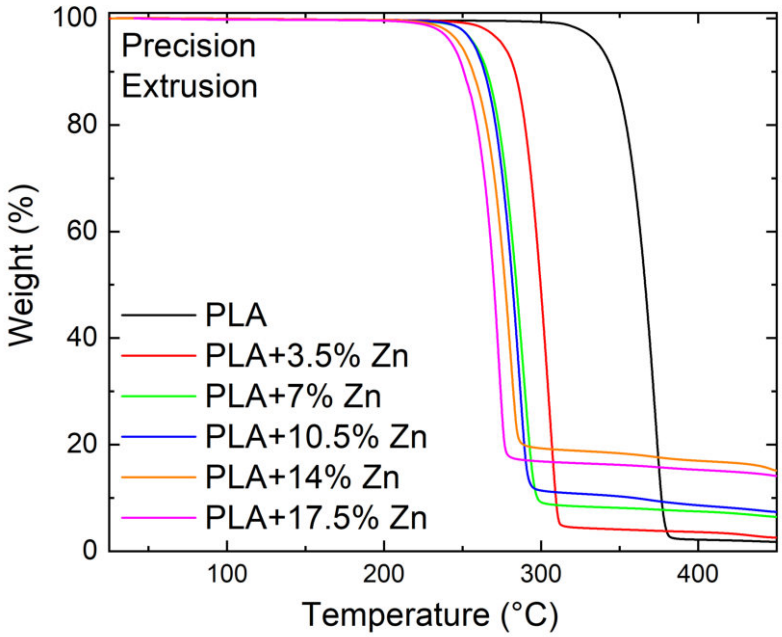

Figure 3.12: Weight loss as a function of temperature during the TGA test in air.

Table 3.5: Tensile properties of the PLA/Mg 3D printed dogbone specimens

Material	Elastic Modulus (GPa)	Strength (MPa)	Strain at Break (%)
PLA	3.1±0.2	45±5	2.1±0.4
PLA-4% Mg	3.1±0.1	42±1	2.3±0.8
PLA-4% Mg+5%PEG	3±0.2	33±1	2.2±0.3

Overall, the results of the TGA tests (Figure 3.12) and of the MFI (Figure 3.14) indicate that the presence of Zn particles accelerates the degradation of the PLA. However, this effect was minimised as the printing temperature for PLA/Zn always remained below the degradation temperature.

3.4.3 Tensile properties of PLA/Mg composites

The tensile stress-strain curves measured in dogbone specimens of PLA, PLA/4% Mg and PLA/4% Mg with 5% PEG are shown in Figure 3.15. The elastic moduli of the three materials were very similar (approximately 3 GPa) but the tensile strength of PLA and PLA/4% Mg was higher (approximately 45 MPa) than that of PLA/4% Mg with 5% PEG (33 ± 1 MPa). The mechanical properties are summarised in Table 3.5. Overall, these mechanical properties are comparable to those reported for PLA for biomedical applications [176] and the reduced strength of the composites with PEG can be attributed to the increase in the polymer chains mobility induced by the presence of PEG.

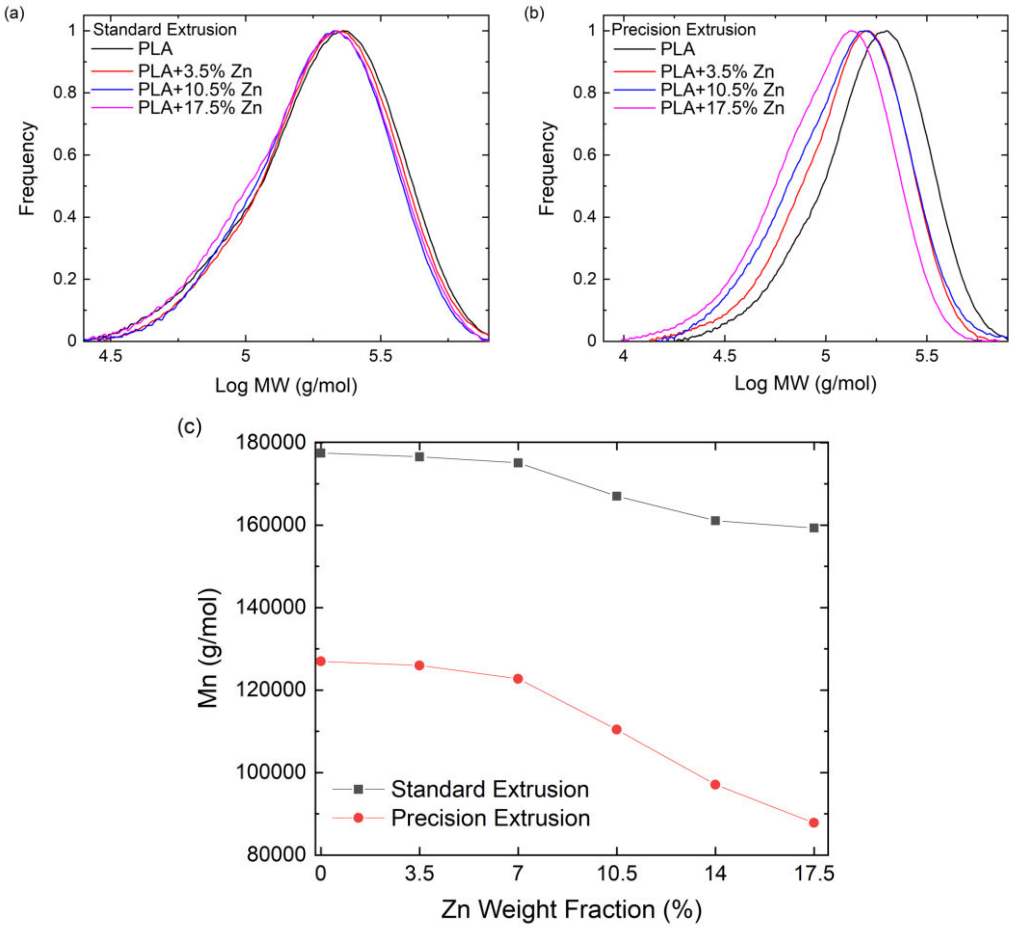

Figure 3.13: MW distributions of PLA/Zn composites. (a) After standard extrusion. (b) After precision extrusion. (c) Evolution of the number average molecular weight (Mn) with Zn content after standard and precision extrusion.

3.4.4 Compressive properties of scaffolds

PLA/Mg scaffolds

The microstructure of the PLA/Mg scaffolds was analysed by means of X-μCT to assess the geometric accuracy and internal porosity. Representative tomograms of the scaffolds printed with PLA, PLA/4% wt. Mg and PLA/4% wt. Mg with 5 % PEG are shown in Figure 3.16. They show that it was possible to print the scaffolds with the complex FCC shape with good geometrical accuracy. However, large internal porosity was found in the PLA/4% Mg scaffolds (Figure 3.16 (b)) compared to those printed with pure PLA filaments (Figure 3.16 (a)). The addition of PEG to the filaments reduced the internal porosity of the scaffolds in addition to making it possible to print the scaffolds with ease at lower temperatures.

The engineering stress-strain curves of the PLA/Mg FCC scaffolds in compression are plotted in Figure 3.17. They were calculated from the applied load and displacement taking into account the initial height and cross-section of the scaffolds. All scaffolds showed ductile behaviour during deformation and the initial elastic region was followed by a plateau region in which the deformation

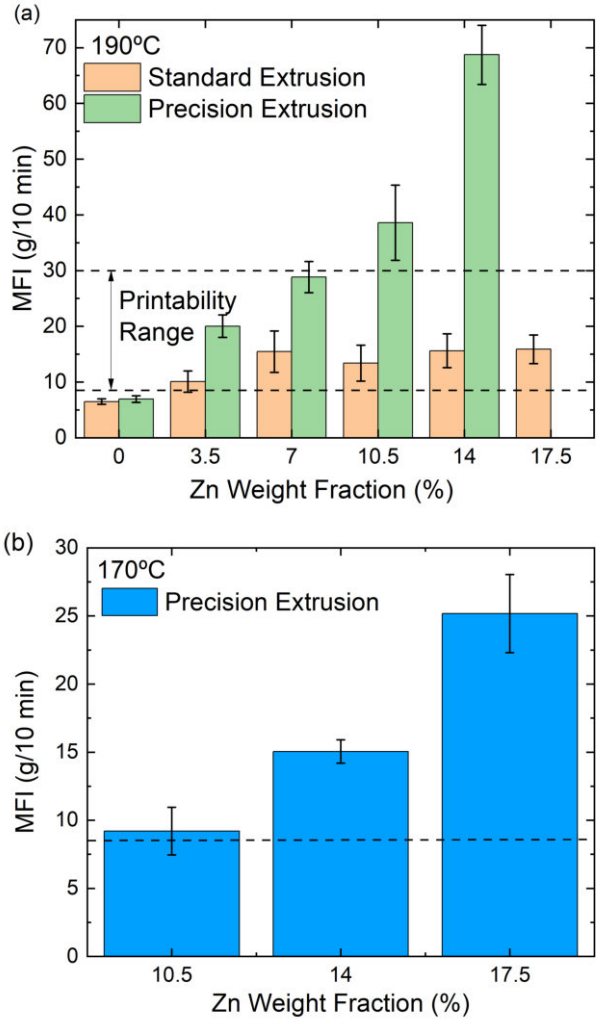

Figure 3.14: (a) MFI at 190°C of standard extruded and precision extruded PLA/Zn filaments as a function of the Zn content. (b) MFI at 170°C of precision extruded filaments of PLA/10.5 wt. % Zn, PLA/14 wt. % Zn and PLA/17.5 wt. % Zn. The MFI printability range is marked by the horizontal dashed lines.

progressed at constant stress. The best mechanical properties were measured in PLA scaffolds due to low internal porosity (Figure 3.16 (a)) and higher material strength (Figure 3.15). The elastic modulus and strength of PLA/4% Mg and PLA/4% Mg/5% PEG scaffolds were reduced due to porosity (Figure 3.16 (a)) or to the lower strength of the material (Figure 3.15), respectively. The average values of the mechanical properties of the 3D printed dogbone samples tested in tension and of the FCC scaffolds deformed in compression are summarised in Table 3.6. Nevertheless, the differences were not very relevant and the addition of PEG facilitates the 3D printing of fully dense scaffolds at lower temperatures.

PLA/Zn Scaffolds

FCC scaffolds were printed from PLA, PLA/3.5% Zn, PLA/7% Zn and PLA/10.5% Zn. It was not possible to print scaffolds with higher Zn content because of high polymer fluidity and

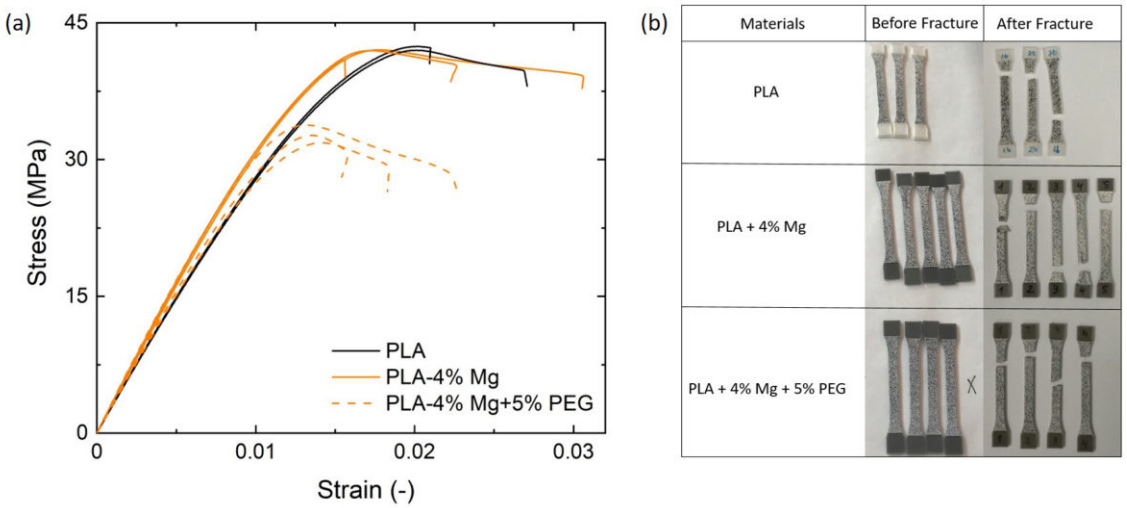

Figure 3.15: (a) Tensile stress-strain curves of dog-bone specimens of pure PLA, PLA-4% Mg and PLA-4% Mg with 5% PEG deformed parallel to the printing direction. (b) Images of the specimens after fracture.

Table 3.6: Compression properties of the PLA/Mg 3D printed scaffolds

Material	Elastic Modulus (MPa)	Strength (MPa)
PLA	650±32	16±1
PLA-4% Mg	540±48	15±1
PLA-4% Mg+5%PEG	533±18	13±1

nozzle clogging problems. 2D sections from X-ray tomography are shown in Figures 3.18(a)-(d), respectively.

The porosity between the filaments and the scaffolds cannot be related, however, the porosity of the scaffolds remained below 0.7%. The figures indicate that the scaffolds have good geometric accuracy and that the Zn particles were homogeneously distributed in the case of the composites. Moreover, slightly higher internal porosity was observed in the case of the PLA/3.5 wt.% scaffold (marked with arrows in Figure 3.18(b)). The addition of higher loads of Zn to the filaments reduced the internal porosity of the scaffolds (and it was possible to print the scaffolds at lower temperatures) probably due to the reduction in viscosity during processing, which facilitated the deposition of the material.

The nominal stress-strain curves in compression of the 3D printed scaffolds are plotted in Figure 3.19. Stress was calculated from the applied load divided by the initial cross-section of the scaffold while the engineering strain was obtained from the displacement measured by the LVDT divided by the initial height. All the samples were deformed up to 10% compressive strain. The PLA scaffolds showed continuous hardening during deformation (or, at least, a constant flow stress), which is indicative of homogeneous deformation. In fact, the optical micrograph of the lateral section of the PLA scaffold at the beginning of the compression test (Figure 3.20 (a)) and after

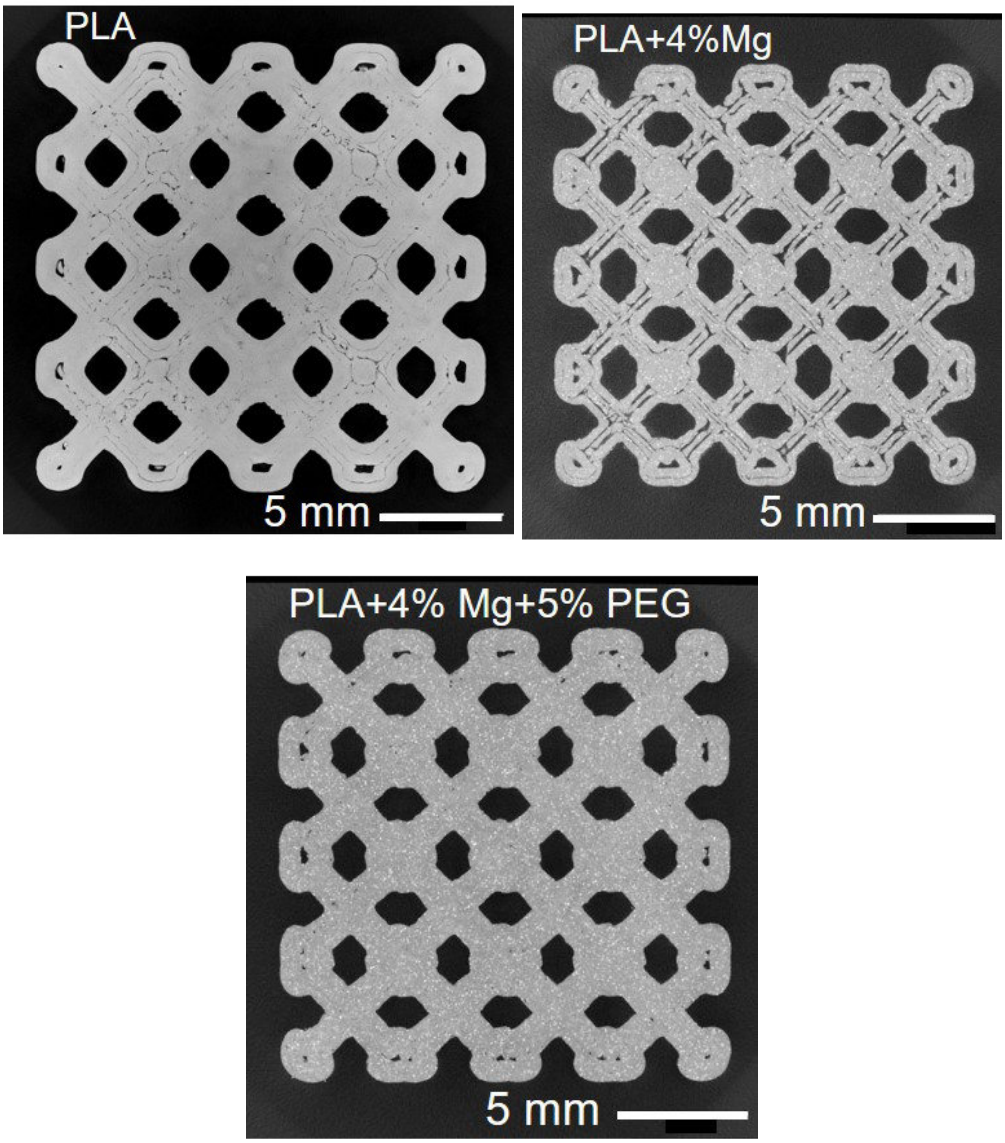

Figure 3.16: Cross-sections fcc scaffolds extracted from the tomograms obtained by X-μCT. (a) PLA. (b) PLA/4% Mg. (c) PLA/4% Mg/5% PEG.

10% of compressive strain (Figure 3.20 (b)) show a slight barreling of the scaffold after deformation. On the contrary, softening after the peak load was found in all the scaffolds containing Zn particles, which is indicative of the early localization of damage. This is shown in Figure 3.20(d), where the lateral view of the PLA/7 wt.% Zn scaffold is depicted after 10% compressive strain. Damage has been localised in the first row of the scaffold lattice and vertical cracks (parallel to the loading direction) have developed. Thus, the presence of Zn particles embrittles the material, leading to early crack formation.

The average value and standard deviation of the elastic modulus and of the strength of the scaffolds with and without Zn particles are indicated in Table 3.7. The mechanical properties of the PLA and PLA/7 wt.% Zn scaffolds were very close while those of the scaffolds with 3.5 wt.% and

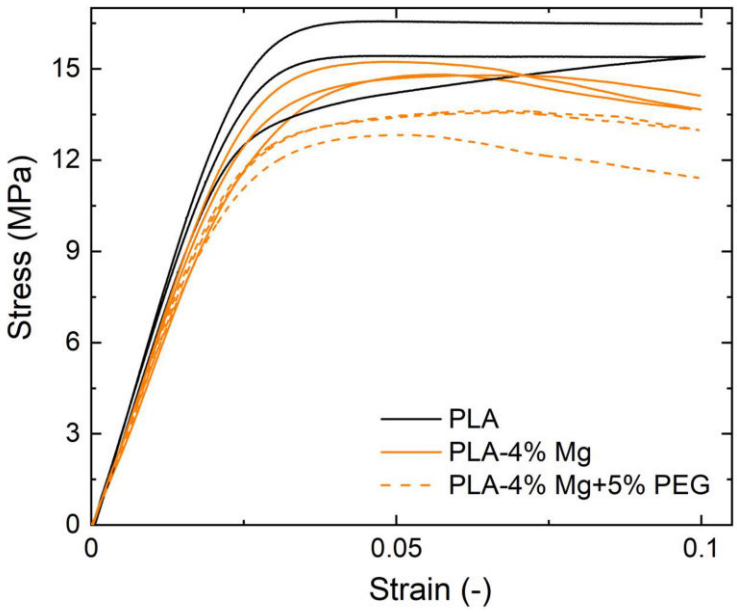

Figure 3.17: Experimental engineering stress-strain curves in compression of PLA, PLA/Mg and PLA/Mg/PEG FCC scaffolds.

Table 3.7: Compression properties of the PLA/Zn 3D printed scaffolds

Material	Elastic Modulus (MPa)	Strength (MPa)
PLA	650±32	16±1
PLA-3.5% Zn	529±1	13±1
PLA-7% Zn	675±103	16±1
PLA-10.5% Zn	517±10	13±1

10.5 wt.% Zn were slightly lower, very likely due to the porosity in the former and to the brittleness induced by the Zn particles in the latter. Thus, PLA + Zn particle scaffolds present properties similar to those found in PLA scaffolds and the main objective of the Zn particle reinforcement should be to tailor the degradation rate and the biocompatibility. Both issues will be addressed in the future.

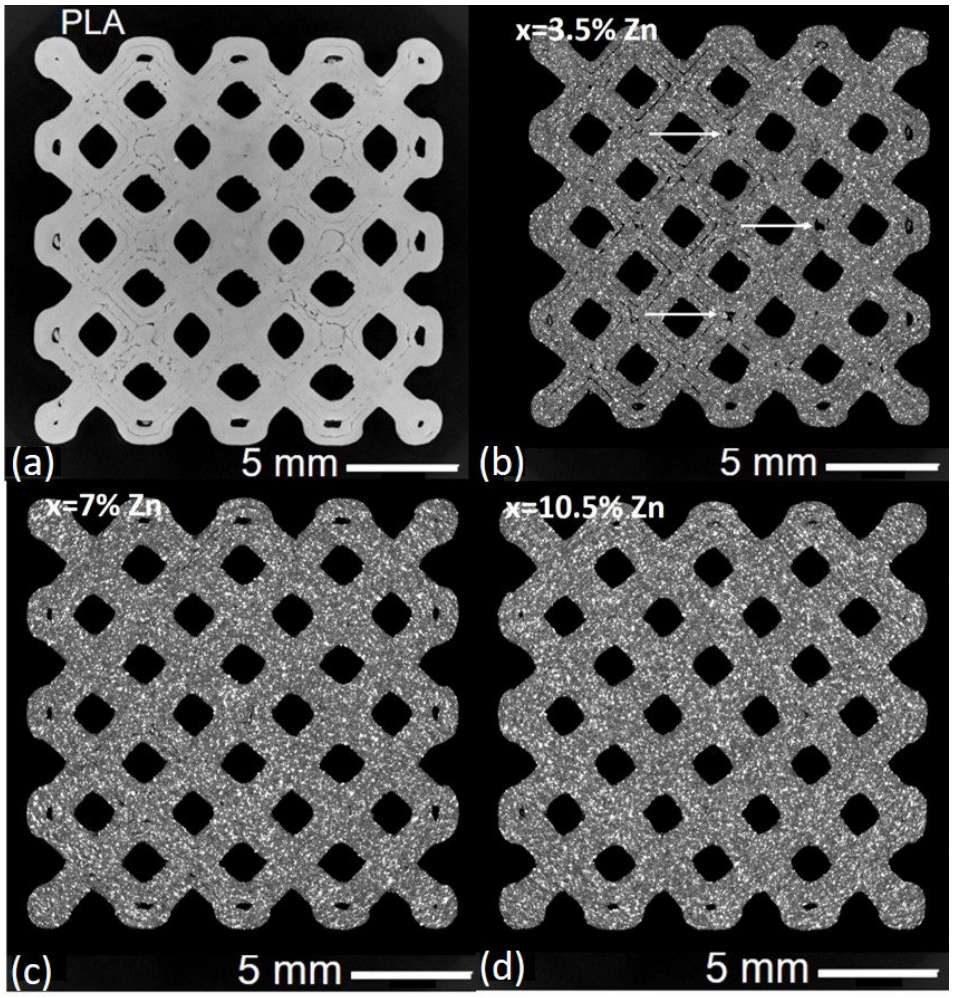

Figure 3.18: (a)-(d) Cross-sections of FCC scaffolds extracted from XCT tomograms. Internal pores are marked with white arrows.

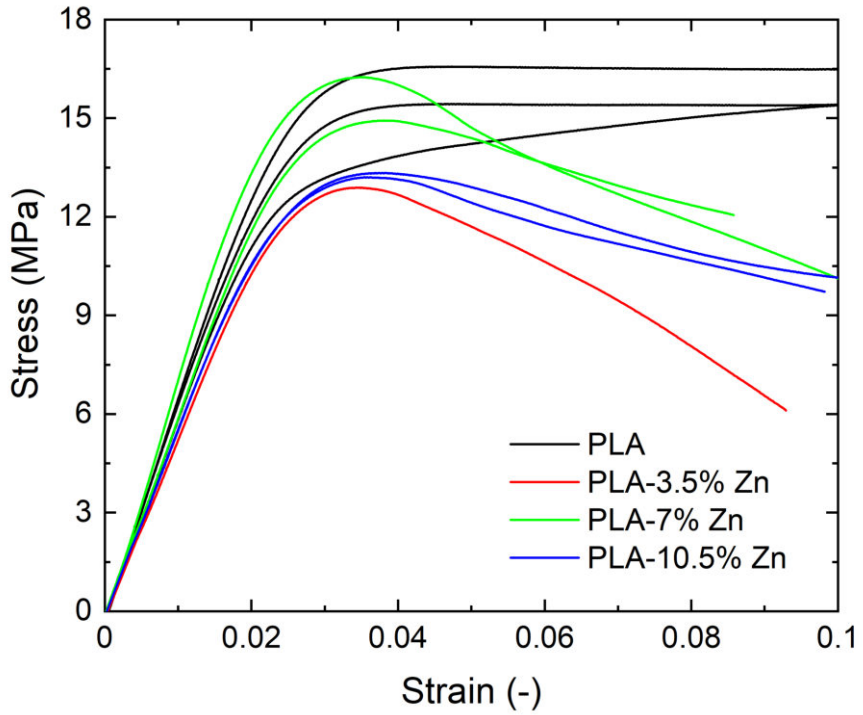

Figure 3.19: Engineering stress-strain curves in compression of 3D printed scaffolds of PLA and PLA with 3.5, 7.0 and 10.5 wt. % of Zn.

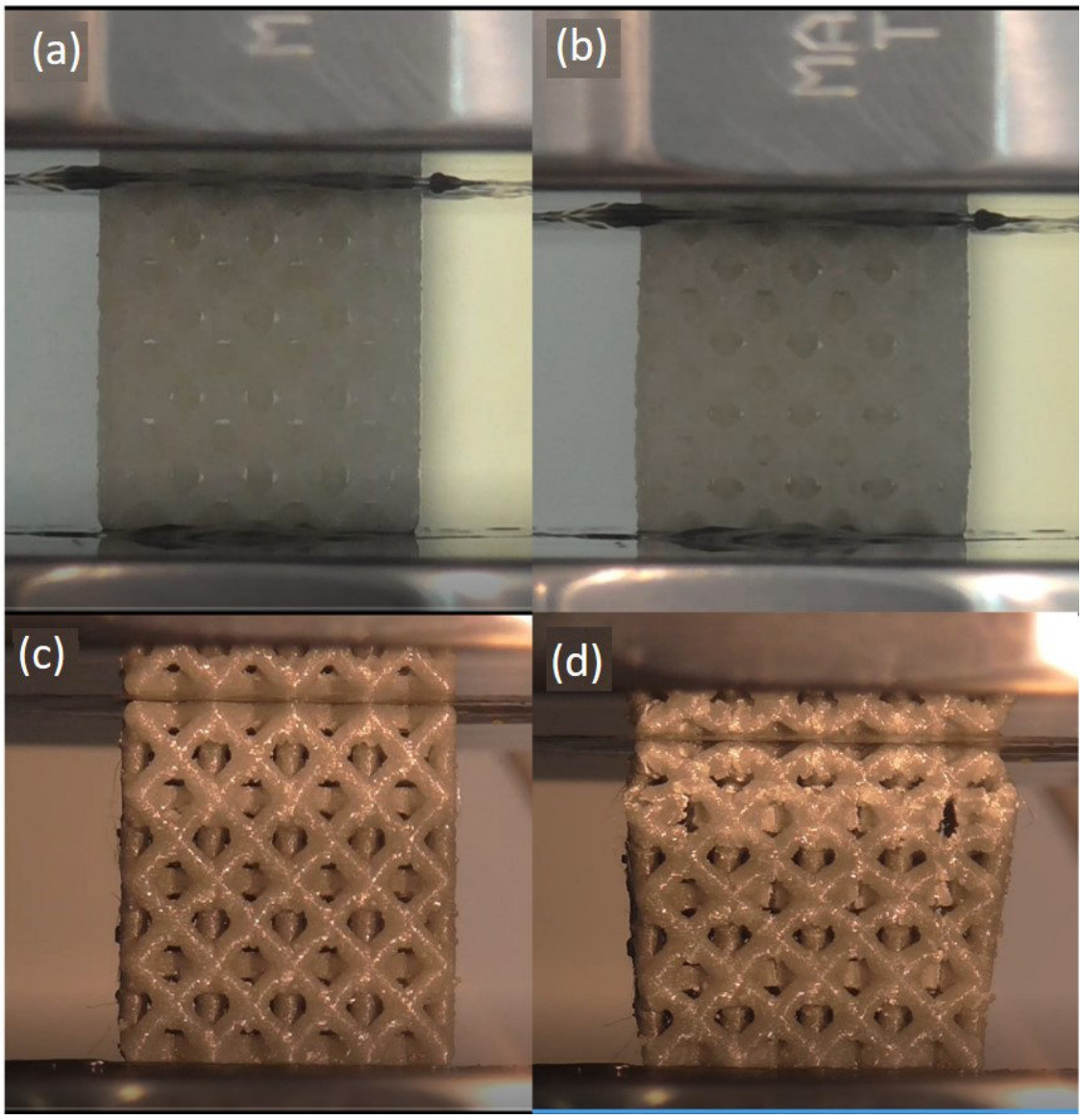

Figure 3.20: Lateral view of the scaffolds. (a) PLA, before testing. (b) PLA, after 10% compressive strain. (c) PLA + 7 wt. % Zn, before testing. (d) PLA + 7 wt. % Zn, after 10% compressive strain.

3.5 Conclusions

A strategy has been developed to manufacture PLA filaments reinforced with either Mg or Zn particles for the fused filament fabrication of porous scaffolds for biomedical applications. The mixture of PLA pellets and metallic particles was extruded twice, the second time using a precision extruder that allows the production of filaments with constant diameter and homogeneous dispersion of metallic particles throughout the PLA matrix. There was a significant reduction in molecular weight and onset thermal degradation temperatures for both PLA/Mg and PLA/Zn materials, due to the longer residence time (> 10 minutes) associated with the second (precision) extrusion step. The precision extrusion step led to a negligible porosity for all weight percentages of Mg content and up to 10.5 wt.% in the case of the PLA/Zn materials.

In the case of the PLA/Mg materials, it was found that the thermal degradation and increased chain mobility of the polymer was catalysed by the presence of Mg particles at high temperatures (180-190°C) and long residence time. This increase in chain mobility led to a significant increase in MFI of the polymer to the point where it was outside of the printability range for any wt.% of Mg above 4%. The addition of PEG to the PLA/Mg composite for weight fractions greater than 4% reduced the precision extrusion temperature to 160°C, and with it, the MFI of the polymer to a value within the printability range.

In terms of the tensile properties of PLA/Mg composites, the addition of Mg particles to the PLA matrix did not significantly alter the values for elastic modulus and strength. However, the enhanced chain mobility in the materials with PEG resulted in a reduction in strength due to the plasticising effect. Porous FCC scaffolds with good geometrical accuracy were printed for PLA, PLA/4% Mg and PLA/4% Mg/5% PEG materials. The lowest internal porosity was achieved in scaffolds manufactured with PLA or PLA/4% Mg/5% PEG filaments and the best mechanical properties (elastic modulus and compressive strength) were achieved in the PLA scaffolds, although the properties of the PLA/4% Mg scaffolds were very similar. The scaffolds manufactured with PLA/4% Mg/5% PEG filaments could be printed at lower temperatures but the strength was reduced due to the effect of PEG on the polymer chain mobility.

In the case of PLA/Zn materials, the addition of Zn led to physicochemical changes in the properties of the PLA. In particular, Zn particles favoured the nucleation of crystals and reduced T_{cc}. Despite the effect on the T_{cc}, and the reduction in MW and onset degradation temperatures, the MFI was not effected and therefore it was possible to print scaffolds with complex shape at 190°C with PLA/Zn composites containing 3.5 and 7 wt.% of Zn and at 170°C when the Zn content was 10.5 wt.%. Composites with higher Zn content could not be printed because of clogging of the nozzle and high fluidity of the material. The dimensional accuracy of FCC scaffolds of 20 x 20 x 20 mm^3 was excellent and the porosity was negligible in scaffolds with 7 wt.% of Zn content, very likely because of the viscosity reduction that facilitates 3D printing. The mechanical properties of the scaffolds containing 7 wt.% of Zn were similar to those of the PLA scaffolds in terms of stiffness and strength, although the presence of Zn particles led to a more brittle failure mode.

This study provided the necessary infrastructure for processing Mg and Zn powder reinforced composite materials for 3D printing. It demonstrated the effects of the addition of Mg and Zn particles on the physicochemical and mechanical properties of PLA. This manufacturing route

seems to be very promising to manufacture biodegradable thermoplastic/metal composite filaments for 3D printing that can take advantage of the different properties of both components from the viewpoint of tissue engineering.

3D Printing of Medical Grade PLDL/Mg and PLDL/Zn Composites for Orthopaedic Applications

4

4.1 Motivation

PLA reinforced with Mg particles or other fillers has been developed in the past for biomedical applications [83, 109, 110, 111, 132, 133, 134, 191]. In the previous chapter, we developed a strategy to manufacture PLA/Mg and PLA/Zn filaments for 3D printing. We characterised the materials in terms of their physicochemical, mechanical, and microstructural properties to determine the suitable volume fraction of metallic particles that can be added to the polymer matrix and still be 3D printed.

This widely used processing strategy for PLA and other thermoplastic polymers presents enormous potential for personalised medicine in which the device/scaffold/implant can be customised to the specific needs of the patient. However, the analysis of the available information in the literature shows that most of the metal/polymer composite filaments for FFF were manufactured from non-medical grade PLA, and thus they are not suitable for biomedical applications. Attempts to overcome these limitations using pure PLA did not obtain filaments with a constant diameter and a homogeneous distribution of the metallic particles [134].

The main objective of this investigation was to apply a dual-extrusion technique, previously developed to manufacture filaments for FFF of non-medical grade PLA reinforced with Mg [180] or Zn [192] to medical grade PLDL/Mg and PLDL/Zn composites. Subsequently, an extensive analysis of the mechanical behaviour, degradation rate, and biocompatibility of the composites was carried out to assess their potential for biomedical applications.

4.2 Polymer Selection

It is important to understand that the processing conditions modify the structure and properties of the polymer matrix. During manufacturing of polymer scaffolds, the polymeric material will be

melted three times during extrusion in the microcompounder, extrusion in the precision filament maker and finally during 3D printing of the final part. The molecular weight is reduced in each processing step and hence the strength of the material. Thus, a thermoplastic polymer with a relatively high molecular weight should be selected as the matrix for these composites.

Another very important factor is cytocompatibility. Many studies have reported that Ingeo Biopolymer 2003D (Natureworks B.V., Netherlands) is suitable for medical/tissue engineering applications and showed cytocompatiblility results [191, 193, 194, 195, 196]. However, the cytocompatibility of Ingeo biopolymer 2003D was tested and a cytotoxic behavior was found, despite of having good anti-bacterial properties. This behaviour agrees with the statements of Natureworks B. V., the provider of the polymer, which indicates that Ingeo 2003D is not a medical grade polymer and should not be used to this purpose. Ingeo Biopolymer 2003D is intended for use in food packaging, is not harmful to food products, and prevents bacterial growth during packaging, but it is not a medical grade polymer.

Contact was established with Corbion B.V. in The Netherlands, a company specialising in medical grade polymers. Corbion provided information on the biomedical grade polymer available with their physical properties: elastic modulus, strength, and elongation at break, in addition to the expected degradation time for each material (Table 4.1).

Table 4.1: Physical properties associated with various polymer families from Corbion. Data provided by Corbion B.V., The Netherlands.

Material	Elastic Modulus (GPa)	Tensile Strength (MPa)	Elongation at break (%)	Degradation Time (Months)
Poly(L-lactide)	3.1-3.7	60-70	2-6	>24
Poly(DL-lactide)	3.1-3.7	45-55	2-6	12-16
Poly(glycolide)	6.5-7	90-110	1-2	6-12
Poly(ϵ-caprolactone)	0.2-0.3	25-35	>300	>24
50/50 DL-lactide/glycolide	3.4-3.8	40-50	1-4	1-2
85/15 L-lactide/glycolide	3.3-3.5	60-70	2-6	12-18
70/30 L-lactide/ϵ-caprolactone	0.02-0.04	18-22	>100	12-24

Five different polymer samples selected from this table (provided by Corbion) were tested for cytocompatibility and molecular weight to determine the most suitable polymer. They were PL38, PDL45, PLDL7038, PLG8531, and PLD9655. The composition for each of these materials along with their inherent viscosity is provided in Table 4.2, while the physical properties of the polymer types can be found in Table 4.1. Cytocompatibility tests were also carried out on a Ti control sample and in the Ingeo 2003D polymer. The inherent viscosity (IV) is another standardised measurement of the molecular weight of a polymeric, often used to characterise the polymerisation state and the degree of polymer chain entanglement. The inherent viscosity is related to the viscosity of a polymer solution compared to the viscosity of the solvent alone. Higher inherent

Table 4.2: List of the five materials that were provided to undergo further testing before deciding which of the polymers would be used to continue work in the thesis studies.

Material	Composition	Inherent Viscosity (dL/g)
PL38	Poly(L-lactide)	3.8
PDL45	Poly(DL-lactide)	4.5
PLDL7038	70/30 L-lactide/DL-lactide copolymer	3.8
PLG8531	85/15 L-lactide/Glycolide copolymer	3.1
PLD9655	96/04 L-lactide/D-lactide copolymer	5.5

viscosity values generally indicate higher molecular weights and longer polymer chains [197].

The results of the indirect cytocomptability tests are plotted in Figure 4.1. The medical grade polymers and the control Ti sample exceeded the cyocompatibility threshold of 70% (with the exception of PDL45 at a concentration of 100% that was slightly below the threshold), while Ingeo 2003D was well below the cytocompatibility threshold up to concentrations of only 10%. In addition, direct tests for the medical grade polymers (and two control samples: Ti and a control in which the samples were not exposed to any material) were carried out to assess the cell/material interaction. The results are shown in Figure (Figure 4.2). The cells were seeded and stained after 24 hours and observed in the confocal microscope. All of them presented excellent interaction with the medical grade polymers.

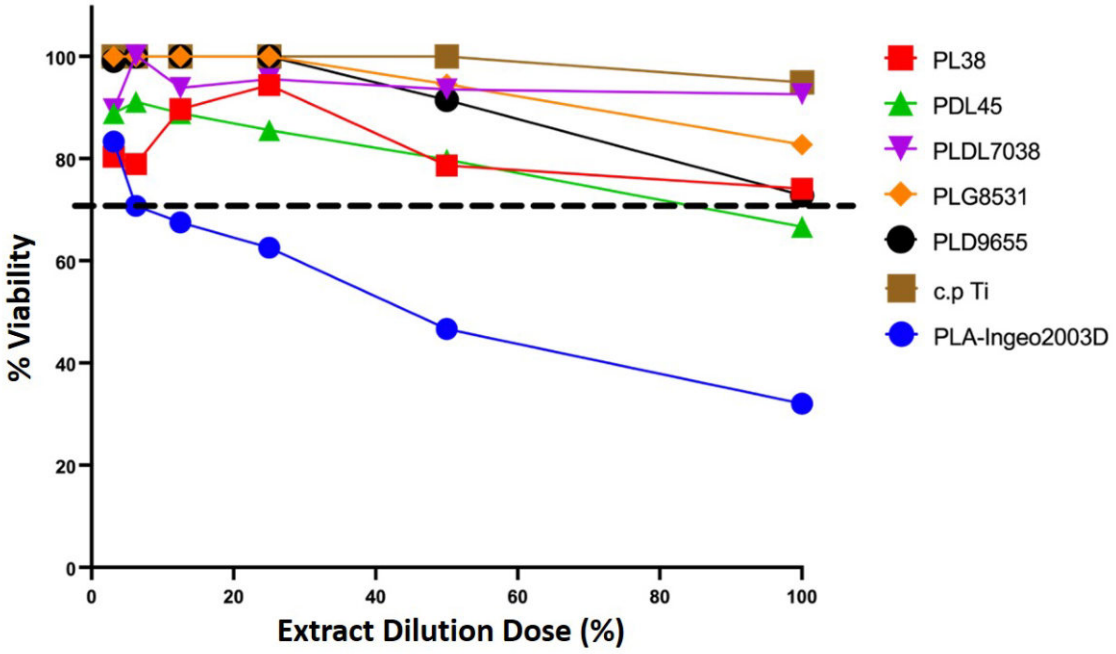

Figure 4.1: Indirect cytocompatibility tests to determine the mitochondrial activity after 24 hours. The horizontal dashed line 70% establishes the cytocompatibility limit.

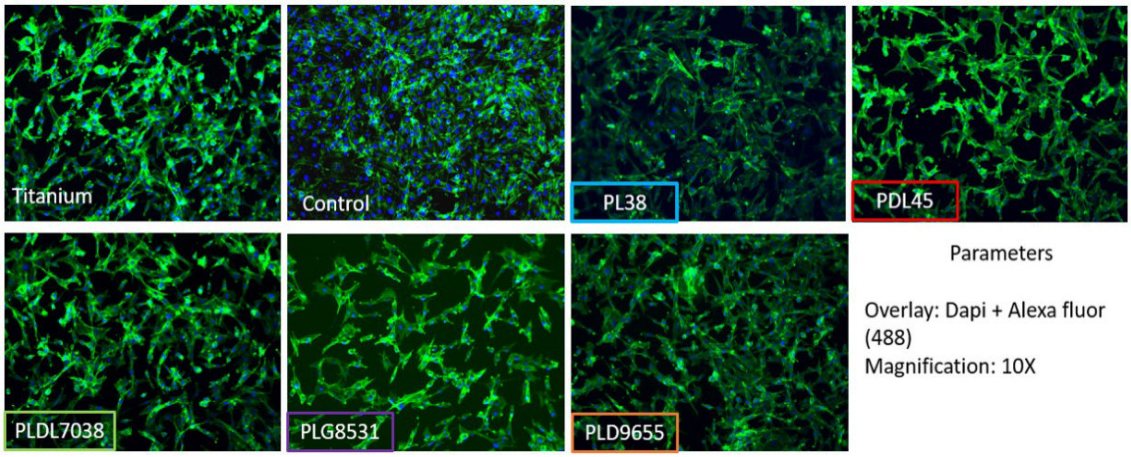

Figure 4.2: Cell-material interaction after cell-seeding on the various medical grade polymers and two control samples (Ti and a control in which the samples were not exposed to any material) after 24 hours. The green regions indicate the cytoskeleton of the cell, while the blue regions are the nucleus.

From the cytocompatibility results, the preliminary GPC tests to determine molecular weight, and the data of the physical properties provided by Corbion, PLDL7038 was selected to manufacture the composites.

4.3 Materials

The polymer/metal composites were manufactured from a medical grade bioabsorbable polymer PLDL7038 (Corbion N.V., Netherlands). The WE43-MEO Mg alloy powders were provided by Meotec GmbH and their composition and characteristics were detailed in the previous chapter. Zn powders with a composition Zn-1 wt.% Mg were manufactured by gas atomisation and purchased from Nanoval GmbH. The particle size distribution was in the range 30-60 μm with $d_{50} = 42.1$ μm. Furthermore, polyethylene glycol (PEG 1000 g/mol) (Sigma-Aldrich, MO, USA) was also used to facilitate the filament extrusion in the case of PLDL and PLDL/Mg composites.

Filaments of three different materials were prepared following the dual extrusion method presented in the previous chapter: PLDL + 5 wt. % of PEG, PLDL + 4 vol. % of Mg particles + 5 wt. % of PEG and PLDL + 4 vol. % of Zn particles. Extrusion of PLDL7038 is difficult and therefore 5 wt. % of PEG was added to improve the processability and reduce the viscosity [198]. PEG was also added to facilitate the extrusion of the composite containing Mg particles, following our previous experience, but it was not necessary in the composite with Zn particles.

300 grams of PLDL7038 were used for each material. The PLDL pellets were dried under vacuum at 105°C for 4 hours to remove any moisture. They were mixed manually with PEG and/or the metallic particles and extruded at 180°C (for the composites with metallic particles) or at 220 °C (for the PLDL+PEG) in the MC 15 microcompounder (Xplore, Sittard, The Netherlands). The residence time was approximately 2 minutes for all materials, and the rotation speed of the screws was 60 rpm for PLDL+PEG and 80 rpm for the materials containing metallic particles.

The second extrusion step was carried out in the 3devo precision extruder. The average screw speed was 5 rpm and the temperatures along the screw are shown in Table 4.3 for each material. Fully dense filaments with a constant diameter of 2.85 mm, and a homogeneous distribution of the metallic particles were obtained.

Table 4.3: Temperature distribution across the individual heaters in the 3devo precision extruder

Material	Heater 4 °C	Heater 3 °C	Heater 2 °C	Heater 1 °C
PLDL7038 + 5 wt. % PEG	190	195	200	195
PLDL7038 + 4 vol. % Mg + 5 wt. % PEG	175	185	182	180
PLDL7038 + 4 vol. % Zn	175	185	182	180

An Ultimaker S5 3D Printer (Ultimaker B.V., Utrecht, The Netherlands) was used to manufacture coupons for characterisation and scaffolds by FFF. The geometries of the printed samples were designed with Autodesk Inventor (Autodesk Inc., CA, USA). Dogbone samples according to ISO 527-1 (Part A) [140] were printed for tensile tests while coins of 13 mm in diameter and 1 mm thickness were prepared for the cytocompatibility tests, while parallelepipedic samples of 100 x 10 x 2 mm^3 were printed for the degradation tests. The printing temperature was 200°C for PLDL+PEG, 190°C for PLDL+Mg+PEG and 170°C for PLDL+Zn. Additionally, porous scaffolds with dimensions of 20 x 20 x 20 mm^3 with an FCC lattice structure were printed from the 3 materials to demonstrate the dimensional accuracy that could be achieved when fabricating complex geometries.

4.4 Methods

4.4.1 Degradation tests

Degradation of the materials was carried out in Gibco dulbecco's phosphate buffer saline (DPBS) (Life Technologies Europe B.V., Bleiswijk, Netherlands) following the ISO 13781 standard as a guideline [151]. The 3D printed rectangles were cut into pellets of approximately 10-35 mg in weight and introduced in an eppendorf which was filled with DPBS to reach a ratio of, at least, 30ml:1g. The eppendorfs were placed in a water bath at 37°C for up to 1 year. The eppendorfs were periodically extracted in triplicate (n=3) and the pH of the DPBS was measured using a pH meter (Sension+ PH3, Hach, Ames, Iowa, United States). Subsequently, the 'wet' mass was measured after drying the samples with tissue paper in an ES125SM balance (Precisa Gravimetrics, Dietikon, Switzerland).

Gel Permeation Chromatography (GPC) (GPC 2414, Waters) was used to monitor the molecular weight of each printed sample as a function of the degradation time. The method used to determine the molecular weight was the same as was implemented in the previous Chapter 3, and the number average molecular weight (Mn) was then determined in each follow-up sample over a 14-week period.

In the case of the composites containing Mg, the progressive corrosion of Mg was determined from the hydrogen evolution using an experimental set up similar to the one described by by [89]. 5 coins of 13 mm in diameter and 2 mm in thickness were placed in a beaker and a glass funnel was placed in an inverted orientation on top of the coins that were immersed in 200 ml of DPBS. A 25 ml burette was placed on top of the inverted funnel and the volume of hydrogen released was measured over time for 16 weeks. The corrosion of Mg in an aqueous environment takes place according to the reaction:

$$Mg + 2H_2O \rightarrow Mg^{2+} + 2OH^- + H_2 \tag{4.1}$$

and the release of 1 molecule of H_2 corresponds to the corrosion of 1 atom of Mg. The number of H_2 moles n is given by

$$n = \frac{P_{H_2}V}{RT} \tag{4.2}$$

where V is the hydrogen volume, R the ideal gas constant, T the absolute temperature and P_{H_2} is the pressure of hydrogen gas, which is given by $P_{H_2} = P_{atm} - P_{H_2O}$ where P_{atm} is the atmospheric pressure and $P_{H_2O} = 47$ mmHg represents the vapour pressure of the DPBS liquid at 37°C [199].

The degradation mechanisms were analysed by means of scanning electron microscopy (SEM). Samples were prepared by impregnation in an epoxy resin (SpeciFix resin system, Struers, Denmark) before being ground with SiC paper ranging from P320 to P2500. Samples were then polished with a diamond paste of 3 and 1 μm grain size (ATM Qness GmbH, Mammelzen, Germany) using MD-Nap polishing plates (Struers, Denmark). They were gold sputtered (Quorum Q150T ES, Quorum Technologies Ltd., East Sussex, England) to ensure electrical conductivity and analysed in either an Apreo 2S LoVac (Thermo Scientific, MA, USA) or a Helios Nanolab 600i (FEI, Hillsboro, OR, USA) scanning electron microscope using secondary electrons at a voltage of 5 kV and with currents in the range 40 to 80 pA. Energy-dispersive X-ray spectroscopy (Oxford Instruments, Abingdon, UK) was used to assess the corrosion mechanisms in the composites with metallic particles.

In addition, differential scanning calorimetry (DSC) was used to determine changes in the thermal properties of the materials as they degraded over time. Samples between 5 and 10 mg were loaded onto a Q200 calorimeter (TA Instruments, Delaware, USA). 2 heating/cooling cycles were applied to materials ranging from 0°C to 200°C at 10°C/min to ascertain changes in the glass transition temperature with degradation time.

4.4.2 Mechanical properties

The mechanical properties in tension were measured on dogbone samples manufactured by FFF following ISO 527 [140]. The length and thickness of the gauge length of the samples were 30 mm and 2 mm, respectively, and the width was 5 mm. Mechanical tests were carried out using an Instron 5966 electromechanical testing machine (Instron, Norwood, MA, United States) under a strain rate of 2 mm/min. The applied load was measured with a 2 kN load cell and the deformation

in the gauge section of the samples was measured by means Digital Image Correlation (DIC) using the appropriate software (VIC 2-D, Correlated Solutions Inc., SC, USA). To this end, the surface of the samples was sprayed by a black and white dot pattern. In addition to as-printed dogbone samples, the mechanical properties were also measured in samples that were placed in a DPBS solution at 37°C ranging from 2 weeks to 12 weeks. The ratio of the DPBS volume to the dogbone sample was always 30 ml:1 g. The gripping ends of the dogbone sample were painted using a vinyl spray to reduce the degradation in these regions and ensure that fracture after degradation took place in the gauge section. The samples were introduced in a water bath at 37°C connected to a pump system that filled a small water tank to surround the sample (See Chapter 2). A minimum of 3 samples were tested in order to achieve the mean and standard deviation of the mechanical properties.

4.4.3 Biological characterisation

The cytocompatibility and cell-material interaction were studied in murine preosteoblast cells of the MC3T3-E1 line (ATCC-CRL-2593), cultured in a complete culture medium consisting of alpha-MEM (Thermo Fisher, MA, USA), 10% foetal bovine serum (FBS) (Thermo Fisher, MA, USA), and 1% penicillin-streptomycin (Thermo Fisher, MA, USA). The cytocompatibility of the materials was assessed by means of indirect and direct tests, following ISO guidelines [155, 156]. The ability of cells to interact with other cells and the materials was studied by immunofluorescence staining of phalloidin and DAPI to observe the morphology of cells and by using SEM to analyse the interaction of cells and the materials.

Cytocompatibility

Cytocompatibility was studied using two different methods: indirect tests using the release of the materials under culture conditions (defined as extracts), and by direct test using the live/dead technique. For the indirect tests, material extracts were obtained by immersing each individual sample in complete culture medium with an area/volume ratio of 3 cm^2 /ml. The samples were incubated at 37°C, 5% CO_2 and 95% relative humidity for 72 hours. Independently, preosteoblast cells were seeded at a density of 10^4 cells/cm^2 for 24 hours. The culture medium was subsequently removed and replaced with prediluted material extracts. Pure extracts were evaluated followed by a 2-fold dilution of extracts (50%, 25%, 12.5%, 6.25% and 3.125%). Cells were then incubated for 24 hours. Next, 5 mg/ml of MTT (3-(4,5- dimethylthiazol-2-yl)-2,5-diphenyltetrazolium bromide) (Sigma-Aldrich, MO, USA) in DPBS was added in each well in a proportion of 10 μl per 100 μl of medium. Cells were incubated at 37°C for 3 hours covered from the light. Then 100 μl of dimethyl sulfoxide (DMSO) (Sigma-Aldrich, MO, USA) was added to dilute the formazan crystals. Finally, the absorbance was read on a spectrophotometer (BioTek EL800, Agilent, CA, USA) with a wavelength of 570 nm. Mitochondrial activity was calculated by normalisation with respect to control wells, in which cells were seeded in the complete medium without extracts. Each experiment was repeated three times (n=3).

In the case of the live/dead assays, samples were placed on a 24 well plate and cleaned twice by immersion in ethanol for 10 minutes, followed by immersion in DPBS twice for 10 minutes. Subsequently, cells were seeded on top of the samples with a concentration of 3x10^4 cells/cm^2 and

immersed in 1 ml of complete culture medium and placed in an incubator at 37°C, 5% CO_2 and 95% relative humidity for 6 days, and the medium was changed every 2 days. The live/dead solution for the assay was prepared by diluting 2 μl of ethidium homodimer-1 (635 nm), and 0.5 μl of of calcein AM (515 nm), in 1 ml of DPBS, followed by thorough mixing. The live/dead solution was then added to the cells, ensuring that they were covered by the solution. The plate was covered in order to protect the solution from light and incubated under physiological conditions for 20 minutes. The live/dead solution was then removed in darkness and the samples were washed twice with DPBS. The sample was left in DPBS and immediately viewed under confocal microscopy (Confocal Olympus Fluoview FV-3000) at 10X magnification.

Cell-material interaction

The ability of cells to interact with other cells and the materials was studied by immunofluorescence staining of phalloidin and DAPI to observe the morphology of cells and by using SEM to analyse the interaction of cells and the materials. For both experiments, cells were seeded directly on top of samples at a concentration of 10^4 cells/cm^2 and incubated at 37°C, 5% CO_2 and 95% relative humidity. A Ti sample was used as a control. A set of samples was cultured for 1 hour to evaluate the early attachment of cells to the surface, while another set of was cultured for 24 hours to assess late attachment, cell morphology and monolayer formation. At the end of each incubation time, cells were fixed with paraformaldehyde (PFA) 4% (Sigma-Aldrich, MO, USA) for 20 minutes at room temperature. The samples were then washed with DPBS.

For the immunofluorescence staining technique, cells were permeabilized with 0.1% Triton X-100 (Sigma-Aldrich, MO, USA) for 15 min. Cells were then washed twice with DPBS and then exposed to Alexa Fluor 488 phalloidin (Thermo Fisher, MA, USA) in a concentration of 1:300 and DAPI (Sigma-Aldrich, MO, USA) in a concentration of 1:1000. The cells were incubated for 1 hour at room temperature in the dark and then washed with DPBS. Subsequently, they were observed in the confocal microscope (Confocal Olympus Fluoview FV-3000) at 20X magnification.

Furthermore, to study the cell-material interaction, another separate set of samples was dehydrated in ethanol at different concentrations (50, 70, 80, 90 and 100%) for 10 minutes each. A second subsequent dehydration process was carried out using hexamethyldisiloxane (HMDS) (Thermo Scientific, MA, USA) diluted in ethanol with concentrations of 33%, 50%, 66%, and 100%, immersing the samples again in each dilution for 10 minutes. These dehydration steps were carried out after fixing the cells with PFA. After the final dilution, samples were left to dry at room temperature overnight. The cells were then observed under SEM (Apreo 2S LoVac, Thermo Scientific, MA, USA).

Live/Dead Assay

In the case of live/dead assays, samples were placed on a 24 well plate and cleaned twice by immersion in ethanol for 10 minutes, followed by immersion in PBS twice for another 10 minutes. Subsequently, cells were seeded on top of the samples with a concentration of 3x10^4 cells/cm^2, immersed in 1 ml of complete culture medium, and placed in an incubator at 37°C, 5% CO_2 and 95% relative humidity for 6 days. The medium was changed every 2 days. The live/dead solution for the assay was prepared by diluting 2 μl of ethidium homodimer-1 (635 nm), and 0.5 μl of of calcein AM (515 nm) in 1 ml of PBS, followed by thorough mixing. The live/dead solution was

then added to the cells, ensuring that they were covered by the solution. The plate was covered to protect the solution from light and incubated under physiological conditions for 20 minutes. The live/dead solution was then removed in darkness and the samples were washed twice with PBS. The sample was left in PBS and immediately viewed under confocal microscopy (Confocal Olympus Fluoview FV-3000, Olympus, Tokyo, Japan) at 10X magnification. The experimental procedure was very similar to the cell staining technique indicated in Figure 2.12, with the only differences being the staining used and the number of days the samples were incubated for.

4.4.4 X-ray computed micro-tomography

X-ray computed microtomography was used to assess geometric accuracy as well as microstructural characteristics (porosity and particle distribution) of the FCC lattice scaffolds manufactured by FFF. Tomography experiments were carried out in a Phoenix Nanotom (General Electric, MA, USA) using a W target and 0-mode nanofocus at 50 kV with a current of 300 μA and the voxel size was 12 μm.

4.4.5 Statistical Analysis

The statistical analysis that was carried out throughout the course of this study was focused on determining the mean and the standard deviation of the results. It was performed using Excel (Microsoft Inc., USA), and the minimum number of tests use to calculate any mean or standard deviation value was 3. Statistical significance studies were not performed.

4.5 Results

4.5.1 Degradation rate and degradation mechanisms

The degradation rate of the different materials was initially assessed from the change in mass and pH as a function of the degradation time at 37°C, which are shown in Figures 4.3(a) and (b), respectively. The PLDL+PEG was very stable during the first 12 weeks and the wet mass and the pH remained relatively constant. Subsequently, it showed a large increase in wet mass (with a peak of 120% at 20 weeks) followed by a large reduction in mass up to 52 weeks, and this reduction was accompanied by a constant reduction in pH, which is indicative of the hydrolysis of the polymer. It should be noted that the experimental scatter in the wet mass of the PLDL+PEG after 31 and 41 weeks was very high. This result could be associated with inhomogeneities in the microstructures created by 3D printing, where some regions are more susceptible to water uptake and degradation than others.

The PLDL+Mg+PEG composite showed a rapid increase in wet mass during the first 14 weeks, which remained constant at $\approx 80\%$ until 30 weeks and then decreased slightly to 60% after 1 year. The rapid wet mass increase during the first 14 weeks was associated with an increase in the pH up to 9, very likely due to the combination of the release of Mg ions into the PBS and the oxidation of the Mg particles. Afterwards, the pH decreased with immersion time. PLDL+Zn also showed an initial increase in wet mass up to week 14, although the maximum only reached $\approx 40\%$. The wet mass started to decrease after 24 weeks and both PLDL+PEG and PLDL+Zn exhibited a mass loss of $\approx -20\%$ after 1 year. The pH of the PLDL+Zn composite was constant during the first 10

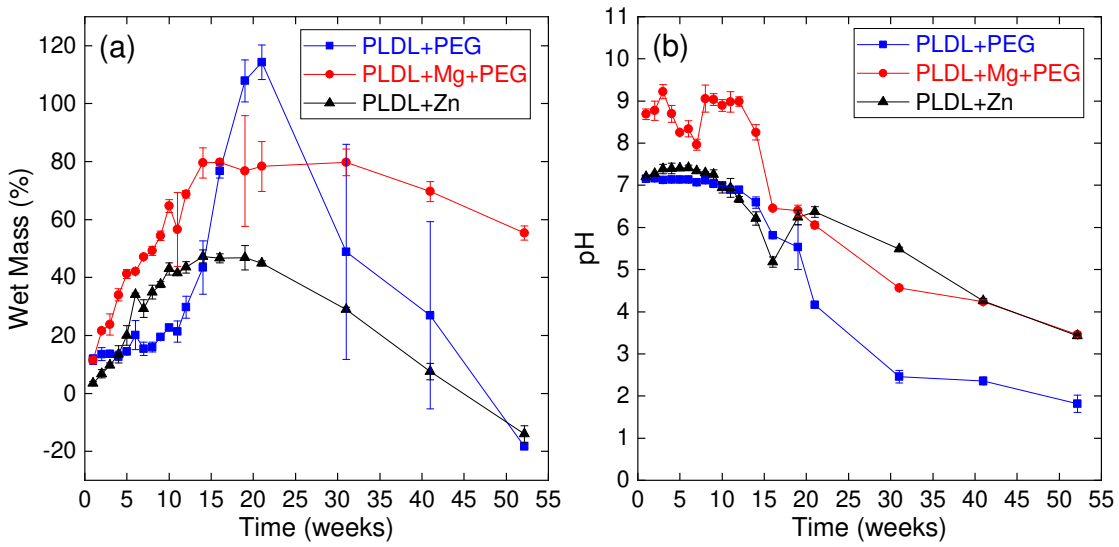

Figure 4.3: (a) Evolution of the wet mass as a function of the degradation time in DPBS at 37°C. (b) Evolution of the pH as a function of the degradation time in DPBS at 37°C.

weeks and then decreased with increasing immersion time, but the final pH after 1 year (≈ 3.5) was equal to that of PLDL+Mg+PEG and higher than that of PLDL+PEG (≈ 1.8). Although pH levels remain relatively stable during the initial 14 weeks for all materials, a rapid decline in pH occurs thereafter. This phenomenon suggests an autocatalysis effect, wherein the initial drop in pH accelerates the degradation of the polymer, leading to a more significant decrease in pH. This cycle then repeats. These findings strongly suggest that an acidic pH environment can accelerate the rate of degradation of the polymer matrix, in agreement with previous observations [200, 201, 202, 203].

The number average molecular weight, Mn, of the PLDL in the three composites was measured by GPC after immersion in DPBS at 37°C up to 14 weeks. The results are plotted in Figure 4.4(a). A significant drop in Mn was observed during the first week in PLDL+PEG and the reduction was more gradual afterwards up to 14 weeks. PLDL+Mg+PEG and PLDL+Zn presented similar behaviours: an obvious reduction in Mn during the first week, followed by a gradual reduction up to 14 weeks. The significant drop in Mn at the beginning of the study can be explained by chain scission of the large chains during the initial uptake of water. It should be noted that the initial Mn of the composites containing Mg and Zn particles was much smaller than that of PLDL+PEG because of the thermal degradation of the polymeric chains catalysed by the presence of metallic particles during processing [180, 192, 200].

The hydrogen evolution in the PLDL+Mg+PEG composite during 16 weeks in DPBS solution at 37°C is plotted in Figure 4.4(b). It shows an initial linear increase in the volume hydrogen generated by the oxidation of Mg particles, leading to a plateau after 14 weeks. This instant coincides with maximum wet mass and the maximum pH in Figures 4.3(a) and (b), respectively, and is confirmed by the large swelling observed in the samples after 14 weeks (Figure 4.4 (c)). It indicates that Mg corrosion was responsible for these phenomena during the first 14 weeks and

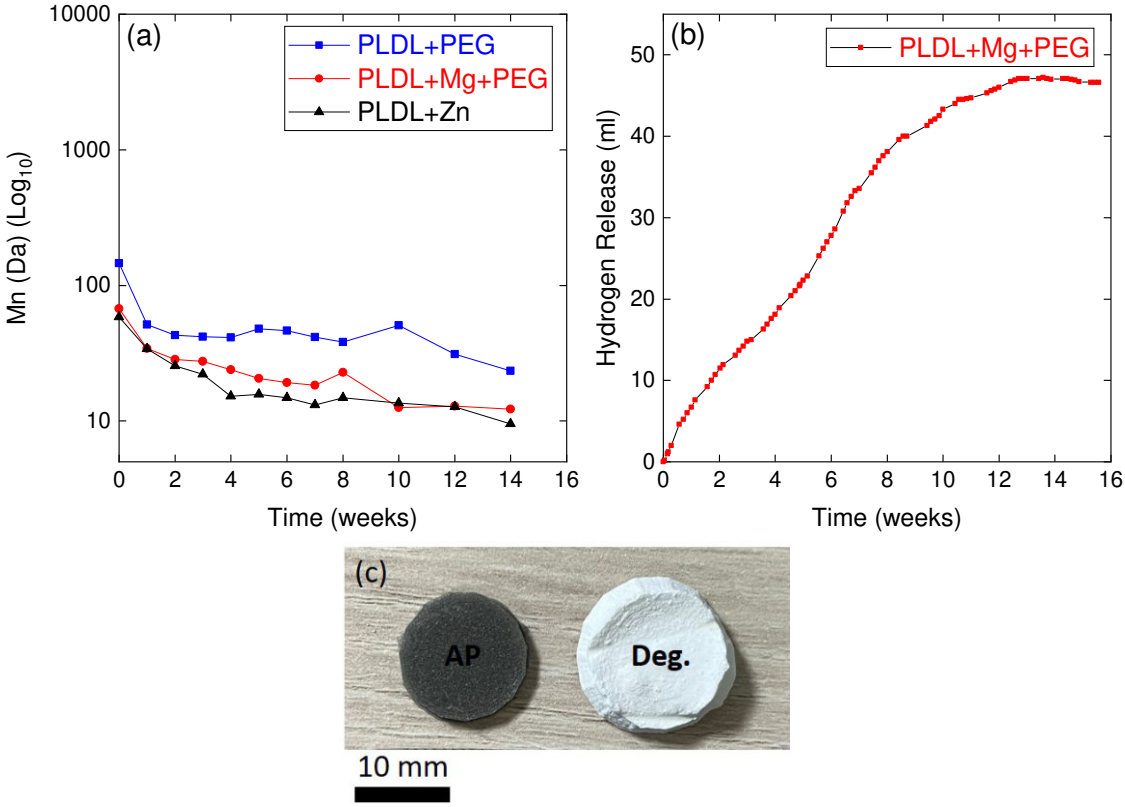

Figure 4.4: (a) Evolution of the number average molecular weight (Mn) of PLDL as a function of the degradation time in DPBS at 37°C. (b) Hydrogen evolution in PLDL+Mg+PEG as a function of the degradation time in DPBS at 37°C. (c) PLDL+Mg+PEG coins in the as-printed (AP) condition and after 14 weeks of degradation (Deg.)

that Mg particles were fully corroded during this period. Interestingly, the theoretical volume of hydrogen expected to be released from the Mg content in the composite was 84.6 ml, much higher than the 47 ml measured experimentally. This difference is in agreement with previous reports [204, 205] and has been attributed to oxygen reduction reactions likely to occur during slow corrosion of Mg [206, 207] or that the hydrogen bubbles were trapped underneath the sample or in the funnel [204].

Scanning electron microscopy was used in order to reveal the degradation mechanisms involved of the three materials over time. Secondary electron images of the PLDL+PEG materials after 16 weeks of immersion in DPBS at 37°C (Figure 4.5). They show that the accelerated degradation (as indicated by the increase in wet mass and drop in pH, see Figure 4.3) was inhomogeneous and it was localized at the interface between the outer perimeters and infill of the printed part, which was more porous and facilitated the ingress of water (Figure 4.5(a)). Therefore, it is likely that these interfaces act as weak regions that are hydrolysed faster, facilitating water uptake and accelerating degradation, as indicated by the white arrows in Figure 4.5 (b).

In the case of the composites containing metallic particles, degradation was localised around the particles. Details of a Mg particle in PLDL+Mg+PEG in the as-printed condition and after

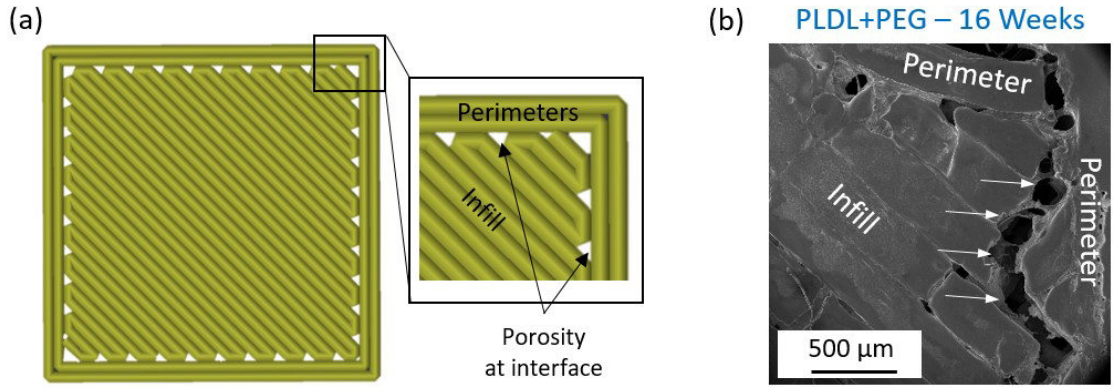

Figure 4.5: (a) Schematic representation of the 3D printing process for a layer of a simple square. The perimeter is printed first, followed by the infill area. The porosity at the interface between the perimeters and infill has been exaggerated for demonstration purposes. (b) Secondary electron image of PLDL+PEG after 16 weeks of immersion in DPBS at 37°C. White arrows indicate regions in which degradation occurred faster, leading to large porosity.

12 weeks of immersion in DPBS are depicted in Figures 4.6(a) and (b), respectively. Degradation after 12 weeks leads to significant oxidation of the Mg particle, confirmed by energy dispersive spectroscopy (EDS), leading to an increase in volume that induces the formation of voids and cracks in the polymer. They facilitate further water ingress, accelerating the degradation process, which is clear from the secondary electron image in Figure 4.6(b) where significant degradation of the polymer matrix is observed, in agreement with previous studies in fibre-reinforced PLA/Mg composites [80, 85]. Moreover, it is also likely that the presence of $Mg(OH)_2$ catalyses the hydrolysis of PLDL around the particle [208].

The detail of a Zn particle in the PLDL+Zn composite in the as-printed condition and after 21 weeks in DPBS at 37°C is shown in Figures 4.7(a) and (b), respectively. The particle is perfectly embedded in the matrix after printing but cracks in the polymer matrix have formed following 21 weeks of immersion (Figure 4.7(b)). Zn and O distributions obtained by energy-dispersive X-ray spectroscopy show an oxide layer on the Zn particle; however, the particle is still present and identifiable through EDS. The presence of a Zn particle with little degradation even after 21 weeks is consistent with the lower corrosion rate of Zn compared to Mg [209, 210].

Finally, DSC was used to ascertain the evolution of the glass transition temperature, T_g, of the polymers with increased degradation time at 37°C in DPBS. T_g is observed as the first endothermic peak during the first heating cycle and usually appears between 35 and 70°C (Figure 4.8). T_g remains in the range 50-55°C during the first 8 weeks in the case of PLDL+PEG and it is reduced to ≈47°C after 16 weeks (Figure 4.8(a)). The evolution of T_g with immersion time in PLDL+Mg+PEG is similar to that of PLDL+PEG although the final T_g after 16 weeks is slightly higher, ≈50°C (Figure 4.8(b)). Finally, the initial T_g of the PLDL+Zn is much higher (> 60°C) and, although it decreases slightly with immersion time, remains above 60°C after 16 weeks of immersion (Figure 4.8 (c)).

The peaks associated with T_g in the DSC curves are related to the energy required to change

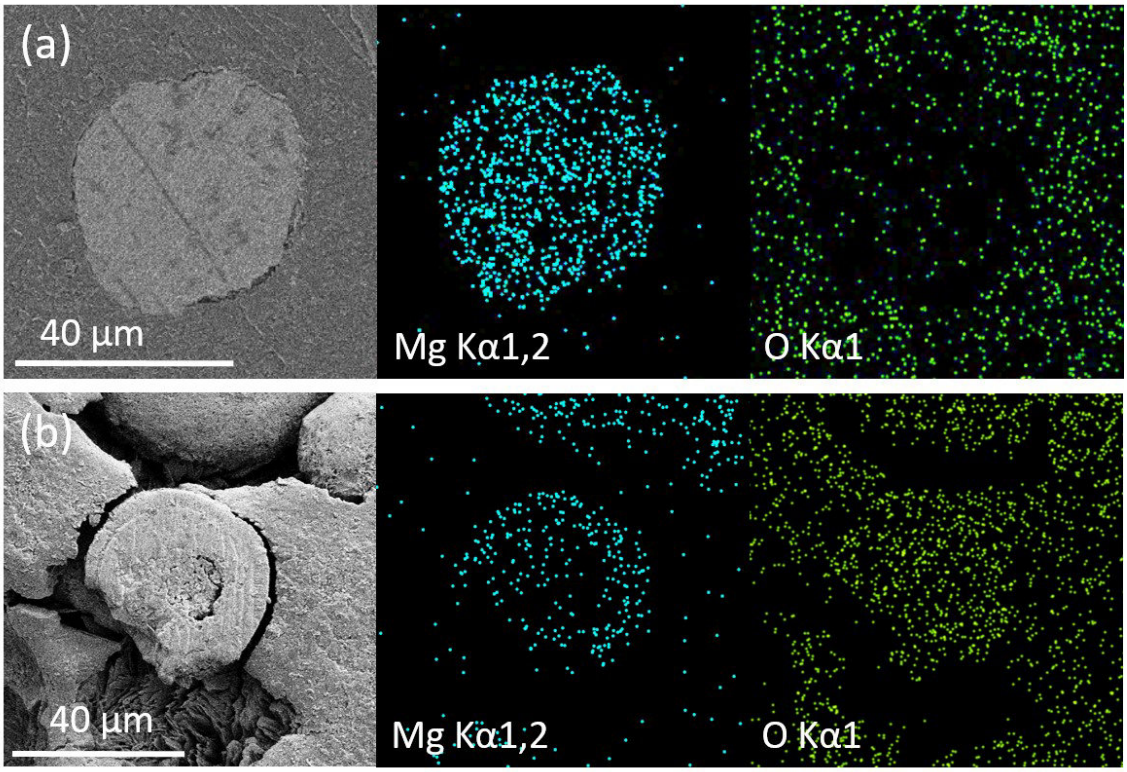

Figure 4.6: Detail of a Mg particle in PLDL+Mg+PEG composite. (a) As printed. (b) After 12 weeks in DPBS at 37°C. Mg and O distributions obtained by energy-dispersive X-ray spectroscopy are plotted along the secondary electron images in each case.

the state by moving the molecular chains in the polymer. Water and plasticising agents such as PEG decrease the T_g, as does breaking the chains thereby decreasing the molecular weight. Thus, the lower T_g of PLDL+PEG and PLDL+Mg+PEG after printing can be attributed to the presence of PEG. Moreover, the reduction in T_g of PLDL+PEG after 8 weeks can be attributed to the plasticiser effect induced by the adsorption of water (which is reflected in the higher wet mass). A similar explanation holds for the reduction in T_g of PLDL+Mg+PEG after 8 weeks, as the increase in wet mass was also important (Figure 4.3). Finally, T_g of the PLDL+Zn in the as-printed condition is substantially higher because of the lack of PEG. This material also shows the lowest water uptake during immersion and, thus, the lowest reduction in T_g with immersion time. Moreover, physical aging during immersion at 37°C is more limited than in the other two materials because of the initially higher T_g.

4.5.2 Mechanical behavior

The tensile stress-strain curves of the as-printed materials are plotted in Figure 4.9. The average values and standard deviations of the elastic modulus, E and of the tensile strength, σ_u are summarised in Table 4.4. The mechanical properties of PLDL+PEG were similar to other values of PLA reported in the literature [200, 211]. The addition of metallic particles led to a slight increase in E and a clear reduction in strength that was associated with the fracture of the tensile specimens

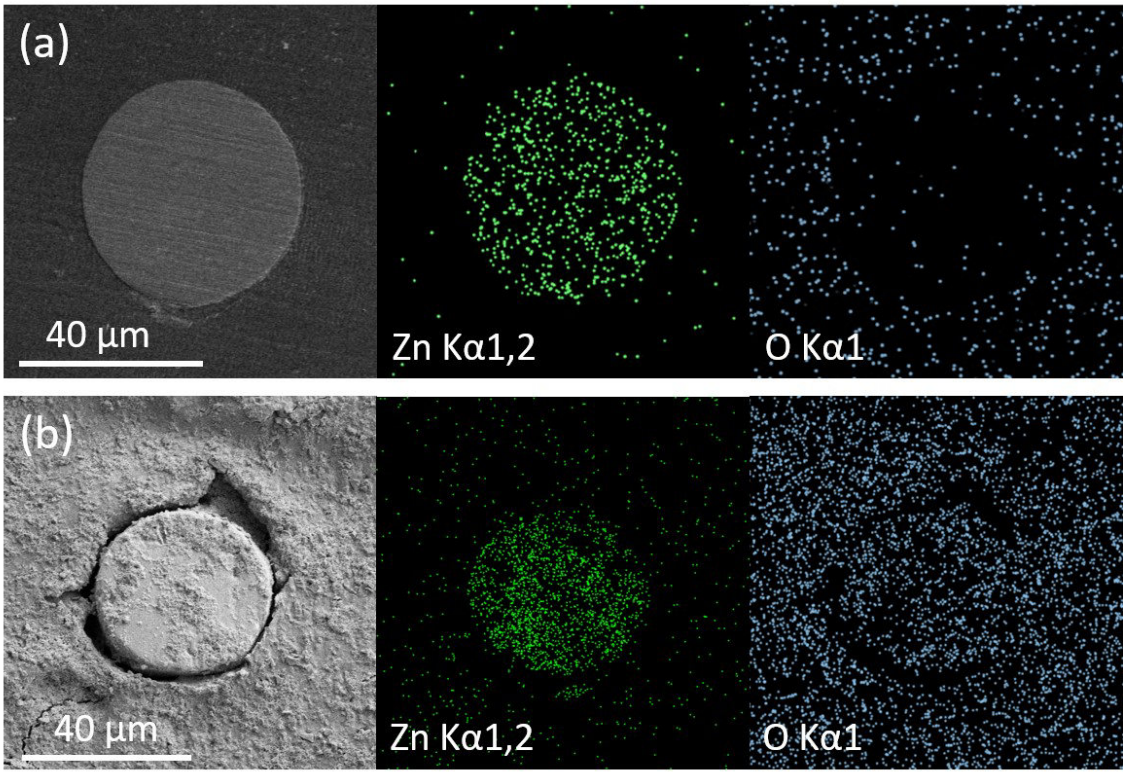

Figure 4.7: Detail of a Zn particle in PLDL+Zn composite. (a) As printed. (b) After 21 weeks in DPBS at 37°C. Zn and O distributions obtained by energy-dispersive X-ray spectroscopy are plotted along the secondary electron images in each case.

at low strains (≈ 1%) while the maximum strength of PLDL+PEG was achieved at ≈ 1.5%. The ductility reduction can be attributed to the stress concentration around the metallic particles. Moreover, the presence of metallic particles also led to a reduction of Mn in the polymer (Figure 4.4(a)), which also leads to a reduction in the strength of the polymeric matrix [212, 213, 200].

Table 4.4: Elastic modulus (E) and tensile strength (σ_u) in the as-printed condition

Material	E (GPa)	σ_u (MPa)
PLDL7038 + 5 wt % PEG	3.0±0.1	38.6±2.2
PLDL7038 + 4 vol. % Mg + 5 wt. % PEG	3.8±0.4	34.1±2.6
PLDL7038 + 4 vol. % Zn	3.2±0.2	27.5±3.7

Immersion tensile tests were also performed on dogbone specimens that had been degraded in DPBS at 37°C during 2, 4, 6, 8, 10, and 12 weeks. The mean values and standard deviations of E and σ_u are plotted in Figures 4.10(a) and (b), respectively, and compared to those of the as-printed samples. PLDL+PEG samples had the best strength retention and both E and σ_u were reduced by ≈ 50% after 8 weeks. The reduction of the mechanical properties of the composites with Mg

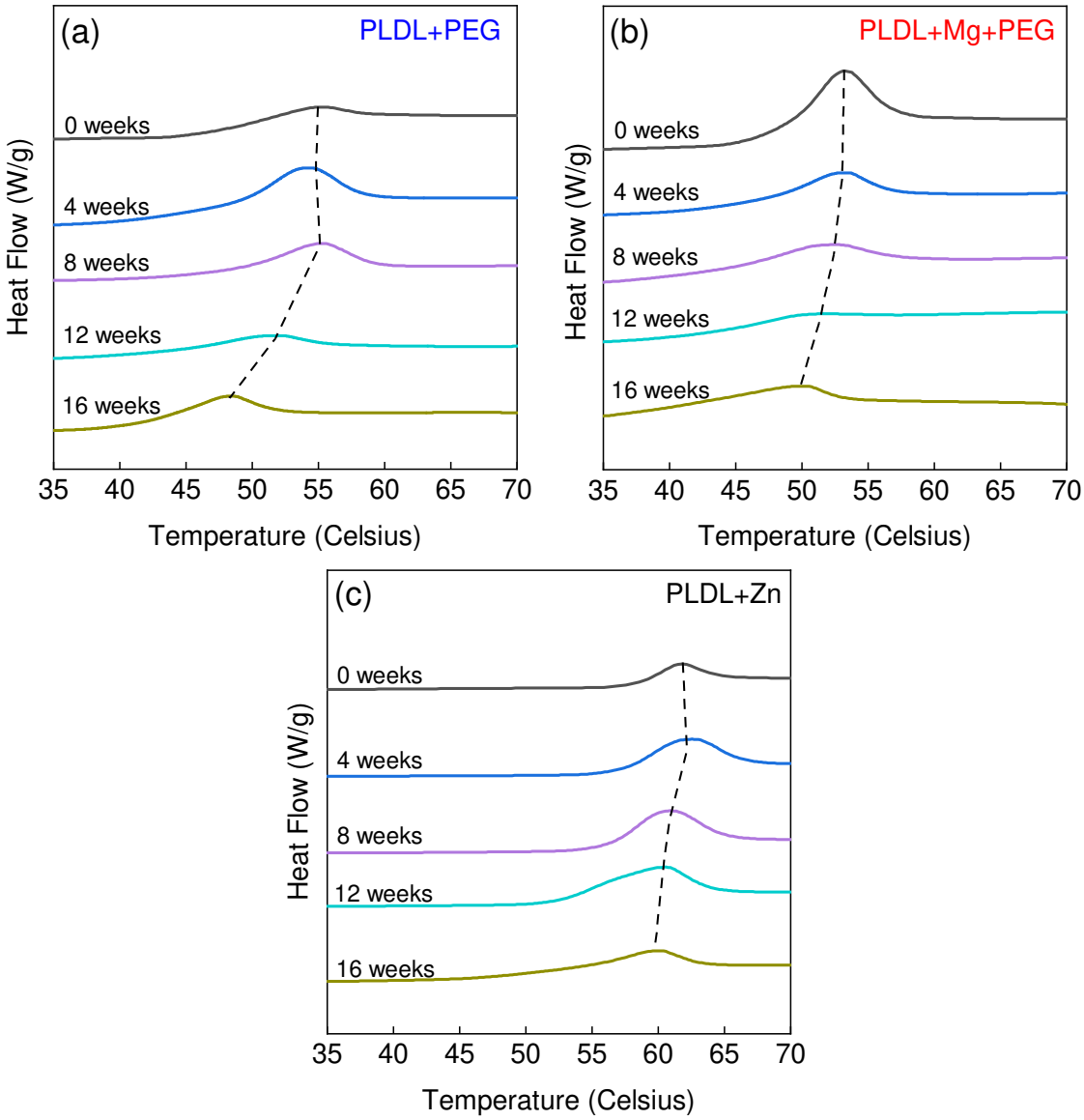

Figure 4.8: Heat flow during DSC after immersion in DPBS at 37°C during different times. (a) PLDL+PEG. (b) PLDL+Mg+PEG. (c) PLDL+Zn. The black dashed line in each figure indicates the evolution of T_g with immersion time.

and Zn particles was much faster and the stiffness and strength have dropped below 50% of the as-printed conditions in both cases after 4 weeks of immersion in DPBS at 37°C. Moreover, in the case of the PLDL+Zn material, a complete strength loss was observed after 10 weeks as the sample was unable to be tested, the same was true for the 12 week specimens, although this behaviour is strange considering that the material did not appear to degrade as fast as the material containing Mg particles.

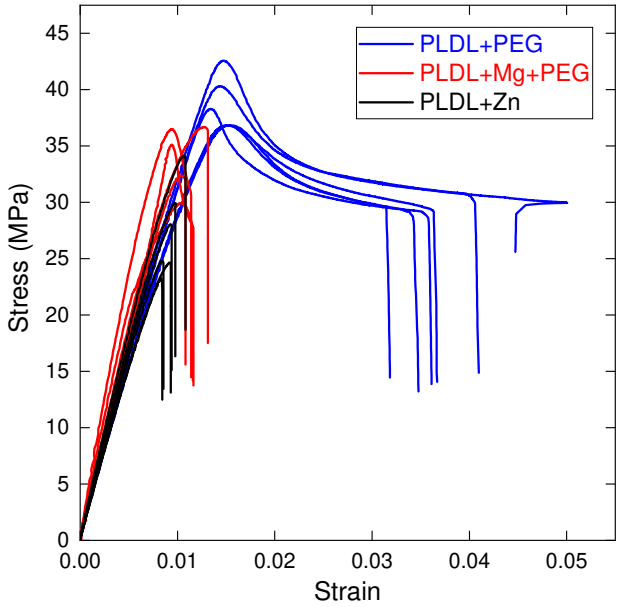

Figure 4.9: Tensile stress-strain curves of PLDL+PEG, PLDL+Mg+PEG and PLDL+Zn in the as-printed condition.

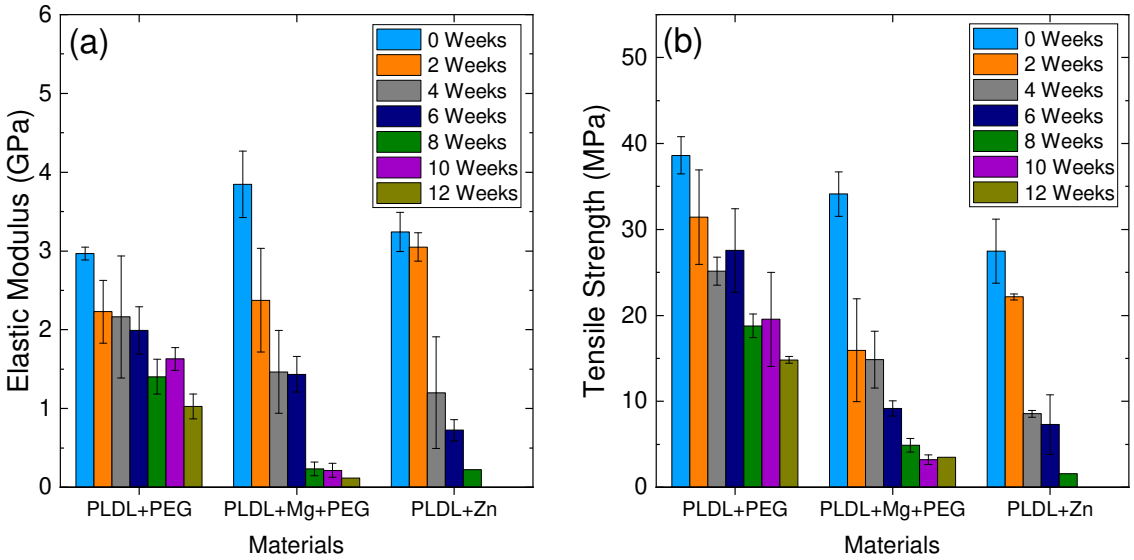

Figure 4.10: Effect of immersion in DPBS at 37°C on the mechanical properties of PLDL+PEG, PLDL+Mg+PEG and PLDL+Zn. (a) Elastic modulus, E. (b) Tensile strength, σ_u.

4.5.3 Cytocompatibility

The mitochondrial activity of MC3T3-E1 preosteoblast cells after 24 h of incubation in culture medium exposed to the 100% extracts of PLDL+PEG, PLDL+Mg+PEG and PLDL+Zn were 90.3% ± 8.7%, 99.4% ± 0.4%, and 87.7% ± 11.3%, respectively, when it was assumed that the mitochondrial activity could not be higher than the control samples (See Figure 4.11). These results

showed high cytocompatibility, considering that a material is cytocompatible if the mitochondrial activity remains above 70% after normalisation with the control.

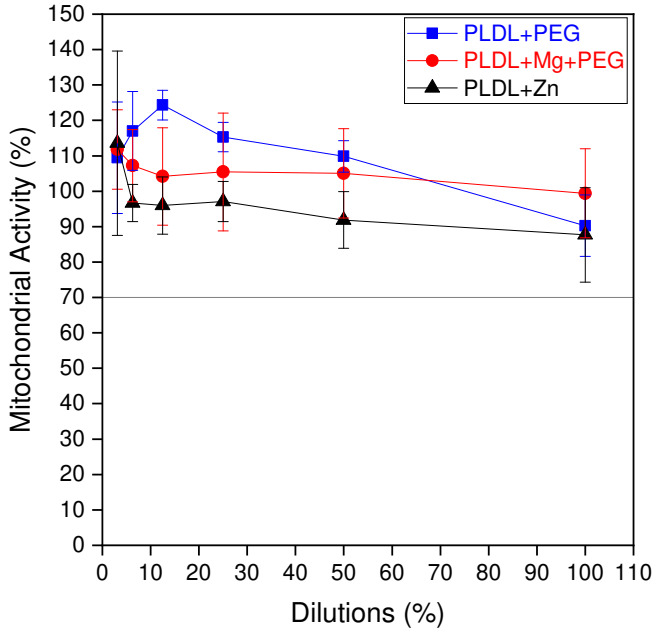

Figure 4.11: MTT assay results for all 3 materials across all dilutions. The scatter bars represent the standard deviation for the three times the experiment was repeated for each material.

These results follow those obtained by the live/dead assays (Figure 4.12) where the ratio between live cells (green) and dead cells (red) was $98.4\% \pm 0.35\%$, $98.6\% \pm 0.4\%$ and $97.5\% \pm 1.3\%$, for PLDL+PEG, PLDL+Mg+PEG and PLDL+Zn, respectively. Additionally, the formation of a cell monolayer on the three materials is observed, indicating the adequate establishment and proliferative capacity of the cells on the material.

Furthermore, confocal microscopy images obtained during direct tests show that the cells respond to rapid adhesion after 1 hour (Figure 4.13 (a-d)) and then interact closely with other cells and the material after 24 hours (Figure 4.13 (e-h)). The fluorescence images allow us to observe the typical morphology of the preosteoblasts with a triangular-shaped morphology and exhibit long cytoplasmic prolongations to adhere to the surface. In the images, the cell cytoskeleton is indicated by a green color (Alexa Flour.), while the nuclei are indicated in blue (Dapi Flour.). Moreover, some cells were observed following surface patterns in terms of their orientation along the 3D printing lines in the materials or the polishing lines in titanium.

In the SEM images (Figure 4.14), the cells can be identified by their particular shape and darker contrast against the lighter background of the composite materials. The cytoplasmic extensions (lamellipodia and filipodia) are shown in all materials, which are indicators of appropriate cell adhesion, and spreading. It can also be seen in these images that cells tend to grow along the printing lines of the material, marked with black arrows, while white arrows indicate the cytoplas-

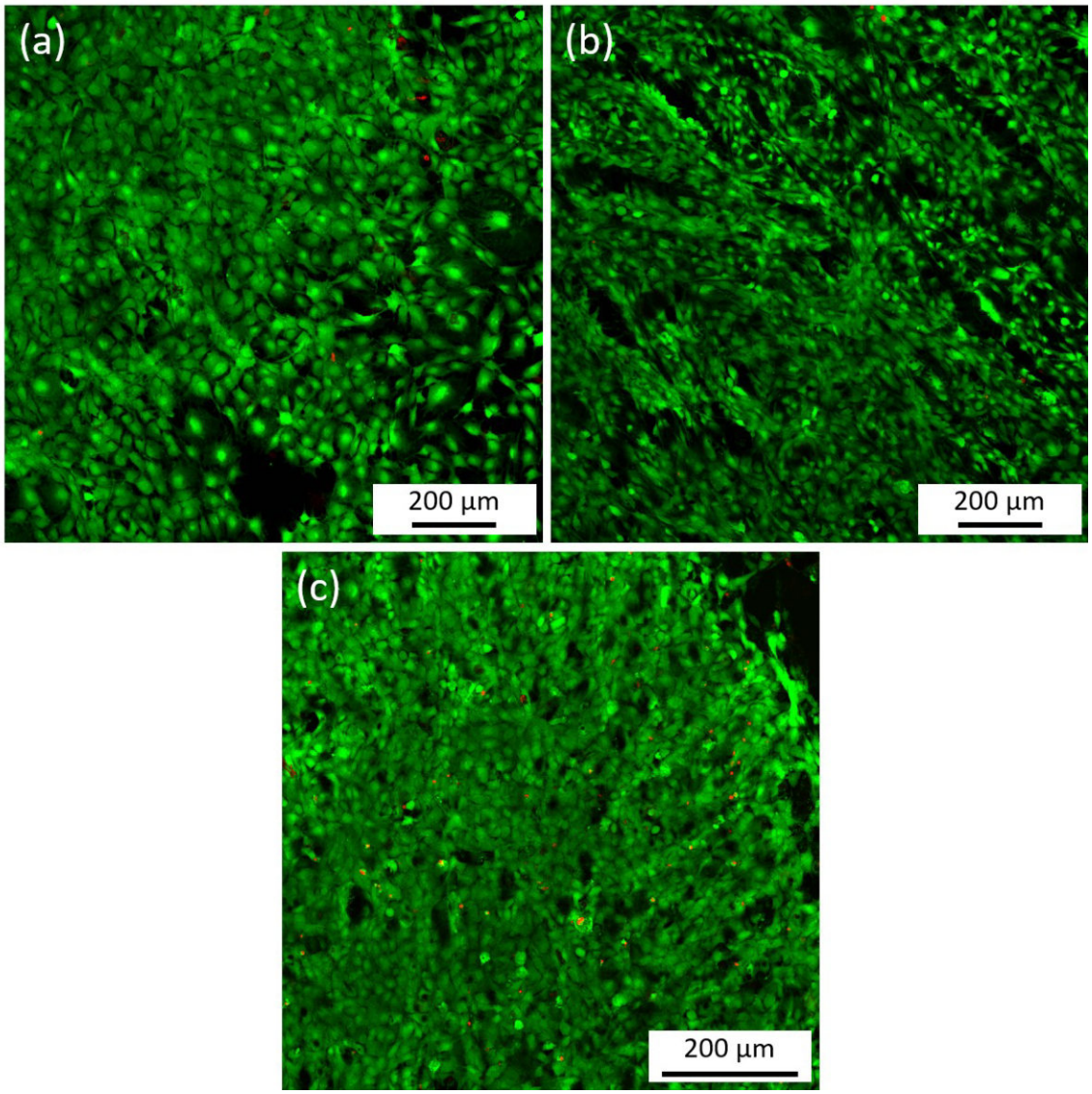

Figure 4.12: Live/Dead images after 6 days of cell cultures under physiological conditions of (a) PLDL+PEG, (b) PLDL+Mg+PEG, and (c) PLDL+Zn. Cells that are alive are stained in green while cells that have died are stained in red.

mic extensions that help the cells adhere to the surface. Higher magnification images in the bottom right corner of the images show the lamellipodia and filopodia interacting with the 3 materials.

4.5.4 3D printing of scaffolds

Cubic porous scaffolds with an FCC lattice structure were printed from the 3 materials and are shown in Figures 4.15(a), (b), and (c). The average strut diameter was 700 μm and the dimensional accuracy of the scaffolds can be appreciated in the cross-sections of the tomograms depicted in Figures 4.15(d), (e) and (f). Some porosity was found within the struts of the PLDL+PEG material (Figure 4.15(d)) but not in the composites containing Mg and Zn particles that were fully dense

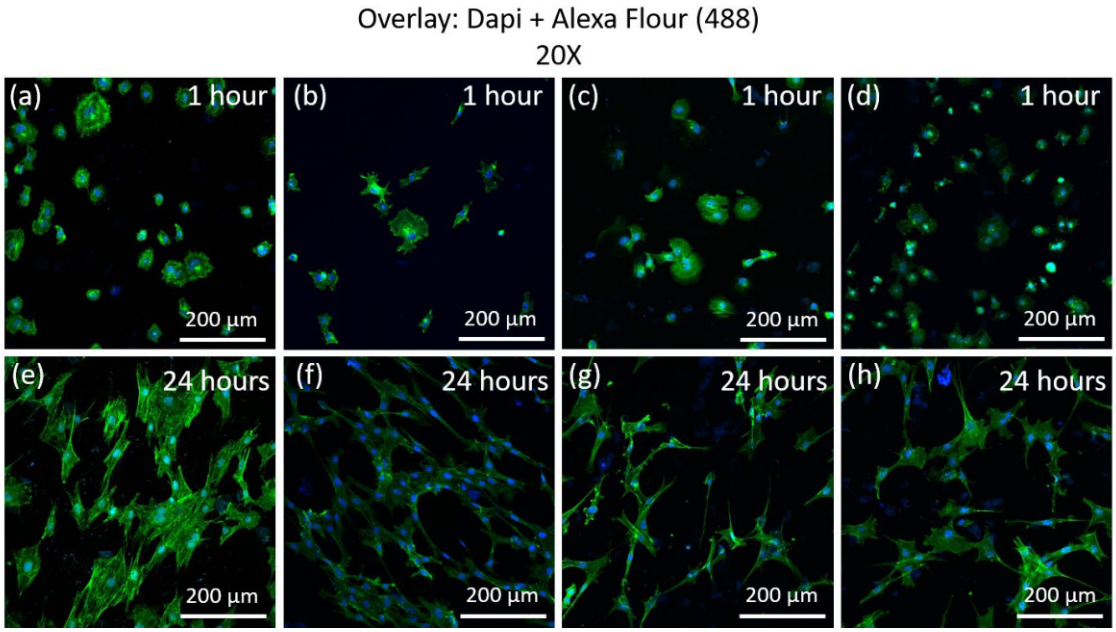

Figure 4.13: Confocal microscopy images of the direct tests showing cells on the surface of the samples. (a) Ti control sample after 1 h. (b) PLDL+PEG after 1 h. (c) PLDL + Mg + PEG after 1 h. (d) PLDL + Zn after 1 h. (e) Ti control sample after 24 h. (f) PLDL + PEG after 24 h. (g) PLDL + Mg + PEG after 24 h. (h) PLDL + Zn after 24 h.

(Figures 4.15(e) and (f)). Moreover, the distribution of the Mg and Zn particles (which appear brighter than the polymeric matrix in the tomograms) was homogeneous throughout the whole cross-section. However, there is some material that has undergone stringing, a phenomenon in which the nozzle is too hot and drags the material from one location to another, as shown by the red circles in Figure 4.15. This phenomenon can be fixed by finding the optimum printing parameters for the scaffold, by reducing temperature or speed or both [214].

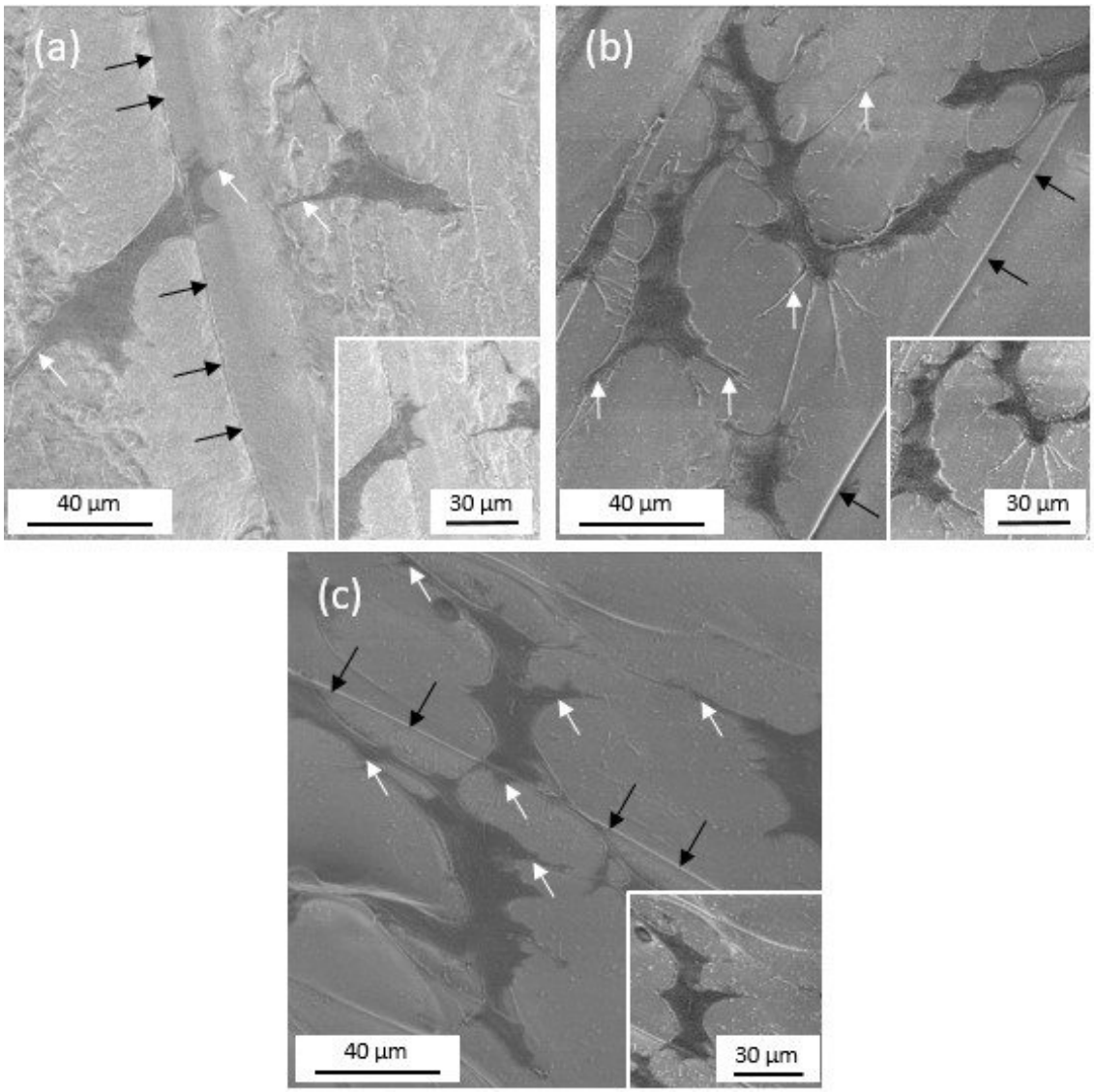

Figure 4.14: Scanning electron microscopy images showing cell attachment after 24 h to the surface of (a) PLDL+PEG, (b) PLDL+Mg+PEG and (c) PLDL+Zn. Black arrows within the images indicate the printing lines while white arrows indicate areas where the cell is spreading.

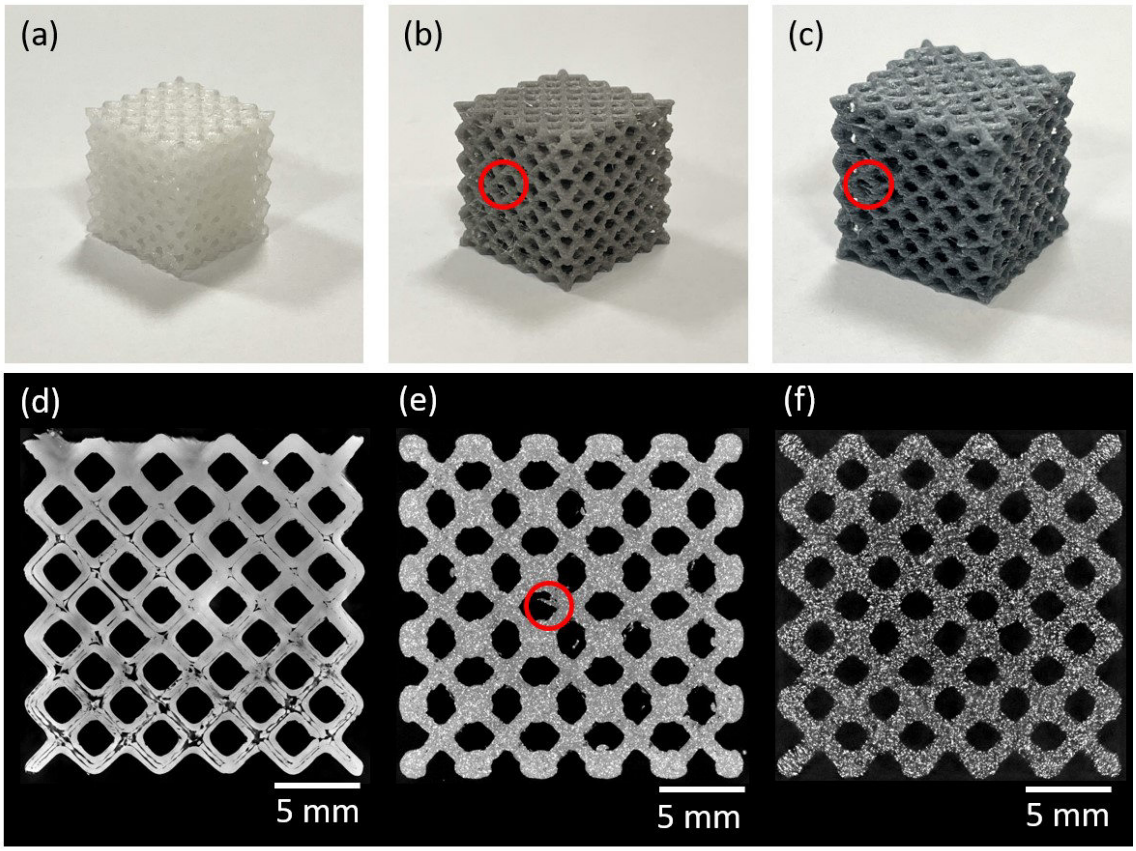

Figure 4.15: (a-c) Optical images of the cubic scaffolds with FCC lattice structure of PLDL+PEG, PLDL+Mg+PEG, and PLDL+Zn, respectively. (d-f) X-ray tomograms showing the cross-section of the PLDL+PEG, PLDL+Mg+PEG, and PLDL+Zn scaffolds, respectively. Red circles on images (b), (c) and (e) represent regions where stringing took place.

4.6 Discussion

This investigation has demonstrated that it is possible to manufacture specimens and scaffolds with controlled porosity and dimensions of medical grade PLDL reinforced with Mg and Zn particles, by 3D printing. In terms of the development of the filaments for FFF, it was required to add PEG to the medical grade PLDL. This was due to processing difficulties which were observed in the form of high viscosity when attempting to extrude filaments. It is hypothesised that medical grade PLDL is more difficult to process than the commonly used commercially-available packaging-grade PLA because the additives present in the latter make it easier to extrude directly from pellets. In addition, PEG was also necessary to extrude Mg-containing composites to increase the melt flow index and reduce viscosity, as reported in the previous chapter. In the case of PLDL+Zn, there was no need to add PEG as the melt flow index MFI was sufficient for 3D printing.

The addition of metallic particles accelerated the degradation of PLDL in PBS at 37°C, leading to a faster drop in mechanical properties (stiffness and strength) with immersion time, as compared with neat PLDL+PEG. This was caused by the reductions in M_n that were introduced to the composite materials during the various processing steps as seen in previous work by this group [180, 192]. It should be noted that the degradation of neat PLDL+PEG was faster than that reported in the literature for this material [49, 56, 51] and this difference can be attributed to the additional processing steps associated with 3D printing (dual extrusion plus 3D printing) that break down the polymeric chain making the polymer more susceptible to degradation. In the composites containing Mg particles, the degradation of the materials were further accelerated during the first 10-14 weeks very likely due to the combined catalytic effect of the oxide layer around the particles in addition to the release of Mg ions. It has also been shown that the polymer matrix is subjected to an accelerated degradation when subjected to an alkaline environment, even more than in an acidic environment [208, 207, 215].

After approximately 14 weeks, both the PLDL+Mg+PEG, and PLDL+Zn materials have attained the maximum water uptake, while this maximum was observed after approximately 20 weeks in the case of the PLDL+PEG. The mass is then reduced by the progressive degradation of the PLDL matrix in all cases, leading to significant reductions in pH. However, the presence of Mg and Zn particles reduced the acidity of the environment during the degradation of PLDL, favouring the biological performance of the composites.

The presence of the Mg and Zn particles slightly increased the elastic modulus and reduced both the strain-to-failure and the strength due to the stress concentrations around the particles. These stress concentrations, along with the oxidation of the particles and the degradation of the polymer matrix, were also responsible for the accelerated reduction in the mechanical properties during degradation. The embrittlement of the materials can be directly related to the molecular weight (M_n) of the materials both before and after degradation, as molecular weight is directly proportional to the strength of polymeric materials [216]. The (M_n) of the Mg and Zn containing materials are lower than that of the PLDL+PEG. Moreover, the strength of the Zn material is slightly lower than that of the PLDL+Mg+PEG which is in agreement with the molecular weight analysis. It is true that the reduction of the strain to failure of the materials to $\approx$1% with the addition of metallic particles appears to be not ideal, however, in some applications it can be

advantageous, for example it has been reported that bone cement applications using PMMA have a strain to failure of ≈1% [217, 218]. Additionally, the materials containing Mg and Zn have an elastic modulus in the range of 100-300 MPa after 8 weeks, which is in the range of mandibular trabecular bone ≈200 MPa and therefore could be considered as viable options for bone repair in that anatomical location [219].

Regardless of the presence of Mg and Zn particles, the materials did not present changes in their excellent biocompatibility. Cell adhesion and proliferation processes were not affected by the presence of metallic particles. This is reflected in the ability of the material to integrate with the tissue even after one week of cell culture where the materials, according to the degradation tests, had already begun a reactivity process.

4.7 Conclusions

Medical grade PLDL and PLDL/Mg and PLDL/Zn filaments were manufactured by a dual extrusion method and used to manufacture coupons and scaffolds with controlled porosity by filament fusion fabrication for the first time. It was found that the presence of 4 vol.% of Mg and Zn particles led to a slight increase in the elastic modulus and to a reduction in tensile strength due to the early fracture associated with the stress concentrations around the particles.

More importantly, the metallic particles accelerated the degradation of PLDL due to catalytic effect of the oxide layer on the hydrolysis of the polymeric chains and to the formation of cracks in the polymer around the particles due to the increase in volume associated with the oxide layer. The latter mechanism also facilitated the ingress of water. Moreover, the acidification of the pH due to degradation of the PLDL was reduced in the composites with metallic particles. Finally, the biocompatibility of the composites was outstanding: cell adhesion and proliferation processes were unaffected by the presence of metallic particles, and the material undergoing degradation was fully integrated with the cells. These results demonstrate the potential of bioabsorbable metal/polymer composites to tailor the mechanical properties, degradation rate, and biocompatibility for specific clinical applications.

3D printing of continuous metal Al wire-reinforced polymer matrix composites

5

5.1 Motivation

3D printing of polymers by Fused Filament Fabrication (FFF) enables the layer-by-layer manufacturing of complex 3D parts to achieve net-shape parts without the need for expensive moulds or sophisticated machining, leading to both financial and time savings [128, 220, 221]. The low cost of FFF 3D printers and the potential for rapid prototyping allows the transition of an idea from concept to prototype in a matter of hours, and the tools and strategies provided by open-source community are just some of the reasons that led to the explosion of 3D printing by FFF in recent years.

One of the main limitations of FFF is that it is limited to thermoplastic polymers (including ABS, PLA, PET, PA6, and PC) which present poor mechanical properties as well as low electrical and thermal conductivity. As a result, prototypes manufactured by 3D printing are often unsuitable for functional-part use [119, 222, 223]. It is also widely known that other manufacturing techniques, such as injection moulding, offer higher tensile strengths than FFF due to the presence of porosity between layers during FFF. Furthermore, the high pressures used during injection moulding lead to improved polymer chain entanglement and improve the stiffness and strength [224, 225, 226].

An obvious strategy to improve the mechanical properties and conductivity of thermoplastics is the reinforcement with stiff, strong, and conductive particles or fibres. For example, PLA matrix composites reinforced with up to 7% vol. of Mg particles manufactured by hot extrusion presented higher creep strength and compression modulus than the unreinforced PLA [227, 228]. Furthermore, solvent casting techniques allow higher volume fractions to be reached ranging from 14 to 58 vol.% of Mg particles [111], showing a significant improvements in elastic modulus and compressive strength. However, these volume fractions cannot be achieved in the case of FFF due to the changes in the rheological properties of the polymer composite and to the inhomogeneous distribution of particles that hinder continuous printing when the filament is fed into the extrusion nozzle [229, 230]. As a result, thermoplastic composites reinforced with ceramic or metallic particles manufactured by FFF are useful to tailor biocompatibility and degradation rates in the case of

biomedical applications [133, 180, 192, 231, 232] but do not lead to significant improvements in strength and stiffness.

3D printed powder-reinforced polymer matrix composites have also been investigated to improve electromagnetic interference shielding and enhance the electrical conductivity in the aerospace and automotive industries. Carbon black, graphene and graphite were added to both PLA and ABS to achieve the desired electrical properties but the mechanical properties were reduced with the increased particle content [233, 234, 235, 236].

In terms of short-fibre reinforced composites, Carneiro et al. [237] manufactured a suitable filament via extrusion, made up of chopped glass fibres in a polypropylene matrix, that could be used for FFF. The strength and stiffness of printed parts were increased by 30% and 40%, respectively, with respect to the unreinforced matrix. Shofner et al. [129] reinforced ABS with 5 vol. % of carbon nanotubes, leading to an increase of 30% in tensile strength. Although these improvements are important, the final mechanical properties of the composite are of the same order than those of the polymer and the presence of fillers compromise the printing accuracy and introduced porosity in the printed parts.

Much larger improvements in mechanical properties can be expected with the addition of continuous fibres to a polymeric matrix. Many studies have demonstrated the potential of FFF-manufactured carbon or aramid fibre reinforced thermoplastics [124, 125, 126, 238, 223, 239], and commercial printers suitable for these composites are available [240]. Nevertheless, FFF of thermoplastics with continuous metallic wires has been elusive so far although metallic wire-reinforced polymer matrix composites are considered for different applications. For instance, PLA/Mg wire composites, manufactured by compression moulding, are currently considered for bioresorbable bone implants because reinforcement of PLA with Mg wires or fibres leads to large improvements in stiffness and strength, accelerates PLA degradation, neutralises acidic by-products, and improves biocompatibility [82, 241, 242, 86]. They are also useful in multifunctional applications that require high mechanical properties together with good electrical/thermal conductivity as a result of the presence of the metallic fibers [243].

The manufacturing of metallic wire-reinforced polymers by FFF is hindered by the largest radius of the metallic wires (> 100 μm), compared to carbon or aramid fibres, which makes extrusion through the nozzle difficult. Ibrahim et al. [123] designed a new hotend in the nozzle to introduce Cu or Ni-Cr wires of 75 μm in diameter into the molten polymer prior to extrusion. They printed a square sample unidirectionally reinforced with the wires, but the volume fraction of the wire was very small (0.7%) and therefore the influence on the mechanical properties was also small. Hamidi et al. [135] used a different strategy to incorporate Cu wires (127 μm in diameter) or stainless steel wires (178 μm in diameter) into a 0.8 mm diameter nozzle to print coupons for tensile tests with the wires orientated parallel to the loading direction. Nevertheless, the wire volume fraction only reached 1.5 % vol. and there was no significant increase in mechanical properties because the porosity of the printed samples was around 20%. Finally, Kim et al. [136] were able to develop a process for embedding Cu wires into a 3D printed part after FFF. However, this investigation focused on the design of the tool to embed the wires, and no information was provided about the final composite and its mechanical properties.

In this chapter, a novel method for manufacturing continuous Al wire-reinforced PLA-matrix composites is developed through a customised multimaterial FFF 3D printer. While one of the print heads on the printer was used to extrude the PLA matrix, the continuous Al wire was deposited through a customised print head, leading to unidirectional composites with a wire volume fraction of up to 25%. The microstructure and mechanical properties of the composites were analysed and demonstrated the manufacturing by FFF of continuous metallic wire reinforced composites with a substantial improvement in mechanical properties due to the presence of the metallic wires, for the first time.

5.2 Development of Wire Reinforced Filaments

The initial idea for creating wire reinforced composites was to use the filament maker (Precision 350, 3devo B.V., Netherlands) similarly to Chapters 3 and 4 to fabricate filaments that contained a continuous metallic wire of 0.3 mm in diameter inside, instead of a powder reinforcement. This was hypothesised to allow for significant increases in the mechanical properties of polymer composite parts to be fabricated, as powder reinforcement had a minimal effect on the mechanical properties. The idea was then that this filament could be printed using a commercial printer either with a diameter of 2.85 mm or 1.75 mm.

To do this, the top plate of the 3devo precision extruder was cut and removed to expose the section of the knee (the point of exit of the barrel just before exiting the nozzle). However, a customised nozzle for the 3devo was developed because permanent, irreversible changes to the internal hardware (knee) of the desktop extruder were not desired at the time. This customised nozzle was longer than the standard nozzle with the idea being that a needle could be placed in the nozzle which would introduce the continuous wire into the filament. A temperature controller (Eurotherm 2500 series, Worthing, United Kingdom) was used in order to account for the loss of temperature along the length of the nozzle, and maintain a the polymer in a molten state (Figure 5.1). The nozzle was developed after many design iterations but it presented several limitations. The problem that was encountered was that the minimum diameter that could be achieved was 1.75 mm but a diameter of approximately 0.5 mm was needed in order to achieve the high volume fraction of wires desired.

To overcome these limitations, the 3devo filament maker was modified. The top plate of the 3devo was cut in order to expose the knee (the point of exit of the barrel just before exiting the nozzle). A hole of 1 mm in diameter was drilled into the centre of the knee. This hole of 1 mm in diameter was the point of entry for the reinforcement wire (Figure 5.2). Then the minimum diameter achievable was reduced to 0.9 mm through standard extrusion of the polymer and relying on the laser/pulley system to control the diameter. This limitation of 0.9 mm was believed to be due to the diameter of the standard 3devo nozzle, which was 4 mm. Therefore, a blank nozzle was ordered from the manufacturer and a hole of 1 mm was drilled into the blank nozzle. The blank nozzle had the same geometry as the standard nozzles, with the exception of the diameter being reduced to 1 mm from 4 mm. Following this modification, a composite filament of 0.5 mm in diameter was achieved which contained a 0.3 mm continuous metallic wire inside coated with PLA on the outside (Figure 5.3 (c)).

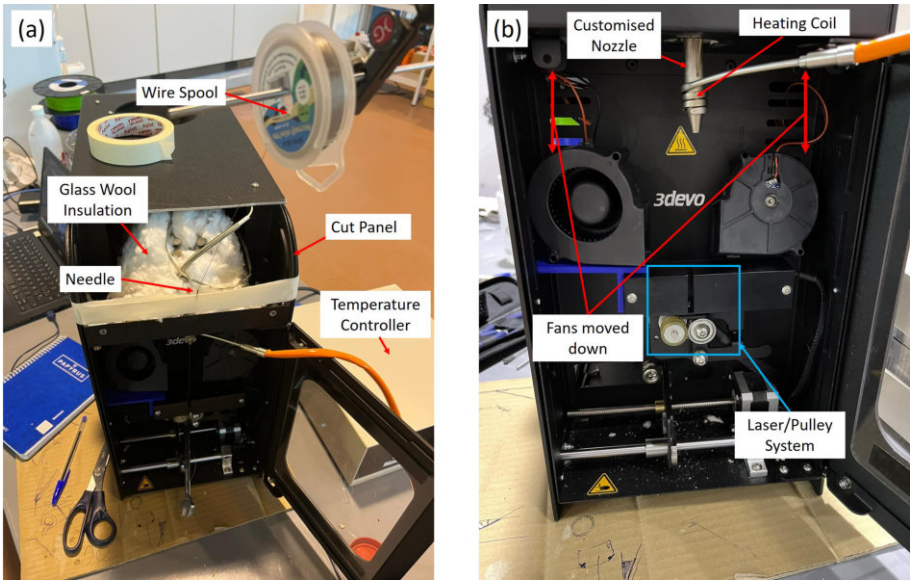

Figure 5.1: 1st design iteration of the modified 3devo extruder showing (a) where the panel was cut to expose the point of exit of the nozzle and make space for a continuous wire to be introduced to the nozzle via a needle. (b) View of the changes to the standard 3devo layout. The customised nozzle can be seen with a heating coil attached which was connected to an external temperature controller. Due to the length of the customised nozzle, the fans were moved down to cool the filament upon exit as opposed to the nozzle. The laser/pulley system is also indicated.

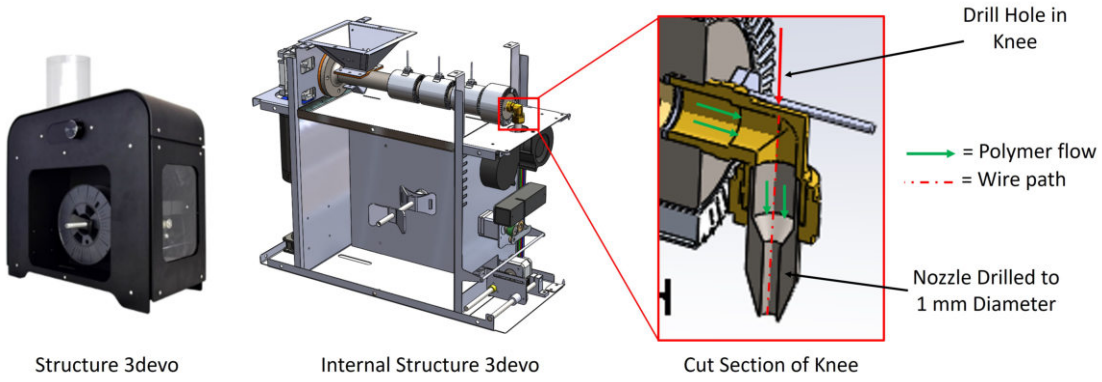

Figure 5.2: Due to restrictions with the processing of the 1st iteration, it was decided to make a permanent change to the internal structure of the 3devo by drilling a hole of 1 mm through the top of the knee. As seen in the cut section of the knee, the idea was to introduce the wire through the top of the knee. The polymer flow from the barrel in combination with the laser/pulley system would pull both the polymer and wire through the new nozzle that was drilled to create the wire reinforced filament.

This method was developed to be able to print continuous wire reinforced composites using a polymeric filament already impregnated with the metallic wire. The advantage being that the volume fraction of wire % would be relatively high, depending on the minimum diameter of the polymer filament with good adhesion and a hypothesised low porosity due to the high adhesion between the polymer and the wire during the filament production process. The main disadvantages

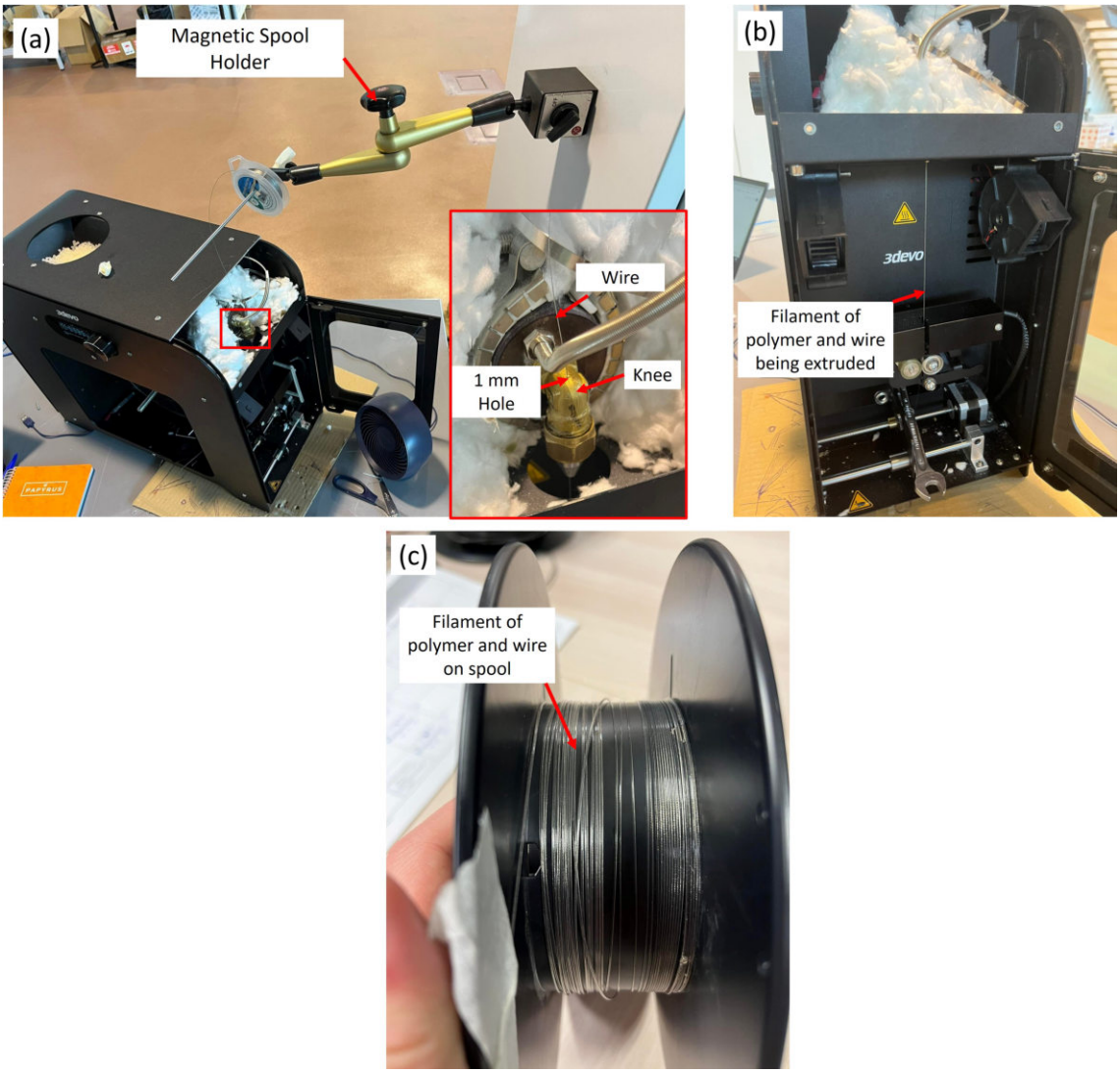

Figure 5.3: (a) Experimental setup showing the wire spool being held directly above the knee to introduce the wire into the molten polymer before exiting the nozzle. A close-up image of the knee is also seen where the wire entering the 1 mm hole is shown. (b) The 3devo setup was returned to its normal layout, the nozzle length was returned to its standard value and therefore changes in fan height were not necessary. (c) Example of a spool of filament with an average diameter of 0.5 mm, and containing a continuous metallic wire of 0.3 mm inside.

of this method are that a customised print head is still required as a method is needed for cutting the wire after each layer, and of course the minimum diameter achievable using the 3devo being 0.5 mm. That being said with some minor improvements to the process of filament production containing the continuous metallic wire inside, it could be easily scaled to produce large lengths of wire reinforced filaments with very high volume fractions. This, in combination with a 3D printer capable of printing the polymer/wire composite would be able to produce complex and customised parts such as bone plates shaped to fit specific geometries of the bones of patients. Despite achieving a filament of 0.5 mm in diameter, the maximum allowable diameter to fit the designed 3D printer with a customised print head was 0.4 mm (Figure 5.6). Moreover, the 3devo

desktop extruder was unable to achieve a filament with a diameter lower than 0.5 mm, as the lowest target diameter possible on the machine was 0.5 mm. Therefore, a filament with a diameter suitable for the customised 3D printer could not be achieved. It was then decided to use separate print heads for the polymer and the wire.

5.3 Development of a Customised 3D Printer

A customised multi-material printer was designed and fabricated (3D Technology Ltd., Galway, Ireland). The printer consisted of 4 individual print heads, 3 of which were dedicated to printing thermoplastic polymers in filament form and one to deposit continuous metallic wires (Figure 5.4 (a)). The XY movement of the printer was controlled by a tool selector, while the z-movement was controlled by the print bed (Figure 5.4 (b)). The tool selector functioned by moving in X and Y and subsequently engaging with one of the chosen print heads. It was only able to engage one print head at a time and therefore the printing was done in a sequential process. This means that while the polymer print head was engaged by the tool selector, the wire print head was 'docked' or disengaged, and vice versa. For instance, when nothing was being printed, the polymer and wire print heads would be in a docked position; however, once printing, the tool selector was used to engage one of the print heads at a time. Figure 5.4 (b) shows the tool selector engaged with the polymer print head before docking the polymer print head again and engaging with the wire print head (Figure 5.4 (c)). In this way the printing of the continuous wire reinforced parts was not done via the simultaneous printing of the polymer and the wire but rather in a sequential process.

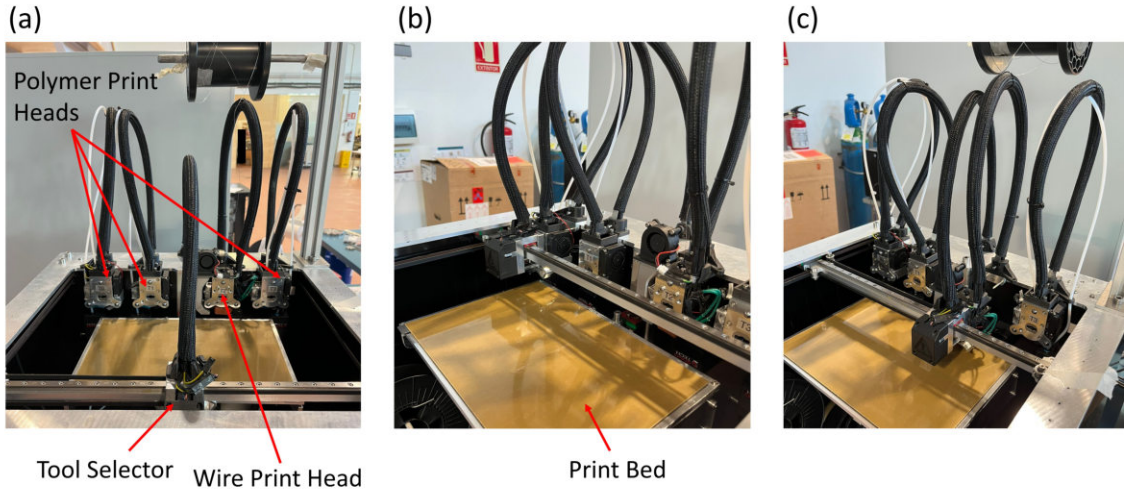

Figure 5.4: (a) Printer in the 'homed' condition, all print heads and the tool selector are docked in position. (b) Tool selector has engaged 'T0', the polymer print head. (c) Tool selector has disengaged the polymer print head and engaged the wire print head 'T2'.

In the case of the 3 print heads for thermoplastic polymers they were comprised of commercially available hot ends (Volcano Hot End, E3D, United Kingdom). Although the polymeric print heads were constructed using readily available commercial parts they were required to be modified just like the wire print head to allow for the tool selector to be able to engage and disengage for printing.

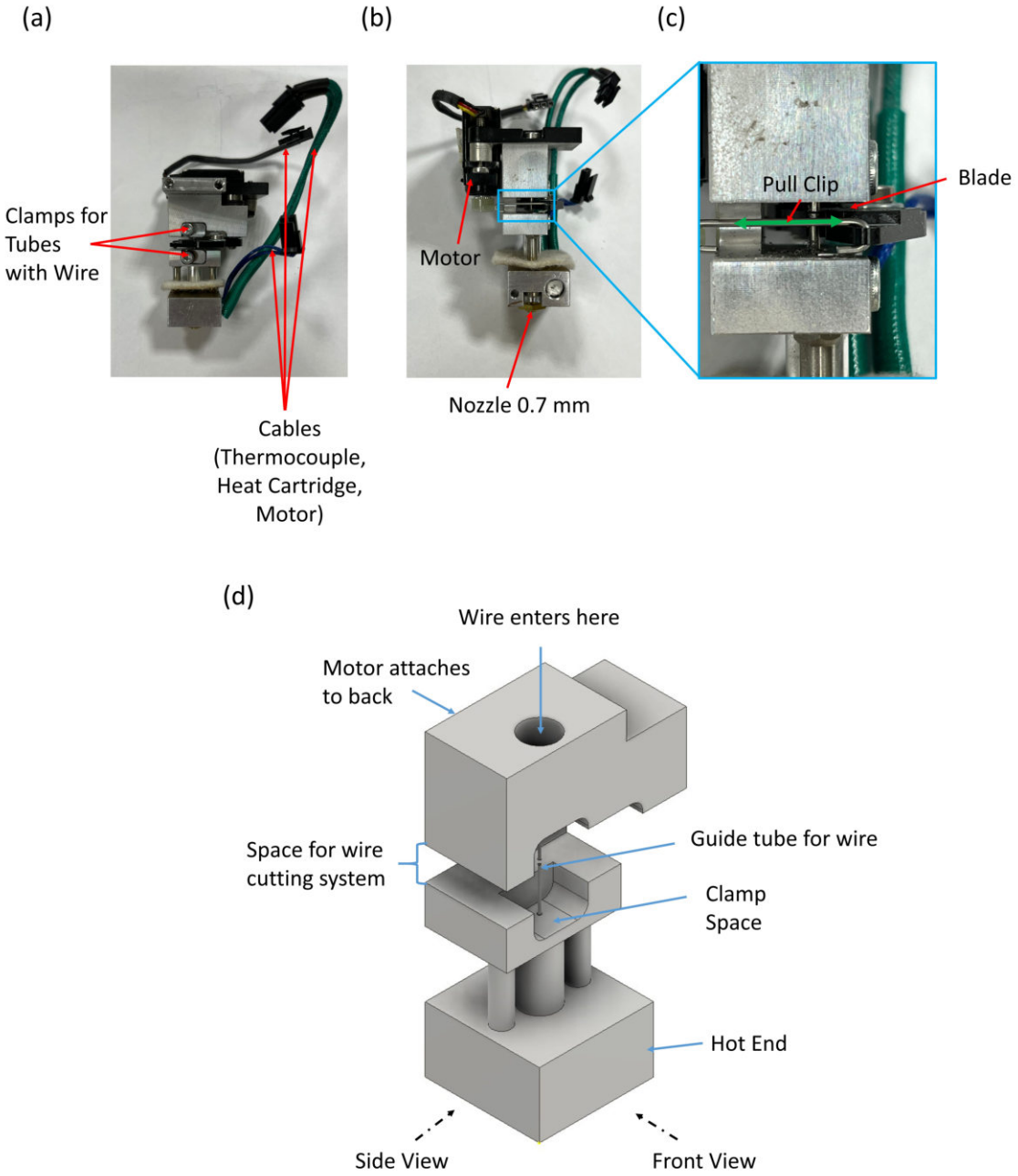

Figure 5.5: (a) Front view of the wire print head. It is mainly comprised of an aluminium piece shaped to allow for the blade to cut the wire. Clamps are used to hold the tubes in place as the wire passes through them. (b) Side view of the wire print head with the nozzle and the motor for controlling the blade being shown. (c) Detailed view of the cutting mechanism, can see the clip attached to the blade and the motor. (d) 3D model of the main housing of the wire print head.

This was done by placing a machined aluminium plate on the front of the print head with a keyhole and a locking key was placed on the tool selector to enable it to engage and disengage with each of the print heads.

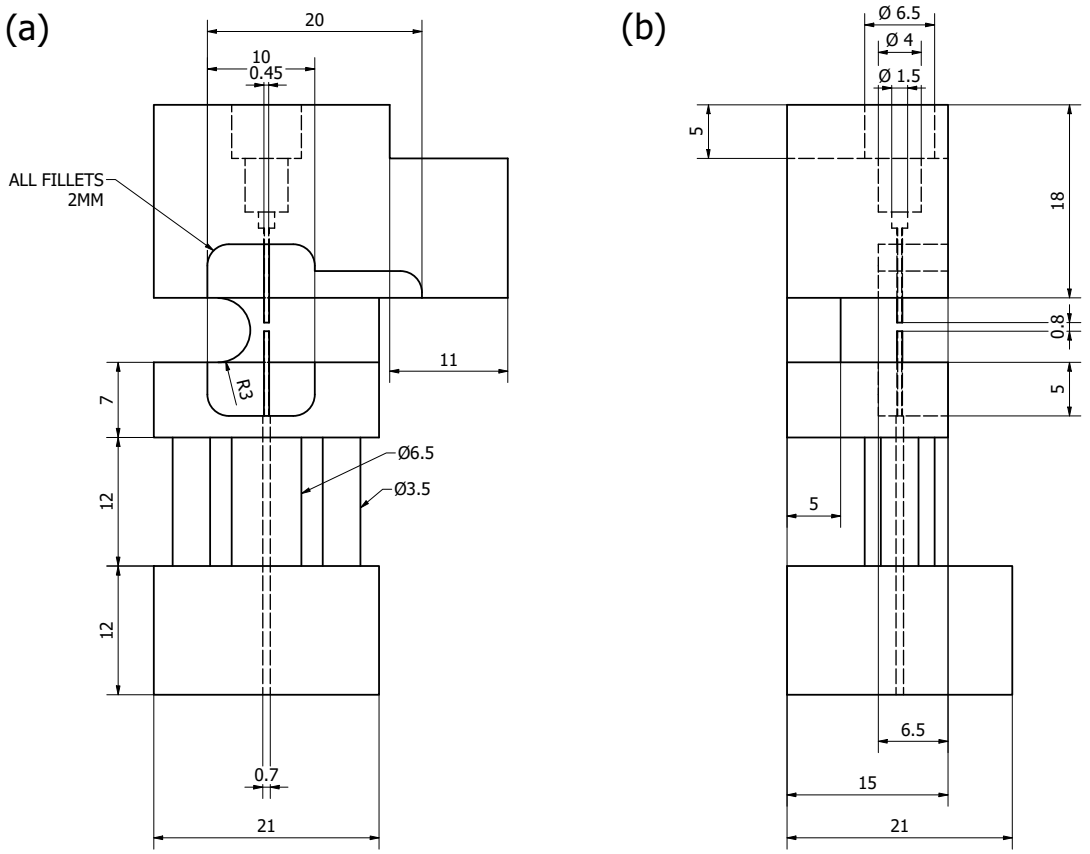

Figure 5.6: Technical drawing of the main housing (Figure 5.5 (d)) of the wire print head with all of the dimensions for (a) the front view and (b) the side view. It should be noted that all dimensions are in mm.

The wire print head was mainly comprised of a custom-machined aluminium piece or housing (Figure 5.5). This piece provided the necessary structure to allow a continuous wire to be deposited and cut. Figures 5.5 (a-c) show the aluminium housing with clamps for maintaining the position of the upper and lower tubes to ensure that they were aligned perfectly. A servo motor attached to the back of the housing (HiTec HS-5087MH, CA, USA) was attached to a blade via a clip that would be pulled through the gap in the wire guiding tubes when the wire was to be cut (Figure 5.5 (b) and (c)). In (c) the small gap can be seen between the upper and lower tubes. Figure 5.5 (d) shows the 3D model of the aluminium housing, labelled accordingly. Moreover, a technical drawing of the aluminium housing according to ISO standards is provided in Figures 5.6 (a) and (b). It is worth noting that a needle with an inner diameter of 0.4 mm was used to help guide the wire into the housing. It is also worth noting that an external fan was attached to the wire print head to aid in cooling during the printing process and that a rubber insulation sleeve was placed around the hot end of the housing.

In order to simplify explanations throughout this paper and due to the fact only one of the polymer print heads along with the wire print head was used, a simplified schematic of the printer will be provided. Figure 5.7, shows the printer comprised of two individual print heads, 1 of which

is used to print thermoplastics and the other print head was specifically designed to deposit metallic wires within the polymer matrix, following specific GCODE instructions.

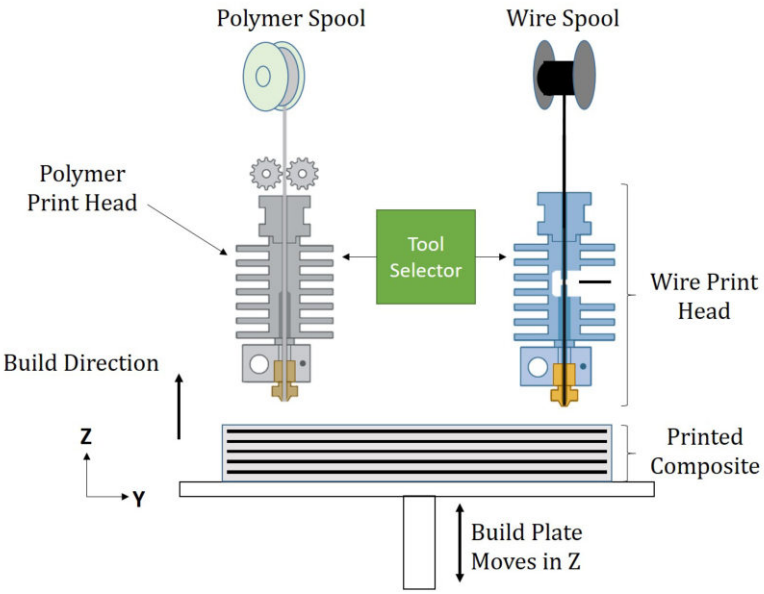

Figure 5.7: Simplified schematic diagram of the 3D printer and process for wire reinforced composites. The simplified version of the printer is comprised of two print heads, one capable of depositing thermoplastics, and the other one capable of printing continuous metallic wires. The printing and XY movement of the individual print heads was controlled through the use of a tool selector.

5.4 Materials and Methods

5.4.1 Materials

Ingeo Natureworks 2003D polylactic acid pellets (Natureworks B.V., The Netherlands) were extruded using a desktop 3devo precision 350 extruder (3devo B.V., Utrecht, The Netherlands) designed for manufacturing filaments for 3D printing. The diameter of the filament was set at 1.75 mm and the extrusion of the filament was controlled with the 3devo comprised of a screw and a barrel with 4 heaters along the barrel to allow different temperature profiles to be set during extrusion. An aluminium (Al) 1050 alloy wire (Gutmann Aluminium Draht GmbH, Germany) with a diameter of 300 μm served as the continuous wire reinforcement material.

5.4.2 3D printing of continuous wire-reinforced composites

Autodesk Inventor (Autodesk Inc., CA, USA) was used to design coupons with dimensions of 120 x 10 x 2.1 mm^3 that were saved as .stl files. An open source slicer (Prusa Slicer, Prusa Research, Prague, Czech Republic) was used to convert the 3D model data into commands readable by the 3D printer. Another coupon was introduced within the slicing software with dimensions 118 x 8 x 2 mm^3 to create the geometry of the path for the wire. To this end, the perimeters were deleted so that only the infill remained (an example of perimeters and infill can be seen in Figure 5.8(a)).

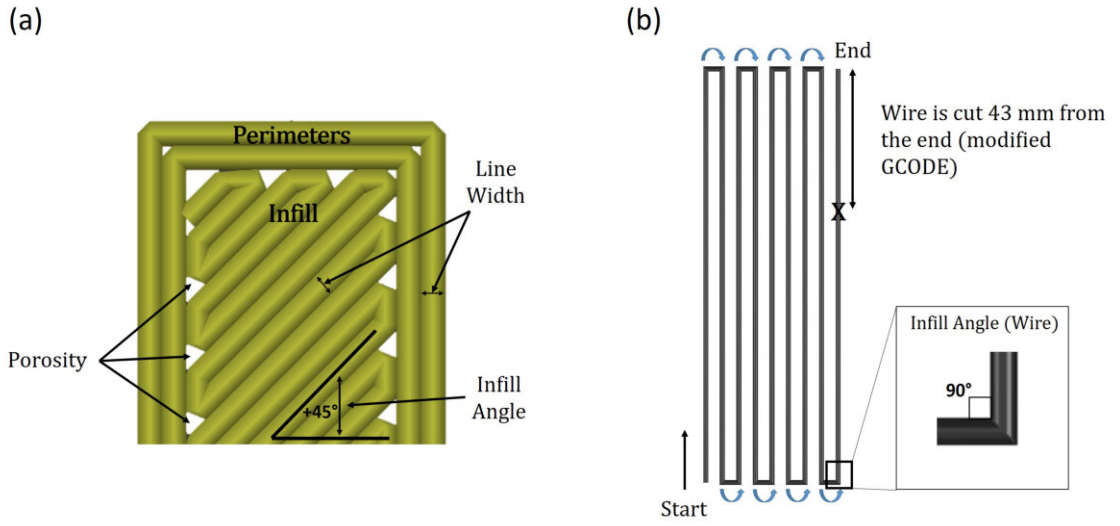

Figure 5.8: (a) Schematic of printing strategy for the polymer layers. (b) Schematic of the path followed by the wire print head during printing of the wire layer. The meandering pattern is known as the rectilinear infill pattern. Images are not to scale.

The number of wires per layer could be determined from the target wire volume fraction, taking the thickness of the polymer layers (0.1 mm), the wire layers (0.4 mm), and the number of polymer layers for each wire layer (4:1), into account (Table 5.1). The infill pattern was rectilinear, which means a 90° infill angle was used (see Figure 5.8(b)). The infill density, which controls the number of times the pattern is repeated, was modified depending on the volume % of wires required (Table 5.2). The averaged distance between the parallel wires at their respective volume percentages are detailed in Table 5.1. Finally, the layer height was modified to be 0.4 mm, and this created the geometry of the wire reinforced layers.

The printing of the continuous wire reinforced parts was not done by simultaneous printing the polymer and the wire, but instead followed a sequential process (Figure 5.9). A 3D schematic cutout of the wire print head is detailed in Figure 5.10. It has a blade attached to a motor to cut the wire. The blade was located 43 mm above the opening of the nozzle, and this information had to be accounted for when executing the wire cutting command during the printing process.

Upon determining the parameters within the slicer, the file was saved and converted into GCODE commands suitable for 3D printing. The GCODE syntax is known for its simplicity, which can be attributed to the historical need to conserve computational power when this technology was initially introduced [244]. In the context of 3D printing, a typical GCODE command comprises a letter specifying the type of action, such as motion, positioning, function, or tool selection, followed by a set of X and Y coordinates. Additionally, a command may include parameters like speed rate or extrusion factor at the end of the line. For instance, a GCODE command might instruct the printer to move to a specific X- and Y-position while simultaneously extruding a defined length of filament.

An important factor when printing with the continuous wire is the ability to cut the wire at the end of each wire layer. A Python script was developed to account for the 43 mm offset between the

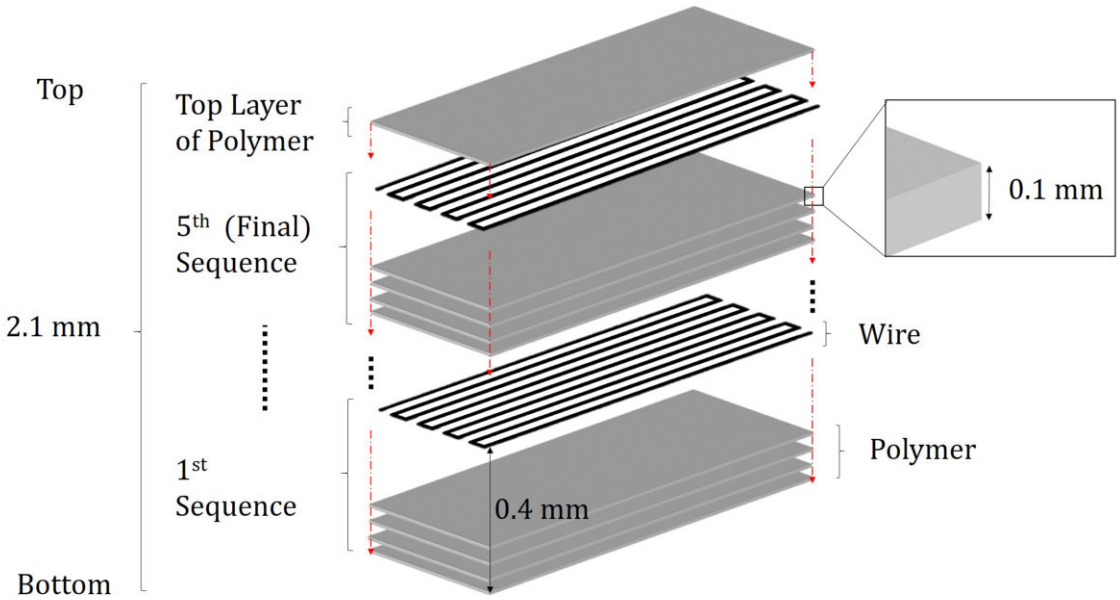

Figure 5.9: Schematic of the breakdown of the layer printing sequence of each coupon of wire-reinforced polymer. The coupon included five sequences of four polymer layers and one wire layer. A final layer of polymer was deposited on top.

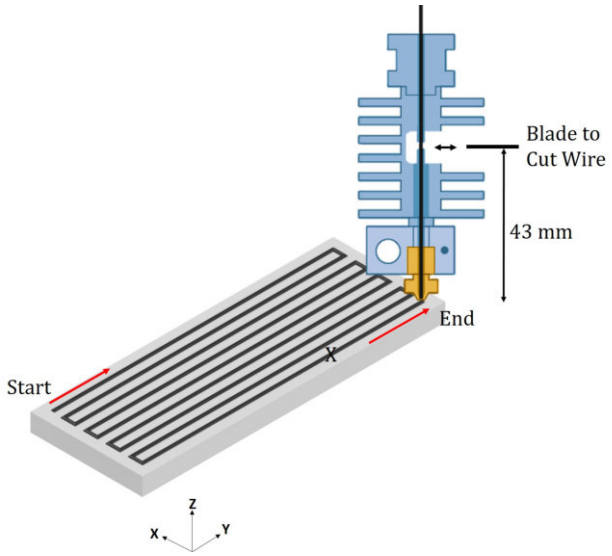

Figure 5.10: Schematic of one of the wire printing sequence in Figure 5.9, showing the path followed by the wire print head. The wire was embedded into the polymer matrix with the cut point of the wire indicated with an 'X', 43 mm from the end of the path.

motor-controlled blade to cut the wire and the opening of the nozzle. The python script found the coordinates of the last line of GCODE and inserted a set of intermediate XY coordinates 43 mm from the last set of coordinates. This meant that the wire always fit perfectly within the geometry of the wire path and material waste was avoided.

Table 5.1: Printing parameters for manufacturing continuous Al wire-reinforced PLA-matrix composites. The explanation of the parameters is indicated in Figures 5.9(a) and 5.8.

Parameters	Values
Nozzle Diameter Polymer	0.4 mm
Nozzle Diameter Wire	0.7 mm
Polymer layer height	0.1 mm
Wire layer height	0.4 mm
Line width	0.8 mm
Infill angle polymer	±45°
Infill angle wire	90°
Wire Spacing (15% vol. Al)	0.9 mm
Wire Spacing (25% vol. Al)	0.5 mm

Table 5.2: Printing parameters for manufacturing continuous Al wire-reinforced PLA-matrix composites.

Material	Printing Temperature (°C)	Print Speed (mm/s)	Fan Speed (%)	Infill Density (%)
PLA	200	40	0	100
15% vol. Al Wires	170	8	100	40
25% vol. Al Wires	170	5	100	70

The printer was controlled using the Duet Web Control Interface (Duet 3D, United Kingdom). Once the GCODE had been modified, it was saved and uploaded to the Duet interface from which the print could then be started. The printing parameters could be changed in the Duet controller during the printing sequence using either an integrated tablet or a computer alongside the printer, allowing full control. Temperature, speed, and babystep distance could be controlled in situ. The babystep distance gives the user the ability to modify the layer height or effectively control how much the nozzle is pressed into the previous layer. This was very important for depositing the wire into the polymer and was set to be 50 and 30 μm in the case of the wire and polymer layers, respectively.

4 coupons of PLA, PLA + 15% and PLA + 25% volume fraction of Al wire were printed with the dimensions mentioned above and using the parameters indicated in Tables 5.1 and 5.2.

5.4.3 Mechanical Tests

Tensile Tests

The coupons manufactured by FFF were deformed in uniaxial tension in an Instron 5966 mechanical testing machine. Prior to testing, the samples were prepared by placing tabs of 40 mm in

length on both ends of the coupons, fixed with epoxy resin. This resulted in a gauge length of 40 mm which was used as the region of interest to determine the strains associated with the coupon during displacement. The strain was measured by means of Digital Image Correlation (DIC). To this end, the coupons were painted white, and black dots were sputtered on the white paint before testing. The movement of the dots was correlated with Vic 2009 2-D DIC software (Correlated Solutions Inc., South Carolina, USA) to obtain the average strain of the coupon. The displacement rate was 2 mm/min and the load was measured with a 10 kN load cell. Single Al wires were also tested in tension to determine their mechanical properties, their respective gripping length was also 30 mm however, the gauge length was 120 mm.

Wire push-out tests

Wire push-out tests were carried out to evaluate the interfacial shear strength between the PLA matrix and the Al wires, following previous investigations [142, 143, 86]. To this end, samples of 10 x 10 x 2.1 mm^3 were cut from the coupons perpendicular to the wires using a high precision punch and subsequently embedded in an epoxy resin (SpeciFix resin system, Struers, Denmark). The samples were then ground using a manual grinding machine (Vector-Metaserv 250, Buehler, IL, USA) with SiC paper ranging from P320 to P2500 up to a thickness of 0.6 $\pm$ 0.03 mm, because the thickness of the sample should be approximately twice the diameter of the wires [144, 85]. Samples were then polished with a diamond paste of 3 and 1 μm grain size (ATM Qness GmbH, Mammelzen, Germany) using MD-Nap polishing plates (Struers, Denmark).

The thin slices of the composite were mounted on a stainless steel support with a groove of 500 μm in width to perform the wire push-out test (Figure 5.11). The wire to be tested was positioned manually at the center of groove with the help of an optical microscope and the slice was fixed with a tape. The support was attached to a stage capable of moving in X and Y directions to position the indenter punch over the desired wire. An indenter with a stainless steel flat tip of $\approx$ 250 μm in diameter was mounted on an Instron 5966 mechanical testing machine with a 100 N load cell. The compressive load was applied on the wire under displacement control at 20 μm/min until the wires were pushed-out from the matrix, which was indicated by a significant drop in load.

The shear strength of the PLA/Al interface, τ, was calculated as

$$\tau = \frac{P_{max}}{2\pi R t} \tag{5.1}$$

where P_{max} is the maximum load, R is the radius of the wire, and t is the thickness of the slice.

5.4.4 Scanning Electron Microscopy and X-ray computed micro-tomography

The fracture surfaces of the broken samples were prepared to be analysed in the scanning electron microsocope (SEM). They were gold sputtered for 60 seconds with a sputtering current of 40 mA (Quorum Q150T ES, Quorum Technologies Ltd., East Sussex, England) to ensure electrical conductivity and analysed in either an Apreo 2S LoVac (Thermo Scientific, MA, USA) or a Helios Nanolab 600i (FEI, Hillsboro, OR, USA) SEM using secondary electrons at a voltage of 5 kV and with currents in the range 40 to 80 pA.

In addition, samples of 10 x 10 x 2.1 mm^3 were cut from the middle sections of the coupons and characterised by X-ray computed micro-tomography. A Phoenix Nanotom 160 NF tomograph

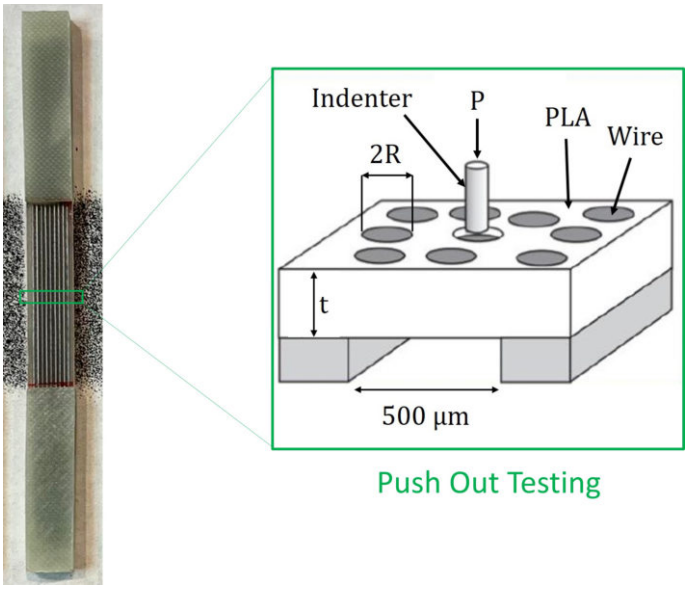

Figure 5.11: Diagram of the wire push-out experimental set up. First, the sample is cut from the coupon and then ground down to a thickness t, twice the diameter of the wire, and a force P is applied perpendicular to the wire until a push-out is achieved.

(General Electric, MA, USA) was used with a W target with a Cu filter and 0-mode nanofocus at 120 kV. The current was 80 μA and the voxel size was 5.4 μm. Subsequently, porosity was calculated using the Fiji (ImageJ, NIH, Maryland, USA) programme for composite coupons with 15% and 25% volume fraction of Al wires. A reference area for the calculation of porosity was isolated in the middle of the tomography sections measuring 3 x 2 mm^2, this was done to exclude regions where it was more difficult for the computer programme to distinguish air voids from bulk material. To this end, a threshold was used to separate the bulk (polymer and wires) from the air voids in $\approx$ 1500 slices of the composite, and the average area fraction of voids was assumed to be the porosity. Additionally, Avizo Software (Thermo Fisher Scientific, MA, USA) was used to create a 3D reconstruction of the PLA+15% vol. coupon for visualisation purposes.

5.5 Results and Discussion

5.5.1 Microstructure

The microstructure of the composites was analyzed by means of X-ray computed tomography. The 3D features of the central section of the reinforced composite with 15% Al wires are depicted in Figure 5.12. Within this figure it is clear to see the good alignment of the wires throughout the volume; however, a number of pores are observed in both the longitudinal section on top of the volume and the transverse section as indicated by the red arrows. Figures 5.13 (a) and (b) show 2D sections of the 15% and 25% Al wire coupons, respectively, and excellent wire alignment can be seen in both cases.

The porosity of the composites with 15% and 25% was 7.4% and 4.8%, respectively. It should be noted that a natural porosity is introduced in the polymer layer via the 3D printing process,

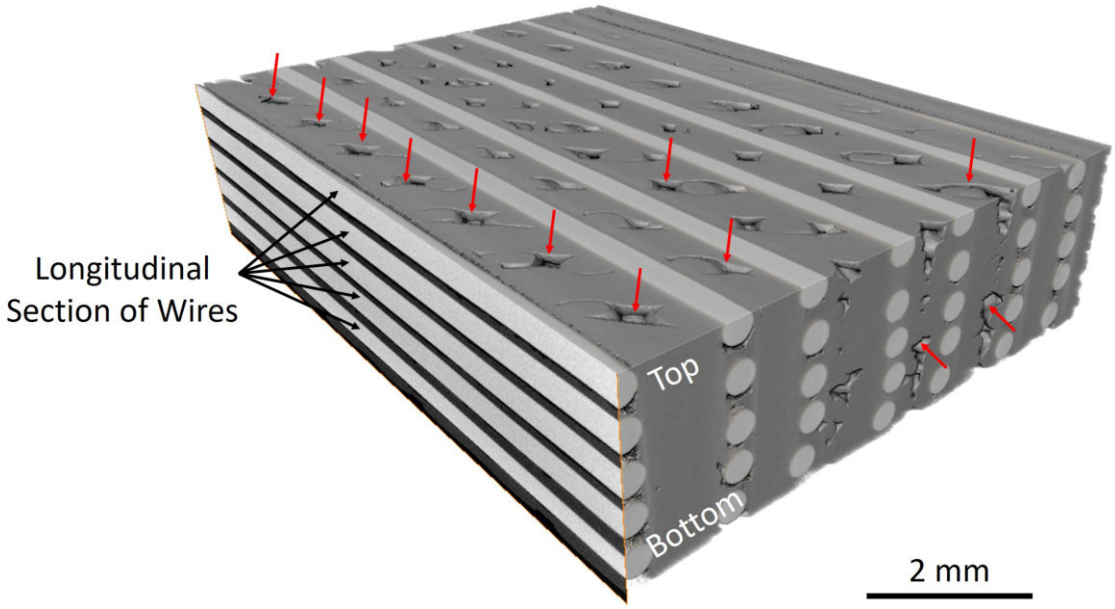

Figure 5.12: 3D reconstruction by X-ray tomography of the composite containing 15 vol. % of Al wires. A longitudinal section from the side of the coupon and the top have been cut to show the alignment of the wires throughout the volume, and the porosity in the z-direction. The wires (light grey) are very well-aligned while the PLA matrix is shown in a darker grey and some of the porosity within the polymer matrix is marked with red arrows.

which can be seen within the slicing software at the interface between the perimeters and the infill (Figure 5.8 (a)). Nevertheless, the large porosity in the composite with 15% Al wires, Figure 5.13 (a), as compared with the composite with 25% vol. Al wires can be ascribed to the printing parameters. Specifically, the wire head passed over the polymer surface 9 times in each wire layer of the 15% coupon, whereas there were 15 passes in the case of the 25% coupon (Figures 5.13 (a) and (b)).

Consequently, the consolidation of the wires in the preceding PLA layer due to deposition of the wires was greater in the composite with 25% wires because the wire print head traversed the layer more times, resulting in a reduced porosity compared to the 15% Al wire coupon, this increased contact time allows for the greater flow of the polymer around the wires leading to a lower porosity. It is also worth noting that in the case of the 25% coupon, the porosity seems to be concentrated more towards the upper part of the coupon. This observation is likely a result of decreased compression forces being exerted in the upper layers of the coupon compared to the lower part. The decreased compression forces at the top were due to the babystep distance which in general deposits the new layer of wire 30 microns into the depth of the previous polymer layer. However, in the case of the upper layers and in order to prevent nozzle blockages, and therefore, a failed print, the babystep distance was relaxed. This in turn led to a higher concentration of porosity to be observed at the top of the coupon as opposed to the bottom.

Furthermore, there are indications of some porosity at the interface between the polymer and wires. Nevertheless, when evaluating the overall porosity of the coupon, this occurrence is negligible. The porosity at the interface between the wire and the polymer is likely attributed to

variations in babystep distances during the process. Consequently, at the time of wire deposition into the polymer, ideal adhesion was not achieved.

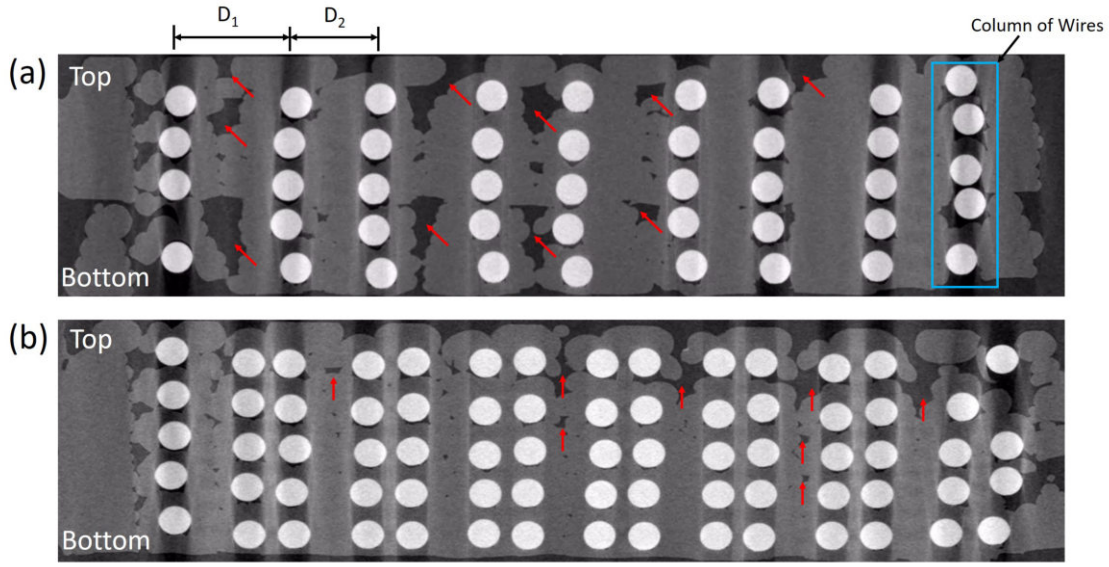

Figure 5.13: (a) X-ray tomography cross-section of the composites with 15 vol. % of Al wires . (b) X-ray tomography cross-section of the composites with 25 vol. % of Al wires . Red arrows in (a) and (b) indicate porosity within the polymer matrix.

The tomography images also yield intriguing insights regarding the porosity and its distribution within the cross-section, particularly in the case of the 15% coupon (as depicted in Figure 5.13 (a)). In this image, the pores are predominantly situated between the columns of wires (blue rectangle), where the spacing between them is relatively wide, for example where $D_1 > D_2$. This pattern is also noticeable in the 25% coupon (shown in (b)), where the larger pores seem to be confined to areas with more significant gaps between the wire columns.

The presence of larger pores in these regions can be attributed to a combination of factors. Firstly, it is imperative to note that the production process for these composites follows a sequential pattern, where four layers of polymer are deposited, followed by a layer of wire, and this sequence repeats. When the wire is deposited, it is not completely embedded in the preceding polymer layer. Consequently, during the deposition of the polymer layers, it is highly conceivable that uneven surfaces, caused by protruding wires, result in less-than-ideal adhesion between the newly deposited polymer layer and the preceding one, primarily because of the presence of the wire layer positioned in between them.

Secondly, it is crucial to note that the wire itself does not undergo melting in this process because of the relatively low temperatures; rather, the polymer is remelted around the wire as it is being deposited. In the case of the 15% coupon, the wire head passes over the coupon fewer times during deposition. Consequently, this allows more time for the wire and the surrounding remelted polymer to cool in an uneven manner, primarily due to the wire deposition pattern (infill pattern in figure 5.8 (b)). As a result, pores tend to manifest in regions characterised by wider spacing between adjacent columns, particularly in areas where the wire deposition nozzle has not made

direct contact.

In addition, within these images, all five layers of wire can be observed in each of the columns, with excellent alignment and a relatively homogeneous distribution within the polymer. However, in a couple of columns, there are some missing wire sections, which likely occurred during the processing of the composite, where the wire may have broken or was removed due to bad adhesion.

5.5.2 Mechanical properties

The stress-strain curves of PLA and Al wires, as well as those of the composites with 15 vol. % and 25 vol. % of Al wires are plotted in Figure 5.14. The presence of the Al wires leads to a large improvement in the stiffness and strength of the composites, compared with the neat PLA, which increases with the wire volume fraction. The average values and standard deviation of the elastic modulus E and of the tensile strength, σ_u, are depicted in Table 5.3. The theoretical values of the elastic modulus of the composites, E_t, according to the rule of mixtures,

$$E_t = fE_f + (1 - f)E_m \tag{5.2}$$

are also depicted in Table 5.3 from the elastic moduli of the Al wires, E_f, and of the PLA matrix, E_m and the wire volume fraction f. They are very close to the experimental ones (particularly for a wire volume fraction of 25%) indicating efficient load transfer from the matrix to the wire during deformation. Moreover, the presence of the stiff wires did not compromise the ductility of the composite that was controlled by the ductility of the PLA matrix. Therefore, the PLA/Al wire composites manufactured by FFF were able to significantly improve mechanical behaviour (up to six times in the case of stiffness) compared to previous attempts [123, 135], showing the potential of FFF to manufacture wire reinforced polymer matrix composites.

Table 5.3: Elastic modulus (E), the tensile strength (σ_u), and the theoretical values for the modulus are represented by E_t. Additionally the shear strength obtained from the wire push-out tests, is represented by τ.

Material	E (GPa)	E_t (GPa)	σ_u (MPa)	τ (MPa)
PLA	3±0.1	–	41±1	–
PLA + 15% vol. Al wires	10±0.3	13	56±2	1.8±0.3
PLA + 25% vol. Al wires	19±1.4	20	67±3	2.3±0.4
Al wires	70	–	90±0.4	–

SEM images of the fracture surfaces of the composite tensile coupons reinforced with 15 vol. % Al wires are shown in Figures 5.15 (a-c), while those of the composite reinforced with 25 vol. % Al wires are depicted in Figures 5.15 (d-f). The fracture surface of the PLA is flat in both cases, indicating that the fracture of the coupon was initiated in the polymer. However, the matrix crack did not propagate into the wires, which were pulled out from the fracture surface. The pull-out

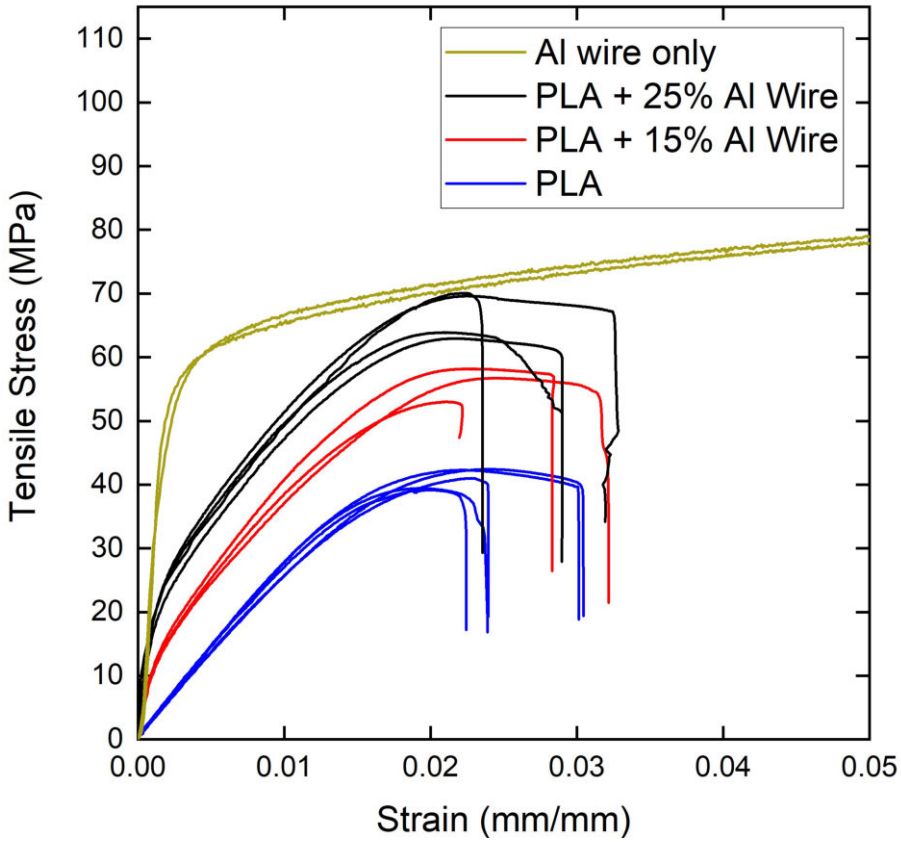

Figure 5.14: Tensile stress-strain curves of PLA, Al wires and PLA reinforced with 15% and 25 vol. % Al wires. The strain in the wires was calculated from the displacement of the cross-head of the machine and the ductility of the wires was approximately 25%.

length was slightly shorter in the composite with 25 % volume fraction of wires and the conical shape of the broken wires indicates a ductile failure mode. Overall in both composites, these failure mechanisms indicate that the bonding between the matrix and wires was weak, leading to interface decohesion and wire pull-out as soon as the matrix crack impinges on the wire.

The load-displacement curves of the wire push-out tests are depicted in Figure 5.16. The initial linear region in the curves corresponds to the elastic bending of the thin slice between the supports, and it is followed by another linear region with higher slope due to the elastic deformation of the wire within the matrix. This zone ends with a maximum in the load, associated with the fracture of the wire/matrix interface and the push-out of the wire, which is associated with a load drop. Once the interface is fully broken, the wire is extracted from the matrix under constant load.

The interface strength was calculated from the maximum load according to eq. 5.1 and the average interface strength, τ, along with the standard deviation are given in Table 5.3. The interface strength in this study is relatively low when compared to other wire-reinforced polymer matrix composites. For instance, the interface strength of PLA reinforced with Mg wires attains 10.9 $\pm$ 1.6 MPa, and can reach 26.3 $\pm$ 1.3 MPa if the surface of the Mg wire was modified by plasma electrolytic oxidation [86]. These higher interface strengths were obtained in composites

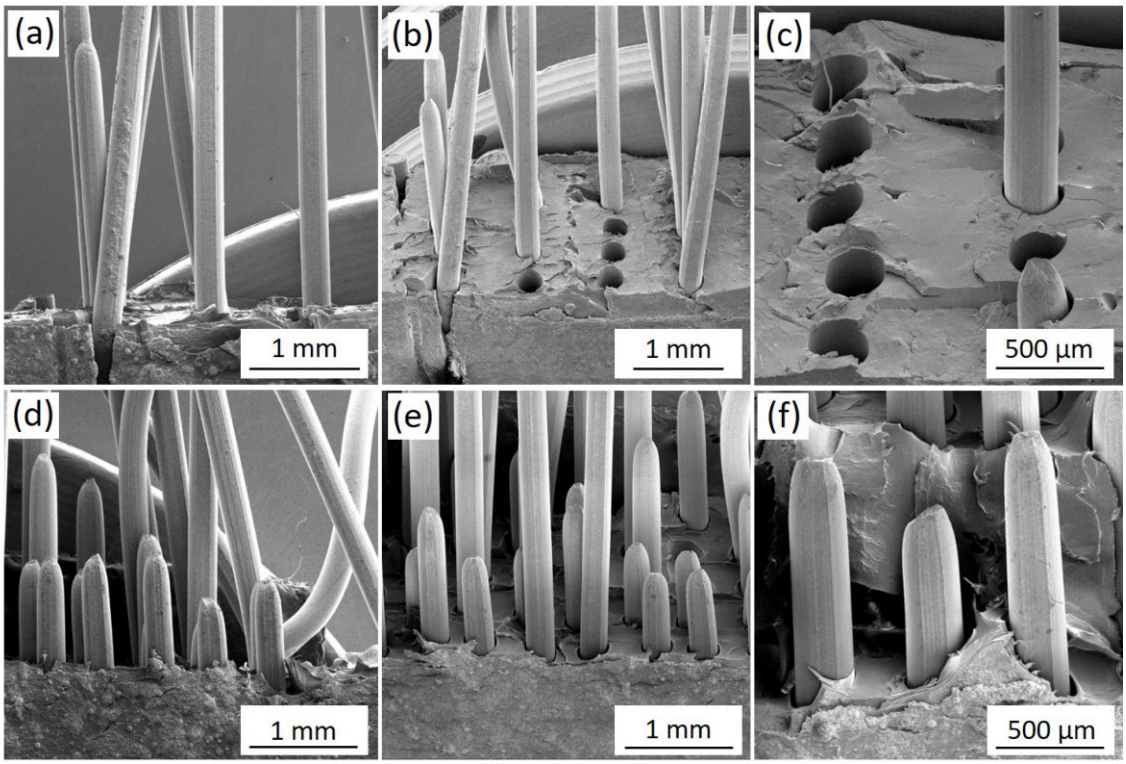

Figure 5.15: (a-c) SEM images of the fracture surfaces of the composites tested in tension. (a-c) PLA + 15% volume fraction of Al wires. (d-f) PLA + 25% volume fraction of Al wires.

manufactured by compression moulding, which ensures an intimate contact between wire and matrix during processing, but they also show that appropriate surface treatments can be applied to improve the wire/matrix adhesion.

The low interfacial strength of the composites aligns with the extensive pull-out length observed in the fracture surfaces (as shown in Figure 5.15). This observation is consistent with the limited chemical interaction between Al and PLA, in contrast to the stronger interaction observed between Mg and PLA [86]. Furthermore, the higher interface strength observed in the composite with 25% volume of wires can be attributed to two factors. Firstly, the porosity is lower in this composite. Secondly, the wires were closer to each other, resulting in a constraint effect, which in turn contributes to the improved interface strength [143, 245]. This constraint is also reflected in the higher slope in the region of the load-displacement curve, which corresponds to the elastic deformation of the wire within the matrix during the push-out test (Figure 5.16). It should be noted that the higher interface strength of the composite with the 25 % vol. of Al wires is reflected in the shorter pull-out length of the wires on the fracture surface (Figure 5.15).

Evidence of wire push-out after the tests is provided by the SEM images of the bottom surface of the thin slices, in which wires pushed out from the matrix are clearly seen (Figure 5.17). It is worth noting the different spacing between wires in the composites with 15% (Figure 5.17 (a-b)) and 25% vol. of wires (Figure 5.17 (c-d)), which was partially responsible for the differences in the interface strength.

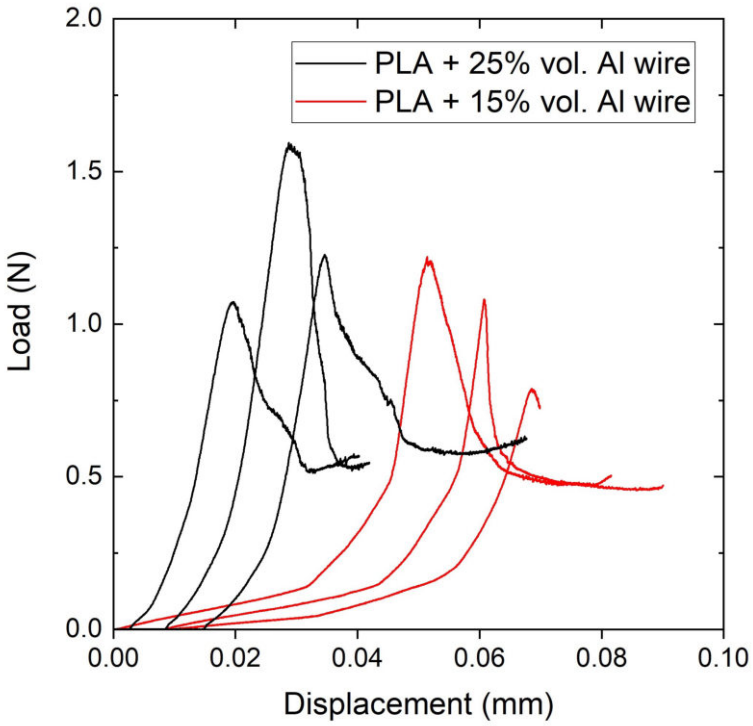

Figure 5.16: Load *vs.* displacement plots of the wire push-out tests.

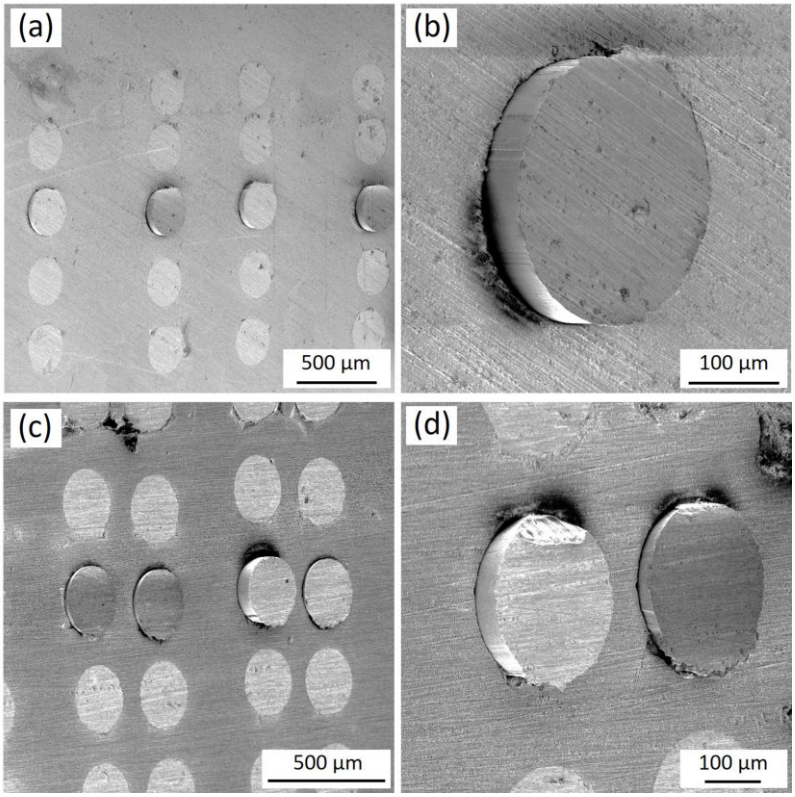

Figure 5.17: SEM images bottom surface of the thin slices of the composites after the push-out test. (a-b) PLA + 15% volume fraction of Al wires. (c-d) PLA + 25% volume fraction of Al wires.

5.6 Conclusions

Polymer matrix composites unidirectionally reinforced with 15% and 25% volume fractions of Al wire were manufactured for the first time using a customised 3D printer that implemented a novel FFF technique. The printer included two different print heads, one of them with a standard nozzle to deposit thermoplastic polymers, while the other print head was specifically designed to print metallic wires through deposition within the polymer matrix. The wire print head was equipped with a cutting system to cut the wire after each wire layer had been deposited. The printer was operated via a computer interface, providing control over key parameters including temperature, speed, and babystep distance in real-time. Additionally, the slicing software provided the capability to predefine wire volume fractions and orientations for each layer before initiating the printing process.

The customised 3D printer was able to position the wires very accurately within each layer although some porosity developed in the PLA polymer matrix during deposition as a result of the inhomogeneous cooling pattern. Moreover, the bonding between the PLA matrix and the Al wire was limited, but it was high enough to allow an efficient load transfer from the matrix to the wires during elastic deformation. Overall, the tensile stiffness increased dramatically due to the wire reinforcement (up to a factor of 6 in the composite with 25% volume fraction of Al wires) while the strength improvement was also noticeable (up to 63% although it was limited by the low strength of the Al wires). Further improvements in properties could be achieved by a detailed analysis of the wire pattern location in the different layers to minimise porosity in the matrix and also by the use of suitable coatings in the wires to enhance the wire/matrix bonding during deposition. These and other process optimisation studies will be able to enhance the quality of the materials processed with this technique.

The novel strategy to manufacture metallic wire-reinforced polymer-matrix composites by FFF presented in this chapter opens the path to improve the mechanical properties of thermoplastic composites and add functional capabilities while maintaining the advantages of FFF. For instance, multidirectional laminates with gradient properties (by changing the wire volume fraction in each layer) can be manufactured. Moreover, very large wire volume fractions can be achieved as the positioning of the individual wires is very precise. Thus, it is expected that further developments and improvements of the technique presented in this paper may have a profound impact in the application of 3D printing of polymer composites in different industrial applications.

Additively Manufactured Continuous Wire-Reinforced PLDL/Mg Composites

6

6.1 Motivation

Biodegradable materials such as synthetic polymers (PLA, PGA and their copolymer PLGA), and hydrolysable metals (Mg, Zn, and Fe) have been increasingly considered in biomedical applications in the past decades for the fabrication of implants and medical devices [246, 247]. Synthetic polymers, such as PLA, are known for their low mechanical properties, long degradation times, and acidic by-products upon degradation, whereas biodegradable metallic materials, such as Mg, are known for their relatively good mechanical properties, rapid degradation times, and basic by-products upon degradation. Thus, the synergy of the combination of biodegradable polymers and metals may achieve novel composites with a customised degradation rate, biocompatibility, and mechanical properties for specific applications. Most of the work in this area has focused on the reinforcement of the polymer with Mg or Zn particles [80, 85, 167, 180, 192, 232, 82] but these composites are limited from the viewpoint of mechanical properties that are equal (or even lower) than those of the polymer (see Chapters 3 and 4)

This limitation of polymer/metal composites can be overcome through the reinforcement of the polymer with metallic wires and a number of studies have investigated the corrosion, mechanical and biological performance of biodegradable polymers reinforced with Mg wires [80, 85, 82, 242, 248, 249, 250]. Composite processing in all these cases was carried out by hot-pressing, a a well-established methodology in the fiber-reinforced composites community. Fully dense composites with excellent mechanical properties along the wire direction can be achieved with this strategy, which has been extended recently to manufacture multidirectional laminates with more isotropic properties through compression moulding [85, 86].

Nevertheless, hot pressing and compression moulding present evident limitations to manufacture implants and scaffolds for biomedical applications that may require complex shapes and curvatures. These limitations are more evident in comparison with additive manufacturing techniques, such as FFF, as discussed in previous chapters of this thesis. However, one of the major limitations for FFF is the limited mechanical properties of the components manufactured by this

technique. This problem was overcome in Chapter 5 through the deposition of a continuous Al wire within a PLA matrix using the FFF process. In this chapter, this methodology is extended to manufacture by FFF PLA matrix composites reinforced with Mg wires. Two different types of Mg wires were used, one of them surface treated by plasma electrolytic oxidation (PEO) to reduce the corrosion rate, and the degradation rate and mechanical properties in physiological environment were studied in detail. Finally, FFF manufactured a proof-of-concept multimaterial biobasorbable coupon made up of pure PLA as well as PLA reinforced with metallic particles and wires. This result demonstrates the capabilities of the methodology develop in this thesis to manufacture components in which both mechanical and degradation properties can be tailored in different regions to optimise the behavior for biomedical applications.

6.2 Materials

The wire reinforced polymer/metal composites were manufactured from a medical grade bioabsorbable polymer, PLDL7038 (Corbion N.V., Netherlands), and WE43-MEO Mg alloy wires of 0.3 mm in diameter provided by Meotec GmbH (Aachen, Germany). The composition of the WE43 wires (wt.%) was 1.4%-4.2% Y, 2.5%-3.5% Nd, <1% (Al, Fe, Cu, Ni, Mn, Zn, Zr), balance Mg. They were manufactured by cold drawing and suitable annealing treatments, as described by Ali et al. [251]. Furthermore, WE43-MEO Mg wires were treated using a continuous PEO process in phosphate-based electrolyte (Kermasorb¨, Meotec GmbH, Germany) which led to a homogeneous and porous oxide layer on the wire surface of approximately 8 μm in thickness mainly composed of MgO and $Mg_3(PO4)_2$ [251] (Figure 6.1). Residual stresses were removed from the both the Mg and Mg-PEO wires before spooling. This was done during processing where the wires were passed through an inline tubular oven of 350 mm in length at 400°C [251].

Furthermore, polyethylene glycol (PEG 1000 g/mol) (Sigma-Aldrich, MO, USA) was also used to facilitate the extrusion of the PLDL filament. Throughout this chapter, the composite made of PLDL and Mg wires will be referred to a PLDL+Mg while the one manufacture with PLDL and Mg wires surface-modified by PEO will be denominated PLDL+Mg-PEO. Finally, PLA Ingeo 2003D (Natureworks B.V., Netherlands) and WE43 powder were used in order to manufacture filaments of PLA/Mg composites (following the procedure detailed in Chapter 3) that were used together with the Mg wires to manufacture multimaterial coupons in the FFF printer with multiple heads.

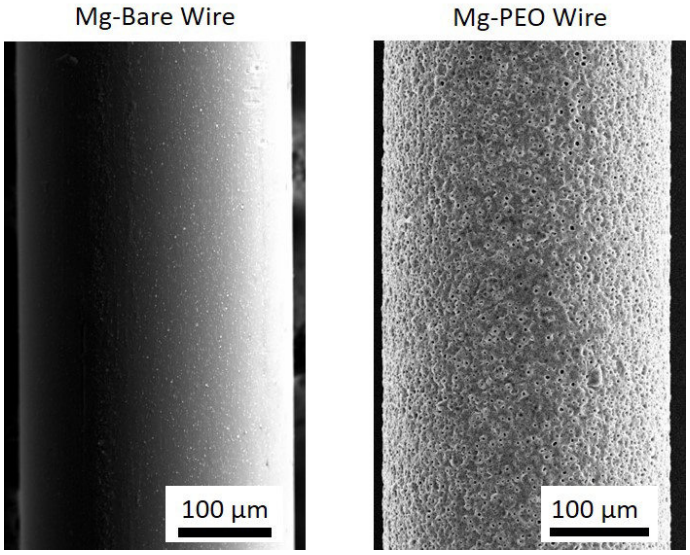

Figure 6.1: SEM images of the WE43-MEO Mg wires. (a) as-printed Mg wire. (b) Mg wire surface-modified by PEO.

6.3 Methods

6.3.1 3D printing of medical grade Mg wire-reinforced PLDL composites

A customised FFF 3D printer (3D Technology Ltd., Galway, Ireland) was used to fabricate unidirectionally reinforced coupons of PLDL+Mg and PLDL+Mg-PEO composites. A PLDL7038 filament containing 5 wt. % of PEG was manufactured using the double extrusion technique detailed in chapters 2-4. Filaments of PLDL and PEG were produced in a MC 15 microcompounder (Xplore, The Netherlands) at 220°C with a residence time of 2 minutes. They were pelletised and subjected to precision extrusion using a 3devo desktop extruder (Precision 350, 3devo B.V., The Netherlands) to fabricate a filament of 1.75 mm in diameter. The temperature profile of the heaters in the 3devo is shown in Table 6.1.

Table 6.1: Temperature distribution across the individual heaters in the 3devo precision extruder

Material	Heater 4 °C	Heater 3 °C	Heater 2 °C	Heater 1 °C
PLDL7038 + 5 wt.% PEG	190	195	200	195

The customised printer comprised of 4 individual print heads and one tool selector which would engage/disengage the 4 print heads as required (as detailed in Chapter 5 (Figure 5.1)). The tool selector controlled which material was printed and was responsible for the XY movement of the various print heads, and only one material would be printed at a time. In this way the printing of the continuous wire reinforced parts was not done via the simultaneous printing of the polymer and the wire but rather in a sequential manner.

Autodesk Inventor (Autodesk Inc., CA, USA) was used to design coupons with dimensions of 120 x 10 x 2.1 mm^3 that were saved as .stl files. An open source slicer (Prusa Slicer, Prusa Research, Prague, Czech Republic) was used to convert the 3D model data into commands that are readable by the 3D printer. Another coupon was introduced within the slicing software with dimensions 118 x 8 x 2 mm^3 to create the geometry of the path for the wire. To this end, the perimeters were deleted so that only the infill remained (an example of perimeters and infill can be seen in Figure 5.8(a) in Chapter 5).

The coupons were designed to have a Mg wire volume fraction of 15%. As indicated in Chapter 5, the number of wires per layer could be determined from the target wire volume fraction, taking the thickness of the polymer layers (0.1 mm), of the wire layers (0.4 mm), and the number of polymer layers for each wire layer (4:1) into account (Table 6.2). The infill pattern was rectilinear, which means that a 90° infill angle was used (Figure 5.8(b)). The infill density, which controls the number of times the pattern is repeated, was 40% to attain the 15% volume fraction of wires (Table 6.3). The averaged spacing between the parallel wires are detailed in Table 6.2. Finally, the layer height was modified to be 0.4 mm, and this created the geometry of the wire reinforced layers.

Finally, the coupons comprised of 4 polymer layers, followed by 1 layer of wire, and this sequence was repeated 5 times. A final layer of polymer of 0.1 mm in height was deposited at the top of the coupon, following the strategy to manufacture the coupons in Chapter 5 (Figure 5.9). The files were saved as GCODE files so that they were readable by the 3D printer.

Recalling from Chapter 5, a blade was used to cut the wire after each wire layer was completed. The distance from the point at which the blade cut the wire to the nozzle exit was 43 mm. This distance of 43 mm had to be anticipated during the 3D printing and so the same Python code used to modify the GCODE in Chapter 5 was again used here to account for this distance and cut the Mg wires with 43 mm of anticipation from the end of the projected wire path.

The printing parameters for the Mg and Mg-PEO coupons are displayed in Tables 6.2 and 6.3. It is important to note that PEG was included to process the PLDL polymer in all materials in Table 6.3 in order to improve processability, as outlined in Chapter 4.

One of the main restrictions to print the Mg wires was the minimum bending radius. Initially, the path of the Mg and Mg-PEO wires followed a rectilinear pattern (Figure 6.2 (a)), similarly to the one used for Al in Chapter 5. However, it soon became clear that the bending radius of 1 mm when the wire turned following the rectilinear pattern led to fracture of the wire. Thus, a different deposition path for the Mg wire, following a concentric pattern, was designed to avoid the fracture of the wire with each turn during printing. The skeleton for this path geometry was provided by the slicing software (Figure 6.2 (b)) but it was not continuous. So the GCODE had to be edited to make a concentric continuous path that is depicted in Figure 6.2(c). The minimum bending radius was 2 mm, large enough to deposit the Mg wires without inducing fracture. It should be noted that the volume fraction of Mg wires parallel to the coupon axis was constant in the central gauge length of 60 mm of the coupon.

The printing parameters, in terms of the temperature, speed, and babystep distance, were first optimised to deposit the Mg wires, as they were different from the parameters used in Chapter 5 for

Table 6.2: Printing parameters for manufacturing PLDL+Mg and PLDL+Mg+PEO wire-reinforced composites. The explanation of the parameters is indicated in Chapter 5 in Figures 5.9 and 5.8.

Parameters	Values
Nozzle Diameter Polymer	0.4 mm
Nozzle Diameter Wire	0.7 mm
Polymer layer height	0.1 mm
Wire layer height	0.4 mm
Line width	0.8 mm
Infill angle polymer	±45°
Infill angle wire	90°
Wire Spacing	0.9 mm

Table 6.3: Printing parameters for manufacturing PLDL+Mg and PLDL+Mg+PEO wire-reinforced composites. PEG was included in all materials to aid in processability.

Material	Printing Temperature (°C)	Print Speed (mm/s)	Fan Speed (%)	Infill Density (%)
PLDL	200	40	0	100
PLDL+15% vol. Mg wires	155	5	50	40
PLDL+15% vol. Mg-PEO wires	185	5	100	40

Al wires. The same printing parameters were required to be modified further to print the Mg-PEO wires but it was soon noticed that the Mg-PEO wire deposited with the concentric patters broke after the first turn in the first layer deposited (Figure 6.3 (a)). It was discovered that the fracture of the Mg wire was not associated with the printing parameters of the bending radius, but with wear damage induced in the soft brass by the hard PEO coating on the Mg wire at the deposition temperature. The erosion groove in the brass nozzle is clearly visible in Figure 6.3 (b). The wire was stuck in the groove and broke under tension while the print head was turning. Thus, fracture of the wire occurred in the same location at the same layer every time. New nozzles were bought to avoid this problem, but it should be noted that deposition of Mg-PEO wires continued to erode the nozzles after relatively short time.

Another issue with the deposition of the Mg-PEO wire was the high friction exerted by the wire on the polymer when deposited at 160°C. The polymer and the wire lifted from the build plate at both ends of the coupon during the printing process (Figure 6.4), very likely because of the high adhesion between the polymer and the oxide layer on the wire surface, in combination with a recoil effect of the Mg-PEO wires caused by the spooling after wire processing. This problem was overcome by increasing the printing temperature to 185°C to reduce friction between the wire and the polymer by reducing the viscosity of the latter during printing.

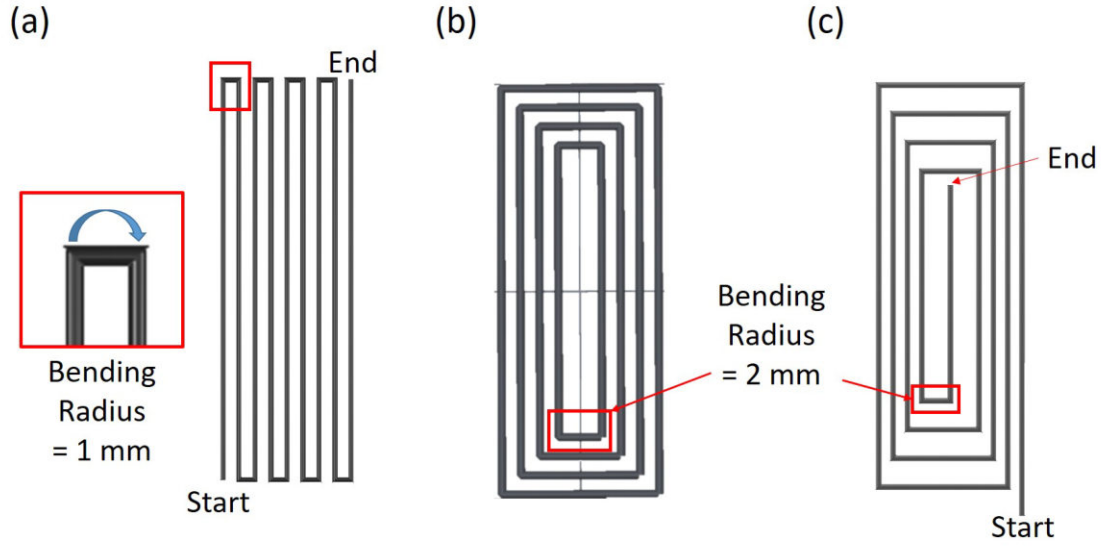

Figure 6.2: (a) Rectilinear deposition path used to deposit Al wires in Chapter 5 (b) Concentric infill geometry provided by the slicing software (c) New deposition path following a continuous concentric pattern suitable to deposit Mg wires with a minimum bending radius of 2 mm. Notice that these images are not to scale.

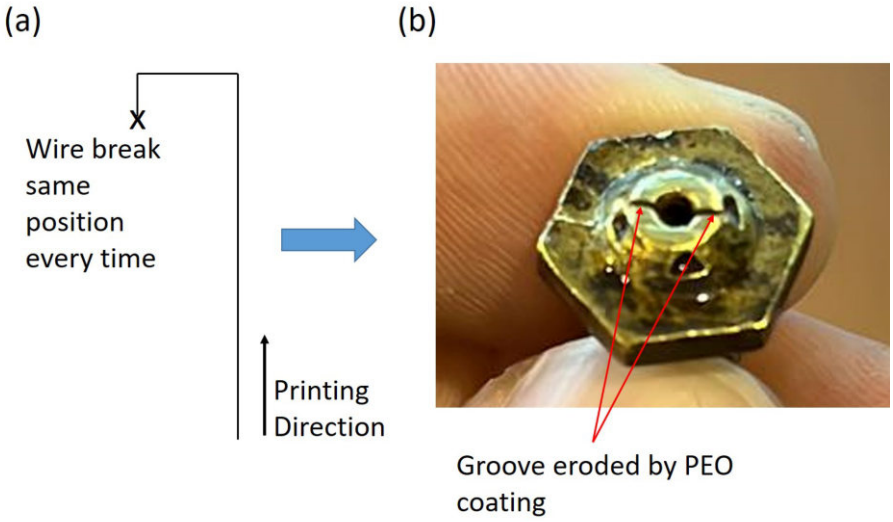

Figure 6.3: (a) Schematic diagram of the point at which the Mg-PEO wire broke during deposition using the concentric path. (b) The groove created into the brass nozzle by Mg-PEO wire is indicated by the red arrows.

Finally, a total of 20 coupons with dimensions of 120 x 10 x 2.1 mm^3 of both PLDL+ 15% vol. Mg and PLDL+15% vol. Mg-PEO were printed. Images of these coupons are depicted in Figures 6.5(a) and (b), respectively. The printing time of each tensile coupon was 45 minutes. The volume fraction of Mg wires in the coupons was limited to 15% due to processing difficulties and a lack of reproducibility at higher volumes, but this limitation should be overcome with more time to find

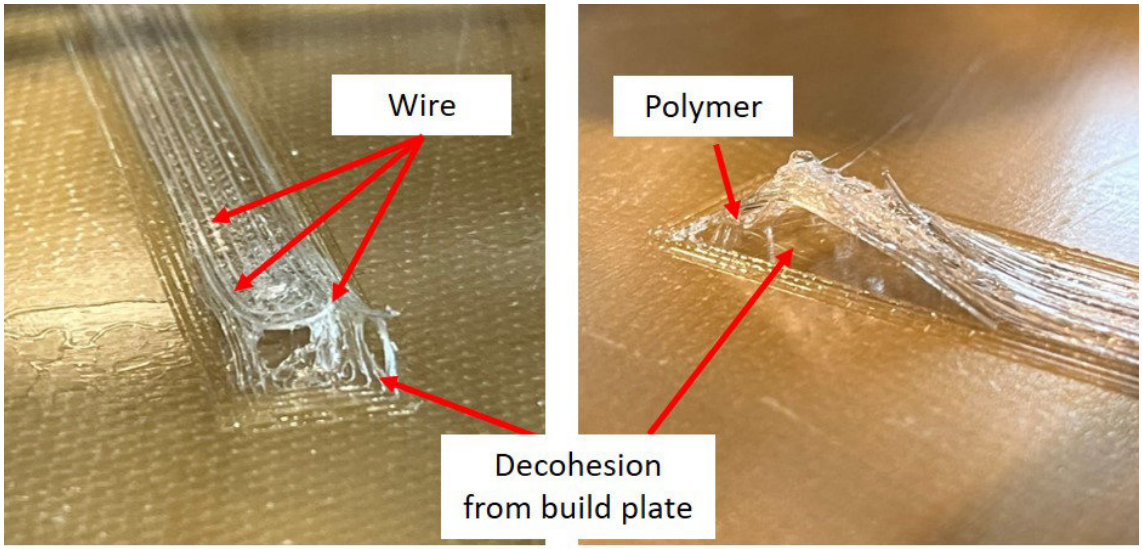

Figure 6.4: Decohesion of the ends of the printer coupon made up of Mg-PEO wire and PLDL from the build plate as a result of the residual stresses in the wire and of the high adhesion between the wire and polymer.

the accurate printing parameters.

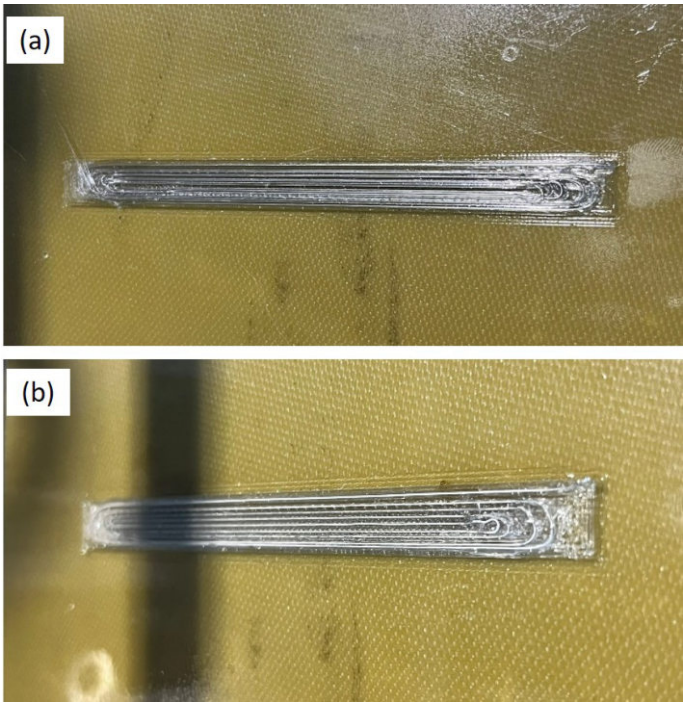

Figure 6.5: (a) 3D printed PLDL+Mg coupon. (b) 3D printed PLDL+Mg-PEO coupon.

6.3.2 *In vitro* degradation tests

In vitro degradation tests were carried out following the ISO 13781 standard as a guideline [151].

Parallelepipedic specimens 10 x 10 x 2.1 mm^3 were cut with a precision punch from the 3D printed wire reinforced coupons of PLDL+Mg and PLDL+Mg-PEO. The ends of the cut sections were coated in a waterproof vinyl spray paint to avoid pipeline corrosion in the form of diffusion along the wire/matrix interface as outlined by Ali et al. [85] and to ensure that degradation occurred through the PLDL matrix.

The samples were immersed in PBS solution (Life Technologies Europe B.V., Bleiswijk, Netherlands) at 37°C in a sealed polypropylene container. The PBS solution had a composition of 140 mM NaCl, 10 mM phosphate buffer, and 3 mM KCl per litre. The volume ratio of the PBS to the mass of the sample was greater than 30 ml/g, following the ISO 13781 standard [151]. The evolution of the mass, pH , and the hydrogen were measured as a function of time following the experimental procedures detailed in Chapters 2 and 4. In the case of the mass/pH, the samples were monitored weekly over a 3-week period. In the case of the hydrogen evolution study, measurements were taken daily. All experiments were carried out in triplicate (n=3).

6.3.3 Mechanical tests

Tensile tests

The coupons manufactured by FFF were deformed in uniaxial tension in an Instron 5966 mechanical testing machine and the applied load was measured with a 10 kN load cell. Prior to testing, the samples were prepared by placing tabs of 30 mm in length on both ends of the coupons, fixed with epoxy resin. Thus, the central gauge length was 60 mm. The specimens were deformed at a displacement rate was 2 mm/min and the average strain was measured in this region by means of DIC. To this end, the coupons were painted white, and black dots were sputtered on the white paint before testing and the position of the dots was recorded every 0.5 s with a high-resolution camera. The displacement of the dots during deformation was correlated with the Vic 2009 2-D DIC software (Correlated Solutions Inc., South Carolina, USA) to obtain the average strain of the coupon (Figure 6.6). PLDL coupons were not tested during this study as the material was already subjected to tensile testing in Chapter 4, and therefore the comparison with the mechanical properties will be using those from that chapter.

Tensile tests were carried out under three different conditions. The first group of samples was tested in air at room temperature (dry as-printed condition). The second group of samples was tested under the as-printed condition in a water bath at 37°C. The experimental setup for the immersed test is the one described in chapter 2 and 4. The samples were left immersed in the water bath for $\approx$ 1 minute before the test commenced.

In the case of the dry as-printed condition, the theoretical elastic modulus of the composite along the wires, E_t, was calculated according to Equation 6.1, following the rule of mixtures,

$$E_t = fE_f + (1 - f)E_m \tag{6.1}$$

where E_f and E_m stand for elastic modulus of the Mg wires and PLDL matrix, respectively and the wire volume fraction is f.

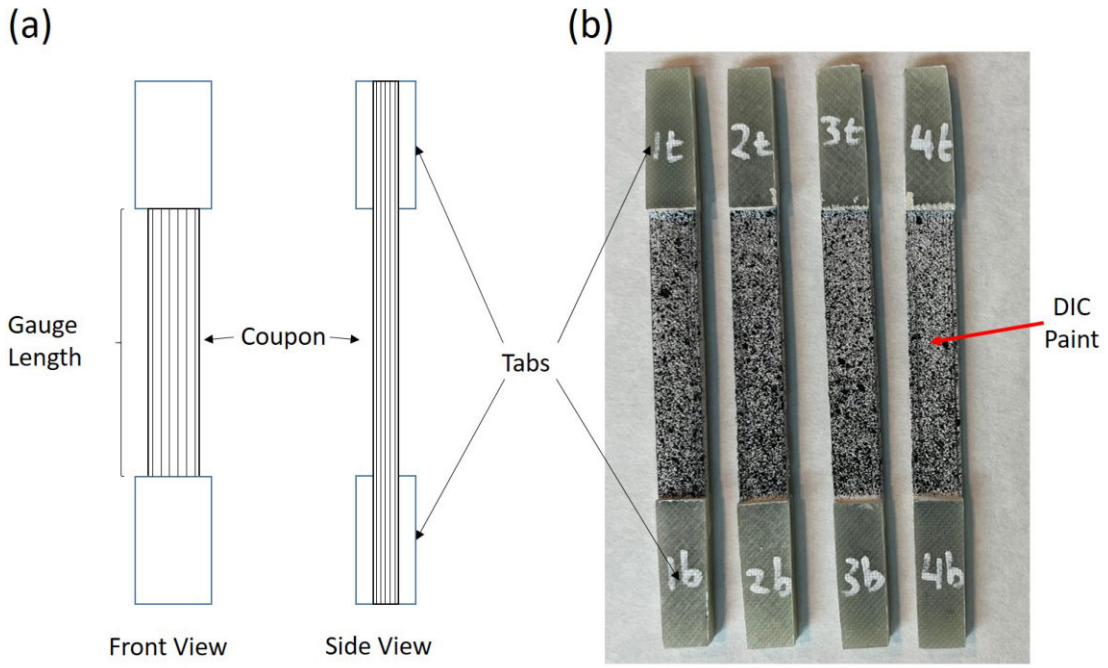

Figure 6.6: (a) Schematic of the Mg wire-reinforced coupons prepared for tensile testing. (b) PLDL+Mg coupons with tabs fixed at the ends and the black/white paint applied. Note the numbers on the tabs correspond to the coupon number and 't' means top while 'b' means bottom. The letters were placed to keep track of the geometry of the coupon after the fracture took place.

Finally, the third group of samples was tested in a water bath at 37°C after three weeks of degradation in PBS at 37°C, following the procedure indicated for the degradation tests in the previous section. Once the degradation period was finished, the coupons were stored in an oven at 37°C for a period of 3 weeks. The black and white speckle pattern for DIC was applied before the tests. At least 3 specimens of each group were tested (n=3).

Wire push-out tests

Wire push-out tests were carried out to evaluate the interfacial shear strength between the PLDL matrix and the Mg wires (without and with PEO surface modification), following previous investigations [86, 142, 143]. To this end, samples with the same dimensions as those for the degradation tests (10 x 10 x 2.1 mm^3) were cut from tensile coupons perpendicular to the wires and subsequently embedded in an epoxy resin (SpeciFix resin system, Struers, Denmark). The samples were then ground using a manual grinding machine (Vector-Metaserv 250, Buehler, IL, USA) with SiC paper ranging from P320 to P2500 up to a thickness of 0.6 ± 0.03 mm, because the thickness of the sample should be approximately twice the diameter of the wires. Samples were then polished with a diamond paste of 3 and 1 μm grain size (ATM Qness GmbH, Mammelzen, Germany) using MD-Nap polishing plates (Struers, Denmark).

Samples of the same dimensions (10 x 10 x 2.1 mm^3) were cut from coupons and both ends of the samples were coated with black vinyl paint, impermeable to water to cover the exposed ends of the wires and ensure that degradation occurred through the PLDL, as opposed to pipeline

corrosion as outlined by Ali et al. [86]. The samples were then placed in PBS at 37°C for a period of 3 weeks. Afterwards, they were removed from the solution, dried, and thin slices for the push-out tests were prepared following the sample preparation method indicated above.

The thin slices of the composite were mounted on a stainless steel support with a groove of 500 μm in width to perform the wire push-out test (Figure 6.7). The wire to be tested was positioned manually at the center of groove with the help of an optical microscope and the slice was fixed with a tape. The support was attached to a stage capable of moving in X and Y directions to position the indenter punch over the desired wire. An indenter with a stainless steel flat tip of $\approx$ 250 μm in diameter was mounted on an Instron 5966 mechanical testing machine with a 100 N load cell. The compressive load was applied on the wire under displacement control at 20 μm/min until the wires were pushed-out from the matrix, which was indicated by a significant drop in load. At least 3 wires were pushed out for each condition (n=3).

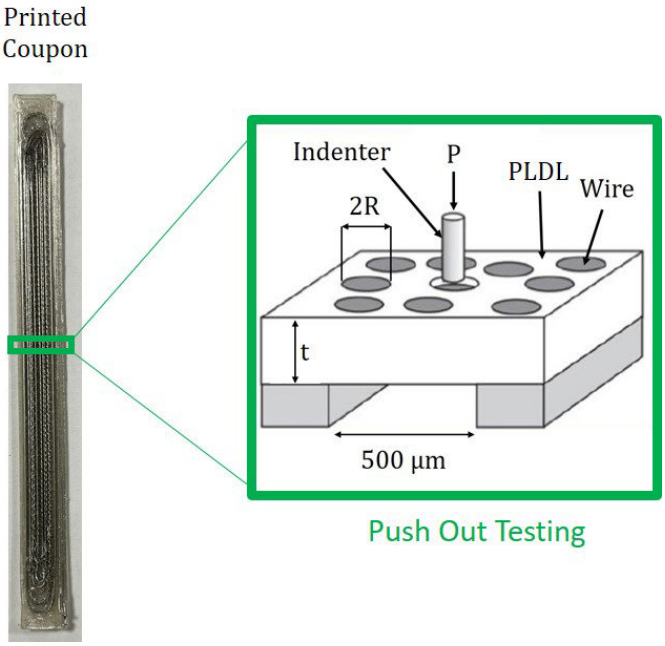

Figure 6.7: Diagram of the wire push-out experimental set up. First, the sample is cut from the coupon and then ground down to a thickness t, twice the diameter of the wire, and a force P is applied perpendicular to the wire until a push-out is achieved.

The shear strength of the PLDL+Mg and PLDL+Mg-PEO interfaces, τ, were calculated as

$$\tau = \frac{P_{max}}{2\pi R t} \tag{6.2}$$

where P_{max} is the maximum load, R is the radius of the wire, and t is the thickness of the slice.

6.3.4 Microstructural Characterisation

The microstructure of the printed coupons was analysed by X-ray tomography. Samples of 10 x 10 x 2.1 mm^3 were cut from the central section of the coupons and characterised by X-ray computed micro-tomography. A Phoenix Nanotom 160 NF tomograph (General Electric, MA, USA) was

used with a W target with a Cu filter and 0-mode nanofocus at 120 kV. The current was 80 μA and the voxel size was 5.4 μm. Subsequently, porosity was calculated using the Fiji (ImageJ, NIH, Maryland, USA) programme. A reference area of 3 x 2 mm^2 in the central region of the sample was isolated. This region was selected to exclude other regions where it was more difficult for the computer programme to distinguish air voids from bulk material. A threshold was used to separate the bulk (polymer and wires) from the air voids in $\approx$ 1500 slices of the composite, and the average area fraction of voids was assumed to be the porosity.

The fracture surfaces of the samples tested in tension as well as of those subjected to the wire push-out test were analysed in the SEM. They were gold sputtered for 60 seconds with a sputtering current of 40 mA (Quorum Q150T ES, Quorum Technologies Ltd., East Sussex, England) to ensure electrical conductivity and studied in an Apreo 2S LoVac (Thermo Scientific, MA, USA) SEM using secondary electrons at a voltage of 5 kV and with currents in the range 40 to 80 pA.

Cross sections of degraded coupons in PBS after a period of 3 weeks were also analysed in the SEM using secondary electron as well as energy dispersive X-ray spectroscopy (EDS) to ascertain the degradation mechanisms. In particular, the wire/polymer interfaces were analysed to understand the formation of corrosion products during degradation in PBS.

In the case of the area loss studies carried out to analyse the degradation of the wires the SZX10 and BX51 optical microscopes (Olympus Corp., Tokyo, Japan) were used to monitor the cross sections of the composite materials. In the case of the multi-material composite material the same microscopes were used to analyse the cross-section of the coupon.

6.4 Results and Discussion

6.4.1 Microstructure of PLDL+Mg and PLDL+Mg-PEO composites

The microstructure of the PLDL+Mg and PLDL+Mg-PEO composites were analysed by means of X-ray tomography. 2D tomograms of sections of the PLDL+Mg and PLDL+Mg-PEO composites are shown in Figure 6.8. Mg wires are white, PLDL polymer grey and the porosity (indicated by red arrows is black. The vertical alignment of the Mg wires was reasonable but not perfect, as opposed to the composite with Al wires seen in Figure 5.13 in Chapter 5. The worse alignment of the Mg wires was associated to the higher bending stiffness because the yield strength of the Al wire was approximately 65 MPa while that of the Mg wires reached approximately 250 MPa [251]. Additionally, the ductility of the Al wires (25%) was approximately 3 times higher than that of the Mg wires (8%). Hence, the Mg wires recoiled much more than the Al wires during deposition, leading to worse alignment of the wires.

The porosity measured in the PLDL+Mg composite (Figure 6.8 (a)) was 2%, much lower than the 4.1% determined in the PLDL+Mg-PEO composite. The porosity in both materials was lower than the one reported in the PLA/Al composites with the same wire volume fraction (7.4%). The higher porosity observed in the PLDL+Mg-PEO material is very likely due to the increased adhesion between the PEO coating and the PLDL matrix, in comparison to Mg wires without PEO surface treatment coating. Although it appears to be counter-intuitive, the increased friction between the oxide coating and the PLDL matrix tore/pulled the polymer matrix during deposition leading to an increased porosity.

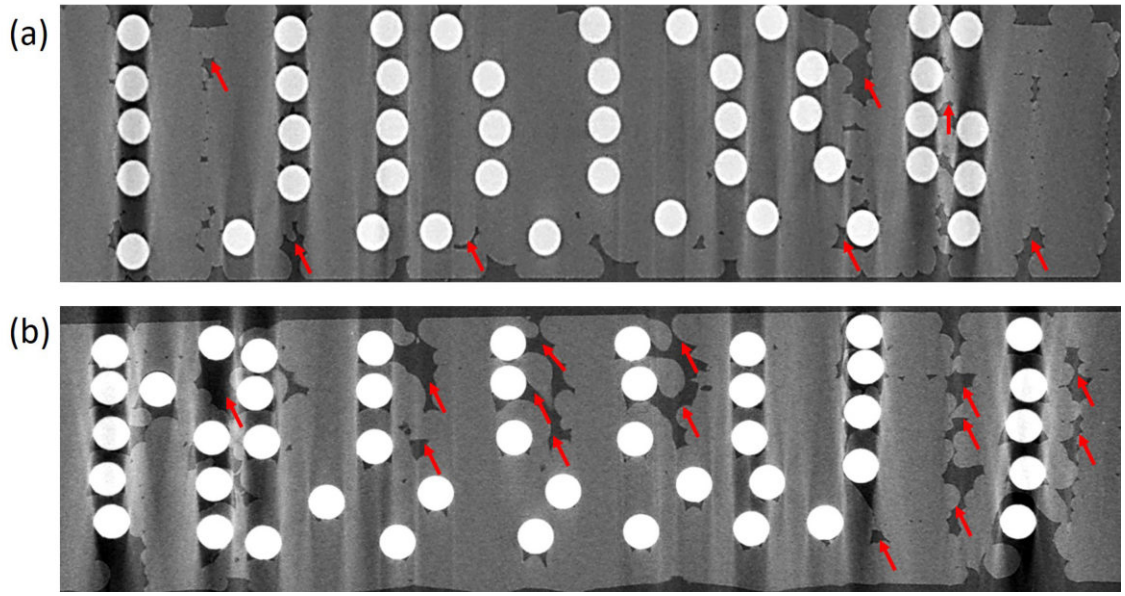

Figure 6.8: (a) X-ray tomography section of the PLDL+Mg composite perpendicular to the wires. (b) X-ray tomography section of the PLDL+Mg-PEO composite perpendicular to the wires. The Mg wires appear as white circles in both samples, while the PLDL is grey. The dark grey/black regions correspond to the porosity within the samples. They are indicated by red arrows in both (a) and (b). The oxide coating on the Mg wires is too thin to appear in the tomograms of (b).

In the case of the PLDL+Mg coupon there is no clear pattern to the porosity and its location within the coupon. However, the porosity in the PLDL+Mg-PEO composite appears to be concentrated towards the top of the coupon. A very similar behaviour was noticed in the case of the PLA/Al coupons in Chapter 5, and it is likely a result of decreased compression forces being exerted in the upper layers of the coupon compared to the lower part. The decreased compression forces at the top were due to the babystep distance which in general deposits the new layer of wire 30 microns into the depth of the previous polymer layer. However, the babystep distance was relaxed in the upper layers to prevent nozzle blockages. This in turn led to a higher concentration of porosity to be observed at the top of the coupon in comparison with the bottom region.

Furthermore, there are indications of some porosity at the interface between the polymer and Mg-PEO wires. Nevertheless, their contribution to the overall porosity of the coupon is negligible. The porosity at the interface between the Mg-PEO wire and the PLDL is likely attributed to variations in babystep distances during the process, in addition to the high adhesion between the PEO coating and the polymer resulting in the polymer being pulled/torn during the printing process.

6.4.2 *In vitro* degradation of PLDL+Mg and PLDL+Mg-PEO composites

The evolution of the mass of the composites and of the pH of the solution are plotted in Figure 6.9(a) and (b), respectively, during 3 weeks of immersion in PBS at 37°. The mass increases rapidly in both composites during the first week because of the water adsorption through the PLDL but the mass gain rate in slows down afterwards following the typical behaviour observed in

diffusion-controlled processes. The mass increase in the composite reinforced with Mg-PEO wires is slightly higher than that measured in PLDL+Mg and this difference can be attributed to the higher porosity in the former, which facilitates water diffusion throughout the bulk.

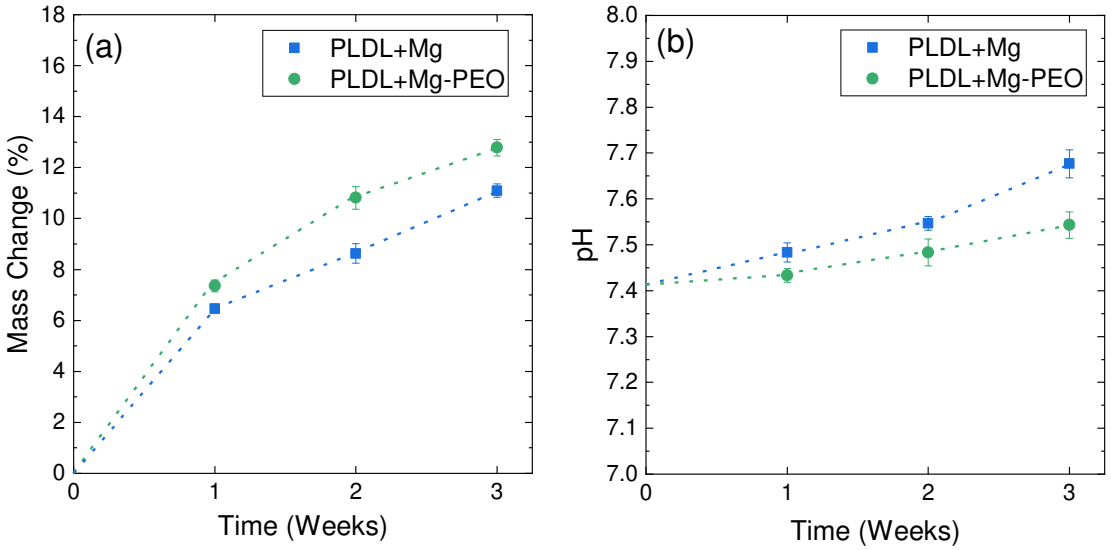

Figure 6.9: (a) Mass change in the composites as a function of immersion time in PBS at 37°C. (b) *Idem* for pH in the solution.

With respect to the pH in the solution, a slight increase is observed with immersion time for both composites, indicating that the degradation of Mg is dominant with respect to the formation of acidic products associated with the degradation of PLDL. Obviously, the increase in the pH of the solution is higher in the PLDL+Mg composite because the oxide layer reduced the corrosion rate in the Mg wires in the case of the PLDL+Mg-PEO composite [86]. However, it should be noted that the variation in pH during the first weeks is very limited in both cases and this behaviour favours biocompatibility [252, 253].

The actual corrosion rate of the Mg wires within the PLDL matrix could be assessed in both composites through the hydrogen evolution tests. The amount of hydrogen released (divided from the nominal wire surface area, which is obtained from the wire volume fraction and the wire diameter in the sample) is plotted in Figure 6.10 (a) for both composites. The hydrogen release rate increases linearly with time in both cases but the rate in the PLDL+Mg composite is 5 times faster than in the PLDL+Mg-PEO composite, showing the effect of the oxide layer on the corrosion rate of Mg.

The hydrogen released divided for the area of the Mg wires in similar composites manufactured by compression moulding in [86] is also plotted in Figure 6.10 (a). The compression moulded composites released less hydrogen than those processed by FFF in the case of the PLDL+Mg. This behaviour is very likely triggered by the porosity in the latter coupons, which facilitates the ingress of water, while the coupons processed by compression moulding were fully dense. The differences between both composites in the case of the PLDL+Mg-PEO materials were, however, negligible, indicating that oxide layer introduced by PEO is very effective protecting the Mg wires

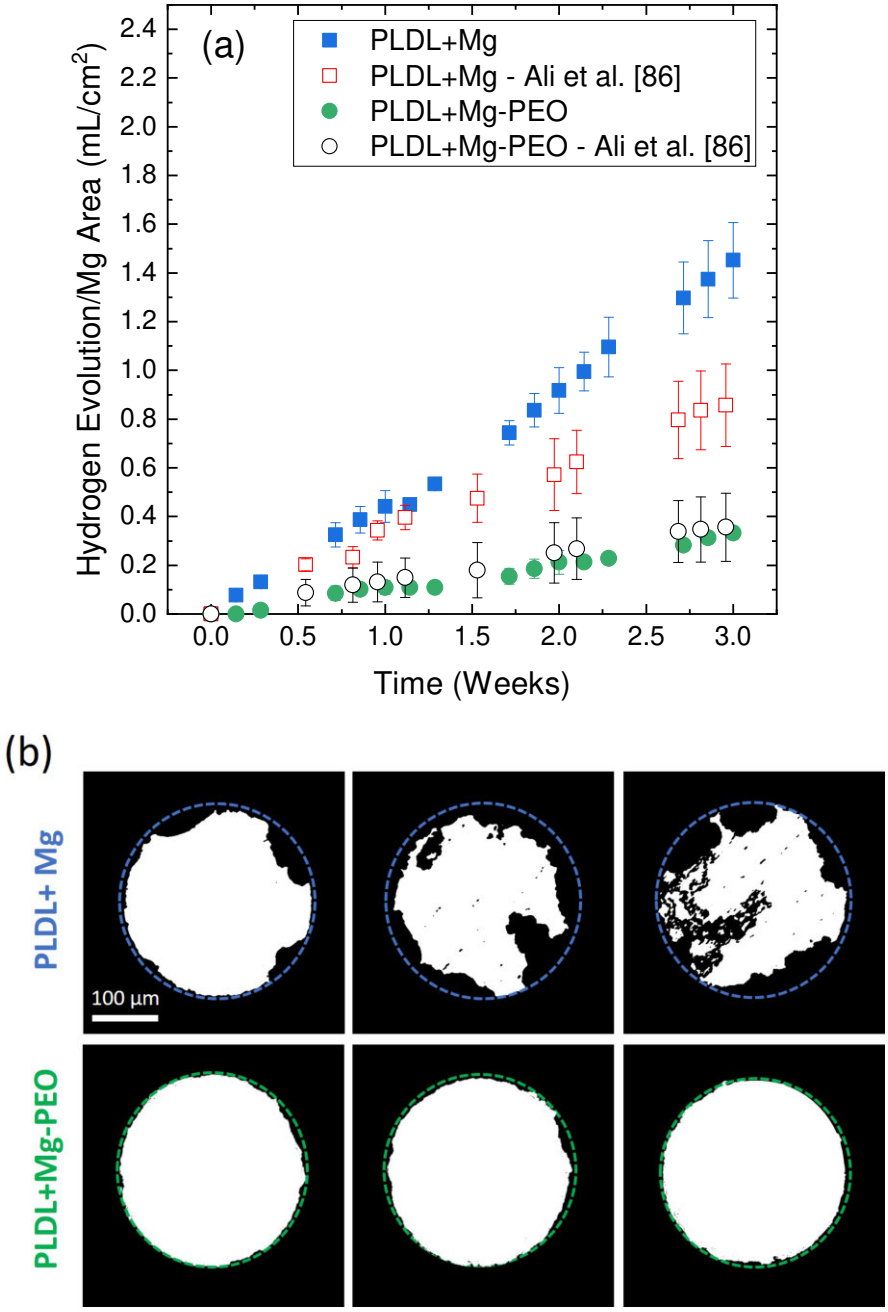

Figure 6.10: (a) Volume of hydrogen released (normalised with respect to the nominal surface area of the Mg wires) as a function of immersion time in PBS at 37°C for both composite materials. The results from Ali *et al.* [86] are also plotted for comparision. (b) Optical micrographs of the cross-section of the Mg wires in PLDL+Mg and PLDL+Mg-PEO composites after 3 weeks of immersion. The dashed-circles in blue and green show the original cross-section of the wire before degradation.

within the PLDL from corrosion.

The effect of the oxide layer on the corrosion of the Mg wires within the PLDL matrix is clearly

shown in the optical images of the cross-section of the Mg wires after 3 weeks of immersion in PBS at 37°C (Figure 6.10 (b)). The bare Mg wires show a large reduction in the cross-section, which is also associated with pitting corrosion. Pitting corrosion dramatically reduces the cross section of the wire in particular locations along the wire, and thus the strength of the wire [80, 86]. In contrast, the presence of the oxide layer not only reduced the corrosion rate but also inhibited pitting, leading to a uniform corrosion of the Mg wire that limits the reduction of mechanical properties with immersion time.

The cross-sections of 3 different wires from both of the composites were used to study the reduction in area of the wires due to corrosion. Average area reductions after 3 weeks in PBS were 29% and 6.9% for the PLDL+Mg and PLDL+Mg-PEO composites, respectively. This area loss can be directly related to the mass loss and hydrogen evolution if one atom of Mg is assumed to release one molecule of hydrogen upon degradation. The estimates for hydrogen release using the area/mass loss images from Figure 6.10 (b) are in good agreement with the actual hydrogen evolution results. From the hydrogen evolution, graph as stated previously the PLDL+Mg material was responsible for the emission of 5 times more hydrogen than the PLDL+Mg-PEO material, which is a similar ratio to that of the area loss study (4 times faster). This discrepancy is consistent with previous reports [204, 205] and has been attributed to oxygen reduction reactions that are likely to occur during slow corrosion of Mg [206, 207, 254] or that hydrogen bubbles were trapped below the sample or in the funnel, or that air bubbles entered the system giving a higher value of hydrogen [204].

Previous investigations [80] have concluded that the reduced degradation rate of the PEO surface-modified wires is associated with the appearance of an external protective and dense corrosion layer containing O, Ca and P. This dense layer is located beneath the PEO but on top of the typical porous oxide layer resulting from the progressive oxidation of Mg to form $Mg(OH)_2$, which is found between the external Ca-P dense layer and the Mg core of the wire. Even though the diffusion process is not fully inhibited, the presence of this dense Ca-P layers seems to slow down migration of Cl^- and other corrosive ions which in turn decreases the elimination of the $Mg(OH)_2$ layer. As a result, the corrosion rate of the Mg wire is reduced, and pitting corrosion is suppressed.

In vitro interface degradation in PLDL+Mg and PLDL+Mg-PEO composites

The wire/matrix interface is a critical element from the point of view of the mechanical behaviour of the composite, and thus, the local corrosion mechanisms at the interface were analysed in detail in the SEM. The Mg wires are fully embedded in the PLDL matrix in the as-printed condition (Figure 6.11(a)) and no porosity is found around the interface.

Nevertheless, high magnification images show a small gap (indicated with a red arrow) between the matrix and the wire. It is worth noting that this gap was not found in the PLDL+Mg composites manufactured by compression moulding [86] very likely because the higher pressure exerted facilitated the intimate contact between wire and matrix. However, this is not the case during matrix extrusion in FFF and, thus, it is not possible to obtain a perfect adhesion between the matrix and wires. Moreover, this lack of pressure can also lead to the formation of pores around the wires, as shown in Figure 6.8. Further analysis by EDS in order showed the presence of Mg in the wire and O in the PLDL, with a clean interface between them.

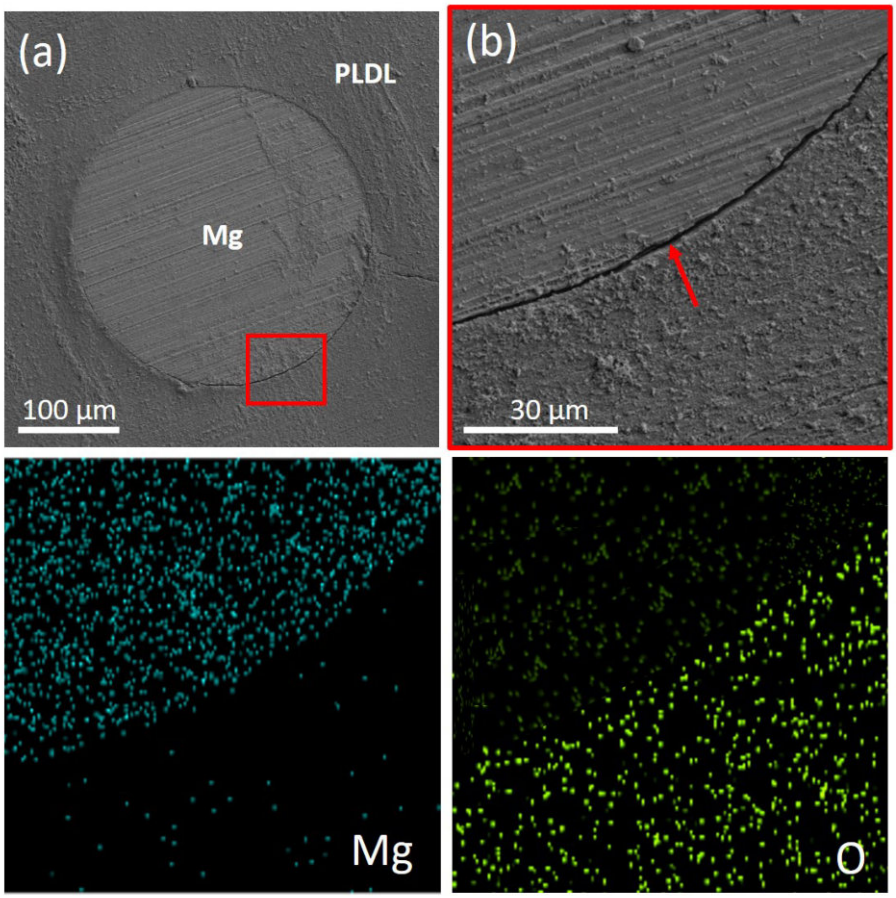

Figure 6.11: (a) Low magnification and (b) high magnification SEM images of the wire/matrix interface in as-printed PLDL+Mg composite. The small gap at the interface between the matrix and wire is indicated with a red arrow. The images at the bottom show the distribution of Mg (in the wire) and of O (in the PLDL) in (b) obtained by energy dispersive X-ray spectroscopy.

The morphology of the wire/polymer interface after 3 weeks of immersion in PBS at 37°C is depicted in Figure 6.12. An oxide layer has formed on the outside of the wire, while there is also a large void around the whole wire, as it shows a receding of the PLDL matrix from the Mg wire (Figure 6.12 (a)). It is also very possible that the void around the wire is more likely a combination of the receding of PLDL from around the wire and the removal of the $Mg(OH)_2$ corrosion products that filled the gap during the sample preparation process, as indicated by Ali et al. [86]. This is confirmed in Figure 6.13, where it is clear to see that the oxide layer (given by the EDS analysis) is much thicker ($\approx$30 μm) than that observed in Figure 6.12.

As previously discussed in this thesis, the degradation of PLDL (a type of PLA) takes place via hydrolysis through the cleavage of ester bonds. This process is accelerated in the alkaline environment created by the oxidation of the Mg wires and PLDL degrades much faster at the interface, as noted by Vaid et al. [215]. Additionally, it should be noted that the local pH at the PLDL+Mg interface can be significantly higher (around 10) than the one in the bulk of the solution that only reached of $\approx$7.7 after 3 weeks [255].

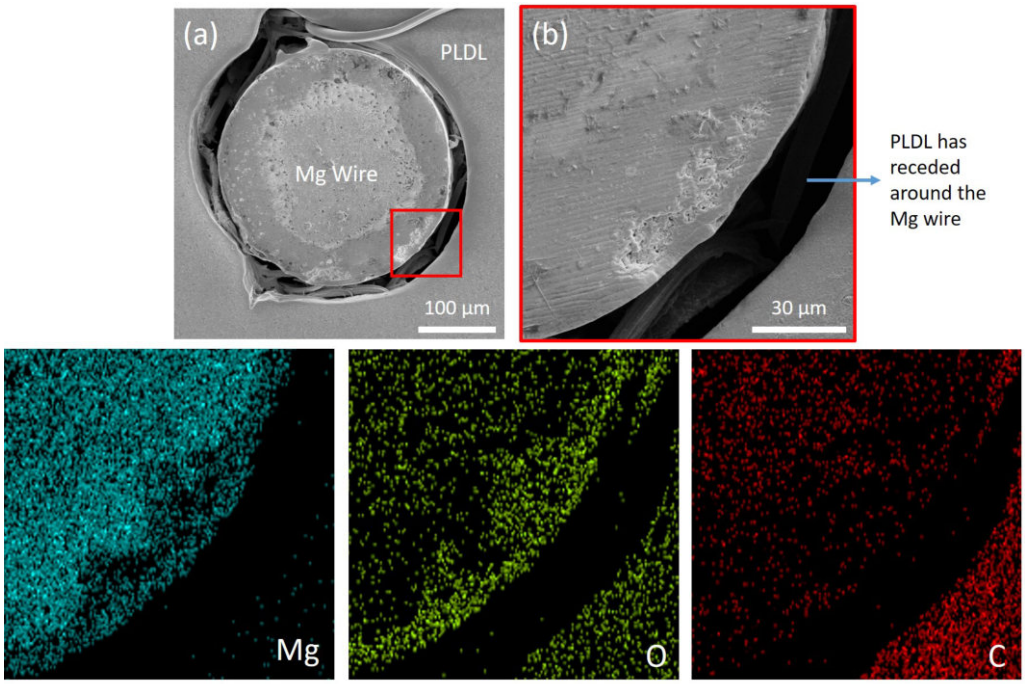

Figure 6.12: (a) Low magnification and (b) high magnification SEM images of the wire/matrix interface in PLDL+Mg composite after 3 weeks of immersion in PBS at 37°C. The images at the bottom show the distribution of Mg, O and C in (b) obtained by energy dispersive X-ray spectroscopy.

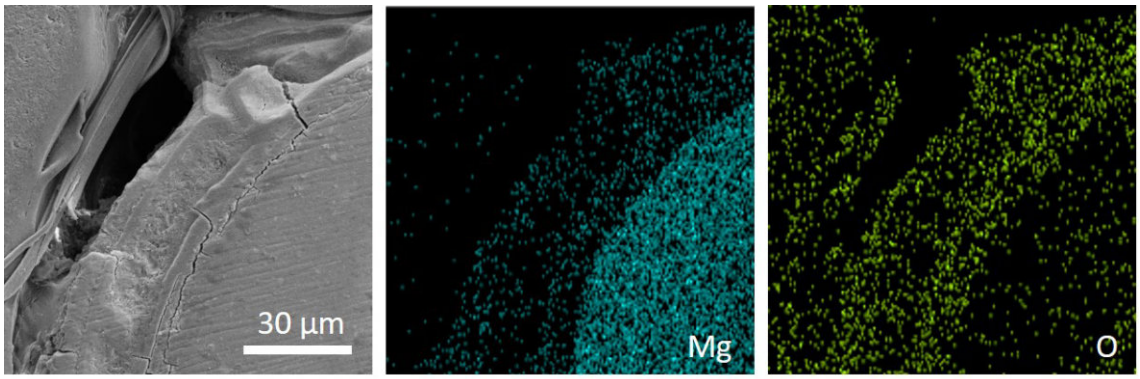

Figure 6.13: SEM image of the oxide layer around the Mg wire after 3 weeks of immersion in PBS at 37°C. The corresponding Mg and O distribution maps obtained by energy dispersive X-ray spectroscopy are also included.

The PLDL+Mg-PEO composite in the as-printed condition is shown in Figures 6.14 (a) and (b). The oxide layer of a few μm in thickness is clearly indicated with the green arrows (b) and its presence is also revealed by the presence of P and O in the composition maps obtained by EDS. Red arrows in (a) indicate porosity regions introduced during the 3D printing process, which was confirmed also by X-ray tomography analysis (Figure 6.8). The interfacial region after 3 weeks of immersion in PBS at 37°C is depicted in Figure 6.15. As indicated previously, the oxide layer

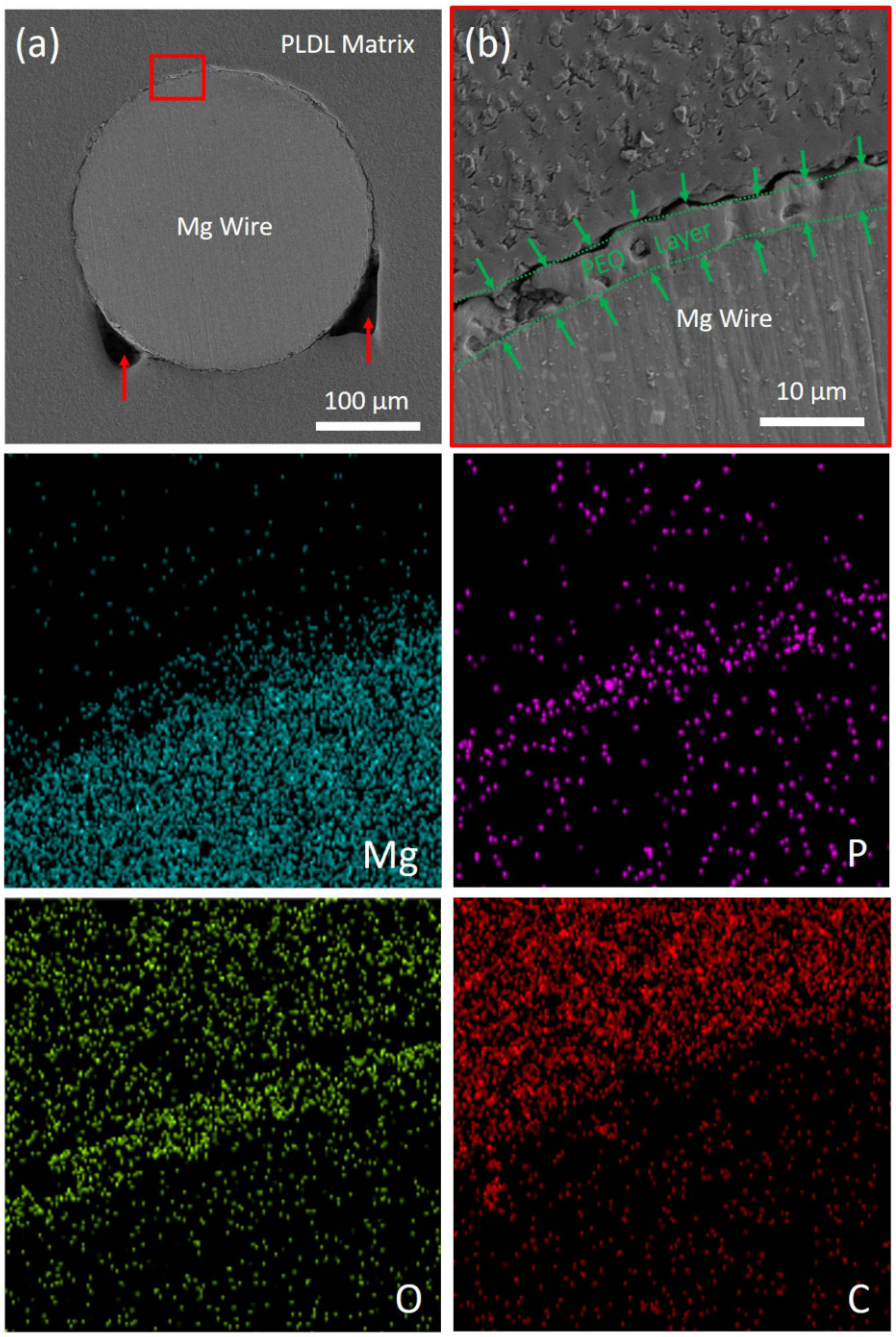

Figure 6.14: (a) Low magnification and (b) high magnification SEM images of the wire/matrix interface in the as-printed PLDL+Mg-PEO composite. The images at the bottom show the distribution of P, Mg, O and C in (b) obtained by energy dispersive X-ray spectroscopy. The PEO coating has been highlighted with green arrows in (b) and its presence is confirmed by the elemental mapping showing the presence of P and O.

formed during PEO (that is characterised by the presence of P and O) has protected the Mg wire from pitting corrosion. Moreover, recession of the PLDL matrix is not observed around the oxide layer (Figure 6.15(b)), indicating that it has hindered the oxidation of Mg and the acceleration

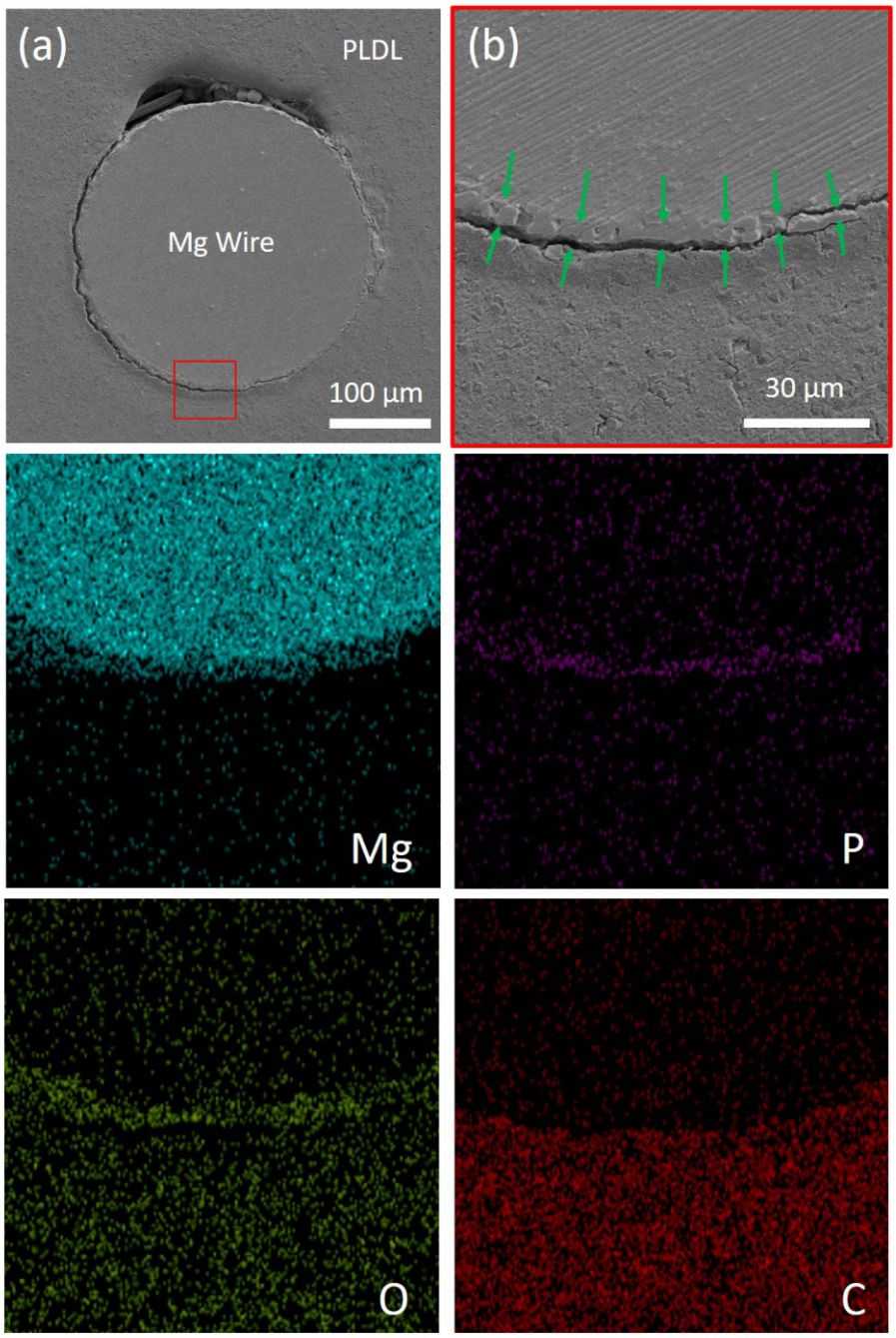

Figure 6.15: (a) Low magnification and (b) high magnification SEM images of the PLDL+Mg-PEO interface after degradation for a period of 3 weeks in PBS at 37°C. The images at the bottom show the distribution of P, Mg, O and C in (b) obtained by energy dispersive X-ray spectroscopy. The presence of Mg identifies the wire, while the combination of O and C stands for the PLDL matrix. P can be found in the oxide layer.

of the PLDL degradation by the combined effect of alkaline pH and $Mg(OH)_2$. The large voids around the interface in the PLDL+Mg-PEO composite ((Figure 6.15(a), indicated with red arrows,

should not be attributed to the recession of the PLDL during degradation but they were introduced during the printing process, as confirmed by the X-ray tomography sections in Figure 6.8, where pores with very similar geometries to those seen in (a) can be seen.

Finally, it should be mentioned that the degradation rate in PBS of the PLDL+Mg and PLDL+Mg-PEO composites manufactured by FFF is much faster than that reported in the same composites manufactured by compression moulding [86, 251]. These differences may be attributed to the higher porosity of the former because very limited pressure was applied to consolidate the composite during FFF, as compared with compression moulded materials.

6.4.3 Interface strength of PLDL+Mg and PLDL+Mg-PEO composites

The load-displacement curves of the wire push-out tests carried out in the as-printed and degraded conditions are plotted in Figure 6.16 (a) and (b), respectively, for PLDL+Mg and PLDL+Mg-PEO composites. After an initial accommodation zone, all curves exhibit a linear region with constant slope, which corresponds to the elastic deformation of the wire within the composite, until a peak load is reached. Wire push-out begins at this maximum load, which is used to calculate the interface strength according to eq. 6.2. Afterwards, the load decreases as the wire is pushed out from the matrix.

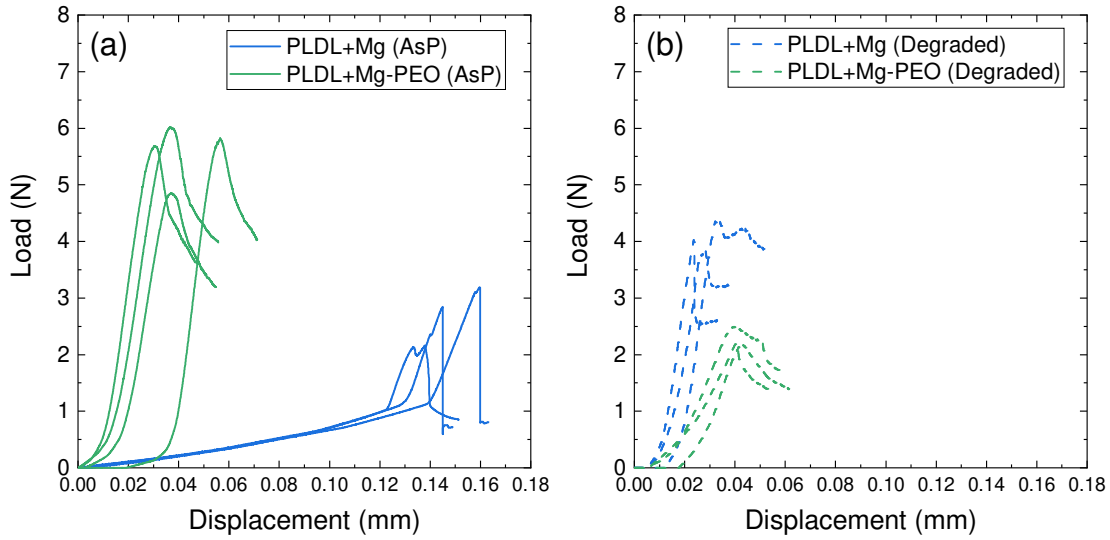

Figure 6.16: Load *vs.* displacement curves of the wire push-out tests. (a) PLDL+Mg composites in the as-printed and degraded condition. (b) PLDL+Mg-PEO composites in the as-printed and degraded condition.

The load-displacement curves of the as-printed PLDL+Mg composite in Figure 6.16 (a) shows a very large accommodation region, which is attributed to the bending of the composite plate, before the elastic deformation of the wire. This large displacement before elastic deformation of the wire is likely due to bending of the specimen during the sample preparation step. This bending then causes an imperfect contact with the stage and so the initial displacement and loading observed in the curves, actually corresponds to the specimen being straightened by the indenter to achieve perfect contact with the stage. After this initial zone is ended, the actual wire push-out test begins.

Table 6.4: Interface strength shear of the PLDL+Mg and PLDL+Mg-PEO composites in the as-printed (AsP) and degraded conditions.

Material	Shear Strength, τ (MPa)
PLDL+Mg (AsP)	4.8±0.7
PLDL+Mg-PEO (AsP)	10±1
PLDL+Mg (Degraded)	7.2±0.5
PLDL+Mg-PEO (Degraded)	4.1±0.3

This is a specimen dependent phenomenon which is why the same behaviour was not observed in the other samples.

Afterwards, the elastic regions for both the PLDL+Mg and PLDL+Mg-PEO show similar slopes, indicating an adequate load transfer from the wire to the matrix, but there are large differences in the the maximum load and, thus, in the interface strength, that improves from 4.8±0.7 MPa to 10±1 MPa as a result of the presence of the oxide layer. The strengthening effect of the oxide layer at the interface was also reported by Ali et al. [86] in the same composites manufactured by compression moulding, although the interfaces strengths were higher (10.9 ± 1.6 MPa and 26.3 ± 1.3 MPa for the PLDL+Mg and PLDL+Mg-PEO) because of better consolidation of the composite obtained by compression moulding. The SEM images of the pushed-wires of both composites in the as-printed condition are shown in Figure 6.17. The Mg wire pushed-out from the PLDL matrix is clean from PLDL, as a result of the limited adhesion between them (Figure 6.17 (a) and (b)). Interface fracture in the case of the PLDL+Mg-PEO composite took place between the PLDL and the oxide layer (Figure 6.17 (c) and (d)). The higher interface shear strength can be attributed to the penetration of PLA into the pores of the oxide layer, providing a mechanical interlock effect, indicated by the red arrows in Figure 6.17 (d).

The load-displacement curves of the composites degraded *in vitro* for a period of 3 weeks are plotted in Figure 6.16 (b). Interestingly, the interfacial shear strength of the PLDL+Mg composite increases with degradation while that of the PLDL+Mg-PEO decreases. As a result, the interface strength of the PLDL+Mg composite after degradation reaches 7.2 ± 0.5 MPa while the one of the PLDL+Mg-PEO decreases to 4.1 ± 0.3 MPa. In the case of the same composites manufactured by compression moulding, immersion in PBS led to a marked reduction of the interface strength in the PLDL+Mg-PEO composite while it increased slightly at short degradation times and then also decreased slightly in the case of PLDL+Mg [86]. The SEM images of the wires pushed-out from the PLDL matrix in both composite materials in the degraded condition are shown in Figure 6.18. Pitting corrosion is clearly observed in the Mg wire of the PLDL+Mg composite (Figure 6.18 (a) and (b)). The recession of the PLDL matrix (which should reduce the interface strength) is balanced by the wedge effect of the corrosion products associated with pitting corrosion, leading to a slight increase in the interface shear strength with degradation. In the case of the degraded PLDL+Mg-PEO composite, the PEO layer is still intact after the wire push-out test (Figure 6.18 (c) and (d)). However, corrosion reduced the interlocking effect between the PLDL and the oxide layer and the lack of corrosion products between them led to a reduction of the interface shear

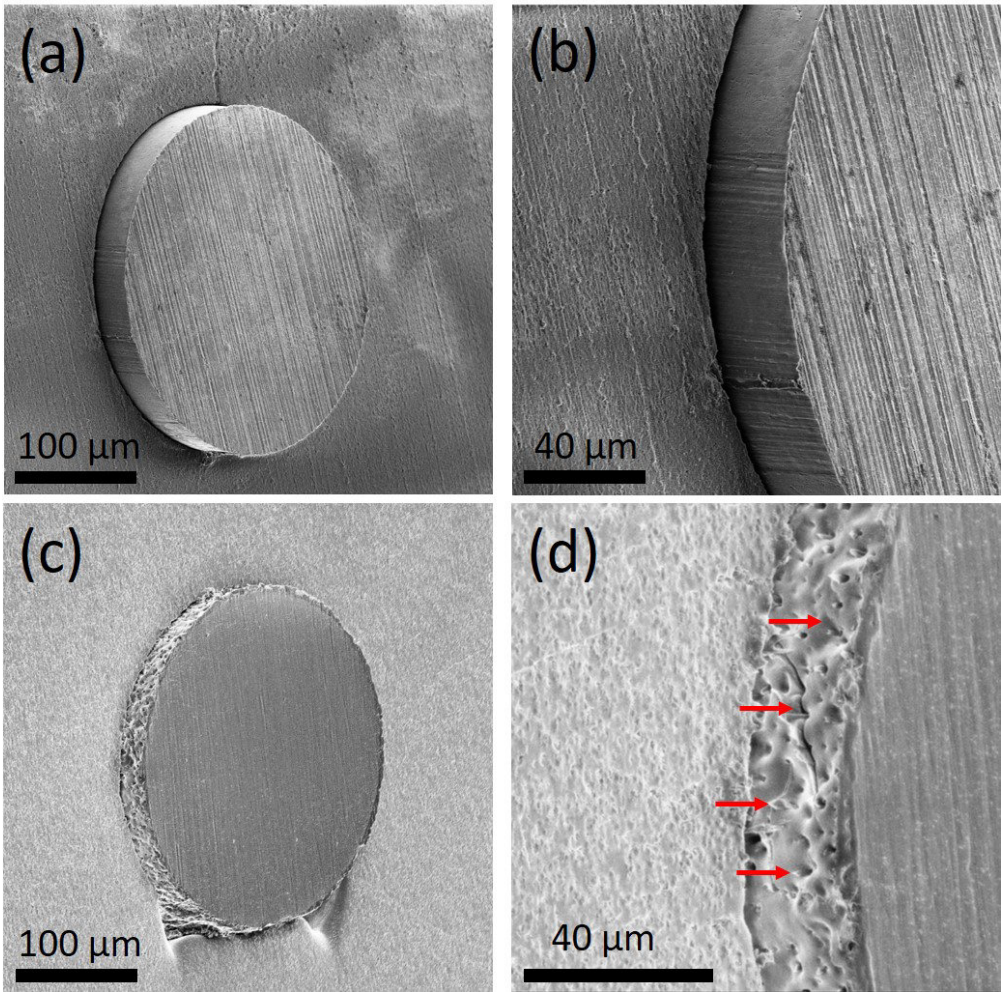

Figure 6.17: SEM images of the wire push-out test of both composite materials in the as-printed condition. (a-b) PLDL+Mg and (c-d) PLDL+Mg-PEO.

strength with degradation.

6.4.4 Tensile properties of PLDL, Mg and Mg-PEO wires

The tensile mechanical properties of the PLDL, Mg and Mg wires surface-modified by PEO are depicted in Table 6.5. The mechanical properties are taken from Chapter 4 [232], while the mechanical properties of the wires are taken from Ali et al. [251].

The properties of the PLDL were very similar to those reported for PLA in the literature, but the strain-to-failure (3.7%) is greater than that reported for PLA (in the range of 1.5-2% [256]). This difference can be attributed to the plasticiser effect induced by the addition of PEG, which is known to increase chain mobility and improve PLA ductility [257].

The properties of the Mg and Mg-PEO wires are extremely similar, and PEO surface modification induces only a small reduction in strength and ductility. The tensile strength is on the order of 300 MPa and the strain-to-failure around 8% for both wires.

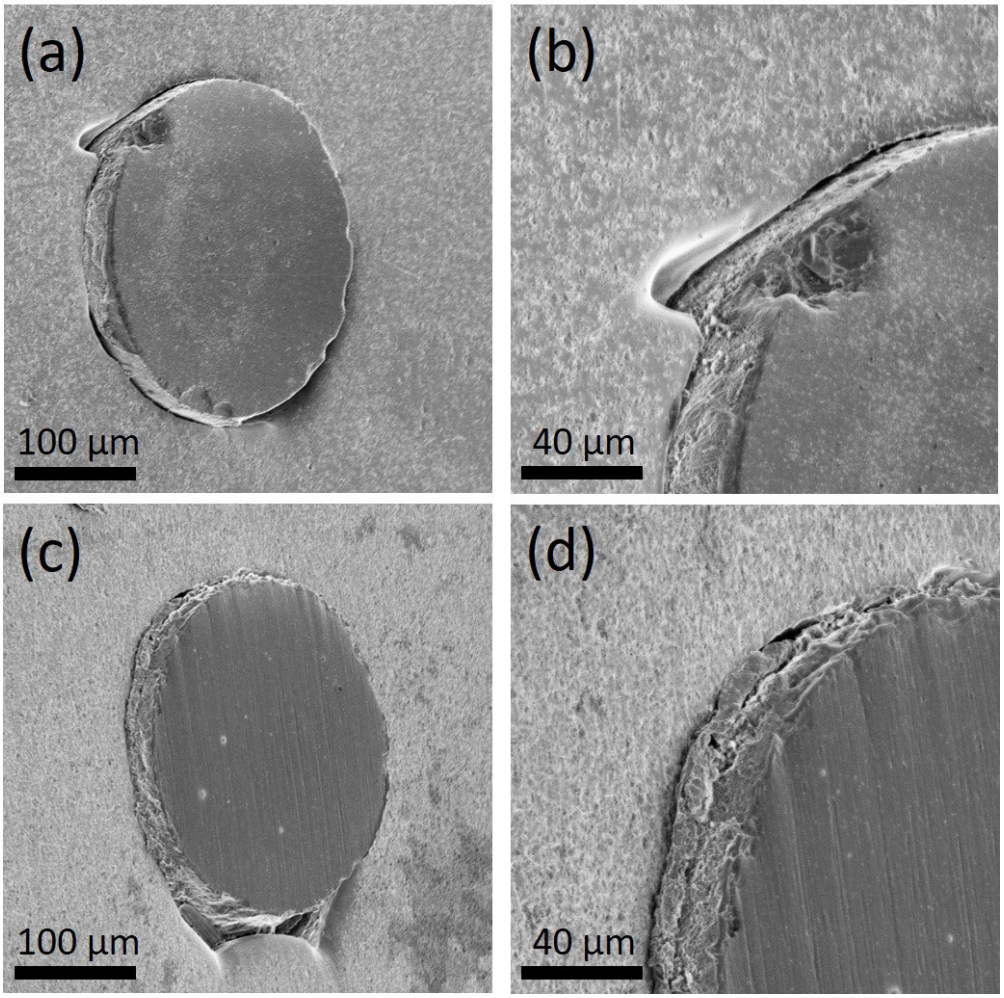

Figure 6.18: SEM images of the wire push-out test of both composite materials in the degraded condition. (a-b) PLDL+Mg, and (c-d) PLDL+Mg-PEO.

Table 6.5: Elastic modulus, E, tensile strength, σ_u and train-to-failure, ϵ_f of PLDL and of the Mg wires with and without PEO surface modification.

Material	E (GPa)	σ_u (MPa)	ϵ_f (%)
PLDL7038 + 5 wt % PEG [232]	3.0±0.1	38.6±2.2	3.7±0.4
Mg Wires [251]	44	305±4	9±1
Mg-PEO Wires [251]	44	285±15	7.5±1.3

6.4.5 Tensile properties of PLDL+Mg and PLDL+Mg-PEO composites

The tensile stress-strain curves of the PLDL+Mg composites are plotted in Figure 6.19 (a). They include the results for the as-printed composite tested in air at room temperature (dry) and tested in

water at 37°C (immersed) and after three weeks of *in vitro* degradation in PBS at 37°C (degraded). The average values and standard deviation of the elastic modulus, E, the tensile strength, σ_u and the strain-to-failure, ϵ_u are detailed in Table 6.6.

Table 6.6: Mechanical properties for the PLDL+Mg material. Elastic modulus and theoretical modulus values are represented by (E), and E_t, respectively. The tensile strength is represented by (σ_u), while the strain to failure is represented by ϵ_f.

Material	E (GPa)	E_t (GPa)	σ_u (MPa)	ϵ_f (%)
Dry	8.1±0.5	9.15	67±3.3	1.9±0.6
Immersed	7.2±1	-	46.2±4.1	9.22±3.1
Degraded	4±0.7	-	40.1±6.7	3.3±0.5

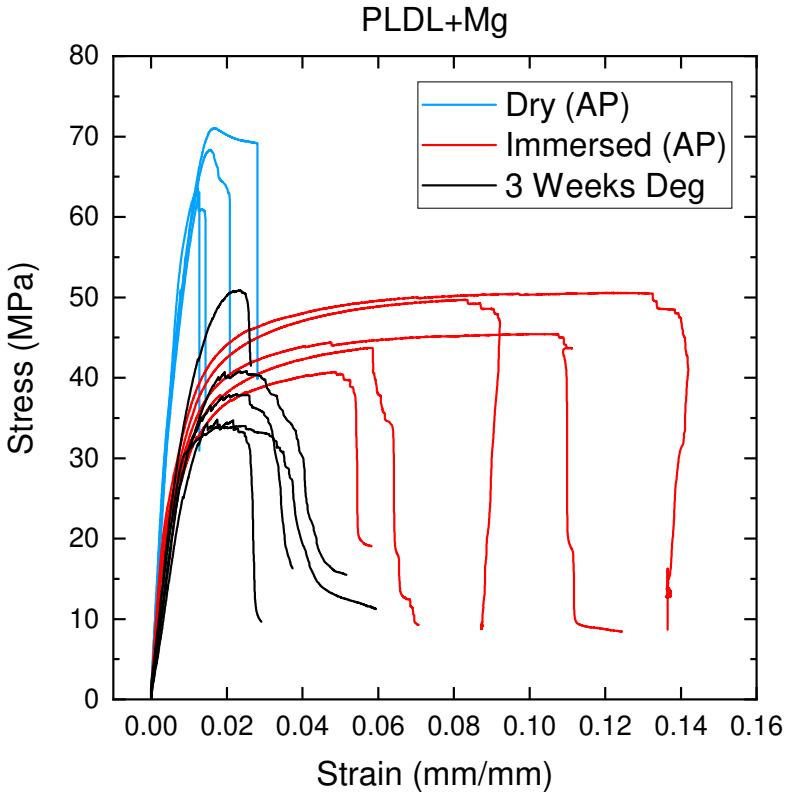

Figure 6.19: Tensile stress-strain curves of the PLDL+Mg composite tested in "dry", "immersed" and "degraded" conditions. (AP means As Printed, while Deg means Degraded)

The elastic modulus of the PLDL+Mg composite in the dry condition is very similar to theoretical one, E_t, predicted by the rule of mixtures eq. 4.1, indicating a good load transfer from the polymer matrix to the wires across the interface. The presence of the wires increases the elastic modulus and the strength of the composite up to 8.1 ± 0.5 GPa, and 67 ± 3.3 MPa, respectively.

The optical images of the broken samples showed that the specimens broke through the propagation of a single crack, indicating that the ductility was controlled by the brittle fracture of the PLDL matrix (Figure 6.20) (a). The analysis of the fracture surfaces around the crack in the SEM (Figure 6.19 (a)) showed extensive wire pull-out, which is associated with a low interface strength of the material. The wire pull-out lengths reached several mm (Figure 6.19 (b) and the fracture surface of the wires (Figure 6.19 (c) showed the cup-cone shape, typical of a ductile fracture mode. The fracture surface of the PLDL matrix was flat and featureless, indicating a brittle behaviour that controlled the ductility of the composite.

Immersion of the PLDL+Mg composite in water at 37°C caused a dramatic change in the deformation and fracture mechanisms, which should be mainly attributed to influence of water on the PLDL. In particular, the elastic modulus and the tensile strength were reduced by 11% and 31%, respectively, while the strain-to-failure increased by 450%. The optical images of the broken samples show that the damage spread in a region whose length ($\approx$ 10 mm) was similar to the width of the sample Figure 6.20 (b). Delamination cracks were observed in the polymer matrix, parallel to the wires, along the gauge length. The analysis of the fracture region in the SEM also showed extensive wire pull-out but the fracture surface of the matrix was completely different (Figure 6.21 (d-f). Ligaments of the matrix were also observed, indicating that water promoted plastic deformation of the PLDL, which deformed like a "chewing gum" and no longer contributes to the strength of the composite. Thus, the PLDL matrix underwent plastic deformation and failed by gradual necking, leading to tearing of the polymer and it can be concluded that PLDL effectively stops contributing to the strength of the composite once immersed in water at 37°C. The overall ductility of the composite was dictated in this case by the ductile failure of the pulled-out wires.

These observations are in agreement with similar studies in the literature. The reduction in the elastic modulus and strength of 3D printed PLA in a water bath at 37°C in comparison to those at room temperature in air has been reported in other investigations. For example, Chandran *et al.* measured a reduction in tensile strength and elastic modulus of 28% and 7%, respectively. Another investigation [258] has shown a decrease of 50% and 20% in the tensile strength and elastic modulus, respectively, as a result of the immersion of 3D printed PLA specimens in water at 37°C for 48 hours. The same research group also carried out a water absorption study and found that the PLA absorbed water within a few minutes, leading to swelling. In addition, increasing the temperature from room temperature to 37°C in air increases chain mobility by allowing more molecular segment motions, which is a potential cause for the increase in strain and reduction in strength [259, 260]. Our results suggest that the water molecules disrupted the intermolecular interactions during the test leading to the plasticisation of the polymer. Then, the synergistic effect of the water and temperature led to a more dramatic decrease in the mechanical properties caused by the plasticising effect of the water and an increase in the strain caused by the increased temperature [261, 262].

Finally, the deformation and fracture the PLDL+Mg composites after 3 weeks of *in vitro* degradation followed the trends observed in the samples deformed in water but include the effect of the corrosion of the Mg wires. Thus, the elastic modulus and the ductility were reduced because of pitting corrosion, that led to the premature failure of the wires at strains around 2%. Damage was localised in wide zones along the gauge length (Figure 6.20 (c) in which wires were pulled-

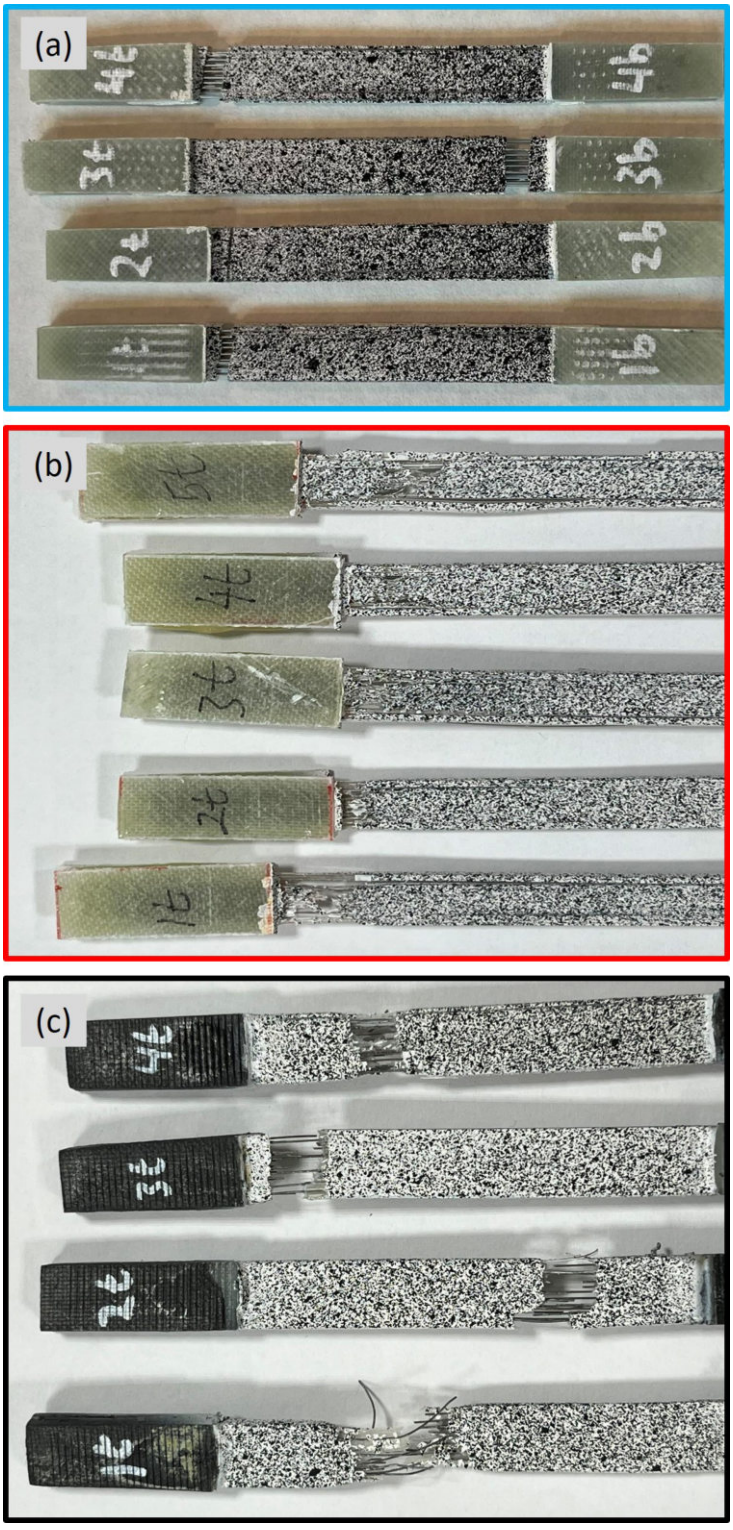

Figure 6.20: Optical images of the broken tensile specimens PLDL+Mg in the (a) 'dry' condition (b)' immersed' condition and (c) 'degraded' condition.

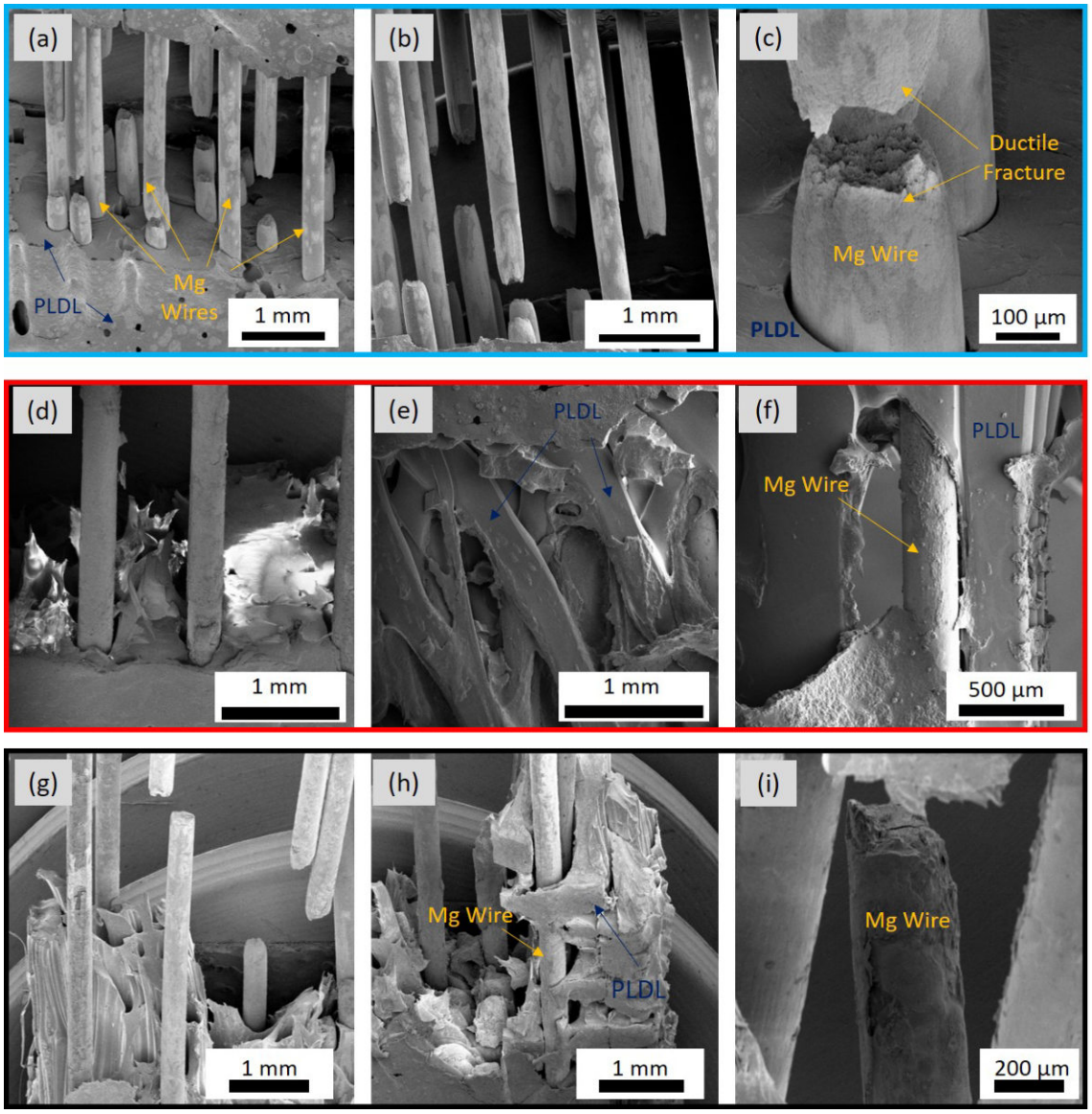

Figure 6.21: Colour coded SEM images of the fracture surfaces of the PLDL+Mg coupons under various loading conditions. (a-c) 'Dry' condition highlighted in light blue. (d-f) 'Immersed' condition highlighted in red. (g-i) 'Degraded' condition highlighted in black.

out from the matrix. The analysis of the fracture surfaces (Figure 6.19 (g-i)) indicated that the contribution of the matrix to the strength was negligible because of the substantial degradation during immersion and the wires showed flat fracture surfaces. So, they underwent brittle fracture in sections in which pitting corrosion was localised.

The tensile stress-strain curves of the PLDL+Mg-PEO samples tested under different conditions are plotted in Figure 6.22 (a). The average values and standard deviation of the elastic modulus, E, the tensile strength, σ_u and the strain-to-failure, ϵ_u are detailed in Table 6.7. Overall, they follow the same trends observed for the PLDL+Mg composites but the PEO surface-treatment led to a slight improvement in the mechanical properties of the composite material.

Table 6.7: Mechanical properties for the PLDL+Mg-PEO material. Elastic modulus and theoretical modulus values are represented by (E), and E_t, respectively. The tensile strength is represented by (σ_u), while the strain to failure is represented by ϵ_f.

Material	E (GPa)	E_t (GPa)	σ_u (MPa)	ϵ_f (%)
Dry	8.3±0.2	9.15	73±3.2	1.9±0.3
Immersed	6.2±1.1	-	49.2±3.7	8.7±1.7
Degraded	4.6±0.5	-	50.5±3.2	2.11±0.5

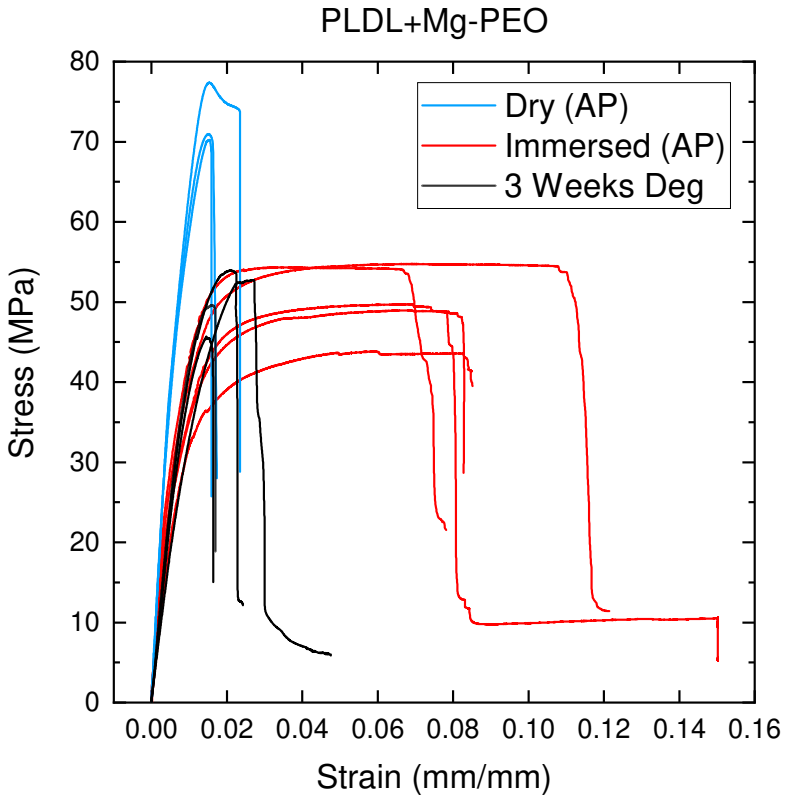

Figure 6.22: Tensile stress-strain curves of the PLDL+Mg composite tested in "dry", "immersed" and "degraded" conditions.

The elastic modulus of the PLDL+Mg-PEO composite in the dry condition is also very similar to theoretical one, E_t, predicted by the rule of mixtures eq. 4.1. It is also slightly higher than that of the PLDL+Mg composite because the oxide layer enhances the adhesion between the polymer and the wire and, thus, the load transfer. Similarly, the strength of the composite is slightly improved with respect to the PLDL+Mg composite but the ductility remains low (1.9% ± 0.3%). The optical images of the fractured samples show that the specimens broke through the propagation of a single crack, indicating that the ductility was controlled by the brittle fracture of the PLDL matrix. Moreover, the analysis of the fracture surfaces in the SEM (Figure 6.24 (a)),

show that the Mg-PEO wires were broken with very little pull-out, and this behavior is associated with the high interface strength (Figure 6.24 (b)). Figure 6.24 (c) shows that PLDL is still stuck to the one of the Mg-PEO wires slightly protruding from the fracture surface. This result supports the hypothesis that the oxide layer promoted by PEO enhanced the adhesion between the PLDL matrix and the wire. The fracture surface of the PLDL matrix was flat and featureless, indicating a brittle behavior that controlled the ductility of the composite.

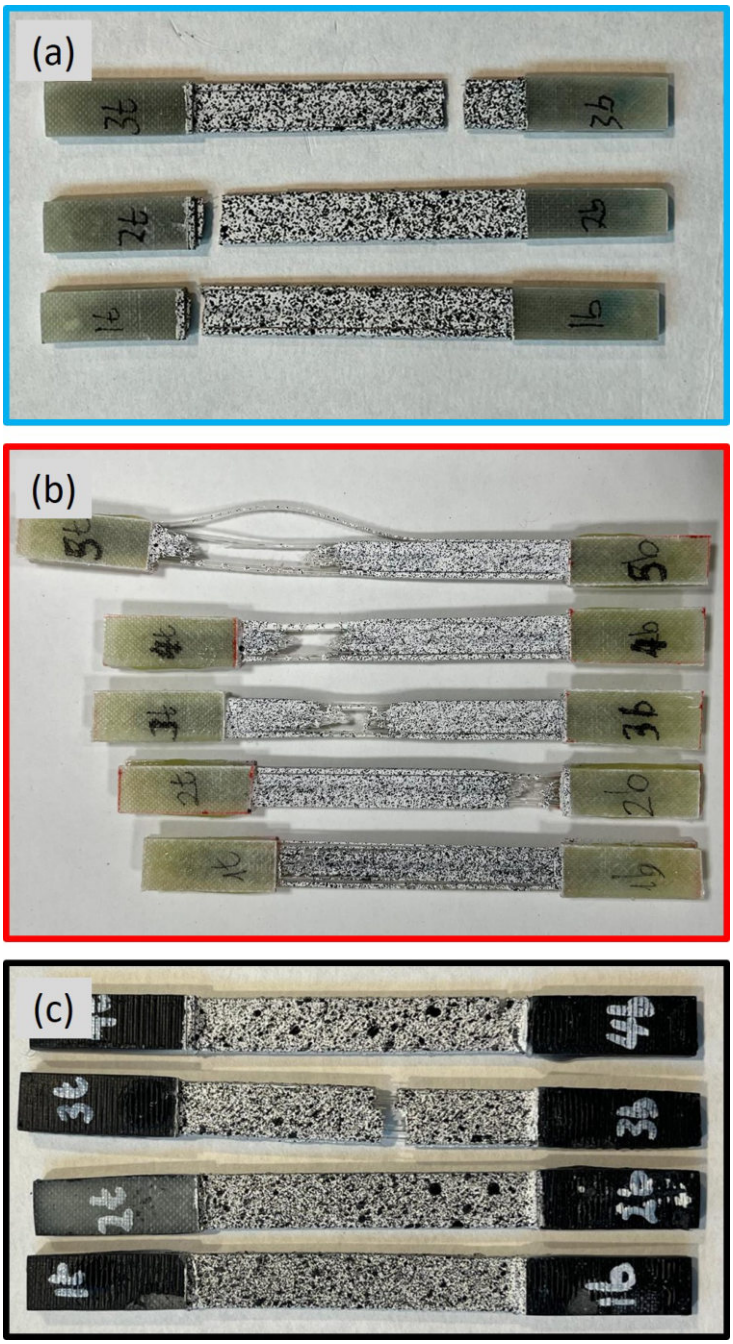

Figure 6.23: Optical images of the post-tensile test specimens for the PLDL+Mg-PEO material in the (a) 'dry' condition (b) 'immersed' condition and (c) 'degraded' condition.

Immersion of the PLDL+Mg-PEO composite in water at 37°C led to a dramatic change in the deformation and fracture mechanisms, mainly attributed to influence of water on the PLDL matrix. In particular, the elastic modulus and the tensile strength were reduced by 25% and 33%, respectively, while the strain-to-failure increased by 460%. Thus, the effect of immersion on the PLDL+Mg-PEO composites is very similar to the one observed in the PLDL+Mg composite above. The optical images of the broken samples (Figure 6.23 (b) show damage was spread over a length of ≈ 10-40 mm along the coupon and delamination cracks in the polymer matrix, parallel to the wires, were observed along the gauge length, as in the PLDL+Mg composite. The analysis of the fracture region in the SEM also showed extensive wire pull-out but the fracture surface of the matrix was completely different (Figure 6.24 (d-f). Wire pull-out in the immersed condition came about a result of the lack of mechanical properties of the PLDL matrix rather than to the reduction of the interface strength. The plasticising effect induced by the water on the polymer, in addition to the higher temperature, led to the disruption to the intermolecular bonds and to the substantial reductions in tensile strength and elastic modulus of the polymer, while increasing the strain-to-failure by over a factor of four [258, 261, 262, 263]. Thus, it can be concluded that PLDL effectively stops contributing to the strength of the composite once immersed in water at 37°C, as observed in the PLDL+Mg material.

Finally, the deformation and fracture of the PLDL+Mg-PEO composites after 3 weeks of *in vitro* degradation followed the trends observed in the samples immersed in water in terms of the tensile strength and modulus, but the effect of pitting corrosion on the wires was minimised because of the oxide layer induced by PEO. Thus, the strength of the composite after degradation was similar to that in the immersed condition and was controlled by the strength of the Mg wires. Failure occurred near the tabs in nearly all of the samples (Figure 6.23 (c)) and one of the samples shows wire-pull out in one of five rows of wires distributed throughout the polymer matrix. The SEM analysis of the fracture surfaces (Figure 6.24 (g-i)) indicated that the matrix underwent brittle fracture and showed negligible corrosion of the Mg-PEO wires, that were able to contribute to the strength, ultimately leading to improved mechanical properties in comparison to the PLDL+Mg composite after degradation.

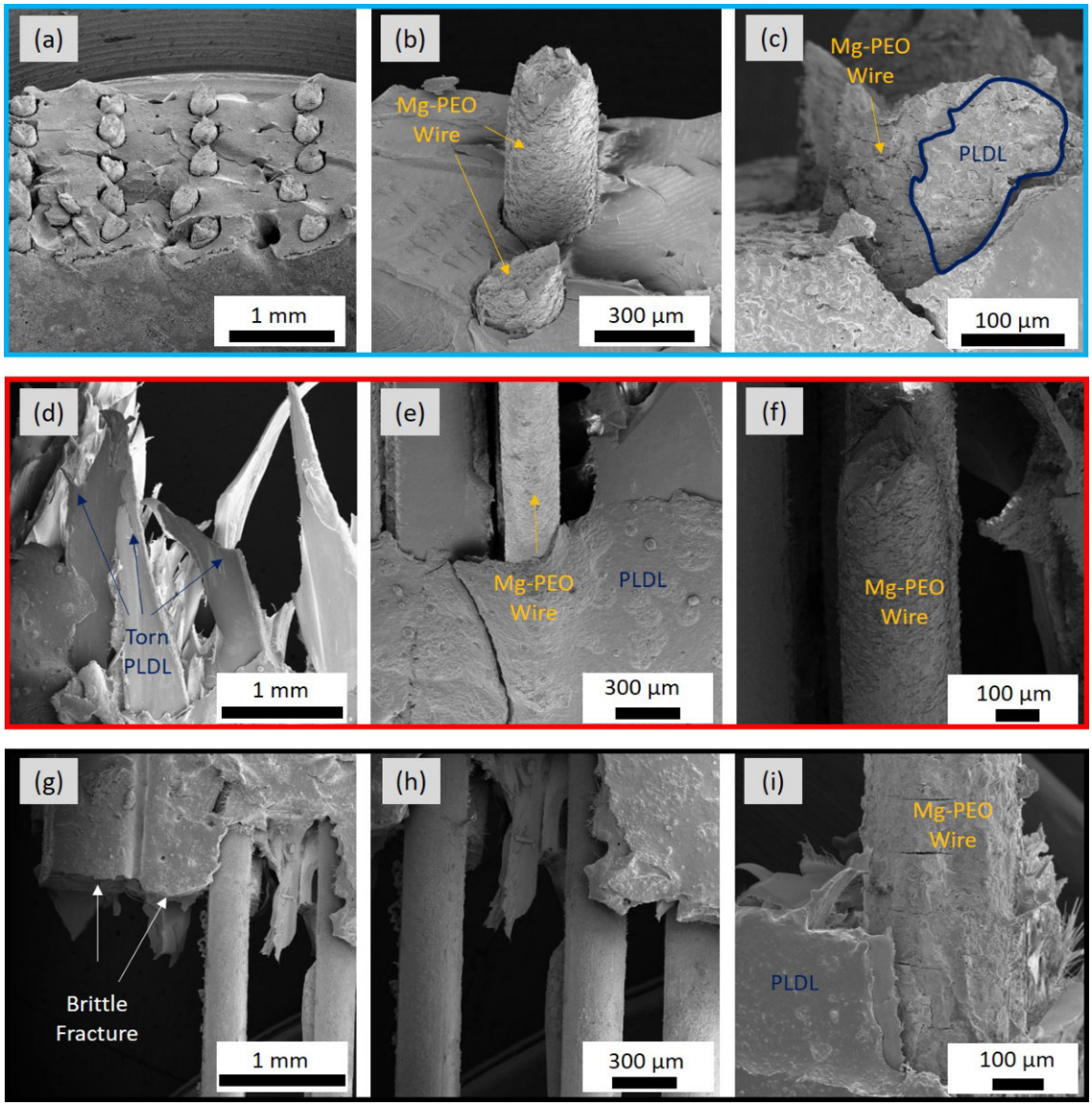

Figure 6.24: Colour coded SEM images of the fracture surfaces of the PLDL+Mg-PEO coupons under various loading conditions. (a-c) 'Dry' condition highlighted in light blue. (d-f) 'Immersed' condition highlighted in red. (g-i) 'Degraded' condition highlighted in black.

6.5 3D printing of a multi-material coupon

Finally, a proof-of-concept multimaterial coupon was manufactured by FFF to demonstrate the capabilities of the multimaterial printer developed in this thesis. The dimensions of the coupon were 120 x 10 x 2 mm^3, and a schematic of the coupon can be seen in Figure 6.25 which shows a cross-section of the coupon with the various material layers. They were made up of PLA, PLA + 4 vol. % Mg particles + 5 wt. % PEG as well as Mg wires and the coupon was designed to have alternating layers of PLA and PLA+Mg+PEG with the deposition of a layer of Mg wires also. In order to print this coupon the same conditions were used as those within this chapter in terms of the printing path and the sequential printing process with the added exception of the additional

print head, meaning 3 out of the 4 available print heads were used to fabricate this coupon. The PLA layers were 0.1 mm in height and the printing temperature was 200°C. The PLA+Mg+PEG material was also printed with a 0.1 mm layer height and the printing temperature used was 190°C. Finally, the Mg wire was deposited at a temperature of 160°C and at a layer height of 0.4 mm. Only one layer of Mg wire was deposited, so as to not complicate the printing of the piece further and risk a failed print, as the only objective was to demonstrate the proof-of-concept multimaterial composite. The sequential pattern was then printed as 4 layers of PLA, followed by the layer of Mg wire, followed by 4 PLA+Mg+PEG layers, then PLA, PLA+Mg+PEG, and finally PLA again. The printing speed was maintained as 40 mm/s for the polymer print heads and 5 mm/s for the deposition of the wire.

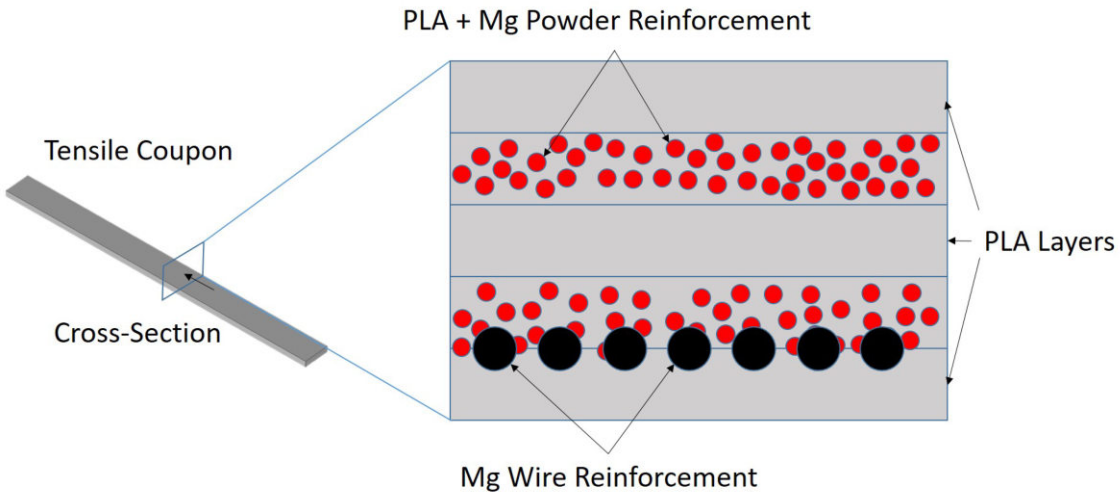

Figure 6.25: Schematic of the multi-material coupon designed to be printed with layers consisting of standard PLA, powder reinforcement, and continuous wire reinforcement.

Two optical images of the top and bottom surfaces of the coupon are shown in Figure 6.26. The Mg wires follow the concentric pattern detailed earlier in this chapter. The red rectangles and arrows in these images represent the cross section and direction in which the distribution of the material layers was analysed under optical microscopy and SEM in Figures 6.27 and 6.28, respectively. The same cross-section of the coupon is shown in Figures 6.27 (a-c), but the different images display the combination of the different layers from PLA, PLA+Mg particles composite, and the Mg wires. Each of the three different materials is labelled and they show that a layered structure was achieved with the multi-material FFF printer. The high-contrast image of the cross section of the coupon in Figure 6.27 (d) shows the presence of porosity resulting from the lack of adhesion between the polymer layers. Obviously, this limitation can be overcome through a careful optimisation of printing parameters.

An SEM image is displayed in Figure 6.28, where the Mg wire, and PLA matrix are labelled accordingly, while red arrows indicate the Mg powder particles from the PLA+Mg+PEG layers. The accompanying EDS analysis clearly indicates the presence of Mg wires and particles, embedded in the PLA matrix that is characterised by the presence of C and O.

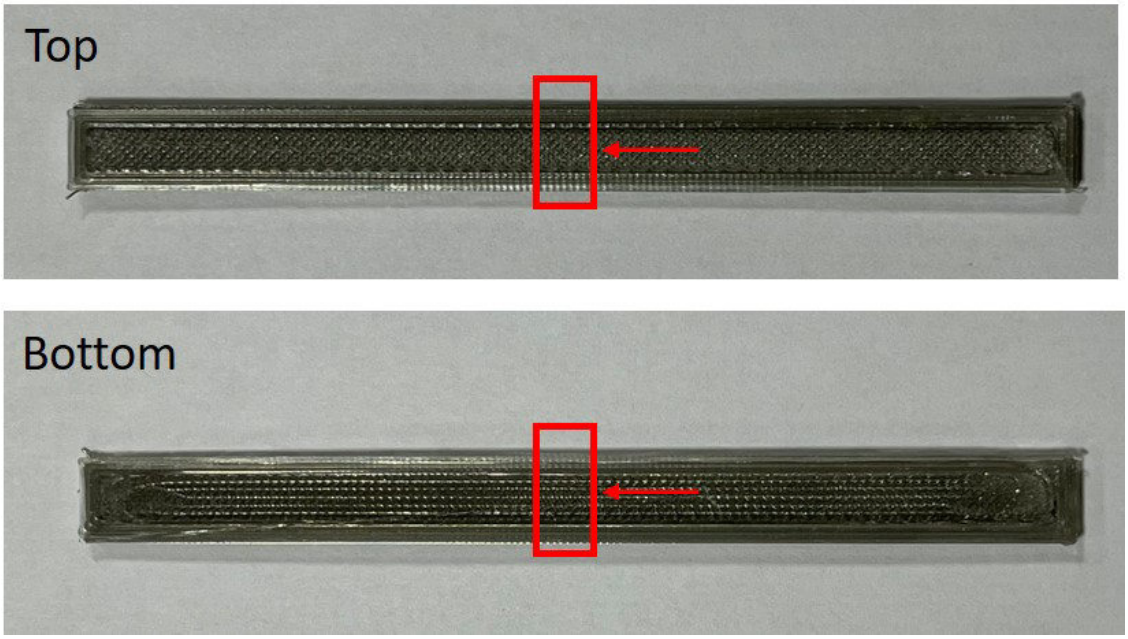

Figure 6.26: Top and bottom surfaces of the multi-material coupon manufactured by FFF.

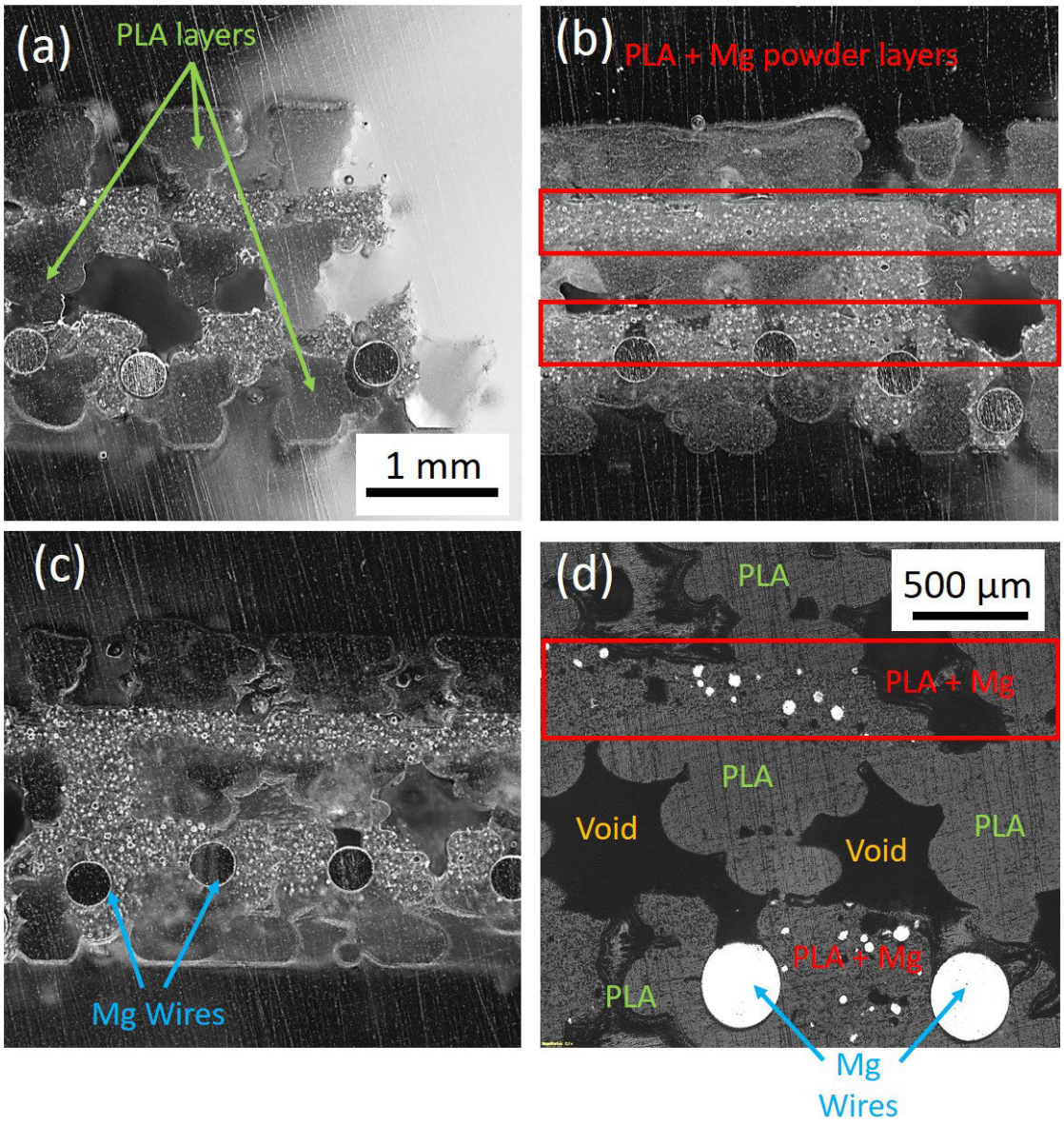

Figure 6.27: (a-c) Optical microscope images of a cross-section of the multi-material composite, showing the different material layers. The scale bar in (a) was the same that in (b) and (c). (d) High-contrast optical microscope image showing the various layers of materials in the cross-section of the multi-material composite.

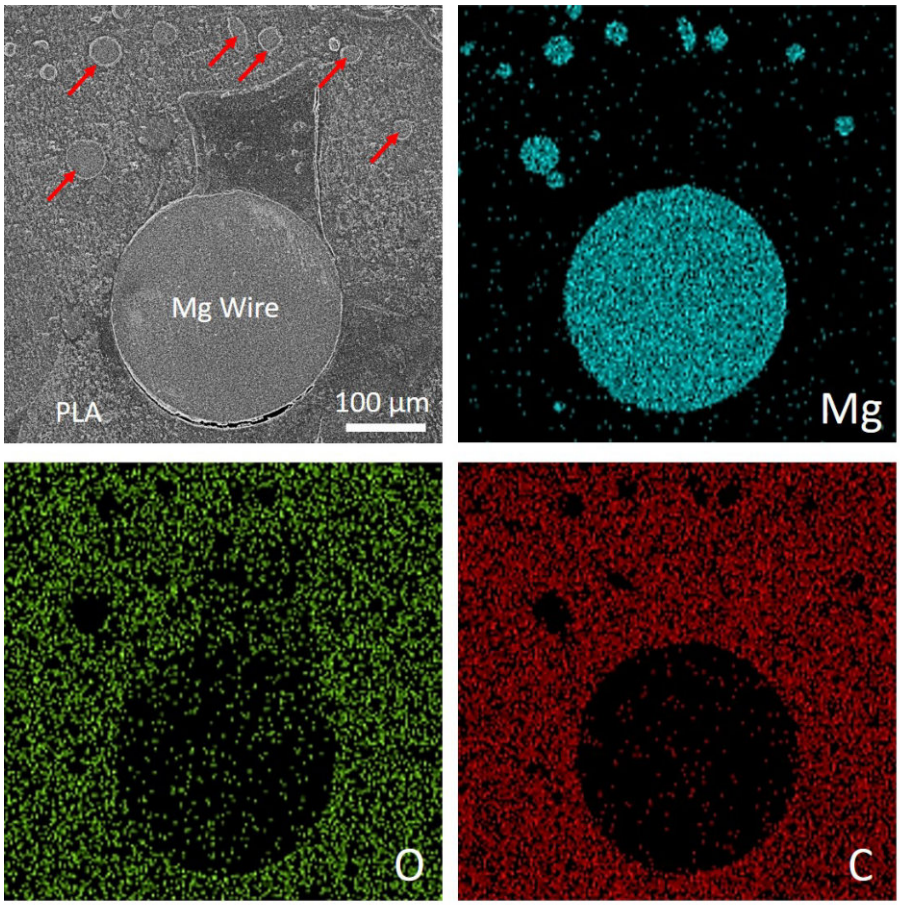

Figure 6.28: SEM and EDS images of the cross-section of the multi-material composite. The SEM image has been labelled to identify the different layers. EDS images confirm the location of the Mg wires as well as of the Mg particles, while the O and C indicated the location of the PLA matrix.

6.6 Conclusions

Manufacturing of coupons of a medical-grade PLDL polymer matrix uniaxially reinforced with a 15% volume fraction of Mg wires was demonstrated for the first time. Two different types of Mg wires, without and with a surface treatment by PEO, were used to manufacture the composites. The composites presented some porosity, particularly in the case of the Mg-PEO wires, that could be reduced by optimisation of the printing parameters.

The PLDL+Mg composites showed a clean interface between the PLDL matrix and the Mg wires and the interface shear strength in the as-printed conditions was relatively low. The PLDL matrix absorbed water rapidly during immersion at 37°C in PBS, leading to the pitting corrosion of Mg wires in the PLDL+Mg composites. Moreover, the alkaline environment induced by the corrosion of the Mg wires accelerated the hydrolysis of the PLDL near the interface with the wires after 3 weeks of immersion in PBS. Curiously, the presence of corrosion products at the wire/matrix interface after 3 weeks of degradation increased the interfacial shear strength, as compared with the as-printed condition.

On the contrary, a strong interface bonding between the oxide layer and the PLDL matrix was found at the interface of the PLDL+Mg-PEO composites because of the interlocking of the polymer that entered the pores of the oxide layer. The PLDL absorbed water rapidly during immersion at 37°C in PBS but pitting corrosion of the Mg wires was hindered by the presence of the oxide layer on the wires and the recession of the PLDL matrix near the interface was also reduced. Overall, the interface shear strength decreased after 3 weeks of immersion in PBS because of the reduced interlocking effect as a result of the degradation of the PLDL.

The elastic modulus and the tensile strength of the PLDL matrix in air at ambient temperature were improved by up to 3 times and up to 80%, respectively, by the addition of 15% volume of Mg or Mg-PEO wires. However, the ductility remained small and was controlled by the brittle fracture of PLDL matrix within the composites. Immersion in water at 37°C led to a marked reduction in both elastic modulus and strength for both composites due to the transformation of the PLDL matrix, which lost most of its load carrying capabilities as a result of the increased chain mobility very likely because the disruption of the intermolecular interactions by the synergistic contribution of water and temperature. Fracture in water at 37°C was controlled by the ductile fracture of the Mg wires and 3 weeks of degradation in PBS at 37°C further reduced the mechanical properties of the composite due to the pitting corrosion of the wires.

The mechanical properties in tension of the PLDL+Mg-PEO composites in air at ambient temperature were slightly better than those of the PLDL+Mg composite because of the enhanced interface adhesion. Nevertheless, fracture was also triggered at low strain because of the brittle fracture of PLDL. Immersion in water at 37°C also modified the mechanical response of the matrix and only the Mg-PEO wires contributed carry the load. The effect of degradation during 3 weeks in PBS at 37°C on the mechanical properties was less marked than in the PLDL+Mg composite because the pitting corrosion of the wires was hindered by the oxide layer.

Finally, a multi-material coupon was manufactured by FFF to demonstrate the capabilities of the multimaterial printer developed in this thesis. The coupon was designed to have alternating layers of PLA and PLA reinforced with Mg particles and a layer of Mg wires. This proof-of-concept

demonstrated the possibility to create multilayer scaffolds by FFF in which the properties of each layer can be tailored to meet specific requirements in terms of mechanical properties, degradation rate and cytocompatibility, opening the path to manufacture 3D printed, multimaterial biomedical devices.

Conclusions and Future Work

7

7.1 Conclusions

This doctoral thesis has focused on the development of medical-grade bioabsorbable composites manufactured by 3D printing for orthopaedic devices. In line with the primary objective of this thesis which was to produce a new generation of composite materials with the required mechanical properties, tailorable degradation times, and excellent biocompatibility for use in orthopaedic applications, a significant contribution to the research field has been made. The main conclusions are the following:

- A two-step extrusion method (standard extrusion followed by precision extrusion) has been developed to manufacture filaments of PLA matrix reinforced with different volume fractions of μm-sized Mg or Zn particles. The filaments were free of voids, had a constant diameter and the metallic particles were homogeneously distributed within the filament. They could be used to manufacture coupons as well as porous scaffolds with high dimensional accuracy by fused filament fabrication. Moreover, manufacturing of filaments and scaffolds from medical-grade PLDL was demonstrated for the first time. This technique is easily scaled and can be used for the industrial production of composite filaments for fused filament fabrication.

- The presence of metallic particles into the thermoplastic matrix accelerated the degradation during immersion in phosphate buffer solution at 37°C of samples manufactured by fused filament fabrication. This behaviour was associated with the reduction of the molecular weight of the polymer during the dual-extrusion process and also with the catalytic action of the metallic particles on the hydrolysis of the polymer. The acidification of the pH in the solution was reduced in the composites with Mg particles, as compared with the thermoplastic polymer. The presence of 4 vol. % of Mg or Zn particles led to a slight increase in the elastic modulus and to a reduction in tensile strength due to the early fracture associated with the stress concentrations around the particles. Finally, the biocompatibility of the composites manufactured with medical-grade polymers was outstanding and cell adhesion and proliferation processes were unaffected by the presence of metallic particles. These results demonstrate that addition of metallic particles to thermoplastic polymers can be used to tailor the degradation rate, without compromising biocompatibility, but not to improve the mechanical response.

- A novel and reproducible technique was developed to manufacture continuous metallic-wire reinforced thermoplastic matrix composites by filament fusion fabrication. To this end, a multimaterial printer was designed and manufactured. The printer contained two types of print heads. One of the them could be used to extrude standard filaments of thermoplastic polymers that may be reinforced with metallic particles. The other print head was specifically designed to print metallic wires through deposition within the polymer matrix. The wire print head was equipped with a cutting system to cut the wire after each wire layer had been deposited. The printer was operated via a computer interface, affording control over key parameters including temperature, speed, and babystep distance in real-time. Additionally, the slicing software provided the capability to predefine wire volume fractions and orientations for each layer before initiating the printing process.

- The capabilities of the new print head to manufactured wire-reinforced composites were demonstrated in uniaxially reinforced Al-wire PLA-matrix composite containing up to 25 vol % of Al wires of 300 μm in diameter. The presence of the Al wires dramatically increased the elastic modulus in the wire direction (up to a factor of 6 in the composite with 25% volume fraction of Al wires) while the strength improvement was also noticeable (up to 63%). Further improvements could be envisaged by optimisation of the processing parameters to reduce the porosity and improve the interface strength.

- The novel print head was use to manufacture medical-grade PLDL matrix composites uniaxially reinforced with up to 15 vol. % of Mg wires. The Mg wires existed in two different conditions: surface modified wires through plasma electrolytic oxidation, and unmodified, bare Mg wires. The oxide layer on the Mg wires introduced by plasma electrolytic oxidation improved the wire/matrix adhesion and suppressed pitting corrosion in the Mg wires during degradation in phosphate buffer solution at 37°C. The presence of the Mg wires led to almost a 3-fold increase in the elastic modulus and to an 80% increase in the tensile strength in comparison with of the thermoplastic polymer in air at ambient temperature. However, the mechanical properties of PLDL matrix were dramatically reduced in the presence of water at 37°C, compromising the mechanical properties of the composite in these circumstances. This degradation was likely due to the increased chain mobility induced by the disruption of the intermolecular interactions by the synergistic contribution of water and temperature.

- Finally, a multi-material coupon was manufactured by fused filament fabrication to demonstrate the capabilities of the multimaterial printer developed in this thesis. The coupon was designed to have alternating layers of PLA and PLA reinforced with Mg particles and a layer of Mg wires. This proof-of-concept demonstrates the possibility to create 3D printed multilayer scaffolds in which the properties of each layer can be tailor to meet specific requirements in terms of mechanical properties, degradation rate, and cytocompatibility, opening the path to manufacture 3D printed, multimaterial biomedical devices.

7.2 Future Work

The results in this thesis suggest the following topics for future work:

- The maximum volume fraction achieved in the PLDL/Mg wire was 15%. This magnitude is well below the theoretical limit of 42% that can be achieved with the printer head. Therefore, optimisation of the 3D printing process should be carried out to increase the wire volume fraction and reduce the porosity.
- The proof of concept multimaterial scaffold should be extended to print multilayers in which the wires are aligned in different orientations to achieve implants with quasi-isotropic in-plane mechanical properties.
- A more detailed characterisation of the mechanical properties of the medical-grade PLDL reinforced with metallic particles should be carried out, with particular emphasis on the behaviour in phosphate buffer solution at 37°C. Taking into account the behaviour of the PLDL matrix in the case of wire-reinforced composites, it is possible that this polymer undergoes excessive degradation during dual-extrusion and 3D printing by fused filament fabrication. If this is the case, other medical-grade PLA-based polymers should be explored to manufacture both metallic particle and wire-reinforced composites by 3D printing.
- Prior to carrying out *in vivo* tests in animal models, the biological performance of particle and wire-reinforced composites should be analysed in more detail. In particular, cell differentiation, gene expression and other tests should be performed to assess the potential of these materials in orthopaedic tissue engineering applications.
- 3D printed multimaterial scaffolds and implants provide a unique opportunity to manufacture implant with complex shape in which different regions mimic the trabecular and cortical bone microstructure (Figure 7.1), the former through polymers or polymers reinforced with metallic particles and the latter through wire-reinforced polymers. Moreover, the degradation rates and, perhaps, the biological response can be tailored through the use of different types of metallic particles or surface treatment of the Mg wires by plasma electrolytic oxidation.

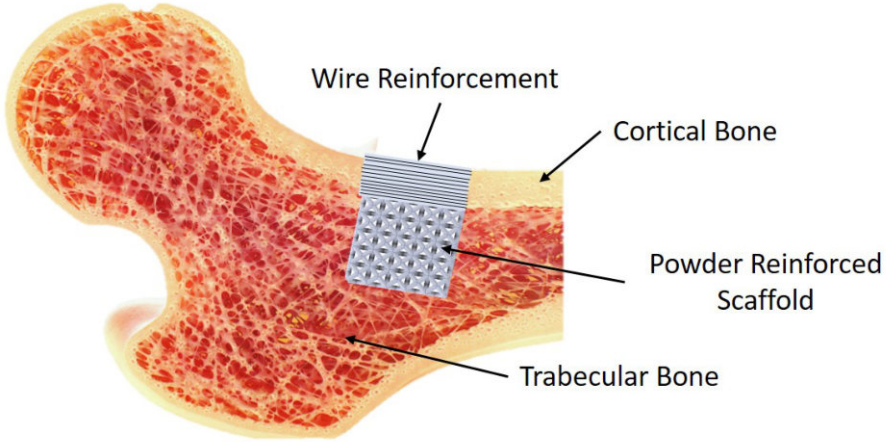

Figure 7.1: Multi-material implant comprised of wire-reinforced layers in the area of the cortical bone and a powder reinforced scaffold to aid in the regeneration of the trabecular bone.

References

[1] X. Feng, "Chemical and Biochemical Basis of Cell-Bone Matrix Interaction in Health and Disease," *Curr. Chem. Biol.*, vol. 3, p. 189, May 2009.

[2] X. Wang and S. Puram, "The Toughness of Cortical Bone and Its Relationship with Age," *Ann. Biomed. Eng.*, vol. 32, pp. 123–135, Jan. 2004.

[3] D. J. Hadjidakis and I. I. Androulakis, "Bone Remodeling," *Ann. N.Y. Acad. Sci.*, vol. 1092, pp. 385–396, Dec. 2006.

[4] J. D. Currey, K. Brear, and P. Zioupos, "The effects of ageing and changes in mineral content in degrading the toughness of human femora," *J. Biomech.*, vol. 29, pp. 257–260, Feb. 1996.

[5] T. M. Boyce and R. D. Bloebaum, "Cortical aging differences and fracture implications for the human femoral neck," *Bone*, vol. 14, pp. 769–778, Sept. 1993.

[6] R. B. Martin, D. B. Burr, and N. A. Sharkey, *Skeletal Tissue Mechanics*. New York, NY, USA: Springer, 1998.

[7] A. L. Boskey and P. G. Robey, "The Composition of Bone," in *Primer on the Metabolic Bone Diseases and Disorders of Mineral Metabolism*, pp. 84–92, Chichester, England, UK: John Wiley & Sons, Ltd., Oct. 2018.

[8] G. Campi, A. Ricci, A. Guagliardi, C. Giannini, S. Lagomarsino, R. Cancedda, M. Mastrogiacomo, and A. Cedola, "Early stage mineralization in tissue engineering mapped by high resolution X-ray microdiffraction," *Acta Biomater.*, vol. 8, pp. 3411–3418, Sept. 2012.

[9] S. Weiner and H. D. Wagner, "THE MATERIAL BONE: Structure-Mechanical Function Relations," *Annu. Rev. Mater. Sci.*, vol. 28, pp. 271–298, Aug. 1998.

[10] D. Lopes, C. Martins-Cruz, M. B. Oliveira, and J. F. Mano, "Bone physiology as inspiration for tissue regenerative therapies," *Biomaterials*, vol. 185, pp. 240–275, Dec. 2018.

[11] A. A. Al-Bari and A. Al Mamun, "Current advances in regulation of bone homeostasis," *FASEB Bioadv.*, vol. 2, p. 668, Nov. 2020.

[12] A. Teti, "Bone Development: Overview of Bone Cells and Signaling," *Curr. Osteoporos. Rep.*, vol. 9, pp. 264–273, Dec. 2011.

[13] E. Seeman, "Bone Modeling and Remodeling," *CRE*, vol. 19, no. 3, 2009.

[14] F. F. Safadi, M. F. Barbe, S. M. Abdelmagid, M. C. Rico, R. A. Aswad, J. Litvin, and S. N. Popoff, "Bone Structure, Development and Bone Biology," in *Bone Pathology*, pp. 1–50, Humana Press, May 2009.

[15] F. G. Evans, "Factors affecting the mechanical properties of bone.," *Bull. N. Y. Acad. Med.*, vol. 49, p. 751, Sept. 1973.

[16] D. Wu, P. Isaksson, S. J. Ferguson, and C. Persson, "Young's modulus of trabecular bone at the tissue level: A review," *Acta Biomater.*, vol. 78, pp. 1–12, Sept. 2018.

[17] M. J. Olszta, X. Cheng, S. S. Jee, R. Kumar, Y.-Y. Kim, M. J. Kaufman, E. P. Douglas, and L. B. Gower, "Bone structure and formation: A new perspective," *Materials Science and Engineering: R: Reports*, vol. 58, pp. 77–116, Nov. 2007.

[18] G. Holzer, G. von Skrbensky, L. A. Holzer, and W. Pichl, "Hip Fractures and the Contribution of Cortical Versus Trabecular Bone to Femoral Neck Strength," *J. Bone Miner. Res.*, vol. 24, pp. 468–474, Mar. 2009.

[19] R. Oftadeh, M. Perez-Viloria, J. C. Villa-Camacho, A. Vaziri, and A. Nazarian, "Biomechanics and mechanobiology of trabecular bone: a review," *J. Biomech. Eng.*, vol. 137, pp. 108021–1080215, Jan. 2015.

[20] Li. Mosekilde, Le. Mosekilde, and C. C. Danielsen, "Biomechanical competence of vertebral trabecular bone in relation to ash density and age in normal individuals," *Bone*, vol. 8, pp. 79–85, Jan. 1987.

[21] T. F. Lang, "The Bone-Muscle Relationship in Men and Women," *Journal of Osteoporosis*, vol. 2011, pp. 1–4, Oct. 2011.

[22] T. P. Ng, S. S. R. Koloor, J. R. P. Djuansjah, and M. R. A. Kadir, "Assessment of compressive failure process of cortical bone materials using damage-based model," *J. Mech. Behav. Biomed. Mater.*, vol. 66, pp. 1–11, Feb. 2017.

[23] D. T. Reilly, A. H. Burstein, and V. H. Frankel, "The elastic modulus for bone," *J. Biomech.*, vol. 7, pp. 271–275, May 1974.

[24] C.-Y. Lin and J.-H. Kang, "Mechanical Properties of Compact Bone Defined by the Stress-Strain Curve Measured Using Uniaxial Tensile Test: A Concise Review and Practical Guide," *Materials (Basel).*, vol. 14, p. 4224., July 2021.

[25] R. M. Slone, M. M. Heare, R. A. Vander Griend, and W. J. Montgomery, "Orthopedic fixation devices," *Radiographics : a review publication of the Radiological Society of North America, Inc*, vol. 11, pp. 823–847, sep 1991.

[26] R. a. Markets, "Global Orthopedic Surgery Market Report, 2017 to 2022 - Procedure Volume Trends by Type, Country, and Region," *GlobeNewswire News Room*, Aug. 2019.

[27] M. Doblaré, J. M. Garcı'a, and M. J. Gómez, "Modelling bone tissue fracture and healing: a review," *Eng. Fract. Mech.*, vol. 71, pp. 1809–1840, Sept. 2004.

[28] L. M. Biga, S. Bronson, S. Dawson, A. Harwell, R. Hopkins, J. Kaufmann, M. LeMaster, P. Matern, K. Morrison-Graham, K. Oja, D. Quick, J. Runyeon, O. Oeru, and OpenStax, *Anatomy & Physiology*. OpenStax/Oregon State University, Sept. 2019.

[29] N. L. Fazzalari, "Bone fracture and bone fracture repair," *Osteoporos. Int.*, vol. 22, pp. 2003–2006, June 2011.

[30] Z. S. A. I.-Aql, A. S. Alagl, D. T. Graves, L. C. Gerstenfeld, and T. A. Einhorn, "Molecular Mechanisms Controlling Bone Formation during Fracture Healing and Distraction Osteogenesis," *J. Dent. Res.*, vol. 87, pp. 107–118, Feb. 2008.

[31] L. C. Gerstenfeld, D. M. Cullinane, G. L. Barnes, D. T. Graves, and T. A. Einhorn, "Fracture healing as a post-natal developmental process: molecular, spatial, and temporal aspects of its regulation," *Journal of cellular biochemistry*, vol. 88, no. 5, pp. 873–884, 2003.

[32] Y. F. Zheng, X. N. Gu, and F. Witte, "Biodegradable metals," *Materials Science and Engineering: R: Reports*, vol. 77, pp. 1–34, 2014.

[33] A. Suryavanshi, V. Borse, V. Pawar, S. Kotagudda ranganath, and R. Srivastava, "Material advancements in bone-soft tissue fixation devices," *Science Advances Today*, vol. 2, pp. 25236–25248, 2016.

[34] J. Maheshwari and A. V. Mhaskar, *Essential Orthopaedics (Including Clinical Methods)*. Jaypee Brothers, Medical Publishers Pvt. Limited, 2019.

[35] M. E. Müller, M. Allgöwer, M. E. Müller, R. Schneider, and H. Willenegger, *Manual of internal fixation: techniques recommended by the AO-ASIF group*. Springer Science & Business Media, 1991.

[36] M. S. Taljanovic, M. D. Jones, J. T. Ruth, J. B. Benjamin, J. E. Sheppard, and T. B. Hunter, "Fracture fixation," *Radiographics*, vol. 23, pp. 1569–1590, Nov. 2003.

[37] "Ilizarov Surgery," Feb. 2022. [Online; accessed 13. Sep. 2023].

[38] "External fixation," June 2022. [Online; accessed 13. Sep. 2023].

[39] G. Reith, V. Schmitz-Greven, K. O. Hensel, M. M. Schneider, T. Tinschmann, B. Bouillon, and C. Probst, "Metal implant removal: benefits and drawbacks–a patient survey," *BMC surgery*, vol. 15, no. 1, p. 96, 2015.

[40] Y. Xin, T. Hu, and P. K. Chu, "In vitro studies of biomedical magnesium alloys in a simulated physiological environment: a review," *Acta biomaterialia*, vol. 7, no. 4, pp. 1452–1459, 2011.

[41] B. ITN, "Description of the Action Annex 1 - BioImplant ITN Horizon 2020," tech. rep., BioImplant ITN, 2019. [Online; accessed 15. Apr. 2020].

[42] D. A. Puleo and W. W. Huh, "Acute toxicity of metal ions in cultures of osteogenic cells derived from bone marrow stromal cells," *Journal of Applied Biomaterials*, vol. 6, no. 2, pp. 109–116, 1995.

[43] C. Lhotka, T. Szekeres, I. Steffan, K. Zhuber, and K. Zweymüller, "Four-year study of cobalt and chromium blood levels in patients managed with two different metal-on-metal total hip replacements," *Journal of Orthopaedic Research*, vol. 21, no. 2, pp. 189–195, 2003.

[44] J. J. Jacobs, N. J. Hallab, A. K. Skipor, and R. M. Urban, "Metal degradation products: a cause for concern in metal-metal bearings?," *Clinical Orthopaedics and Related Research®*, vol. 417, pp. 139–147, 2003.

[45] J. Nagels, M. Stokdijk, and P. M. Rozing, "Stress shielding and bone resorption in shoulder arthroplasty," *Journal of shoulder and elbow surgery*, vol. 12, no. 1, pp. 35–39, 2003.

[46] J. Park and R. S. Lakes, *Biomaterials: an introduction*. Springer Science & Business Media, 2007.

[47] M. P. Staiger, A. M. Pietak, J. Huadmai, and G. Dias, "Magnesium alloys as degradable biomaterials," *Biomaterials*, vol. 27, no. 9, pp. 1728–1734, 2006.

[48] G. O. Hofmann, "Biodegradable implants in orthopaedic surgery—a review on the state-of-the-art," *Clinical materials*, vol. 10, no. 1-2, pp. 75–80, 1992.

[49] L. S. Nair and C. T. Laurencin, "Biodegradable polymers as biomaterials," *Progress in polymer science*, vol. 32, no. 8-9, pp. 762–798, 2007.

[50] B. K. Montgomery, J. G. Gamble, S. T. Kha, G. G. Hecht, J. S. Vorhies, and J. F. Lucas, "Indications for and Risks Associated With Implant Removal After Pediatric Trauma," *JAAOS Global Research & Reviews*, vol. 6, p. e22.00050, Apr. 2022.

[51] T. V. Shah and D. V. Vasava, "A glimpse of biodegradable polymers and their biomedical applications," *e-Polymers*, vol. 19, no. 1, pp. 385–410, 2019.

[52] H. Ahmad, A. Arya, S. Agrawal, and A. K. Dwivedi, "PLGA scaffolds: building blocks for new age therapeutics," in *Materials for Biomedical Engineering*, pp. 155–201, Elsevier, 2019.

[53] C. Li, C. Guo, V. Fitzpatrick, A. Ibrahim, M. J. Zwierstra, P. Hanna, A. Lechtig, A. Nazarian, S. J. Lin, and D. L. Kaplan, "Design of biodegradable, implantable devices towards clinical translation," *Nature Reviews Materials*, pp. 1–21, 2019.

[54] A. S. for Testing and Materials, "ASTM F2902 - 16e1 Standard Guide for Assessment of Absorbable Polymeric Implants," tech. rep., American Society for Testing and Materials, 2016. Online; accessed 27. Sep. 2023.

[55] M. Vert, Y. Doi, K.-H. Hellwich, M. Hess, P. Hodge, P. Kubisa, M. Rinaudo, and F. Schué, "Terminology for biorelated polymers and applications (IUPAC Recommendations 2012)," *Pure and Applied Chemistry*, vol. 84, no. 2, pp. 377–410, 2012.

[56] J. C. Middleton and A. J. Tipton, "Synthetic biodegradable polymers as orthopedic devices," *Biomaterials*, vol. 21, no. 23, pp. 2335–2346, 2000.

[57] C. M. Agrawal, "Biodegradable Polymers for Orthopaedic Applications," in *Polymer Based Systems on Tissue Engineering, Replacement and Regeneration*, pp. 25–36, Springer, 2002.

[58] N. L. Davison, F. Barrère-de Groot, and D. W. Grijpma, "Degradation of biomaterials," in *Tissue Engineering*, pp. 177–215, Elsevier, 2014.

[59] D. da Silva, M. Kaduri, M. Poley, O. Adir, N. Krinsky, J. Shainsky-Roitman, and A. Schroeder, "Biocompatibility, biodegradation and excretion of polylactic acid (PLA) in medical implants and theranostic systems," *Chemical Engineering Journal*, vol. 340, pp. 9–14, 2018.

[60] A. R. Amini, J. S. Wallace, and S. P. Nukavarapu, "Short-term and long-term effects of orthopedic biodegradable implants," *Journal of long-term effects of medical implants*, vol. 21, no. 2, 2011.

[61] Corbion Purac, *Physical Properties PURASORB Polymers*, Mar. 2015. [Online; accessed 19. Sep. 2023].

[62] P. Gunatillake, R. Mayadunne, and R. Adhikari, "Recent developments in biodegradable synthetic polymers," *Biotechnology annual review*, vol. 12, pp. 301–347, 2006.

[63] Synthes, "Johnson and Johnson/ De Puy Synthes." [Online; accessed 12. Jun. 2023].

[64] Biomet, "ComposiTCP Interference Screws." [Online; accessed 21. Sep. 2023].

[65] B. Heimbach and M. Wei, "Composite Orthopedic Fixation Devices," in *Orthopedic Biomaterials*, pp. 399–425, Springer, 2017.

[66] Stryker, "Stryker - Delta Brochure." [Online; accessed 12. Jun. 2023].

[67] BIORETEC, "Biodegradable Screws." [Online; accessed 7. Sep. 2023].

[68] "mm.X implant technology - medical magnesium," Oct. 2020. [Online; accessed 19. Sep. 2023].

[69] FDA, "Class 1 Device Recall Absorb Bioresorbable Vascular Scaffold (BVS) System," 2017. [Online; accessed 12. Jun. 2023].

[70] J. Lopez, N. Siegel, A. Reategui, M. Faateh, P. N. Manson, and R. J. Redett, "Absorbable fixation devices for pediatric craniomaxillofacial trauma: A systematic review of the literature," *Plastic and reconstructive surgery*, vol. 144, no. 3, pp. 685–692, 2019.

[71] J.-M. Seitz, M. Durisin, J. Goldman, and J. W. Drelich, "Recent Advances in Biodegradable Metals for Medical Sutures: A Critical Review," *Adv. Healthcare Mater.*, vol. 4, pp. 1915–1936, Sept. 2015.

[72] Z. Sheikh, S. Najeeb, Z. Khurshid, V. Verma, H. Rashid, and M. Glogauer, "Biodegradable Materials for Bone Repair and Tissue Engineering Applications," *Materials*, vol. 8, p. 5744, Sept. 2015.

[73] H. Yang, B. Jia, Z. Zhang, X. Qu, G. Li, W. Lin, D. Zhu, K. Dai, and Y. Zheng, "Alloying design of biodegradable zinc as promising bone implants for load-bearing applications," *Nat. Commun.*, vol. 11, 2020.

[74] M. Niinomi, "Recent metallic materials for biomedical applications," *Metallurgical and materials transactions A*, vol. 33, no. 3, p. 477, 2002.

[75] B. D. Ratner, A. S. Hoffman, F. J. Schoen, and J. E. Lemons, *Biomaterials science: an introduction to materials in medicine*. Elsevier, 2004.

[76] X. N. Gu, W. R. Zhou, Y. F. Zheng, Y. Cheng, S. C. Wei, S. P. Zhong, T. F. Xi, and L. J. Chen, "Corrosion fatigue behaviors of two biomedical Mg alloys–AZ91D and WE43–in simulated body fluid," *Acta Biomaterialia*, vol. 6, no. 12, pp. 4605–4613, 2010.

[77] R. Waksman, R. Pakala, P. K. Kuchulakanti, R. Baffour, D. Hellinga, R. Seabron, F. O. Tio, E. Wittchow, S. Hartwig, and C. Harder, "Safety and efficacy of bioabsorbable magnesium alloy stents in porcine coronary arteries," *Catheterization and Cardiovascular Interventions*, vol. 68, no. 4, pp. 607–617, 2006.

[78] G. Mani, M. D. Feldman, D. Patel, and C. M. Agrawal, "Coronary stents: a materials perspective," *Biomaterials*, vol. 28, no. 9, pp. 1689–1710, 2007.

[79] "Magmaris | Magmaris," Sept. 2023. [Online; accessed 21. Sep. 2023].

[80] W. Ali, M. Echeverry-Rendón, G. Dominguez, K. van Gaalen, A. Kopp, C. González, and J. LLorca, "Bioabsorbable WE43 Mg alloy wires modified by continuous plasma electrolytic oxidation for implant applications. Part II: Degradation and biological performance," *Biomaterials Advances*, vol. 147, pp. 21–33, Apr. 2023.

[81] R. Willumeit-Römer, "The Interface Between Degradable Mg and Tissue," *JOM*, vol. 71, pp. 1447–1455, Apr. 2019.

[82] W. Ali, A. Mehboob, M. G. Han, and S. H. Chang, "Effect of fluoride coating on degradation behaviour of unidirectional Mg/PLA biodegradable composite for load-bearing bone implant application," *Composites Part A: Applied Science and Manufacturing*, vol. 124, no. March, pp. 54–64, 2019.

[83] Y. H. Wu, N. Li, Y. Cheng, Y. F. Zheng, and Y. Han, "In vitro Study on Biodegradable AZ31 Magnesium Alloy Fibers Reinforced PLGA Composite," *J. Mater. Sci. Technol.*, vol. 29, pp. 545–550, June 2013.

[84] H. Dieringa, L. Fuskova, D. Fechner, and C. Blawert, "Mechanical and corrosion behaviour of a hydroxyapatite reinforced magnesium alloy WE43," in *Proceedings of the 17th International Conference on Composite Materials, ICCM, Edinburgh, UK*, pp. 27–31, 2009.

[85] W. Ali, M. Echeverry-Rendón, A. Kopp, C. González, and J. LLorca, "Strength, corrosion resistance and cellular response of interfaces in bioresorbable poly-lactic acid/Mg fiber composites for orthopedic applications," *J. Mech. Behav. Biomed. Mater.*, vol. 123, pp. 1–10, Nov. 2021.

[86] W. Ali, M. Echeverry-Rendón, A. Kopp, C. González, and J. LLorca, "Effect of surface modification on interfacial behaivor in bioabsorbable magnesium wire reinforced poly-lactic acid polymer composites," *npj Mater. Degrad.*, vol. 7, pp. 1–14, Aug. 2023.

[87] K. van Gaalen, F. Gremse, F. Benn, P. E. McHugh, A. Kopp, and T. J. Vaughan, "Automated ex-situ detection of pitting corrosion and its effect on the mechanical integrity of rare earth magnesium alloy-we43," *Bioactive Materials*, vol. 8, pp. 545–558, 2022.

[88] K. van Gaalen, C. Quinn, M. Weiler, F. Gremse, F. Benn, P. E. McHugh, T. J. Vaughan, and A. Kopp, "Predicting localised corrosion and mechanical performance of a peo surface modified rare earth magnesium alloy for implant use through in-silico modelling," *Bioactive Materials*, vol. 26, pp. 437–451, 2023.

[89] J. Grogan, B. O'brien, S. Leen, and P. McHugh, "A corrosion model for bioabsorbable metallic stents," *Acta biomaterialia*, vol. 7, no. 9, pp. 3523–3533, 2011.

[90] H. E. Friedrich and B. L. Mordike, *Magnesium technology*, vol. 788. Springer, 2006.

[91] Z. Li, X. Gu, S. Lou, and Y. Zheng, "The development of binary Mg–Ca alloys for use as biodegradable materials within bone," *Biomaterials*, vol. 29, no. 10, pp. 1329–1344, 2008.

[92] X. N. Gu, X. H. Xie, N. Li, Y. F. Zheng, and L. Qin, "In vitro and in vivo studies on a Mg–Sr binary alloy system developed as a new kind of biodegradable metal," *Acta biomaterialia*, vol. 8, no. 6, pp. 2360–2374, 2012.

[93] Z. Wen, C. Wu, C. Dai, and F. Yang, "Corrosion behaviors of Mg and its alloys with different Al contents in a modified simulated body fluid," *Journal of Alloys and Compounds*, vol. 488, no. 1, pp. 392–399, 2009.

[94] M. Y. Kolawole, J. O. Aweda, F. Iqbal, A. Ali, and S. Abdulkareem, "Mechanical properties of powder metallurgy processed biodegradable zn-based alloy for biomedical application," *Int. J. Mater. Metall. Eng*, vol. 13, no. 12, pp. 558–563, 2019.

[95] J. Venezuela and M. S. Dargusch, "The influence of alloying and fabrication techniques on the mechanical properties, biodegradability and biocompatibility of zinc: A comprehensive review," *Acta Biomater.*, vol. 87, pp. 1–40, Mar. 2019.

[96] V. Tsakiris, C. Tardei, and F. M. Clicinschi, "Biodegradable Mg alloys for orthopedic implants – A review," *J. Magnesium Alloys*, vol. 9, pp. 1884–1905, Nov. 2021.

[97] D. Vojtěch, J. Kubásek, J. Šerák, and P. Novák, "Mechanical and corrosion properties of newly developed biodegradable Zn-based alloys for bone fixation," *Acta Biomaterialia*, vol. 7, no. 9, pp. 3515–3522, 2011.

[98] M. Razavi, M. H. Fathi, and M. Meratian, "Microstructure, mechanical properties and biocorrosion evaluation of biodegradable AZ91-FA nanocomposites for biomedical applications," *Mater. Sci. Eng., A*, vol. 527, pp. 6938–6944, Oct. 2010.

[99] X. Liu, Y. Osawa, S. Takamori, and T. Mukai, "Microstructure and mechanical properties of AZ91 alloy produced with ultrasonic vibration," *Materials Science and Engineering: A*, vol. 487, no. 1-2, pp. 120–123, 2008.

[100] H. Hermawan, D. Dubé, and D. Mantovani, "Developments in metallic biodegradable stents," *Acta biomaterialia*, vol. 6, no. 5, pp. 1693–1697, 2010.

[101] L. W. F. Mackenzie, B. Davis, F. J. Humphreys, and G. W. Lorimer, "The deformation, recrystallisation and texture of three magnesium alloy extrusions," *Materials Science and Technology*, vol. 23, no. 10, pp. 1173–1180, 2007.

[102] Y. S. Jeong and W. J. Kim, "Enhancement of mechanical properties and corrosion resistance of Mg–Ca alloys through microstructural refinement by indirect extrusion," *Corros. Sci.*, vol. 82, pp. 392–403, May 2014.

[103] Y. Wan, G. Xiong, H. Luo, F. He, Y. Huang, and X. Zhou, "Preparation and characterization of a new biomedical magnesium–calcium alloy," *Mater. Des.*, vol. 29, pp. 2034–2037, Dec. 2008.

[104] T. Thamaraiselvi and S. Rajeswari, "Biological evaluation of bioceramic materials-a review," *Carbon*, vol. 24, no. 31, p. 172, 2004.

[105] S. K. Nandi, S. Roy, P. Mukherjee, B. Kundu, D. K. De, and D. Basu, "Orthopaedic applications of bone graft & graft substitutes: a review," *Indian Journal of Medical Reseach*, vol. 132, no. 1, pp. 15–30, 2010.

[106] S. L. Evans and P. J. Gregson, "Composite technology in load-bearing orthopaedic implants," *Biomaterials*, vol. 19, no. 15, pp. 1329–1342, 1998.

[107] "Composite Materials," Nov. 2021. [Online; accessed 20. Sep. 2023].

[108] M.-S. Scholz, J. P. Blanchfield, L. D. Bloom, B. H. Coburn, M. Elkington, J. D. Fuller, M. E. Gilbert, S. A. Muflahi, M. F. Pernice, and S. I. Rae, "The use of composite materials in modern orthopaedic medicine and prosthetic devices: A review," *Composites Science and Technology*, vol. 71, no. 16, pp. 1791–1803, 2011.

[109] J. Yang, J. L. Guo, A. G. Mikos, C. He, and G. Cheng, "Material processing and design of biodegradable metal matrix composites for biomedical applications," *Annals of biomedical engineering*, vol. 46, no. 9, pp. 1229–1240, 2018.

[110] T. O. Xu, H. S. Kim, T. Stahl, and S. P. Nukavarapu, "Self-neutralizing PLGA/magnesium composites as novel biomaterials for tissue engineering," *Biomedical Materials*, vol. 13, no. 3, p. 35013, 2018.

[111] A. Brown, S. Zaky, H. Ray Jr, and C. Sfeir, "Porous magnesium/PLGA composite scaffolds for enhanced bone regeneration following tooth extraction," *Acta biomaterialia*, vol. 11, pp. 543–553, 2015.

[112] P. K. Mallick, "Thermoplastics and thermoplastic–matrix composites for lightweight automotive structures," in *Materials, Design and Manufacturing for Lightweight Vehicles*, pp. 174–207, Elsevier, 2010.

[113] "Short-Fibre Reinforced," 2020. [Online; accessed 12. Jun. 2023].

[114] Biocomposites, "Interference Screws." [Online; accessed 21. Sep. 2023].

[115] Teknimed, "Interference Screw PLA/TCP." [Online; accessed 21. Sep. 2023].

[116] Biomet, "Zimmer Biomet - Lactosorb Range." [Online; accessed 21. Sep. 2023].

[117] Ossio, "Ossio - Product Range." [Online; accessed 21. Sep. 2023].

[118] "How are composites manufactured?," Sept. 2023. [Online; accessed 25. Sep. 2023].

[119] T. D. Ngo, A. Kashani, G. Imbalzano, K. T. Q. Nguyen, and D. Hui, "Additive manufacturing (3D printing): A review of materials, methods, applications and challenges," *Composites Part B: Engineering*, vol. 143, pp. 172–196, 2018.

[120] "A Guide to FDM Printale Plastics and 3D Printing Filament | 3devo," Sept. 2023. [Online; accessed 30. Sep. 2023].

[121] A. K. Sood, R. K. Ohdar, and S. S. Mahapatra, "Parametric appraisal of mechanical property of fused deposition modelling processed parts," *Materials & Design*, vol. 31, no. 1, pp. 287–295, 2010.

[122] O. A. Mohamed, S. H. Masood, and J. L. Bhowmik, "Optimization of fused deposition modeling process parameters: a review of current research and future prospects," *Advances in Manufacturing*, vol. 3, no. 1, pp. 42–53, 2015.

[123] Y. Ibrahim, G. W. Melenka, and R. Kempers, "Fabrication and tensile testing of 3D printed continuous wire polymer composites," *Rapid Prototyping Journal*, vol. 24, no. 7, pp. 1131–1141, 2018.

[124] F. Ning, W. Cong, J. Qiu, J. Wei, and S. Wang, "Additive manufacturing of carbon fiber reinforced thermoplastic composites using fused deposition modeling," *Composites Part B*, vol. 80, pp. 369–378, Oct. 2015.

[125] F. Ning, W. Cong, Y. Hu, and H. Wang, "Additive manufacturing of carbon fiber-reinforced plastic composites using fused deposition modeling: Effects of process parameters on tensile properties," *J. Compos. Mater.*, vol. 51, pp. 451–462, Apr. 2016.

[126] N. Li, Y. Li, and S. Liu, "Rapid prototyping of continuous carbon fiber reinforced polylactic acid composites by 3D printing," *J. Mater. Process. Technol.*, vol. 238, pp. 218–225, Dec. 2016.

[127] V. Mirón, S. Ferrándiz, D. Juárez, and A. Mengual, "Manufacturing and characterization of 3D printer filament using tailoring materials," *Procedia Manufacturing*, vol. 13, pp. 888–894, 2017.

[128] A. El Moumen, M. Tarfaoui, and K. Lafdi, "Additive manufacturing of polymer composites: Processing and modeling approaches," *Composites Part B*, vol. 171, pp. 166–182, Aug. 2019.

[129] M. L. Shofner, K. Lozano, F. J. Rodríguez-Macías, and E. V. Barrera, "Nanofiber-reinforced polymers prepared by fused deposition modeling," *Journal of applied polymer science*, vol. 89, no. 11, pp. 3081–3090, 2003.

[130] F. Ning, W. Cong, J. Qiu, J. Wei, and S. Wang, "Additive manufacturing of carbon fiber reinforced thermoplastic composites using fused deposition modeling," *Composites Part B: Engineering*, vol. 80, pp. 369–378, 2015.

[131] X. Tian, T. Liu, C. Yang, Q. Wang, and D. Li, "Interface and performance of 3D printed continuous carbon fiber reinforced PLA composites," *Composites Part A: Applied Science and Manufacturing*, vol. 88, pp. 198–205, 2016.

[132] J. L. Dávila, M. S. de Freitas, P. Inforçatti Neto, Z. d. C. Silveira, J. V. L. da Silva, and M. A. D'Ávila, "Fabrication of PCL/β-TCP scaffolds by 3D mini-screw extrusion printing," *Journal of Applied Polymer Science*, vol. 133, no. 15, 2016.

[133] F. S. Senatov, K. V. Niaza, A. A. Stepashkin, and S. D. Kaloshkin, "Low-cycle fatigue behavior of 3d-printed PLA-based porous scaffolds," *Composites Part B: Engineering*, vol. 97, pp. 193–200, 2016.

[134] I. Antoniac, D. Popescu, A. Zapciu, A. Antoniac, F. Miculescu, and H. Moldovan, "Magnesium Filled Polylactic Acid (PLA) Material for Filament Based 3D Printing," *Materials*, vol. 12, no. 5, p. 719, 2019.

[135] A. Hamidi and Y. Tadesse, "Single step 3D printing of bioinspired structures via metal reinforced thermoplastic and highly stretchable elastomer," *Compos. Struct.*, vol. 210, pp. 250–261, Feb. 2019.

[136] C. Kim, D. Espalin, A. Cuaron, M. A. Perez, M. Lee, E. MacDonald, and R. B. Wicker, "Cooperative tool path planning for wire embedding on additively manufactured curved surfaces using robot kinematics," *Journal of Mechanisms and Robotics*, vol. 7, no. 2, 2015.

[137] "Orthopedic Devices Market Size, Share & Trends Analysis Report By Application (Hip, Knee, Spine, Cranio-Maxillofacial, Dental, SET), By Product (Accessories, Surgical Devices), By Region, And Segment Forecasts, 2022 - 2030," Sept. 2023. [Online; accessed 8. Sep. 2023].

[138] "Trauma Fixation Devices Market Size & Share Analysis - Industry Research Report - Growth Trends," Sept. 2023. [Online; accessed 8. Sep. 2023].

[139] "Trauma Fixation Devices Market Size, Industry Trends 2030," May 2022. [Online; accessed 8. Sep. 2023].

[140] I. O. for Standardization, "Plastics — determination of tensile properties — part 1: General principles," tech. rep., International Organization for Standardization, Vernier, Geneva, Switzerland, 2012. [Online; accessed 17. Feb. 2023].

[141] "EngArc - L - Tensile Test," Mar. 2015. [Online; accessed 27. Sep. 2023].

[142] C. González and J. Llorca, "Micromechanical modelling of deformation and failure in ti–6al–4v/sic composites," *Acta Materialia*, vol. 49, no. 17, pp. 3505–3519, 2001.

[143] L. P. Canal, C. González, J. Segurado, and J. LLorca, "Intraply fracture of fiber-reinforced composites: Microscopic mechanisms and modeling," *Composites science and technology*, vol. 72, no. 11, pp. 1223–1232, 2012.

[144] M. N. Kallas, D. A. Koss, H. T. Hahn, and J. R. Hellmann, "Interfacial stress state present in a "thin-slice" fibre push-out test," *J. Mater. Sci.*, vol. 27, pp. 3821–3826, July 1992.

[145] "DSC curve isolated on a white background. Differential scanning...," Sept. 2023. [Online; accessed 27. Sep. 2023].

[146] "Thermogravimetric Analysis (TGA) | Leibniz Institute of Polymer Research Dresden," Nov. 2022. [Online; accessed 27. Sep. 2023].

[147] ASTM International, "Standard test method for melt flow rates of thermoplastics by extrusion plastometer," Tech. Rep. D1238-20, American Society for Testing and Materials, 2023. Online; accessed 27. Sep. 2023.

[148] A. Shenoy and D. Saini, "Melt flow index: More than just a quality control rheological parameter. part i," *Advances in Polymer Technology*, vol. 6, no. 1, pp. 1–58, 1986.

[149] S. Wang, L. Capoen, D. R. D'hooge, and L. Cardon, "Can the melt flow index be used to predict the success of fused deposition modelling of commercial poly (lactic acid) filaments into 3d printed materials?," *Plastics, Rubber and Composites*, vol. 47, no. 1, pp. 9–16, 2018.

[150] "Melt Viscosity Properties | TORELINA™ | TORAY PLASTICS | TORAY," June 2023. [Online; accessed 27. Sep. 2023].

[151] I. O. for Standardization, "Implants for surgery — homopolymers, copolymers and blends on poly(lactide) — in vitro degradation testing," tech. rep., International Organization for Standardization, Vernier, Geneva, Switzerland, 2017. [Online; accessed 17. Feb. 2023].

[152] E. L. Boland, R. N. Shirazi, J. A. Grogan, and P. E. McHugh, "Mechanical and Corrosion Testing of Magnesium WE43 Specimens for Pitting Corrosion Model Calibration," *Adv. Eng. Mater.*, vol. 20, p. 1800656, Oct. 2018.

[153] "Gel Permeation Chromatography - an overview | ScienceDirect Topics," Sept. 2023. [Online; accessed 28. Sep. 2023].

[154] "Scanning Electron Microscope | SEM Sample Preparation - ES," Mar. 2023. [Online; accessed 21. Mar. 2023].

[155] ISO10993-12, "Biological evaluation of medical devices — Part 12: Sample preparation and reference materials," tech. rep., 2012. [Online; accessed 16. Feb. 2023].

[156] ISO10993-5, "Biological evaluation of medical devices — Part 5: Tests for in vitro cytotoxicity," tech. rep., 2009. [Online; accessed 16. Feb. 2023].

[157] "BioRender," Sept. 2023. [Online; accessed 28. Sep. 2023].

[158] B. Tyler, D. Gullotti, A. Mangraviti, T. Utsuki, and H. Brem, "Polylactic acid (pla) controlled delivery carriers for biomedical applications," *Advanced Drug Delivery Reviews*, vol. 107, pp. 163–175, 2016.

[159] F. Auricchio and S. Marconi, "3d printing: clinical applications in orthopaedics and traumatology," *EFORT open reviews*, vol. 1, no. 5, pp. 121–127, 2016.

[160] A. Ferrández-Montero, M. Lieblich, J. L. González-Carrasco, R. Benavente, V. Lorenzo, R. Detsch, A. Boccaccini, and B. Ferrari, "Development of biocompatible and fully bioabsorbable pla/mg films for tissue regeneration applications," *Acta biomaterialia*, vol. 98, pp. 114–124, 2019.

[161] A. Ferrández-Montero, M. Lieblich, R. Benavente, J. L. González-Carrasco, and B. Ferrari, "Study of the matrix-filler interface in pla/mg composites manufactured by material extrusion using a colloidal feedstock," *Additive Manufacturing*, vol. 33, p. 101142, 2020.

[162] Á. Díaz-García, J. Law, A. Cota, A. Bellido-Correa, J. Ramírez-Rico, R. Schäfer, and V. Franco, "Novel procedure for laboratory scale production of composite functional filaments for additive manufacturing," *Materials Today Communications*, vol. 24, p. 101049, 2020.

[163] S. Waheed, J. M. Cabot, P. Smejkal, S. Farajikhah, S. Sayyar, P. C. Innis, S. Beirne, G. Barnsley, T. W. Lewis, M. C. Breadmore, *et al.*, "Three-dimensional printing of abrasive, hard, and thermally conductive synthetic microdiamond–polymer composite using low-cost fused deposition modeling printer," *ACS applied materials & interfaces*, vol. 11, no. 4, pp. 4353–4363, 2019.

[164] S. Feliu Jr, A. Pardo, M. Merino, A. Coy, F. Viejo, and R. Arrabal, "Correlation between the surface chemistry and the atmospheric corrosion of az31, az80 and az91d magnesium alloys," *Applied Surface Science*, vol. 255, pp. 4102–4108, 2009.

[165] M. Esmaily, J. Svensson, S. Fajardo, N. Birbilis, G. Frankel, S. Virtanen, R. Arrabal, S. Thomas, and L. Johansson, "Fundamentals and advances in magnesium alloy corrosion," *Progress in Materials Science*, vol. 89, pp. 92–193, 2017.

[166] T. Motoyama, T. Tsukegi, Y. Shirai, H. Nishida, and T. Endo, "Effects of mgo catalyst on depolymerization of poly-l-lactic acid to l, l-lactide," *Polymer degradation and stability*, vol. 92, pp. 1350–1358, 2007.

[167] S. C. Cifuentes, M. Lieblich, F. López, R. Benavente, and J. L. González-Carrasco, "Effect of mg content on the thermal stability and mechanical behaviour of plla/mg composites processed by hot extrusion," *Materials Science and Engineering: C*, vol. 72, pp. 18–25, 2017.

[168] C. G. Fraga, "Relevance, essentiality and toxicity of trace elements in human health," *Molecular Aspects of Medicine*, vol. 26, pp. 235–244, 2005.

[169] B. Hennig, R. Slim, M. Toborek, and L. W. Robertson, "Linoleic acid amplifies polychlorinated biphenyl-mediated dysfunction of endothelial cells," *Journal of Biochemical and Molecular Toxicology*, vol. 13, pp. 83–91, 1999.

[170] N. S. Murni, M. S. Dambatta, S. K. Yeap, G. R. A. Froemming, and H. Hermawan, "Icytotoxicity evaluation of biodegradable zn-3mg alloy toward normal human osteoblast cells," *Materials Science and Engineering C*, vol. 49, pp. 560–566, 2015.

[171] C. Shen, X. Liu, B. Fan, P. Lan, F. Zhou, X. Li, H. Wang, X. Xiao, L. Li, and S. Zhao, "Mechanical properties, in vitro degradation behavior, hemocompatibility and cytotoxicity evaluation of zn-1.2 mg alloy for biodegradable implants," *RSC Advances*, vol. 6, pp. 86410–86419, 2016.

[172] H. Gong, K. Wang, R. Strich, and J. G. Zhou, "In vitro biodegradation behavior, mechanical properties, and cytotoxicity of biodegradable zn-mg alloy," *Journal of Biomedical Materials Research Part B*, vol. 103, pp. 1632–1640, 2015.

[173] S. C. Cifuentes, R. Gavilán, M. Lieblich, R. Benavente, and J. L. González-Carrasco, "In vitro degradation of biodegradable polylactic acid/magnesium composites: Relevance of mg particle shape," *Acta Biomaterialia*, vol. 32, pp. 348–357, 2016.

[174] A. Kovalcik, L. Sangroniz, M. Kalina, K. Skopalova, P. Humpolíček, M. Omastova, N. Mundigler, and A. J. Müller, "Properties of scaffolds prepared by fused deposition modeling of poly (hydroxyalkanoates)," *International Journal of Biological Macromolecules*, 2020.

[175] S. Cesur, F. N. Oktar, N. Ekren, O. Kilic, D. B. Alkaya, S. A. Seyhan, Z. R. Ege, C.-C. Lin, S. E. Kuruca, G. Erdemir, *et al.*, "Preparation and characterization of electrospun polylactic acid/sodium alginate/orange oyster shell composite nanofiber for biomedical application," *Journal of the Australian Ceramic Society*, pp. 1–11, 2019.

[176] S. Farah, D. G. Anderson, and R. Langer, "Physical and mechanical properties of pla, and their functions in widespread applicationsÑa comprehensive review," *Advanced drug delivery reviews*, vol. 107, pp. 367–392, 2016.

[177] M. Li, F. Benn, T. Derra, N. Kroeger, M. Zinser, R. Smeets, J. M. Molina-Aldareguía, A. Kopp, and J. LLorca, "Microstructure, mechanical properties, corrosion resistance and cytocompatibility of WE43 Mg alloy scaffolds fabricated by laser powder bed fusion for biomedical applications," *Materials Science and Engineering C*, vol. 119, p. 111623, 2021.

[178] H. Windhagen, K. Radtke, A. Weizbauer, J. Diekmann, Y. Noll, U. Kreimeyer, R. Schavan, C. Stukenborg-Colsman, and H. Waizy, "Biodegradable magnesium-based screw clinically equivalent to titanium screw in hallux valgus surgery: short term results of the first prospective, randomized, controlled clinical pilot study," *BioMedical Engineering OnLine*, vol. 12, p. 62, 2013.

[179] C. Zhao, H. Wu, J. Ni, S. Zhang, and X. Zhang, "Development of pla/mg composites for orthopedic implant: tunable degradation and enhanced mineralization," *Composites Science and Technology*, vol. 147, pp. 8–15, 2017.

[180] C. Pascual-González, C. Thompson, J. de la Vega, N. B. Churruca, J. P. Fernández-Blázquez, I. Lizarralde, D. Herráez-Molinero, C. González, and J. LLorca, "Processing and properties of PLA/Mg filaments for 3D printing of scaffolds for biomedical applications," *Rapid Prototyping Journal*, vol. 28, pp. 884–894, Dec. 2021.

[181] ISO, "527-1. plastics determination of tensile properties part 1: General principles," *International Organization of Standardization: Geneva, Switzerland*, 2012. [Online; accessed 3. Apr. 2023].

[182] J. Martínez, J. Diéguez, J. Ares, A. Pereira, and J. Pérez, "Modelization and structural analysis of fdm parts," in *AIP Conference Proceedings*, vol. 1431, pp. 842–848, American Institute of Physics, 2012.

[183] J. Butt, Y. Hewavidana, V. Mohaghegh, S. Sadeghi-Esfahlani, and H. Shirvani, "Hybrid manufacturing and experimental testing of glass fiber enhanced thermoplastic composites," *Journal of Manufacturing and Materials Processing*, vol. 3, no. 4, p. 96, 2019.

[184] J. L. Colón Quintana, T. Heckner, A. Chrupala, J. Pollock, S. Goris, and T. Osswald, "Experimental study of particle migration in polymer processing," *Polymer Composites*, vol. 40, no. 6, pp. 2165–2177, 2019.

[185] S. Goris and T. Osswald, "Process-induced fiber matrix separation in long fiber-reinforced thermoplastics," *Composites Part A: Applied Science and Manufacturing*, vol. 105, pp. 321–333, 2018.

[186] J.-T. Yeh, C.-Y. Huang, W.-l. Chai, and K.-N. Chen, "Plasticized properties of poly (lactic acid) and triacetine blends," *Journal of Applied Polymer Science*, vol. 112, no. 5, pp. 2757–2763, 2009.

[187] M. Baiardo, G. Frisoni, M. Scandola, M. Rimelen, D. Lips, K. Ruffieux, and E. Wintermantel, "Thermal and mechanical properties of plasticized poly (l-lactic acid)," *Journal of Applied Polymer Science*, vol. 90, no. 7, pp. 1731–1738, 2003.

[188] R. Requena, A. Jiménez, M. Vargas, and A. Chiralt, "Effect of plasticizers on thermal and physical properties of compression-moulded poly [(3-hydroxybutyrate)-co-(3-hydroxyvalerate)] films," *Polymer Testing*, vol. 56, pp. 45–53, 2016.

[189] F. Carrasco, P. Pagès, J. Gámez-Pérez, O. Santana, and M. L. Maspoch, "Processing of poly (lactic acid): Characterization of chemical structure, thermal stability and mechanical properties," *Polymer Degradation and Stability*, vol. 95, no. 2, pp. 116–125, 2010.

[190] L.-T. Lim, R. Auras, and M. Rubino, "Processing technologies for poly (lactic acid)," *Progress in polymer science*, vol. 33, no. 8, pp. 820–852, 2008.

[191] L. Siqueira, F. R. Passador, M. M. Costa, A. O. Lobo, and E. Sousa, "Influence of the addition of β-TCP on the morphology, thermal properties and cell viability of poly (lactic acid) fibers obtained by electrospinning," *Mater. Sci. Eng., C*, vol. 52, pp. 135–143, July 2015.

[192] C. Pascual-González, J. de la Vega, C. Thompson, J. P. Fernández-Blázquez, D. Herráez-Molinero, N. Biurrun, I. Lizarralde, J. S. del Río, C. González, and J. LLorca, "Processing and mechanical properties of novel biodegradable poly-lactic acid/Zn 3D printed scaffolds for application in tissue regeneration," *J. Mech. Behav. Biomed. Mater.*, vol. 132, pp. 105–115, Aug. 2022.

[193] E. H. Backes, L. D. N. Pires, C. A. G. Beatrice, L. C. Costa, F. R. Passador, and L. A. Pessan, "Fabrication of biocompatible composites of poly (lactic acid)/hydroxyapatite envisioning medical applications," *Polymer Engineering & Science*, vol. 60, no. 3, pp. 636–644, 2020.

[194] E. H. Backes, L. de Nóbile Pires, H. S. Selistre-de Araujo, L. C. Costa, F. R. Passador, and L. A. Pessan, "Development and characterization of printable pla/β-tcp bioactive composites for bone tissue applications," *Journal of Applied Polymer Science*, vol. 138, no. 5, p. 49759, 2021.

[195] A. Abdal-hay, K. H. Hussein, L. Casettari, K. A. Khalil, and A. S. Hamdy, "Fabrication of novel high performance ductile poly(lactic acid) nanofiber scaffold coated with poly(vinyl alcohol) for tissue engineering applications," *Mater. Sci. Eng., C*, vol. 60, pp. 143–150, Mar. 2016.

[196] K. M. Zadeh, A. S. Luyt, L. Zarif, R. Augustine, A. Hasan, M. Messori, M. K. Hassan, and H. C. Yalcin, "Electrospun polylactic acid/date palm polyphenol extract nanofibres for tissue engineering applications," *emergent mater.*, vol. 2, pp. 141–151, June 2019.

[197] L. H. Sperling, *Introduction to Physical Polymer Science*. Wiley, Nov. 2005.

[198] T. Serra, M. Ortiz-Hernandez, E. Engel, J. A. Planell, and M. Navarro, "Relevance of peg in pla-based blends for tissue engineering 3d-printed scaffolds," *Materials Science and Engineering: C*, vol. 38, pp. 55–62, 2014.

[199] A. Bacher, "Effects of body temperature on blood gases," *Intensive Care Medicine*, vol. 31, pp. 24–27, Jan. 2005.

[200] S. Farah, D. G. Anderson, and R. Langer, "Physical and mechanical properties of PLA, and their functions in widespread applications — A comprehensive review," *Advanced Drug Delivery Reviews*, vol. 107, pp. 367–392, Dec. 2016.

[201] K. A. Athanasiou, C. M. Agrawal, F. A. Barber, and S. S. Burkhart, "Orthopaedic applications for PLA-PGA biodegradable polymers," *Arthroscopy: The Journal of Arthroscopic & Related Surgery*, vol. 14, pp. 726–737, Oct. 1998.

[202] B. S. Zolnik and D. J. Burgess, "Effect of acidic pH on PLGA microsphere degradation and release," *J. Controlled Release*, vol. 122, pp. 338–344, Oct. 2007.

[203] A. C. Vieira, J. C. Vieira, J. M. Ferra, F. D. Magalhães, R. M. Guedes, and A. T. Marques, "Mechanical study of PLA–PCL fibers during in vitro degradation," *J. Mech. Behav. Biomed. Mater.*, vol. 4, pp. 451–460, Apr. 2011.

[204] N. T. Kirkland, N. Birbilis, and M. P. Staiger, "Assessing the corrosion of biodegradable magnesium implants: A critical review of current methodologies and their limitations," *Acta Biomaterialia*, vol. 8, pp. 925–936, 2012.

[205] M. Li, F. Benn, T. Derra, N. Kröger, M. Zinser, R. Smeets, J. M. Molina-Aldareguía, A. Kopp, and J. LLorca, "Microstructure, mechanical properties, corrosion resistance and cytocompatibility of WE43 Mg alloy scaffolds fabricated by laser powder bed fusion for biomedical applications," *Materials Science and Engineering C*, vol. 119, pp. 111–123, 2021.

[206] C. Wang, W. Xu, D. Höche, M. L. Zheludkevich, and S. V. Lamaka, "Exploring the contribution of oxygen reduction reaction to mg corrosion by modeling assisted local analysis," *Journal of Magnesium and Alloys*, vol. 11, pp. 100–109, 2023.

[207] W. Ali, M. Echeverry-Rendón, A. Kopp, C. González, and J. LLorca, "Exploring the contribution of oxygen reduction reaction to mg corrosion by modeling assisted local analysis," *npj Materials Degradation*, p. submitted for publication, 2023.

[208] T. Motoyama, T. Tsukegi, Y. Shirai, H. Nishida, and T. Endo, "Effects of mgo catalyst on depolymerization of poly-l-lactic acid to l, l-lactide," *Polymer Degradation and Stability*, vol. 92, no. 7, pp. 1350–1358, 2007.

[209] J. Kubásek, D. Dvorský, J. Šedý, S. Msallamová, J. Levorová, R. Foltán, and D. Vojtěch, "The Fundamental Comparison of Zn–2Mg and Mg–4Y–3RE Alloys as a Perspective Biodegradable Materials," *Materials*, vol. 12, pp. 22–30, Nov. 2019.

[210] H. Gong, K. Wang, R. Strich, and J. G. Zhou, "In vitro biodegradation behavior, mechanical properties, and cytotoxicity of biodegradable Zn-Mg alloy," *Journal of Biomedical Materials Research Part B*, vol. 103, pp. 1632–1640, Nov. 2015.

[211] K. Van de Velde and P. Kiekens, "Biopolymers: overview of several properties and consequences on their applications," *Polymer Testing*, vol. 21, pp. 433–442, Jan. 2002.

[212] G. Perego, G. D. Cella, and C. Bastioli, "Effect of molecular weight and crystallinity on poly(lactic acid) mechanical properties," *J. Appl. Polym. Sci.*, vol. 59, pp. 37–43, Jan. 1996.

[213] W. G. Perkins, N. J. Capiati, and R. S. Porter, "The effect of molecular weight on the physical and mechanical properties of ultra-drawn high density polyethylene," *Polymer Engineering & Science*, vol. 16, no. 3, pp. 200–203, 1976.

[214] "Stringing or Oozing | Simplify3D Software," Feb. 2023. [Online; accessed 3. Apr. 2023].

[215] R. Vaid, E. Yildirim, M. A. Pasquinelli, and M. W. King, "Hydrolytic Degradation of Polylactic Acid Fibers as a Function of pH and Exposure Time," *Molecules*, vol. 26, pp. 75–87, Dec. 2021.

[216] R. W. Nunes, J. R. Martin, and J. F. Johnson, "Influence of molecular weight and molecular weight distribution on mechanical properties of polymers," *Polym. Eng. Sci.*, vol. 22, pp. 205–228, Mar. 1982.

[217] M. Mazaheri, N. Eslahi, F. Ordikhani, E. Tamjid, and A. Simchi, "Nanomedicine applications in orthopedic medicine: state of the art," *Int. J. Nanomed.*, vol. 10, pp. 6039–6054, 2015.

[218] H. Khellafi, M. M. Bouziane, A. Djebli, A. Mankour, and E. B. O. Chikh, "Investigation of Mechanical Behaviour of the Bone Cement (PMMA) under Combined Shear and Compression Loading," *Journal of Biomimetics, Biomaterials and Biomedical Engineering*, vol. 41, pp. 37–48, Apr. 2019.

[219] R. Oftadeh, M. Perez-Viloria, J. C. Villa-Camacho, A. Vaziri, and A. Nazarian, "Biomechanics and mechanobiology of trabecular bone: a review," *J. Biomech. Eng.*, vol. 137, pp. 108021–1080215, Jan. 2015.

[220] C. W. Hull, "Apparatus for production of three-dimensional objects by stereolithography," *United States Patent, Appl., No. 638905, Filed*, 1984.

[221] R. Matsuzaki, M. Ueda, M. Namiki, T.-K. Jeong, H. Asahara, K. Horiguchi, T. Nakamura, A. Todoroki, and Y. Hirano, "Three-dimensional printing of continuous-fiber composites by in-nozzle impregnation," *Sci. Rep.*, vol. 6, pp. 1–7, Mar. 2016.

[222] B. N. Turner, R. Strong, and S. A. Gold, "A review of melt extrusion additive manufacturing processes: I. process design and modeling," *Rapid prototyping journal*, vol. 20, no. 3, pp. 192–204, 2014.

[223] X. Tian, T. Liu, C. Yang, Q. Wang, and D. Li, "Interface and performance of 3D printed continuous carbon fiber reinforced PLA composites," *Composites Part A*, vol. 88, pp. 198–205, Sept. 2016.

[224] M. Lay, N. L. N. Thajudin, Z. A. A. Hamid, A. Rusli, M. K. Abdullah, and R. K. Shuib, "Comparison of physical and mechanical properties of PLA, ABS and nylon 6 fabricated using fused deposition modeling and injection molding," *Composites Part B*, vol. 176, p. 107341, Nov. 2019.

[225] Z. Weng, J. Wang, T. Senthil, and L. Wu, "Mechanical and thermal properties of abs/montmorillonite nanocomposites for fused deposition modeling 3d printing," *Materials & Design*, vol. 102, pp. 276–283, 2016.

[226] S. Liparoti, V. Speranza, A. Sorrentino, and G. Titomanlio, "Mechanical properties distribution within polypropylene injection molded samples: Effect of mold temperature under uneven thermal conditions," *Polymers*, vol. 9, no. 11, p. 585, 2017.

[227] S. C. Cifuentes, R. Gavilán, M. Lieblich, R. Benavente, and J. L. González-Carrasco, "In vitro degradation of biodegradable polylactic acid/magnesium composites: Relevance of Mg particle shape," *Acta Biomater.*, vol. 32, pp. 348–357, Mar. 2016.

[228] S. C. Cifuentes, M. Lieblich, F. A. López, R. Benavente, and J. L. González-Carrasco, "Effect of Mg content on the thermal stability and mechanical behaviour of PLLA/Mg composites processed by hot extrusion," *Mater. Sci. Eng., C*, vol. 72, pp. 18–25, Mar. 2017.

[229] Á. Díaz-García, J. Y. Law, A. Cota, A. Bellido-Correa, J. Ramírez-Rico, R. Schäfer, and V. Franco, "Novel procedure for laboratory scale production of composite functional filaments for additive manufacturing," *Mater. Today Commun.*, vol. 24, p. 101049, Sept. 2020.

[230] S. Waheed, J. M. Cabot, P. Smejkal, S. Farajikhah, S. Sayyar, P. C. Innis, S. Beirne, G. Barnsley, T. W. Lewis, M. C. Breadmore, and B. Paull, "Three-Dimensional Printing of Abrasive, Hard, and Thermally Conductive Synthetic Microdiamond–Polymer Composite Using Low-Cost Fused Deposition Modeling Printer," *ACS Appl. Mater. Interfaces*, vol. 11, pp. 4353–4363, Jan. 2019.

[231] X. Wei, D. Li, W. Jiang, Z. Gu, X. Wang, Z. Zhang, and Z. Sun, "3D Printable Graphene Composite," *Sci. Rep.*, vol. 5, pp. 1–7, July 2015.

[232] C. Thompson, G. Domínguez, P. Bardisa, Y. Liu, J. P. Fernández-Blázquez, J. Sánchez del Río, M. Echeverry-Rendon, C. González, and J. Llorca, "Medical grade 3D printable bioabsorbable PLDL/Mg and PLDL/Zn composites for biomedical applications," *Submitted for Publication*, Aug. 2023.

[233] N. Jayanth, P. Senthil, and B. Mallikarjuna, "Experimental investigation on the application of FDM 3D printed conductive ABS-CB composite in EMI shielding," *Radiat. Phys. Chem.*, vol. 198, pp. 110263–110273, Sept. 2022.

[234] K. Prashantha and F. Roger, "Multifunctional properties of 3D printed poly(lactic acid)/graphene nanocomposites by fused deposition modeling," *Journal of Macromolecular Science, Part A*, vol. 54, pp. 24–29, Jan. 2017.

[235] S. W. Kwok, K. H. H. Goh, Z. D. Tan, S. T. M. Tan, W. W. Tjiu, J. Y. Soh, Z. J. G. Ng, Y. Z. Chan, H. K. Hui, and K. E. J. Goh, "Electrically conductive filament for 3D-printed circuits and sensors," *Appl. Mater. Today*, vol. 9, pp. 167–175, Dec. 2017.

[236] Z. Viskadourakis, K. C. Vasilopoulos, E. N. Economou, C. M. Soukoulis, and G. Kenanakis, "Electromagnetic shielding effectiveness of 3D printed polymer composites," *Appl. Phys. A*, vol. 123, pp. 1–7, Dec. 2017.

[237] O. S. Carneiro, A. F. Silva, and R. Gomes, "Fused deposition modeling with polypropylene," *Mater. Des.*, vol. 83, pp. 768–776, Oct. 2015.

[238] H. L. Tekinalp, V. Kunc, G. M. Velez-Garcia, C. E. Duty, L. J. Love, A. K. Naskar, C. A. Blue, and S. Ozcan, "Highly oriented carbon fiber–polymer composites via additive manufacturing," *Compos. Sci. Technol.*, vol. 105, pp. 144–150, Dec. 2014.

[239] T. Cersoli, B. Yelamanchi, E. MacDonald, J. G. Carrillo, and P. Cortes, "3D printing of a continuous fiber-reinforced composite based on a coaxial Kevlar/PLA filament," *Composites and Advanced Materials*, vol. 30, pp. 263–273, Jan. 2021.

[240] "3D Printing Materials | Markforged," May 2023. [Online; accessed 8. May 2023].

[241] X. Li, W. Yu, L. Han, C. Chu, J. Bai, and F. Xue, "Degradation behaviors of Mg alloy wires/PLA composite in the consistent and staged dynamic environments," *Mater. Sci. Eng., C*, vol. 103, pp. 765–775, Oct. 2019.

[242] H. Cai, X. Li, F. Xue, C. Chu, C. Guo, J. Bai, and X. Zhang, "In Vitro Study on Cytocompatibility of Mg Wire/Poly(Lactic Acid) Composite Rods," *J. Mater. Eng. Perform.*, vol. 30, pp. 7214–7222, Oct. 2021.

[243] J. Delmonte, *Metal/Polymer Composites*. Springer US, 1990.

[244] X. Xu, "Machine Tool 4.0 for the new era of manufacturing," *Int. J. Adv. Manuf. Technol.*, vol. 92, pp. 1893–1900, Sept. 2017.

[245] C. M. Medina, J. M. Molina-Aldareguía, C. González, M. F. Melendrez, P. Flores, and J. LLorca, "Comparison of push-in and push-out tests for measuring interfacial shear strength in nano-reinforced composite materials," *Journal of Composite Materials*, vol. 50, no. 12, pp. 1651–1659, 2016.

[246] C. Li, C. Guo, V. Fitzpatrick, A. Ibrahim, M. J. Zwierstra, P. Hanna, A. Letchtig, S. J. Lin, and D. L. Kaplan, "Design of biodegradable, implantable devices towards clinical transition," *Nature Review Materials*, vol. 5, pp. 61–81, 2020.

[247] R. Singh, M. J. Bathaei, E. Istif, and L. Beker, "A review of bioresorbable implantable medical devices: materials, fabrication and implementation," *Advanced Healtcare Materials*, vol. 9, pp. 200–208, 2020.

[248] H. Cai, Y. Zhang, X. Li, J. Meng, F. Xue, C. Chu, L. Tao, and J. Bai, "Self-reinforced biodegradable Mg-2Zn alloy wires/polylactic acid composite for orthopedic implants," *Compos. Sci. Technol.*, vol. 162, pp. 198–205, July 2018.

[249] H. Cai, Y. Zhang, J. Meng, X. Li, F. Xue, C. Chu, L. Tao, and J. Bai, "Enhanced fully-biodegradable Mg/PLA composite rod: Effect of surface modification of Mg-2Zn wire on the interfacial bonding," *Surf. Coat. Technol.*, vol. 350, pp. 722–731, Sept. 2018.

[250] X. Li, C. Chu, Y. Wei, C. Qi, J. Bai, C. Guo, F. Xue, P. Lin, and P. K. Chu, "In vitro degradation kinetics of pure PLA and Mg/PLA composite: Effects of immersion temperature and compression stress," *Acta Biomater.*, vol. 48, pp. 468–478, Jan. 2017.

[251] W. Ali, M. Li, L. Tillmann, T. Mayer, C. González, J. LLorca, and A. Kopp, "Bioabsorbable WE43 Mg alloy wires modified by continuous plasma-electrolytic oxidation for implant applications. Part I: Processing, microstructure and mechanical properties," *Biomaterials Advances*, vol. 146, pp. 21–33, Mar. 2023.

[252] W. K. Ramp, L. G. Lenz, and K. K. Kaysinger, "Medium pH modulates matrix, mineral, and energy metabolism in cultured chick bones and osteoblast-like cells," *Bone Miner.*, vol. 24, pp. 59–73, Jan. 1994.

[253] Z. Zhang, Q. Lai, Y. Li, C. Xu, X. Tang, J. Ci, S. Sun, B. Xu, and Y. Li, "Acidic pH environment induces autophagy in osteoblasts," *Sci. Rep.*, vol. 7, pp. 1–9, Apr. 2017.

[254] D. Mei, S. V. Lamaka, X. Lu, and M. L. Zheludkevich, "Selecting medium for corrosion testing of bioabsorbable magnesium and other metals – A critical review," *Corros. Sci.*, vol. 171, pp. 10–22, July 2020.

[255] C. Wang, W. Xu, D. Höche, M. L. Zheludkevich, and S. V. Lamaka, "Exploring the contribution of oxygen reduction reaction to Mg corrosion by modeling assisted local analysis," *J. Magnesium Alloys*, vol. 11, pp. 100–109, Jan. 2023.

[256] A. Sabik, M. Rucka, A. Andrzejewska, and E. Wojtczak, "Tensile failure study of 3D printed PLA using DIC technique and FEM analysis," *Mech. Mater.*, vol. 175, p. 104506, Dec. 2022.

[257] D. Li, Y. Jiang, S. Lv, X. Liu, J. Gu, Q. Chen, and Y. Zhang, "Preparation of plasticized poly (lactic acid) and its influence on the properties of composite materials," *PLoS One*, vol. 13, no. 3, pp. 46–57, 2018.

[258] A. Moetazedian, A. Gleadall, X. Han, and V. V. Silberschmidt, "Effect of environment on mechanical properties of 3D printed polylactide for biomedical applications," *J. Mech. Behav. Biomed. Mater.*, vol. 102, pp. 10–20, Feb. 2020.

[259] M. Grasso, L. Azzouz, P. Ruiz-Hincapie, M. Zarrelli, and G. Ren, "Effect of temperature on the mechanical properties of 3D-printed PLA tensile specimens," *Rapid Prototyping Journal*, vol. 24, pp. 1337–1346, Oct. 2018.

[260] S. St. Lawrence, J. L. Willett, and C. J. Carriere, "Effect of moisture on the tensile properties of poly(hydroxy ester ether)," *Polymer*, vol. 42, pp. 5643–5650, June 2001.

[261] O. Vyavahare, D. Ng, and S. L. Hsu, "Analysis of Structural Rearrangements of Poly(lactic acid) in the Presence of Water," *J. Phys. Chem. B*, vol. 118, pp. 4185–4193, Apr. 2014.

[262] A. Herrera-Gómez, G. Velázquez-Cruz, and M. Martín-Polo, "Analysis of the water bound to a polymer matrix by infrared spectroscopy," *Journal of Applied Physics*, vol. 89, no. 10, p. 5431 – 5437, 2001. Cited by: 40.

[263] V. Chandran, J. Kalman, K. Fayazbakhsh, and H. Bougherara, "A comparative study of the tensile properties of compression molded and 3D printed PLA specimens in dry and water saturated conditions," *J. Mech. Sci. Technol.*, vol. 35, pp. 1977–1985, May 2021.